MODELLING CARBIDE PRECIPITATION IN ALLOY STEELS

By
Nobuhiro Fujita
Darwin College, Cambridge

University of Cambridge
Department of Materials Science and Metallurgy
Pembroke Street, Cambridge CB2 3QZ

A dissertation submitted for the degree of Doctor of Philosophy at the University of Cambridge
February 2000

PREFACE

This dissertation is submitted for the degree of Doctor of Philosophy at the University of Cambridge. The research described herein was conducted under the supervision of Professor H. K. D. H. Bhadeshia in the Department of Materials Science and Metallurgy, University of Cambridge, between October 1996 and October 1998.

This work is to the best of my knowledge original, except where acknowledgement and references are made to previous work. Neither this, nor any substantially similar dissertation has been or is being submitted for any degree, diploma or other qualification at any other university. The work has been presented in the following publications:

Fujita, N and Bhadeshia, H. K. D. H.: *Advanced Heat Resistant Steel for Power Generation,* ed. Viswanathan, R. and Nutting, J., The Institute of Materials (1998) 223–233.

Fujita, N and Bhadeshia, H. K. D. H.: *Materials Science and Technology* **15** (1999) 627-634.

Fujita, N and Bhadeshia, H. K. D. H.: *Modelling of Microstructural Evolution in Creep Resistant Materials,* ed. Strang, A. and McLean, M., The Institute of Materials, London (1999) 105-114.

Nobu. Fujita

Nobuhiro Fujita

February 2000

ACKNOWLEDGEMENTS

I would like to thank Professors A. H. Windle and C. J. Humphreys for the provision of laboratory facilities in the Department of Materials Science and Metallurgy at the University of Cambridge. I would like to express my sincere thanks to my supervisor Professor H. K. D. H. Bhadeshia for his great encouragement. I am indebted to Dr J. D. Robson for his support throughout this work.

I gratefully acknowledge Dr Satoshi ITO and Dr Manabu TAKAHASHI at Nippon Steel Corporation for giving me the opportunity to study at the University of Cambridge. I would like also to thank Mr K. Kimura for his kind help with experimental work at Nippon Steel Corporation. I am indebted to grants from the Personnel Division of Nippon Steel Corporation and would like to acknowledge the generosity of the organisation for the financial support.

I would like to express my appreciation to all members of the PT-Group in Cambridge for the help and friendship, in particular, Dr Kazutoshi Ichikawa (now at Nippon Steel Corporation), Dr Mike Lord, Dr Catherine Neal, Mr Philippe Opdenacker, Mr Harasha Sree Lalam and Eur. Ing. John Street. Many thanks also to my other friends.

I wish to express my thanks to Hiromi, my wife for her dedicated support to my life in Cambridge. I am also grateful to my lovely three daughters, Miku, Sayo and Kana for their encouragement. Finally, I deeply thank my parents for their cordial encouragement throughout my life.

ABSTRACT

The purpose of the work in this thesis was to model carbide precipitation in practical steels.

There is a brief introduction of previous work about modelling precipitation in Chapter 1. The importance of precipitation in industrial steels is introduced with typical applications, including high strength low alloy steels and secondary hardening steels of the kind used in power plant.

The basic theory for precipitation processes, including a recent theory for simultaneous precipitation reactions, is reviewed in Chapter 2. Theory about the nucleation and growth of individual particles is on the whole well–established. There has been some significant progress in the theory for the overall transformation kinetics of transformations which happen at the same time. The new theory is an adaptation of the classical Avrami model. However, the concepts have only been tested against limited data so in the present work the theory has been validated with new experimental data on a number of power plant steels (Chapter 4). The experimental procedures are described in Chapter 3.

There are a number of fundamental problems which are outside of the framework of simultaneous transformations, associated with the growth of individual phases, which in the present work have been found to prevent accurate solutions. For example, new methodologies have been developed for the growth of needle–shaped and spherical precipitates, taking proper account of mass balance during multicomponent diffusion–controlled growth whilst at the same time dealing with the associated capillarity effects. These methods have been tested on molybdenum carbide precipitation in martensite (Chapter 5) and on niobium carbide precipitation in austenite (Chapter 6). Both were satisfactorily validated against published experimental data. This includes the estimation of changes in the volume fractions and particle sizes of equilibrium alloy carbides in ternary steels with coarsening emerging as a natural consequence of capillarity, without any need for a separate explicit treatment.

Precipitate fractions are quite small in typical power plant steels. This has been used to advantage by eliminating the distinction between extended and real space, thus allowing the precipitate size distribution and number densities to be estimated. In the course of this work, it was discovered that most previous treatments have an incorrect treatment of the number density of nucleation sites by many orders of magnitude. New calculations have been carried out which show the proper physical behaviour and good agreement with experimental data,

not only about volume fractions but also particle sizes for each alloy carbide in 3Cr1.5Mo and $2\frac{1}{4}$Cr1Mo steels.

Computer programs incorporating all the research have been documented and placed on a materials algorithms library for free access.

Contents

NOMENCLATURE AND ABBREVIATIONS

A	Area of collector–plate
A_1	Constant relating the volume fractions of two phases precipitating simultaneously
A_2	Constant relating solubility product
A_{r1}	Transformation temperature for ferrite + austenite $\rightarrow$ ferrite + cementite
A_{r3}	Transformation temperature for austenite $\rightarrow$ ferrite + austenite
B_1	Constant relating the volume fractions of two phases precipitating simultaneously
B_2	Constant relating solubility product
C	Carbon
C_1	Constant relating parabolic growth
C_2	Constant relating the volume fractions of two phases precipitating simultaneously
C_l	Speed of light in a vacuum
c	Concentration of solute atoms
c_C	Concentration of carbon
c_M	Concentration of substitutional solute M
c_t	Concentration of carbon for cementite with thickness d
$c^{\alpha\beta}$	Concentration of solute in α in equilibrium with β
$c_C^{\alpha\beta}$	Concentration of carbon in α in equilibrium with β
$c_M^{\alpha\beta}$	Concentration of substitutional solute M in α in equilibrium with β
$c_r^{\alpha\beta}$	Concentration of solute in α in equilibrium with a curved β interface
$c_p^{\alpha\gamma}$	Concentration of solute in α in equilibrium with γ for paraequilibrium
$\overline{c}$	Mean concentration of solute
$\overline{c}_p$	Mean concentration of solute with paraequilibrium cementite
$\overline{c}'$	Instantaneous mean concentration of solute due to soft–impingement
D	Diffusion coefficient
D_0	Pre–exponent factor for diffusion coefficient
D_C	Diffusion coefficient for carbon
D_M	Diffusion coefficient for substitutional solute M
D_b	Diffusion coefficient for grain boundary diffusion
D_v	Diffusion coefficient for volume diffusion
d	Thickness of M_3C plate
d_{hkl}	Spacing of hkl planes
d_v	Size of collector–plate

$\overline{d}$	Mean distance between particles
e	Charge of an electron
G	Free energy
G^*	Free energy barrier to nucleation
G^β	Free energy for β
G_r^β	Free energy for β with a curved interface of radius r
ΔG	Free energy change
ΔG_0	Overall free energy change for transformation
$\Delta G_{0\beta}$	Overall free energy change for β precipitation per mole
ΔG_β	Overall free energy change for β precipitation per mole due to soft–impingement
ΔG_n	Driving force for nucleation per mole by common tangent
ΔG_m	Driving force for nucleation per mole by parallel tangent
ΔG_v	Chemical driving force for nucleation per unit volume of nucleus
h	Planck's constant
hkl	Lattice plane indices
I	Nucleation rate per unit volume
I'	Instantaneous nucleation rate per unit volume
J	Diffusion flux across a unit area
k	Boltzmann's constant
$\overline{l}$	Mean needle length
L	Camera length
L_{gb}	Length of grain boundary per unit volume
m	Constant in Zener–Hillert equation
m_a	Time exponent in Avrami equation
m_c	Constant in Zener–Hillert equation
m_e	Electron rest mass
N	Number density of sites or particles
N_0	Initial number density of sites
$N_{0\beta}$	Initial number density of sites for β
N_c	Number density of grain boundary corners
N_s	Number of particles per unit area
N_v	Number density of particles
N_V	Fixed number density of sites
N_β	Number density of particles for β

Q	Activation energy (for diffusion or nucleation)
R	Molar gas constant
R_{hkl}	Measured distance between transmitted and diffracted spots on micrograph
R_l	Length of a precipitate on grain boundaries
r	Radius
r^*	Critical radius for viable nucleus
r_0	Average particle size before Ostwald ripening
r_c	Critical radius of curvature
r^f	Final radius
r^I	Instantaneous radius
r_m	Top radius giving maximum growth rate
$\overline{r}$	Mean particle radius
S	Thickness of a precipitate on grain boundaries
S_{gb}	Area of grain boundary per unit volume
T	Temperature
t	Time
t_c	Time for enrichment of solute to cementite with thickness d
V	Volume fraction
V_{ac}	Accelerating voltage
V^{eq}	Equilibrium volume fraction
V^{Max}	Maximum volume fraction
V_β	Volume fraction of β
V_β^e	Extended volume fraction of β
V'	Instantaneous volume fraction
v	Growth rate
v^β	Molar volume of β
w_c	Carbon concentration in wt%
w_τ	Volume of each particle nucleated at time of τ
$\overline{x}$	Mean diameter of particles
z	Position co–ordinate
z^*	Instantaneous position
z_d	Effective diffusion distance
α	Ferrite
α_3	3–dimensional parabolic growth constant

Γ	Capillarity coefficient
γ	Austenite
δ	Thickness of grain boundary
λ	Electron wavelength
κ	Constant used in the general form of the Avrami equation
μ_M^α	Chemical potential of solute M in α
$\mu_{M,r}^\alpha$	Chemical potential of solute M in α with a curved interface
Ω	Dimensionless supersaturation
Ω_r	Dimensionless supersaturation with capillarity effect
Φ	Extent of reaction parameter
ϕ	Aspect ratio of needle
σ	Interfacial energy per unit area
τ	Incubation time
θ_B	Bragg angle
ζ	Volume fraction untransformed
$\frac{dO}{dn}$	Change of interface area with an extra atom transformed from matrix
HSLA	High strength low alloy
MTDATA	Metallurgical and Thermochemical Databank
SCE	Saturated calomel electrode
SGTE	Scientific Group Thermodata Europe
TEM	Transmission electron microscopy
TTP	Time–temperature–precipitation

CHAPTER ONE

Introduction

1.1 Aim of this work

Steels are the most important and popular structural materials because they are cheap and their mechanical properties can be controlled over a very wide range of values. The mechanical properties are dependent on the microstructure which in turn can be varied by changing the chemical composition and thermomechanical processing conditions. Therefore, microstructure control is very important for alloy design (Fig. 1.1).

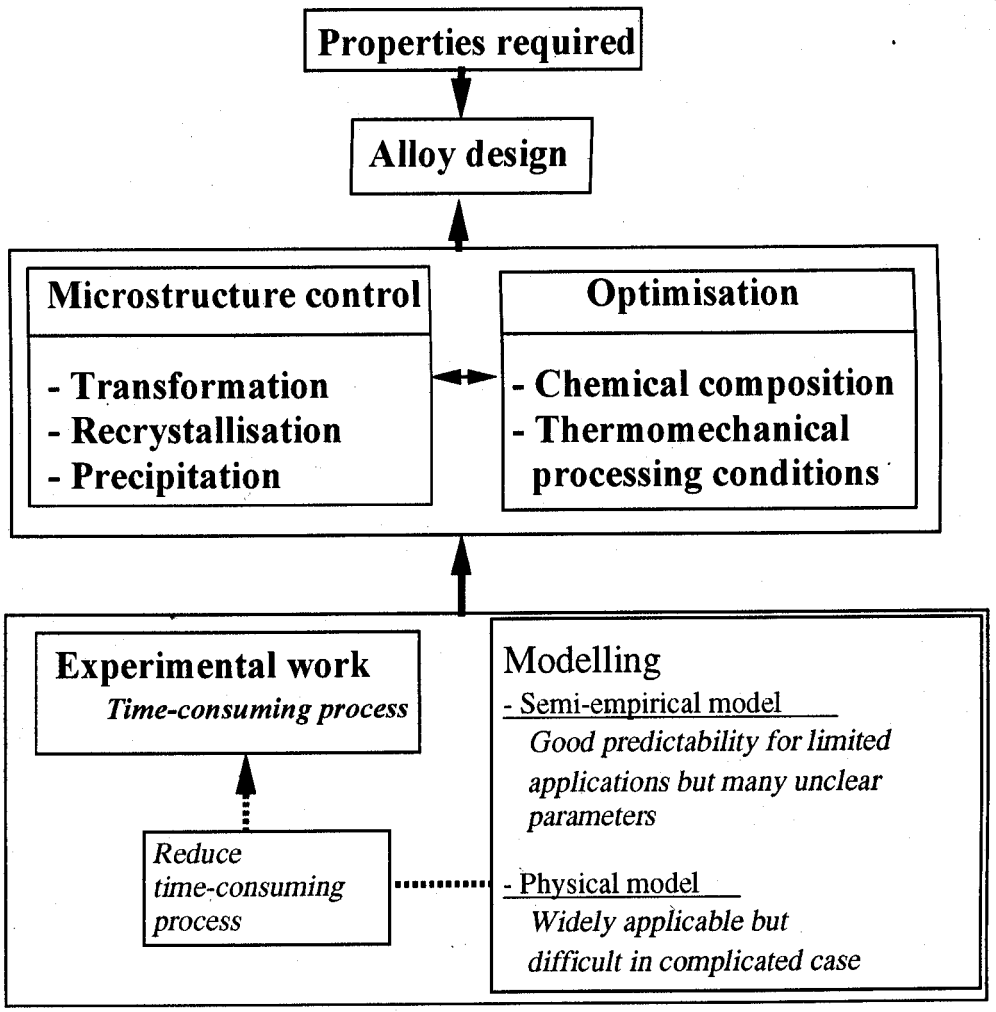

Fig. 1.1: Schematic illustration for alloy design.

Precipitation reactions are important in design of suitable microstructures for specific applications. Table 1.1 shows some of the typical examples of precipitation systems in several commercial steels. As shown in Table 1.1, alloy carbide precipitation has played an important role in industrial steels, especially for strengthening micro–alloyed steels (High Strength Low Alloy steel, termed HSLA) and secondary–hardened heat resistant steels. A great deal of experimental work generally is often required to get the desired properties. Modelling is very useful method to reduce such time–consuming experimental work (Fig. 1.1).

Steels	Precipitates concerned	Role of precipitates	Industrial application
Interstitial Free Steel	TiC, NbC, TiN, NbN	Reduce carbon and nitrogen for good formability	Panel for automobiles
High Strength Low Alloy Steel	TiC, NbC, VC, VN	Precipitation strengthening	Pipe lines
Heat resistant Steel	MC, M_2C, M_7C_3, $M_{23}C_6$, Intermetallic compounds	Strengthening for creep resistance	Power plant
Stainless Steel	$M_{23}C_6$, MC, Intermetallic compounds	Creep resistance, Corrosion resistance	Chemical plant Power plant

Table 1.1: Examples of alloy carbides in commercial steels.

Table 1.2 shows some examples of previous work on the modelling of precipitates in steels (Le Bon *et al.*, 1975; Dutta and Sellars, 1987; Saito *et al.*, 1988; Akamatsu *et al.*, 1992; Liu and Jonas, 1988; Miyahara *et al.*, 1995; Okamoto and Suehiro, 1998; Gustafson *et al.*, 1998). Most of these deal with the precipitate as an equilibrium phase and some of them use overall transformation theory based on the extended volume concept (Kolmogorov, 1937; Johnson and Mehl, 1939; Avrami, 1939, 1940, 1941). Recently, Sellars pointed out that semi–empirical models have been applied successfully for HSLA steel but there is not still a full understanding (1998). Dutta and Sellers modelled NbC precipitation in austenite during hot deformation (1987). This was a semi–empirical model and in good agreement with experiments obtained by several researchers. However, it was necessary to adjust several parameters which did not always have clear physical meaning. This kind of a semi–empirical model must be limited in its application. Akamatsu *et al.* also suggested a model for NbC precipitating on dislocations during hot deformation in austenite. This model was based on nucleation and growth theory. The nucleation sites were assumed to be on dislocations which changed as recovery proceeded.

Authors	Precipitate	Steel	Conditions	Comments
A. Le. Bon J. Vernis C. Rossard	NbC	HSLA	Deformation at high temperatures	The relationship between fraction recrystallised and Nb precipitation kinetics were investigated. Experimental data were related using the KJMA theory.
B. Dutta C. M. Sellars	NbC	HSLA	Deformation at high temperatures	Initial nucleation density of NbC was determined experimentally and the time for 0.05% of equilibrium fraction was obtained with Zener-Hollmon parameter.
Y. Saito C. Shiga T. Enami	NbC	HSLA	Deformation at high temperatures	Volume fraction of NbC was calculated by classical nucleation and growth using the KJMA theory.
S. Akamatsu T. Senuma M. Hasebe	NbC	HSLA	Deformation at high temperatures	Volume fraction and size of NbC were calculated by classical nucleation and diffusion–controlled growth.
R. Okamoto H. Suehiro	Nb(C,N)	HSLA	Isothermal heat-treatment	Volume fraction and size of NbC were calculated by classical nucleation, diffusion–controlled growth and capillarity.
W. J. Liu J. J. Jonas	TiC	HSLA	Deformation at high temperatures	Precipitation starting time was determined experimentally using a relaxation test.
K. Miyahara J. Hwang T. Iwamoto Y. Hosoi	Laves	10 wt%Cr heat-resisting steel	Tempering	Volume fraction of Laves phase was calculated using the KJMA theory.
Å. Gustafson L. Höglund J. Ågren	(V,Nb)N	10 wt%Cr heat-resisting Steel	Isothermal heat-treatment	Size of (V,Nb)N in ripening was calculated by multicomponent diffusion (DICTRA).

Table 1.2: Review of precipitation models. KJMA stands for Kolmogorov–Johnson–Mehl–Avrami, who originally proposed the extended volume concept.

The growth was dealt with taking proper account of the diffusion both Nb and C, with few adjustable parameters. In the context of multicomponent diffusion, the computer software DICTRA has been developed for the analysis of growth (Andersson *et al.*, 1990). Gustafson *et al.* modelled the ripening of (V, Nb)N in 10Cr wt% power plant steel with DICTRA (1998). The particle size was predicted and consistent with experimental data. All of these models can cope with only one precipitation reaction occurring at any instance, as an equilibrium phase. In practice, many reactions may occur simultaneously and non-equilibrium phases are often important. For example, heat–resisting steels contain many kinds of carbide precipitates, only some of which enhance creep resistance and many of which are metastable. In fact, the precipitation and dissolution processes continue during service at elevated temperature as equilibrium is approached. The conventional models described above cannot be applied directly to such simultaneous reactions in practical steels (Fig. 1.2).

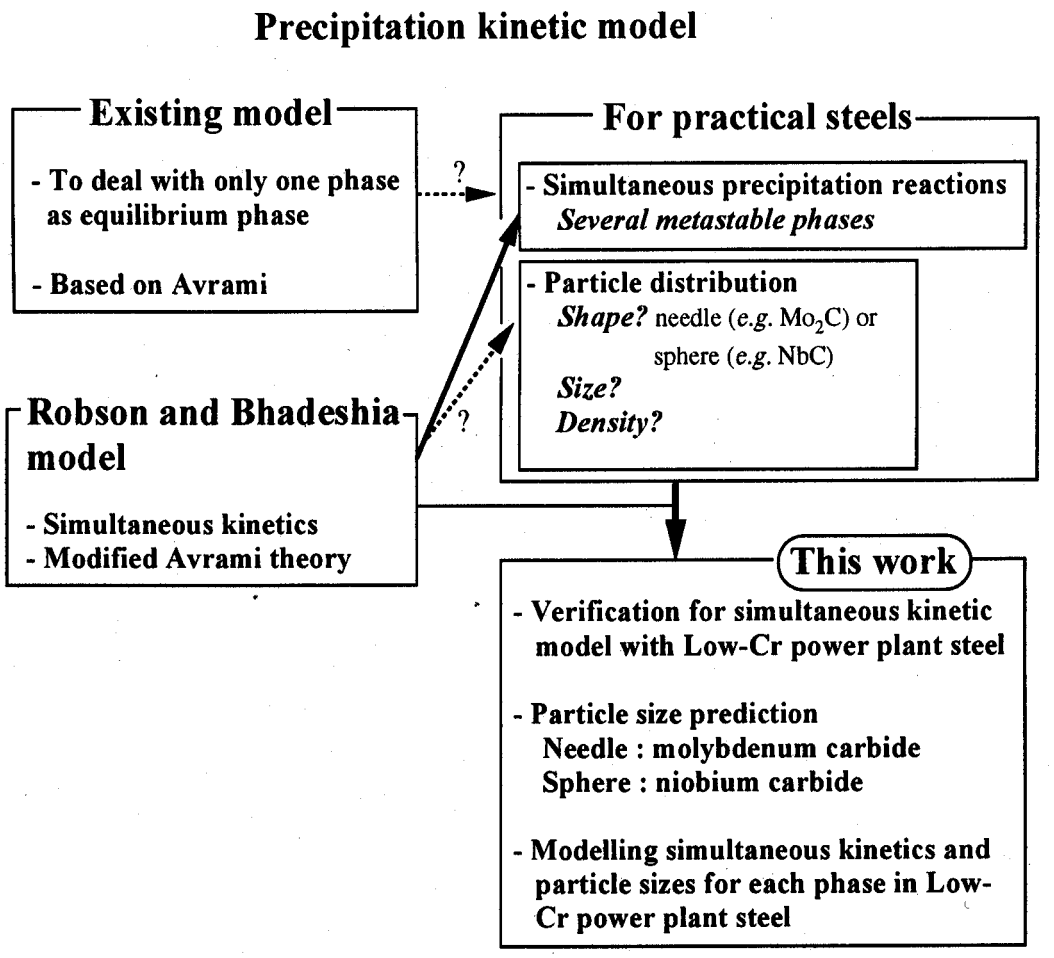

Fig. 1.2: Schematic illustration of activities for modelling simultaneous precipitation reactions.

Recently, a new theory which generalises the extended volume concept to simultaneous precipitation reactions has been established (Jones and Bhadeshia, 1997; Robson and Bhadeshia, 1997a). Its application to secondary hardened steels has been confirmed experimentally with very limited data (Robson and Bhadeshia, 1997b), just the change in the volume fraction of each precipitate which occurs during the isothermal heat treatment of power plant steels. Precipitation strengthening strictly depends on particle size and on the distribution of precipitates, rather than just on the volume fraction.

The purpose of the work presented in this thesis was firstly to check comprehensively the validity of the Robson and Bhadeshia model (1997a), and secondly to create a better model for alloy carbide precipitation, which is able to cope with particle sizes and coarsening phenomena as a natural consequence of aging. In this work, niobium carbide in HSLA steel (as a spherical precipitate), molybdenum carbide in secondary hardening steel (as a needle–shaped precipitate) and alloy carbide sequence in low chromium power plant steels have been chosen for being modelled.

1.2 Carbides in practical steels

1.2.1 High strength low alloy steels

For certain critical applications, such as in the construction of pipelines for the oil and gas industries, there is an overriding need for good toughness and strength, and hence the need for careful microstructural control (Tamura *et al.*, 1988), embodied in thermomechanical processing which leads to a general refinement of the microstructure. Small amounts of niobium, titanium or vanadium, lead to the precipitation of fine carbides or nitrides which pin austenite grain boundaries, prevent grain growth and hence lead to a reduction in grain size. Because of relatively easy way to get high strength, there are now a number of industrial applications, not only for critical applications in which toughness is vital, but also for many other applications, for example, in the reduction in weight of automotive vehicles (Esaka *et al.*, 1985).

Thermomechanical processing

During cooling after hot–rolling, the fine austenite grains transform to even smaller ferrite grains which nucleate at the austenite grain boundaries. Obviously, the size of the carbonitride particles and their volume fraction are very important factors. According to Zener (1948), the finer particle size, the more effective is the pinning. To ensure fine particles it is necessary to

consider aspects of the precipitate solubility at the temperatures where hot–rolling is carried out. During hot deformation the steel is heated ("homogenised") at higher temperature and then rolled. During homogenisation, the solute dissolves in the austenite. During rolling and subsequent cooling, the solubility decreases and fine precipitation ensues with typical alloy concentrations (Fig. 1.3). Fig. 1.4 shows that the carbides and nitrides can dissolve at temperatures in excess of 1200 °C with precipitation at typical rolling temperatures (*e.g.* 900 °C). Therefore, very fine particles can be obtained during hot–rolling and cooling as schematically shown in Fig. 1.3.

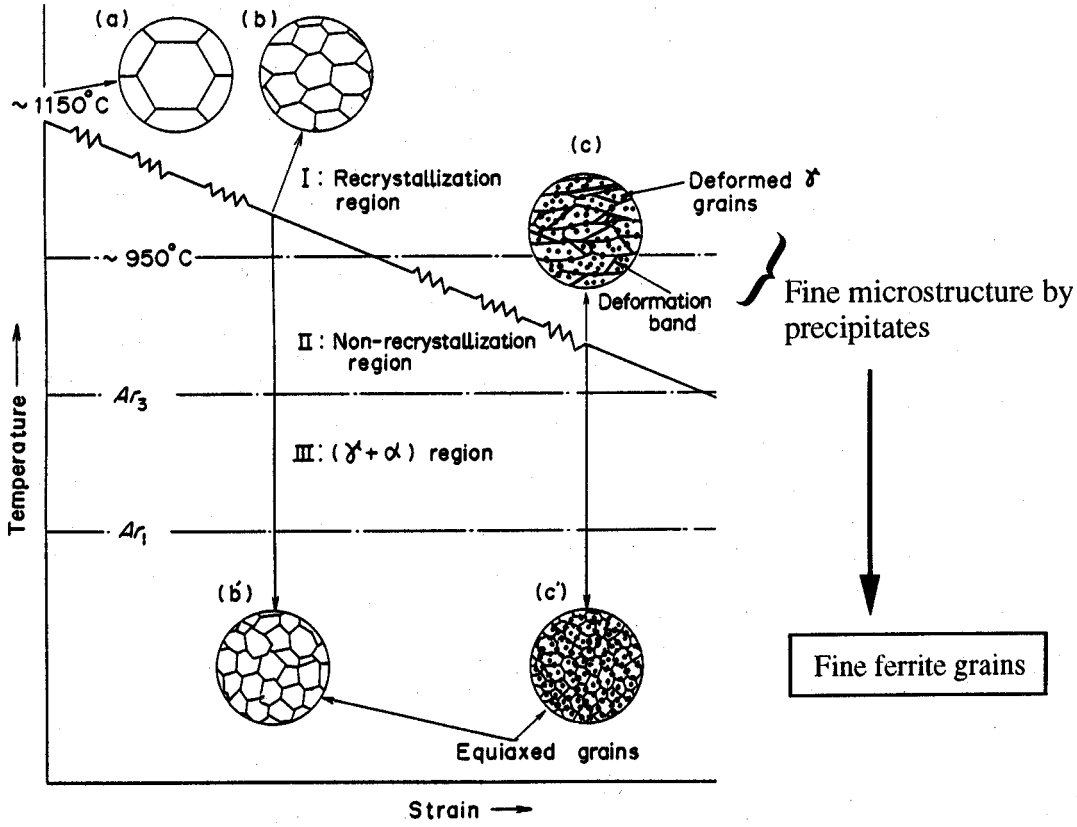

Fig. 1.3: Schematic illustration of the thermomechanical processing that leads to fine grains in micro–alloyed steels. A_{r3} and A_{r1} represent transformation temperatures for $\gamma \rightarrow \gamma + \alpha$ and $\alpha + \gamma \rightarrow \alpha$+carbide respectively, where γ is austenite (face–centred cubic structure) and α is ferrite (body–centred cubic structure) (Tanaka, 1981).

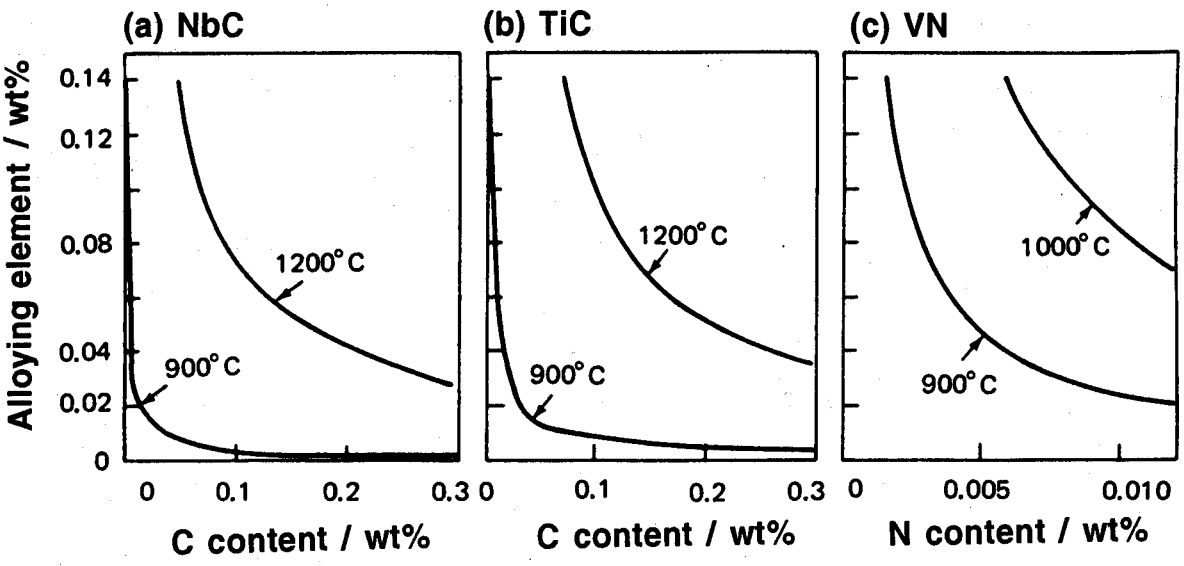

Fig. 1.4: Solubility of (a) niobium carbide: NbC, (b) titanium carbide: TiC and (c) vanadium nitride: VN as a function of temperature and carbon or nitrogen content (adapted from Meyer *et al.*, 1976). These were derived from enthalpy data for each precipitate formation, NbC in 0.005C to 0.18C–0Nb to 0.92Nb wt% steel, TiC in 0.1C–0.058Ti to 0.35Ti wt% steel and VN in 0 to 0.017N–0.35V to 2.78V wt% steels respectively.

Effect of Nb, Ti or V addition

Fig. 1.5 shows the effect of Nb, Ti and V additions on the ferrite grain size (Meyer *et al.*, 1976). The fine grain and particle size leads to an increase in the strength and toughness. Table 1.3 shows the basic crystallographic data for the carbide and nitride important in micro–alloyed steels.

As shown in Fig. 1.5, Nb has the most effective to get fine grains. This is because Nb addition does not only form fine carbide but also retard recrystallisation in hot deformation (Le Bon, *et al.*, 1975). The retardation of recrystallisation by Nb is more effective than by alloying elements such as Ti and V (Fig. 1.5). Therefore, there have been several studies of NbC precipitation during hot deformation, as already listed in Table 1.2. In many cases, the nucleation sites were assumed to be dislocations. Because of the complexity of hot deformation, in which recovery, recrystallisation and precipitation occur at same time, such models include many parameters, some of which are not well–understood physically but used as fitting parameters. It would be useful to develop a basic model with general applicability.

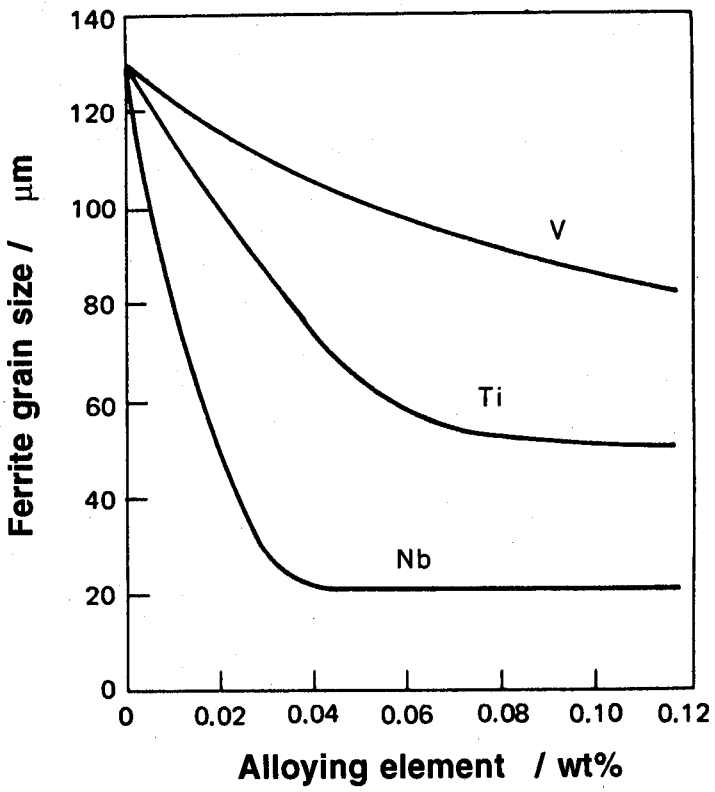

Fig. 1.5: Effect of Nb, Ti and V on ferrite grain size (Meyer *et al.*, 1976).

Precipitate	structure	Lattice parameter / Å
NbC	Cubic-F	a=4.471
TiC	Cubic-F	a=4.380
VN	Cubic-F	a=4.139

Table 1.3: Data for alloy carbides and nitride from the ASTM card index.

1.2.2 Power plant steels

Efficient energy generation is a prime goal for all industrialised economies. This calls for steels which can withstand higher operating temperatures over long periods of time. Table 1.4 gives the typical pressure, temperature and efficiency data for power plant (Kougami and Isaka,

1990). If the present main steam temperature which is 538 °C at 25 MPa is raised up to 650 °C at 35 MPa, then the efficiency will increase to 45%, an 8% improvement. To reach these objectives, it will be necessary to develop new types of high chromium ferritic steels and possibly austenitic stainless steel.

	Main steam temperature in °C and pressure in MPa		
	538 °C - 25 MPa (present condition)	595 °C - 32 MPa	650 °C - 35 MPa
Efficiency / %	41.5	44.0	44.8
Improvement of efficiency / %	0	6.0	8.0
Reduction in coal consumption / 10^3 tons year^{-1}	0	130	150

Table 1.4: Present and expected conditions of main steam temperature, pressure and efficiency (Kougami and Isaka, 1990). Improvement of efficiency and possible amount of coal to be reduced are compared with current values.

Table 1.5 shows the anticipated materials for each component (Kougami and Isaka, 1990). Basically, the materials must have good heat resistant properties, in which the improvement of high temperature creep properties is generally the most important.

	Main steam temperature in °C and pressure in MPa		
	538 °C - 25 MPa (present condition)	595°C - 32 MPa	650 °C - 35 MPa
Main tube in boiler	$2\frac{1}{4}$Cr1Mo	9CrMo	Austenitic steel
Valve in boiler	$2\frac{1}{4}$Cr1Mo	9CrMo	Austenitic steel
Main rotor in turbine	CrMoV	12Cr	Austenitic steel

Table 1.5: The expected materials for each component (Kougami and Isaka, 1990).

High temperature creep deformation

Creep can be defined as time dependent plastic deformation at stresses below the normal yield strength. Creep deformation occurs at a significant rate at temperatures greater than about half of the absolute melting temperature.

There are several methods of strengthening against creep. Firstly, solid solution strengthening is basically due to the lattice strain caused by misfitting solute atoms. One advantage of this mechanism in the context of creep is that its contribution remains constant during service as long as precipitation does not deplete solute. Unfortunately, the magnitude of the effect is not very large at high temperatures. However, solutes may affect the creep rate through the stacking fault energy and via the overall diffusion coefficient (Barrett and Sherby, 1965). Secondly, precipitation strengthening provides obstacles to the movement of dislocations (McLean, 1962). For high strength, the particles should be small and dispersed homogeneously. The effect of precipitation strengthening is generally much higher than that of solid solution strengthening. However, over long periods in service at elevated temperatures, precipitates can coarsen or transform.

Necessity of new ferritic steels

Besides the basic demand of creep resistance, there has recently been another requirement, that of thermal fatigue resistance. Changing electricity demands means that it may be necessary to make power plant capable of intermittent operation. For thermal fatigue resistance, the material must have a low coefficient of thermal expansion and a high thermal conductivity. A ferritic steel with body–centred cubic structure is therefore better than an austenitic steel with face–centred cubic structure (Yamanaka *et al.*, 1967). On the other hand, a ferritic steel is weaker at high temperatures. Therefore, it is especially necessary to strengthen ferritic steels at high temperatures or to reduce the expansivity of austenitic steels. The latter is difficult and expensive, so that the priority is to focus on new ferritic alloys. Table 1.6 shows the developing history of new ferritic steels, including their main chemical constituents and properties (Masuyama, 1998).

Tempering martensite

To get a good balance between hardness and ductility in such ferritic heat resistant steels as shown in Table 1.6, the tempering of martensite is usually carried out at temperatures, between 150 °C and 700 °C. During tempering, excess carbon is rejected from supersaturated

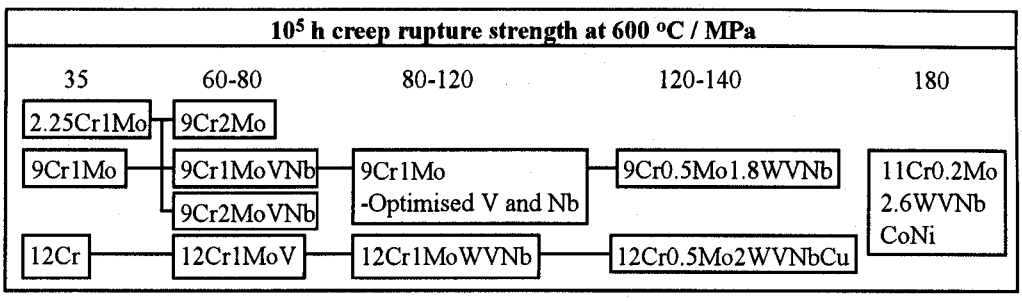

Table 1.6: The developing history of new ferritic steels including the main chemical constituents in wt%. (Masuyama, 1998)

solid solution to form carbides. Whereas tempering at low temperatures (less than about 500 °C) results mostly in the formation of cementite or other iron-rich transition carbides, substitutional solute-rich "alloy carbides" are able to form as the tempering temperature is raised to a level where these solutes become mobile. Extensive studies have been carried out on carbide changes during the tempering of power plant steels. Most of the research has focused on the popular ferritic heat resistant steels, *e.g.* 1CrMoV and $2\frac{1}{4}$Cr1Mo steels. The microstructure changes during tempering have been reported to occur in four stages as follows (Balluffi *et al.*, 1951; Baker and Nutting, 1959; Nutting, 1999).

Stage 1

The first stage of tempering of martensite is that the hexagonal ϵ carbide with the composition of $Fe_{2.4}C$ precipitates as narrow plates with a well defined orientation relationship. After ϵ carbide precipitates, the martensite may still be supersaturated with carbon.

Stage 2

During the second stage of tempering, any retained austenite present in the microstructure decomposes and cementite (Fe_3C) forms.

Stage 3

During this stage, cementite precipitates at the expense of the transition iron-carbides (such as ϵ) and grows. It is likely that the cementite nucleates at the interface between ϵ carbide and the matrix which is no longer supersaturated with carbon and hence is referred to as ferrite.

Stage 4

If the material is a plain carbon steel, cementite coarsens and there will eventually be spherical cementite and equiaxed ferrite grains formed in this last stage of tempering. However, all power plant steels contain strong carbide–forming alloying elements, such as Cr, Mo, V, Nb and W to improve the resistance to creep deformation. These alloying elements are able to diffuse at reasonable rates at tempering temperatures greater than about 500 °C to form more stable alloy carbides than cementite, which starts to dissolve. The alloy carbides are finer and at first coherent or semi-coherent with the ferrite. This causes an increase in the strength and have the term "secondary hardening".

The first three stages of tempering are completed in a relatively short time compared with stage 4 which requires the diffusion of substitutional solute. Those alloy carbides may nucleate early, even though they may not be the most stable from a thermodynamic point of view. This leads to a sequence of precipitation reactions as equilibrium is approached. Fig. 1.6 shows an example of experimental results on carbide sequence in $2\frac{1}{4}$Cr1Mo steel which is one of the most popular power plant steels (Nutting, 1999). The specific details of this sequence strongly affects the creep properties.

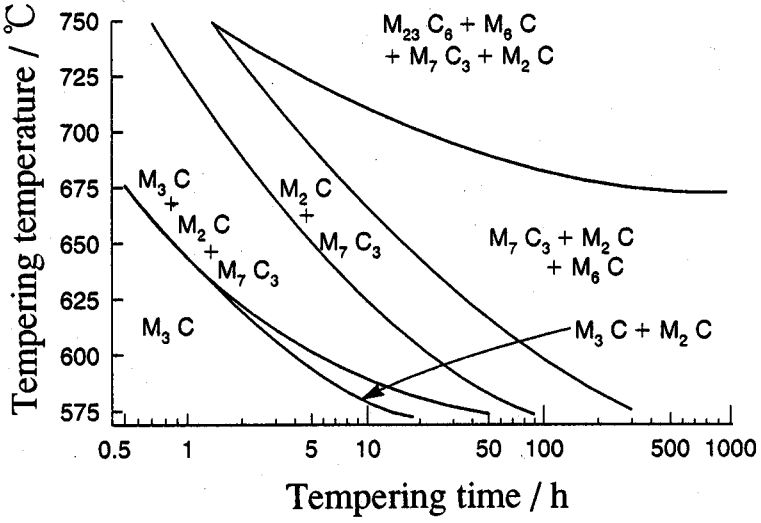

Fig. 1.6: Carbide sequence in $2\frac{1}{4}$Cr1Mo steel (Nutting, 1999). "M" stands for metallic elements.

Structure of alloy carbides

There have been many studies on alloy carbide precipitation in power plant steels (*e.g.* Kou, 1953; Shaw and Quarrel, 1957; Baker and Nutting, 1959; Woodhead and Quarrel, 1965; Yakel, 1985). Table 1.7 contains same details of typical alloy carbides in power plant steels are summarised (Andrews *et al.*, 1967). Because of many alloying elements, the chemical formulae are often written with M which stands for total metallic elements partitioned to each alloy carbide.

Precipitate	structure	Lattice parameter / Å
Fe_3C	Orthorhombic	a=4.5241, b=5.0883, c=6.7416
M_7C_3	Trigonal	a=13.982, c=4.506
Mo_2C	Hexagonal	a=3.002, c=4.724
$M_{23}C_6$	Cubic-F	a=10.638
M_6C	Cubic-F	a=11.082

Table 1.7: Data for alloy carbides in this work (Andrews *et al.*, 1967).

M_3C

Cementite in plain carbon steels forms with the composition Fe_3C. The structure is approximately hexagonal closed–packed in which iron atoms are arranged with localised distortions to accommodate the interstitial carbon atoms. Each carbon atom is surrounded by 6 iron atoms with a triangular prism as shown in Fig. 1.7 (Jack and Jack, 1973).

In alloy steels, other metallic elements may partition into the cementite in which case its composition is written M_3C which frequently remains iron–rich with the same orthorhombic structure as Fe_3C. Woodhead and Quarrel (1965) reported that Mn and Cr can be soluble into M_3C. For example, Thomson has reported more than 30 wt % Cr was detected in the cementite in a $2\frac{1}{4}$Cr1Mo steel during tempering at 565 °C (1994a, 1994b). Other elements, Ni, Mo, W and V which are often added to power plant steels have also been found to dissolve in M_3C.

M_3C formation occurs by a paraequilibrium mechanism (details in Chapter 2), in which interstitial atoms can reach equilibrium but substitutional atoms cannot diffuse (Hultgren, 1947; Bhadeshia and Christian, 1990). This means that alloying elements are trapped in cementite

with the same concentration ratio to iron as the parent phase. Solute partitioning can occur subsequently to allow equilibrium to be achieved. The enrichment of solutes is dependent on the size of the particles and the partitioning ratios of the ferrite matrix (Bhadeshia, 1989). Thomson reported that in low chromium power plant steels the enrichment rate is so slow that the composition of cementite may not reach the equilibrium within the design life time (1992).

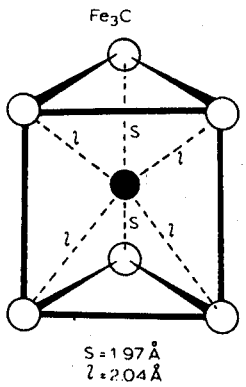

Fig. 1.7: The prism environment of iron atoms around carbon in Fe_3C (Jack and Jack, 1973).

M_2C

M_2C is a molybdenum–rich carbide with a hexagonal structure. Cr, V and Fe readily dissolve in this phase (Vyrostkova *et al.*, 1998). M_2C commonly precipitates as fine needles parallel to the $< 110 >_\alpha$ direction in ferrite with the specific orientation relationship (Pitsch–Schrader, 1958):

$$(0001)_{M_2C} \parallel (011)_\alpha \quad \text{and} \quad [11\bar{2}0]_{M_2C} \parallel [100]_\alpha$$

M_7C_3

M_7C_3 is a chromium–rich carbide with the trigonal crystal structure. Fe dissolves in M_7C_3, with smaller solubilities for Mn, V and Mo. M_7C_3 tends to nucleate near cementite or on the interface between cementite and ferrite (Baker and Nutting, 1959; Kuo, 1953). Woodhead and Quarrel (1965) stated that M_7C_3 would only be observed when the chromium concentration is

high enough. Beech and Warrington (1966) reported that there might be a chromium–enriched zone left when cementite dissolves, forming an ideal site for M_7C_3 precipitation.

The diffraction pattern of M_7C_3 often includes characteristic streaks which are attributed to faults lying on (10.0) planes (Beech and Warrington, 1966). This feature is very useful to distinguish M_7C_3 from other carbides.

$M_{23}C_6$

This phase is also a chromium–rich carbide with the face–centred cubic structure. Fe, Mo and W are significantly soluble in $M_{23}C_6$. For many power plant steels, this carbide is often one of the equilibrium phases observed during tempering at elevated temperatures. The nucleation of this phase have not been fully investigated but may occur on the prior austenite grain boundaries, martensite lath boundaries (Senior, 1989) or adjacent to M_7C_3 (Nutting, 1999). The morphology of $M_{23}C_6$ particles does not change much during aging (Nutting, 1999). It precipitates rapidly as a large particle which may stabilise the lath boundaries (Bjärbo, 1994) so that $M_{23}C_6$ is thought not to directly contribute to creep strength.

M_6C

M_6C is a molybdenum–rich carbides with the face–centred cubic structure frequently containing Fe but not Cr. For power plant steels containing Mo, M_6C is often one of equilibrium phases at elevated temperatures. Nucleation tends to occur on the M_2C and $M_{23}C_6$ interphase boundaries (Kurzydlowski and Zielinski, 1984), prior austenite boundaries or martensite lath boundaries. However, recently, Nutting reported the phase may not nucleate by an in–situ transformation from previously existing carbides (1999). As dissolution of former precipitated carbides occurs, solutes dissolve into the matrix and then are transferred into M_6C by diffusion (Nutting, 1999). This carbide may also be so large and its formation causes less stable fine carbides to dissolve, leading to a reduction in the creep strength.

Fig. 1.8 shows the calculated equilibrium composition for each alloy carbide at 600 °C for 3Cr1.5Mo and $2\frac{1}{4}$Cr1Mo steels, both of which are described in later chapters. During tempering, chromium may diffuse from one carbide to another (Thomson, 1992).

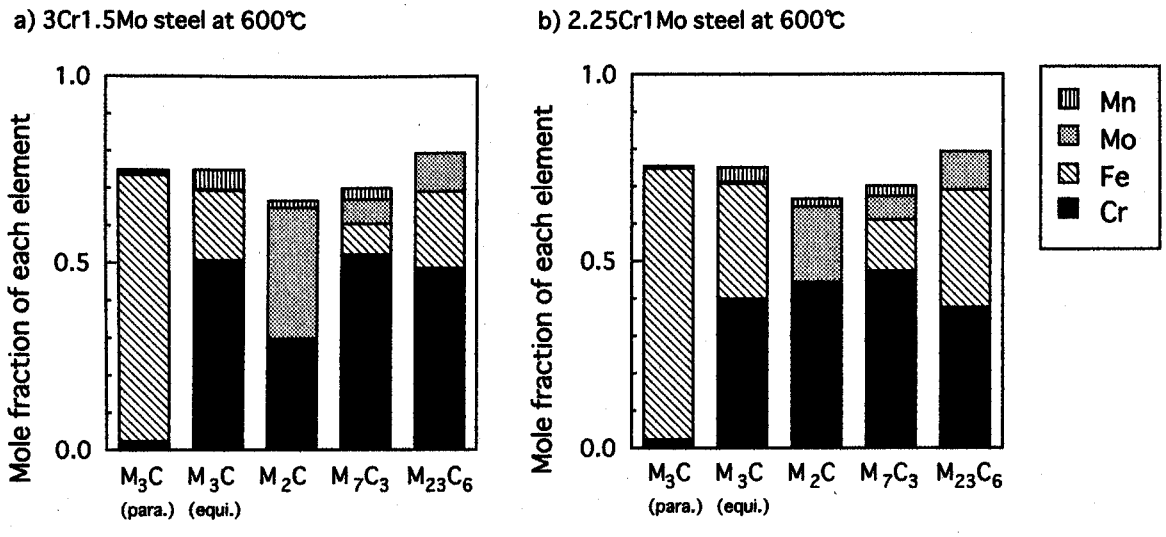

Fig. 1.8: The equilibrium composition for each alloying element in each alloy carbide at 600 °C for (a) 3Cr1.5Mo and (b) $2\frac{1}{4}$Cr1Mo steels, which will be investigated in later chapters. The calculations have been done using MTDATA (Hodoson, 1989) and SGTE database, allowing existence of ferrite and each carbide in each case. M_3C (para.) and M_3C (equi.) represent cementite with paraequilibrium and equilibrium respectively.

1.3 Summary

Alloy carbides are of great importance in obtaining reliable mechanical properties in a variety of steels. Especially in HSLA steel and Power Plant steel, they play very important role to control microstructure and to obtain applicable strength. Although a great deal of experimental work has been done to characterise the precipitation process and although semi–empirical models have been successfully applied, the precipitation process is not still fully understood. Therefore, there is a big demand for the physical modelling of transformation kinetics.

CHAPTER TWO

Theory for precipitation reactions in steels

2.1 Introduction

The formation of an individual particle involves its nucleation and growth but the overall precipitation process must also account for impingement effects. The latter phenomenon can be dealt with using the theory for overall transformation kinetics as first expressed by Kolmogorov (1937), Johnson and Mehl (1939) and Avrami (1939, 1940, 1941). They are reviewed in this chapter.

2.2 Classical nucleation

When a new phase is created during a heterophase fluctuation, its interfacial energy with the matrix tends to oppose its formation giving rise to an activation barrier even though the parent phase is thermodynamically of a higher free energy. When a spherical embryo with a radius r is created by a thermal fluctuation, the change of free energy, ΔG, is given by

$$\Delta G = \frac{4}{3}\pi r^3 \Delta G_v + 4\pi r^2 \sigma \quad (\Delta G_v \leq 0) \tag{2.1}$$

where ΔG_v (negative) is the chemical free energy change per unit volume, σ is the interfacial energy per unit area, assumed to be isotropic. Equation 2.1 also assumes that the strain energy can be neglected. Fig. 2.1 shows the relationship between ΔG and r.

The maximum free energy occurs at a critical radius, r^*, when the net free energy change has a value, G^*, known as the activation energy. A nucleus with a bigger radius than r^* will tend to grow rather than dissolve since its growth leads a decrease of free energy. At $r = r^*$, $d\Delta G/dr$ equals to zero, so that G^* is given by:

$$G^* = \frac{16\pi\sigma^3}{3\Delta G_v^2} \tag{2.2}$$

The nucleation rate depends on the attempt frequency, which can be written as kT/h, where h is the Planck constant, k is the Boltzmann constant and T is the absolute temperature. Thus, the nucleation rate in the untransformed region I is given by (Christian, 1975);

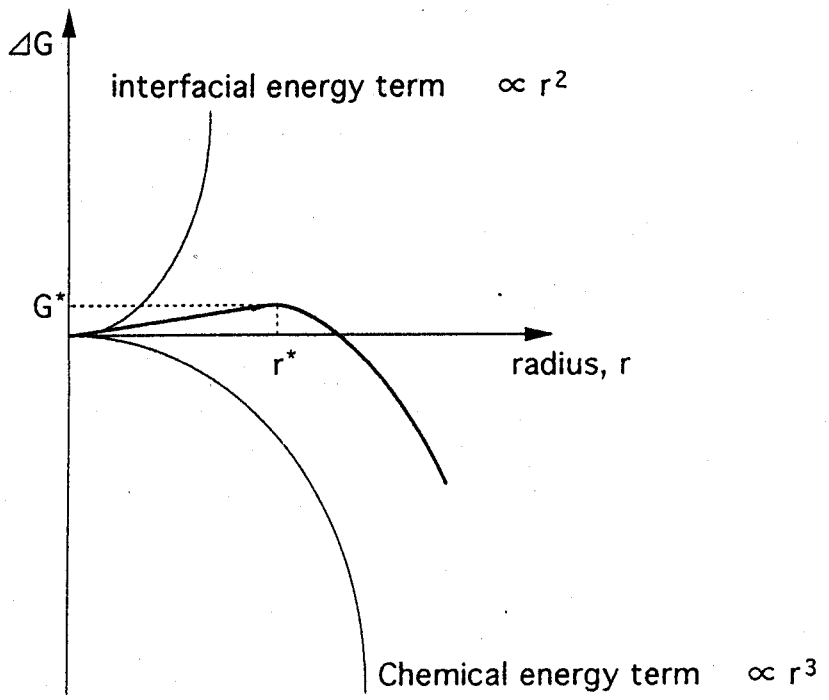

Figure 2.1: The free energy change associated with the formation of a nucleus as a function of radius r.

$$I = N_0 \frac{kT}{h} \exp\left(-\frac{G^* + Q}{kT}\right) \tag{2.3}$$

where N_0 is the number of nucleation sites per unit volume, Q is the activation energy for the transfer of atoms across the embryo / matrix boundary. Turnbull and Fisher suggested that this equation 2.3 is for nucleation process without long–range diffusion (1948). If long–range diffusion occurs as in carbide precipitation, Q will be the activation energy for solute diffusion and the equation should be multiplied by mole fraction of the diffusing solute $\overline{c}$ for nucleation process (Turnbull and Fisher, 1948). Then, the nucleation rate per unit volume at any instance I' can be assumed to be:

$$I' = \overline{c} N_0 \frac{kT}{h} \exp\left(-\frac{G^* + Q}{kT}\right) \tag{2.4}$$

In order to evaluate this equation, it is necessary to determine G^*. While Q can be assumed

to be the activation energy for solute diffusion and independent of temperature, G^* is strongly dependent on temperature. The calculations of G^* require a knowledge of the chemical driving force for nucleation ΔG_v which depends on the chemical composition. Fig. 2.2 shows schematically the free energy curve of the matrix α and precipitate β in a Fe-M binary system. Equilibrium precipitation leads to a reduction ΔG_0 in free energy as shown in Fig. 2.2(a). The corresponding free energy per unit of equilibrium precipitate is given by $\Delta G_n = \Delta G_0/f$ where $f = (\overline{c} - c^{\alpha\beta})/(c^{\beta\alpha} - c^{\alpha\beta})$ is the fraction of precipitate. However, ΔG_n does not properly describe the change in free energy during nucleation because the composition of the matrix hardly changes as a consequence of nucleation. Furthermore, the composition of the nucleus need not be that corresponding to equilibrium (*i.e.* $c^{\beta\alpha}$) since an alternative composition may lead to a larger free energy change. The composition that maximises the free energy change at the nucleation stage is given by the parallel tangent construction illustrated in Fig. 2.2(b) (Bhadeshia, 1992).

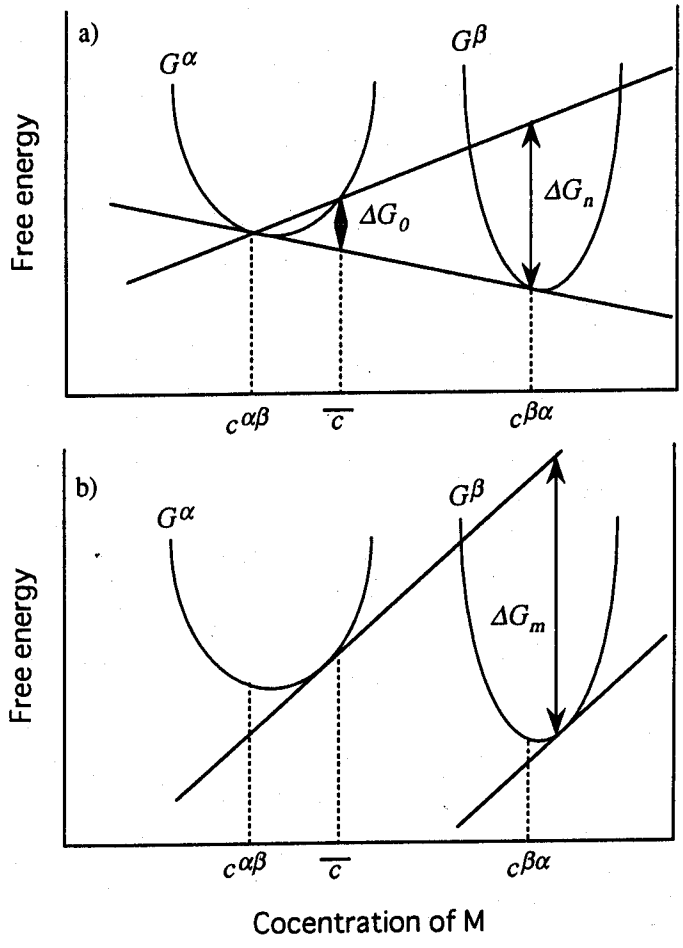

Figure 2.2: An illustration about construction for finding the driving force for nucleation.

Thus, ΔG_m is the correct term to use as the chemical driving force in any nucleation equation. In steels, where the solubility of carbon in ferrite is limited, $\Delta G_n \simeq \Delta G_m$ so that ΔG_n may be used as a good approximation. Since free energies are often expressed as molar quantities, they can be converted into the free energy per unit volume by division with the molar volume of the phase concerned.

2.3 Interfacial energy during nucleation

One of the major difficulties associated with the application of the classical nucleation theory is how to decide on the interfacial energy σ. A typical critical nucleus size may be in the range 1-2 nm and it could be argued that σ should depend on the size itself (Christian, 1975). In the solid–state σ may reasonably be expected to depend also on the orientation of the interface plane. Detailed information of this kind is simply not available and it is usual therefore to consume a constant value of σ to describe the entire nucleation process. This assumption adds enormous uncertainty to any calculations of nucleation rates.

However, the recent work by Miyazaki (1999) has demonstrated that the approximation of a constant value of σ is in fact justified. They measured the critical particle size in a concentration gradient (*i.e.* as a function of the driving force) by direct observation and demonstrated that a single interfacial energy could describe data, irrespective of the particle size.

The method they used not only confirms that it is reasonable to use a single value of σ for nucleation but also provides a precise technique for the experimental determination of the interfacial energy during the nucleation process.

2.4 Diffusion–controlled growth in a binary system

2.4.1 Rate control

The velocity of the interface between matrix and precipitate depends on the mobilities of atoms and is related to the atom transfer across the interface. These processes are in series. There is a dissipation of free energy during the motion of an interface. Growth is said to be diffusion–controlled when much of this free energy is dissipated in the diffusion of solute ahead of the interface. In this case, the compositions of the phases at the interface are given approximately by a tie–line of the phase diagram (Fig. 2.4) as shown in Fig. 2.3 (a) (Bhadeshia, 1985).

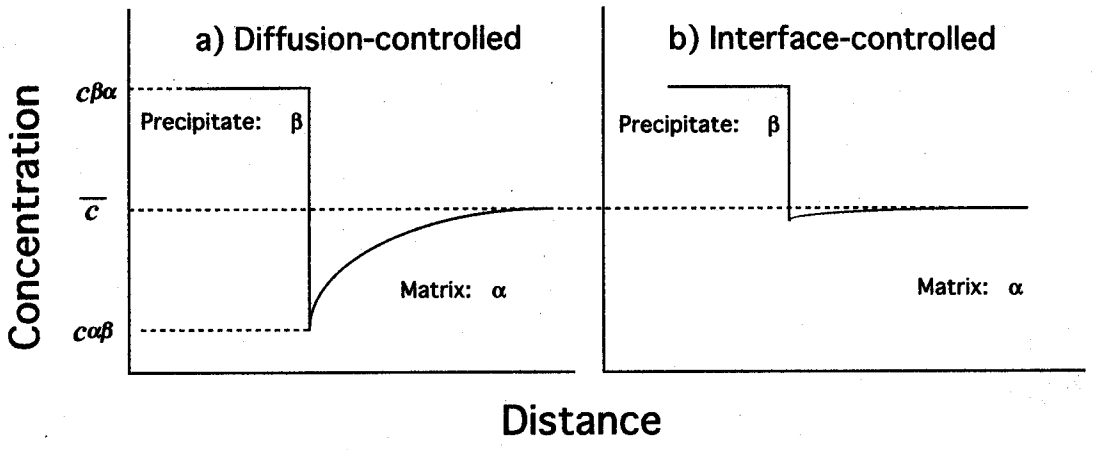

Figure 2.3: Schematic illustrations of the solute concentration profile at the interface between the matrix α and the growing precipitate β for (a) diffusion–controlled growth and (b) interface–controlled growth. The concentration in α which is in local equilibrium with β is $c^{\alpha\beta}$, whereas that in α which is in local equilibrium with β and $c^{\beta\alpha}$ respectively. $\overline{c}$ is the mean composition.

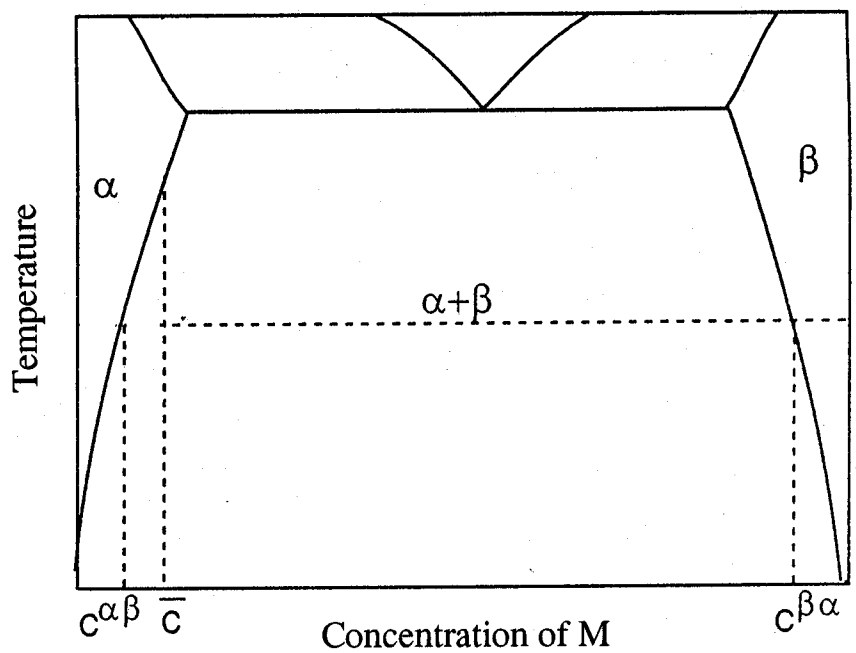

Figure 2.4: A schematic phase diagram showing the equilibrium compositions of α and β phases at the transformation temperature.

By contrast, interface–controlled growth is said to occur when most of the available free energy is dissipated in the transfer of atoms across the boundary. The compositions of the phase at the interface will no longer be given by the phase diagram as schematically shown in Fig. 2.3(b) (Bhadeshia, 1985).

Since the diffusion of solute is rather difficult in the solid–state, it is reasonable to assume that, at high temperatures, most solid–state transformations will occur with diffusion being the rate controlled process.

2.4.2 Zener model for diffusion–controlled growth

For simplicity, we consider at first one-dimensional growth of a planar interface with a constant far–field solute concentration.

The solute concentration profile at the interface during diffusion–controlled growth is illustrated in Fig. 2.5. The flux J at the interface is given by Fick's first law:

$$J_{z=z^*} = -D(dc/dz)_{z=z^*} \tag{2.5}$$

where z^* is the position of the interface along the co–ordinate z, D is the diffusion coefficient of the solute in the matrix and c is the concentration of the solute.

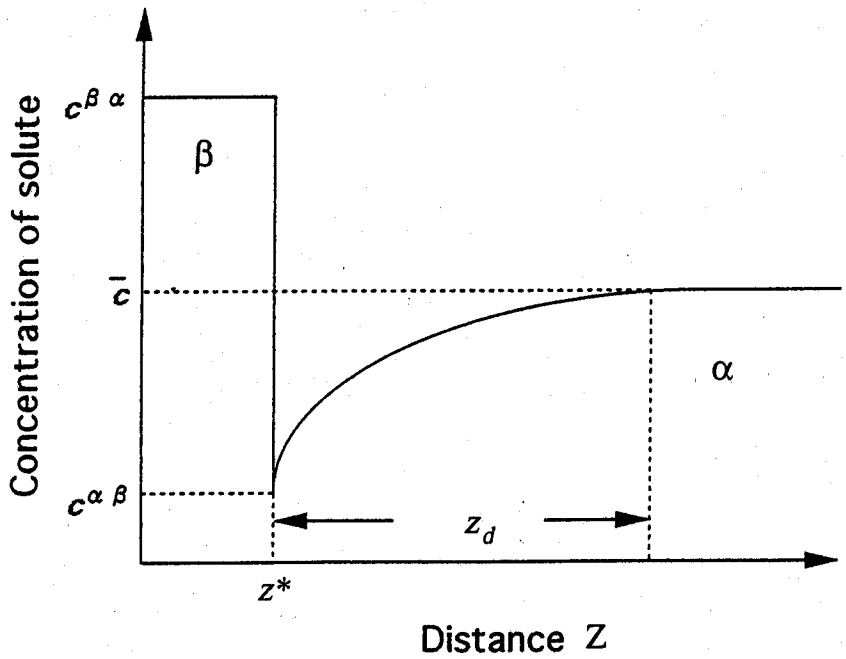

Figure 2.5: Schematic illustrations of the solute concentration profile at the interface between matrix α and growing precipitate β. z_d is a nominal diffusion distance and z^* is the position of the interface.

In order to maintain a constant concentration at the interface, this flux must equal the rate at which the solute is partitioned:

$$v(c^{\beta\alpha} - c^{\alpha\beta}) = J_{z=z^*} \tag{2.6}$$

where v is growth rate, $c^{\beta\alpha}$ is the solute concentration in the precipitate β which is in local equilibrium with the matrix α and $c^{\alpha\beta}$ is the solute concentration in α which is in local equilibrium with β. These concentrations are from the phase diagram as shown in Fig. 2.4 for a binary system.

One simplification is the Zener approximation (1946) in which the concentration gradient ahead of the interface is assumed to be constant (Fig. 2.6) so that,

$$dc/dz = (\overline{c} - c^{\alpha\beta})/z_d \tag{2.7}$$

where $\overline{c}$ is an alloying concentration of the solute, z_d is the "diffusion distance".

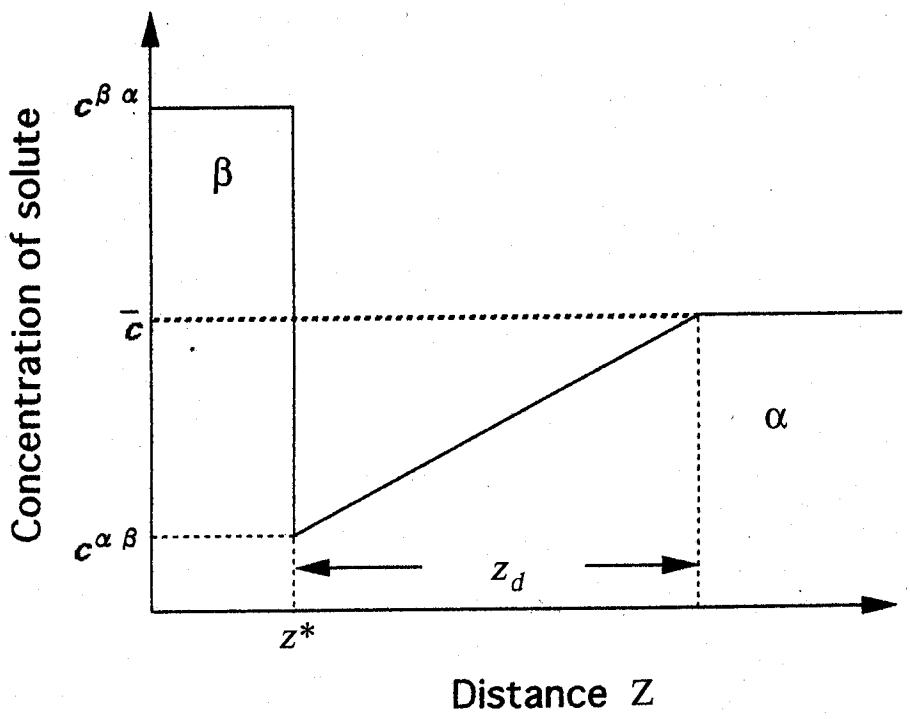

Figure 2.6: The constant concentration gradient approximation profile of solute atoms (Zener, 1946).

Solving these equations 2.5, 2.6 and 2.7, the precipitate growth can be calculated in terms of the dimensionless supersaturation Ω given by:

$$\Omega = \frac{(\overline{c} - c^{\alpha\beta})}{(c^{\beta\alpha} - c^{\alpha\beta})} \tag{2.8}$$

It follows from equations 2.5 to 2.8 that the growth rate is given by:

$$v = \frac{D\Omega}{z_d} \tag{2.9}$$

z_d can be estimated from mass conservation by writing

$$\frac{1}{2} z_d (\overline{c} - c^{\alpha\beta}) = (c^{\beta\alpha} - \overline{c}) z^* \tag{2.10}$$

so that

$$z_d = \frac{2\,(c^{\beta\alpha} - \overline{c})}{(\overline{c} - c^{\alpha\beta})}\, z^* \tag{2.11}$$

By substitution of the equation 2.11 into the equation 2.7, growth rate is driven:

$$v = \frac{dz^*}{dt} = \frac{D}{2}\Omega \frac{(\overline{c} - c^{\alpha\beta})}{(c^{\beta\alpha} - \overline{c})} z^* \tag{2.12}$$

In many cases, it can be assumed that $(c^{\beta\alpha} - \overline{c}) \simeq (c^{\beta\alpha} - c^{\alpha\beta})$. Then,

$$\frac{dz^*}{dt} = \frac{D}{2}\Omega^2 z^* \tag{2.13}$$

Integration of the expression for the growth rate gives

$$z^* = \Omega\sqrt{Dt} \tag{2.14}$$

The precipitate size corresponding to the planar interface position therefore varies with the square root of time, giving the classical parabolic law for one–dimensional growth in a binary system. It applies in all circumstances where the diffusion distance ahead of the interface increases as the particle grows.

2.4.3 Capillarity effect on concentrations at the interface

The example considered above is for one–dimensional growth with a planar interface. The state of equilibrium between two phases changes with the curvature of the interface separating them.

This well–established *capillarity effect* scales with the interfacial energy because additional work has to be done to create new interfacial area when a curved interface moves. This is the well known Gibbs–Thomson effect.

The equilibrium phase diagram applies to large phases with flat interfaces. For a curved interface, there must be the increase of the interface area as the particle grows. The increase of free energy due to expanding interface area is given by (Fig. 2.7) (Christian, 1975 p.181):

$$G_r^\beta - G^\beta = \sigma \frac{dO}{dn} \tag{2.15}$$

where G_r^β is the free energy of β with a curved interface, σ is the interfacial energy per unit area for the precipitate which contacts with the matrix and dO/dn is the change of the interface area with an extra atom transferred from the matrix to the precipitate.

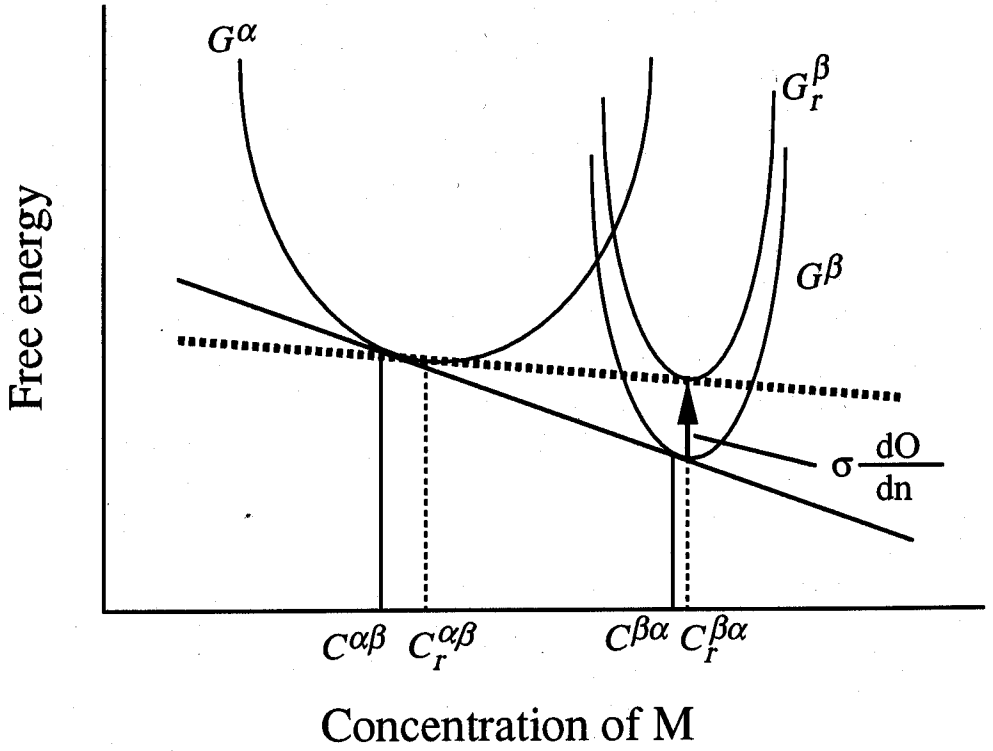

Figure 2.7: Schematic illustration of free energy and interface concentration changes due to the capillarity effect in a Fe–M binary system. G_r^β is free energy for precipitate β which is in contact at a curved interface with radius of curvature r. $c_r^{\alpha\beta}$ and $c_r^{\beta\alpha}$ are the corresponding equilibrium concentrations in matrix and precipitate, respectively.

dO/dn depends on the interface shape which affects the change of interface area during growth (Christian, 1975).

For hemispherical interface as in spherical particles or at the tip of needles,

$$\frac{dO}{dn} = \frac{2v^{\beta}}{r} \tag{2.16a}$$

For edges of plate–shaped particles,

$$\frac{dO}{dn} = \frac{v^{\beta}}{r} \tag{2.16b}$$

where v^{β} is the molar volume of the β phase, r is the radius of the curvature at the interface.

The changes in the equilibrium compositions are shown in Fig. 2.7. The equilibrium compositions, $c^{\alpha\beta}$ and $c^{\beta\alpha}$ which correspond to the concentrations for a planar interface with $r = \infty$, are changed to $c_r^{\alpha\beta}$ and $c_r^{\beta\alpha}$, respectively for a curved interface with radius of curvature r. By the common tangent construction, it follows that (Christian, 1975):

$$\mu_{M,r}^{\alpha} - \mu_M^{\alpha} \simeq \sigma \frac{dO}{dn} \frac{1 - c^{\alpha\beta}}{c^{\beta\alpha} - c^{\alpha\beta}} \tag{2.17}$$

where $\mu_{M,r}^{\alpha}$ and μ_M^{α} are the chemical potentials of the solute M in matrix with a curved interface and with a planar interface, respectively. Assuming a constant activity coefficient, the left hand side in the equation 2.17 can be approximated by:

$$\mu_{M,r}^{\alpha} - \mu_M^{\alpha} \approx kT \ln \frac{c_r^{\alpha\beta}}{c^{\alpha\beta}} \tag{2.18}$$

where k is Boltzmann constant, T is absolute temperature. Equations 2.17 and 2.18 lead to the following relationship between the concentrations $c^{\alpha\beta}$ and $c_r^{\alpha\beta}$:

$$\ln \frac{c_r^{\alpha\beta}}{c^{\alpha\beta}} \approx \frac{c_r^{\alpha\beta} - c^{\alpha\beta}}{c^{\alpha\beta}} = \frac{\sigma}{kT} \frac{dO}{dn} \frac{1 - c^{\alpha\beta}}{c^{\beta\alpha} - c^{\alpha\beta}} \tag{2.19}$$

The modified concentrations by the curved interface are given by (Christian, 1975) :

For spherical particle and hemispherical tip of needle,

$$c_r^{\alpha\beta} = (1 + \frac{2\Gamma}{r}) c^{\alpha\beta} \tag{2.20a}$$

For plate edge and cylinder,

$$c_r^{\alpha\beta} = (1 + \frac{\Gamma}{r})c^{\alpha\beta} \tag{2.20b}$$

where Γ is capillarity coefficient, given by (Christian, 1975):

$$\Gamma = \frac{\sigma v^\beta}{kT} \frac{1 - c^{\alpha\beta}}{c^{\beta\alpha} - c^{\alpha\beta}} \tag{2.21}$$

2.4.4 Growth of plate–shaped and needle–shaped particles

For plate–shaped and needle–shaped particles, the growth is greatly affected by the capillarity effect because of the small radius of curvature at the interface. Assuming the curvature on the interface is constant (*e.g.* needle tip as hemisphere), the concentration change by capillarity effect is constant over the curved interface. The supersaturation is then given by:

$$\Omega_r = \frac{(\overline{c} - c_r^{\alpha\beta})}{(c_r^{\beta\alpha} - c_r^{\alpha\beta})} \tag{2.22}$$

Assuming that the value of $(c_r^{\beta\alpha} - c_r^{\alpha\beta})$ is nearly equal to that of $(c^{\beta\alpha} - c^{\alpha\beta})$, this can be simplified by writing:

$$\Omega_r = (1 - \frac{r_c}{r})\Omega \tag{2.23}$$

where r_c is critical tip radius at which growth ceases. Assuming that diffusion field z_d is equal to a tip radius, the growth rate v, following equation 2.9, is given by (Christian, 1975):

$$v = \frac{D\Omega_r}{z_d} = \frac{D\Omega}{r}(1 - \frac{r_c}{r}) \tag{2.24}$$

Note that the critical radius for a needle is twice as large as that for plate (Trivedi, 1970). The supersaturation for a needle–shaped precipitate is therefore smaller than that for plate.

This equation only expresses the relationship between growth rate and the tip radius. To calculate the growth rate, it is necessary to evaluate the value of r. Zener assumed that the particle selects a radius which gives maximum rate of growth, in this case at $r = 2r_c$. This has been demonstrated experimentally for solid–state reactions in a few cases (Purdy, 1971). The growth rate is given by:

$$v = \frac{D\Omega}{4r_c} \tag{2.25}$$

The critical radius r_c is given by (Christian, 1975):

For plate,

$$r_c = \frac{c^{\alpha\beta}\Gamma}{(\overline{c} - c^{\alpha\beta})} \tag{2.26a}$$

For needle,

$$r_c = \frac{2c^{\alpha\beta}\Gamma}{(\overline{c} - c^{\alpha\beta})} \tag{2.26b}$$

where Γ is the capillarity coefficient. Note that in the absence of soft–impingement, the growth rates for plate and needle shaped particles do not depend on time because the solute is partitioned to the sides of the precipitate.

Hillert has given more rigorous treatment of the diffusion problem for plate growth. The concentrations at the interface in two co–ordinates which are in the direction of growth and normal to the plane were taken into account. Then, the steady–state growth rata is given by (1957):

$$v = \frac{D\Omega}{2}\frac{(c^{\beta\alpha} - c_r^{\alpha\beta})}{(c^{\beta\alpha} - \overline{c})}\frac{1}{m}(1 - \frac{m_c}{m}) \tag{2.27}$$

where m and m_c are arbitrary constants, approximately equal to r and r_c respectively. Compared with equation 2.24, the diffusion field z_d is corresponding to:

$$z_d = 2\frac{(c^{\beta\alpha} - \overline{c})}{(c^{\beta\alpha} - c_r^{\alpha\beta})}r \tag{2.28}$$

Trivedi has given the most satisfactory solution for the growth of needles and plates, taking into account the variation of capillarity and interface kinetics effect at different particles along the interface (1970). It has been assumed that the needle shape remains paraboloid of revolution even when the needle grows. In this treatment, the curvature will change along the interface and the composition will also change along with it. However, the maximum rate hypothesis is still necessary. In general, when the supersaturation is low enough, predictions by both models may not be very different.

2.4.5 Growth of spherical particles

For the growth of spherical particle, parabolic growth is expected because solute can only be partitioned ahead of the interface. The radius of r^I of the sphere, which is also the radius of curvature at the interface, is given by as a function of time t:

$$r^I = C_1 t^{\frac{1}{2}} \tag{2.29}$$

To obtain the value of C_1, it is necessary to evaluate the diffusion equations as follows:

$$\frac{\partial c}{\partial t} = D\left(\frac{\partial^2 c}{\partial r^2}\right) + \frac{2D}{r}\left(\frac{\partial c}{\partial r}\right) \tag{2.30}$$

This equation is for three–dimensional growth. The boundary conditions for a solution of the equation are $c(r^I, t) = c_r^{\alpha\beta}$ and $c(r^I, 0) = \overline{c}$. For simplicity, r is big enough that $c_r^{\alpha\beta} \approx c^{\alpha\beta}$. Zener showed that if $c(r^I, t)$ was constant $c^{\alpha\beta}$, then the distribution of solute is given by (Christian, 1975):

$$c(r,t) = \overline{c} + (c^{\alpha\beta} - \overline{c})\,\frac{\phi_3[r/(Dt)^{0.5}]}{\phi_3[r^I/(Dt)^{0.5}]} \tag{2.31}$$

where $\phi_3(x) = \int_x^\infty \eta^2 \exp(-\eta^2/4)d\eta$.

For parabolic growth, the term, $r^I/(Dt)^{0.5}$, is a dimensionless function of the solute concentration. This term is written as α_3, the parabolic rate constant (for 3–dimensional growth). α_3 can be obtained as follows (Christian, 1975):

$$\frac{1}{\Omega}\frac{dr^I}{dt} = \frac{\alpha_3^{-2}}{\phi_3[\alpha_3]}\exp(\frac{-\alpha_3^2}{4})(Dt)^{\frac{1}{2}} \tag{2.32}$$

and hence

$$\alpha_3^3 = \frac{2\Omega\exp(\frac{-\alpha_3^2}{4})}{\phi_3[\alpha_3]} \tag{2.33}$$

This equation is an implicit expression for any supersaturation, the growth law is given by:

$$r^I = \alpha_3 (Dt)^{0.5} \tag{2.34}$$

In case of low supersaturations, the value of α_3 is given by:

$$\alpha_3 \simeq \sqrt{2}\frac{(\overline{c} - c^{\alpha\beta})^{\frac{1}{2}}}{(c^{\beta\alpha} - \overline{c})^{\frac{1}{2}}} \tag{2.35}$$

This parabolic growth law can be applied only for spherical or cylindrical particles growing radially in which the particle radius is big enough so that the capillarity effect on equilibrium concentration is small.

2.5 Diffusion–controlled growth in a multicomponent system

A reasonable approximation for isothermal diffusion–controlled growth is that the compositions of the phases in contact at the interface are locally in equilibrium, as described earlier. For a binary system, it follows that the compositions at the interface are given by a tie–line of the equilibrium phase diagram. The concentration profile which develops during the precipitation of a solute–rich phase β from a matrix α is illustrated in Fig. 2.5. In this case, only one mass conservation equation needs to be satisfied for a binary system with the tie–line passing through alloy composition.

$$v(c^{\beta\alpha} - c^{\alpha\beta}) = -D\frac{\partial c_M}{\partial z}\bigg|_{z=z^*} \tag{2.36}$$

Practical steels, however, contain many solute elements. In a multicomponent system, the mass conservation equations for each element should be satisfied simultaneously if equilibrium is to be maintained at the moving interface. Therefore, for an alloy carbide in a Fe–M–C system, at least two mass conservation equations, one for the substitutional solute M and the other for the interstitial carbon C, must be satisfied simultaneously :

$$\begin{aligned} v(c_M^{\beta\alpha} - c_M^{\alpha\beta}) &= -D_M\frac{\partial c_M}{\partial z}\bigg|_{z=z^*} \\ v(c_C^{\beta\alpha} - c_C^{\alpha\beta}) &= -D_C\frac{\partial c_C}{\partial z}\bigg|_{z=z^*} \end{aligned} \tag{2.37}$$

This poses difficulties in the choice of the tie–line since the interstitial and substitutional elements have vastly different diffusion coefficients.

Coates (1973) and Kirkaldy (1958) realised that because $D_M \ll D_C$, it would in general be impossible to satisfy these equations simultaneously for a tie–line passing through $\overline{c}$, apparently implying that growth cannot occur with equilibrium at the interface. However, for a ternary alloy, there is an additional degree of freedom given by the phase rule so that there is a choice of tie–lines at any given temperature. Fig. 2.8 shows the common tangent construction for two coexisting phases, α and β, in a ternary system. The contact of the tangent plane with the free energy surfaces defines the equilibrium compositions but since the plane can be rocked while remaining in contact with the surfaces, it is possible to define an infinite set of tie–lines which in turn generated the $\alpha + \beta$ phase field at a constant temperature.

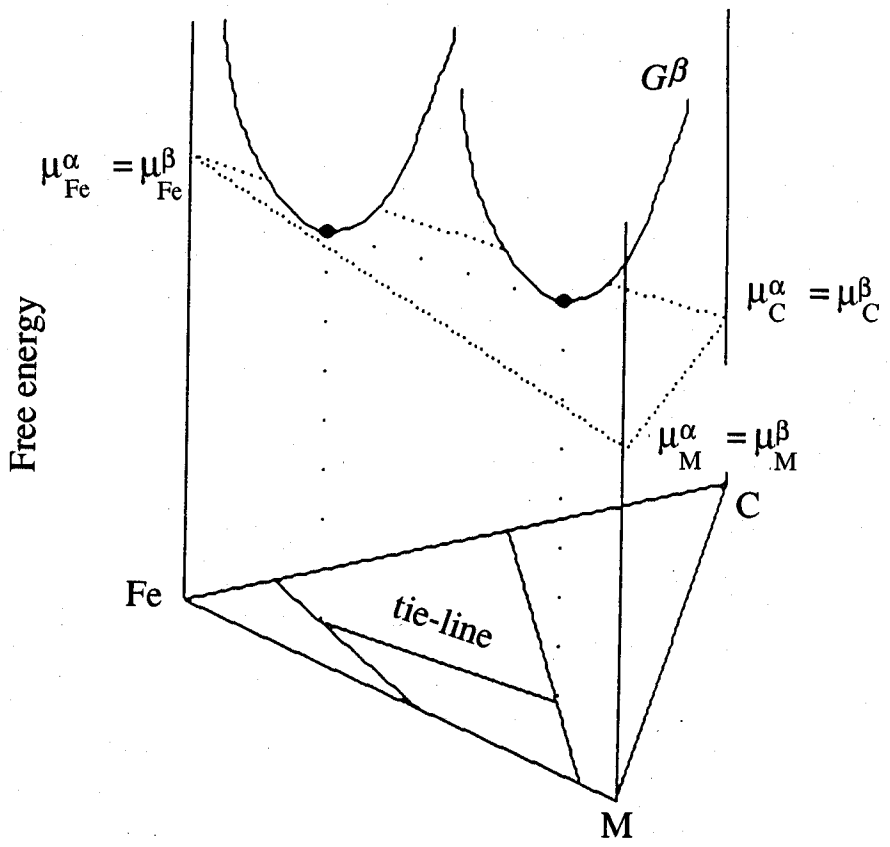

Figure 2.8: Schematic illustration of common tangent construction in a Fe-M-C ternary system. Note that μ_M^α and μ_M^β are the chemical potentials for solute M in α and β phases respectively and those for Fe and C are indicated in the same way.

It is this choice of tie–lines which allows multicomponent diffusion with local equilibrium at the interface. For example, the local equilibrium condition can be maintained by choosing a tie–line which either minimises the concentration gradient of carbon (thus allowing the the flux of element M to keep pace) or maximises the gradient of the substitutional solute to compensate for its small diffusivity. These are two ways in which the mass conservation equations for elements of M and C can be satisfied simultaneously. The first is to choose a tie–line which greatly increases the concentration gradient of element M to compensate for its low diffusivity. This would require the precipitate (carbide) to have virtually the same concentration of element M as the matrix with very little partitioning of element M, but with a sharp concentration spike at the interface in order to maintain local equilibrium (Coates, 1973; Kirkaldy, 1958). This situation is called "Negligible Partitioning Local Equilibrium" (termed

as NP–LE). NP–LE is only possible at very large driving forces. For alloy carbide precipitation in commercial steels, it is well–established that the carbide is usually substitutional solute–rich so that NP–LE may not be possible. All micro–alloyed steels strictly involve precipitation at low supersaturations. In these circumstances, the only alternative is to choose a tie–line which reduces the concentration gradient of element C (carbon) to such an extent that the flux of carbon is decreased to a level consistent with that of element M. This is called "Partitioning Local Equilibrium" (termed as P–LE). In Fig. 2.9, the concentration profiles for NP–LE and P-LE between phases, α (ferrite) and γ (austenite) in steels, were illustrated (Bhadeshia, 1992)

2.6 Non–equilibrium transformations

The transformation mentioned above is constrained by the need to maintain local equilibrium at the interface. There are other transformations which require great driving forces and less diffusion when compared with equilibrium growth. Such a transformation may therefore occur rapidly and hence have a kinetics advantage.

2.6.1 Paraequilibrium transformation

Local equilibrium breaks down when the driving force is large and transformation is too rapid for substitutional atoms to redistribute. Hultgren (1947) introduced the term "*paraequilibrium*" to describe a reaction, in which interstitial atoms can reach equilibrium subject to the constraint that substitutional atoms are trapped in the same concentration ratio to iron. Therefore, the paraequilibrium will occur when the time is long enough for diffusion of interstitial atoms but too short for the substitutional atoms to be mobile. For example, cementite formation in power plant steels during fast cooling from the normalising temperature is known to occur by the paraequilibrium mechanism. In that case, only carbon can redistribute but the substitutional atoms are trapped.

2.6.2 Martensitic transformation

Martensitic transformation often occurs when steels are cooled rapidly from austenite. Martensite is very hard and brittle because the carbon dissolved in austenite is trapped in the martensite. By tempering martensitic steels, it is frequently possible to obtain a good balance between toughness and strength so that such tempered steels are widely applied, including as power plant steels.

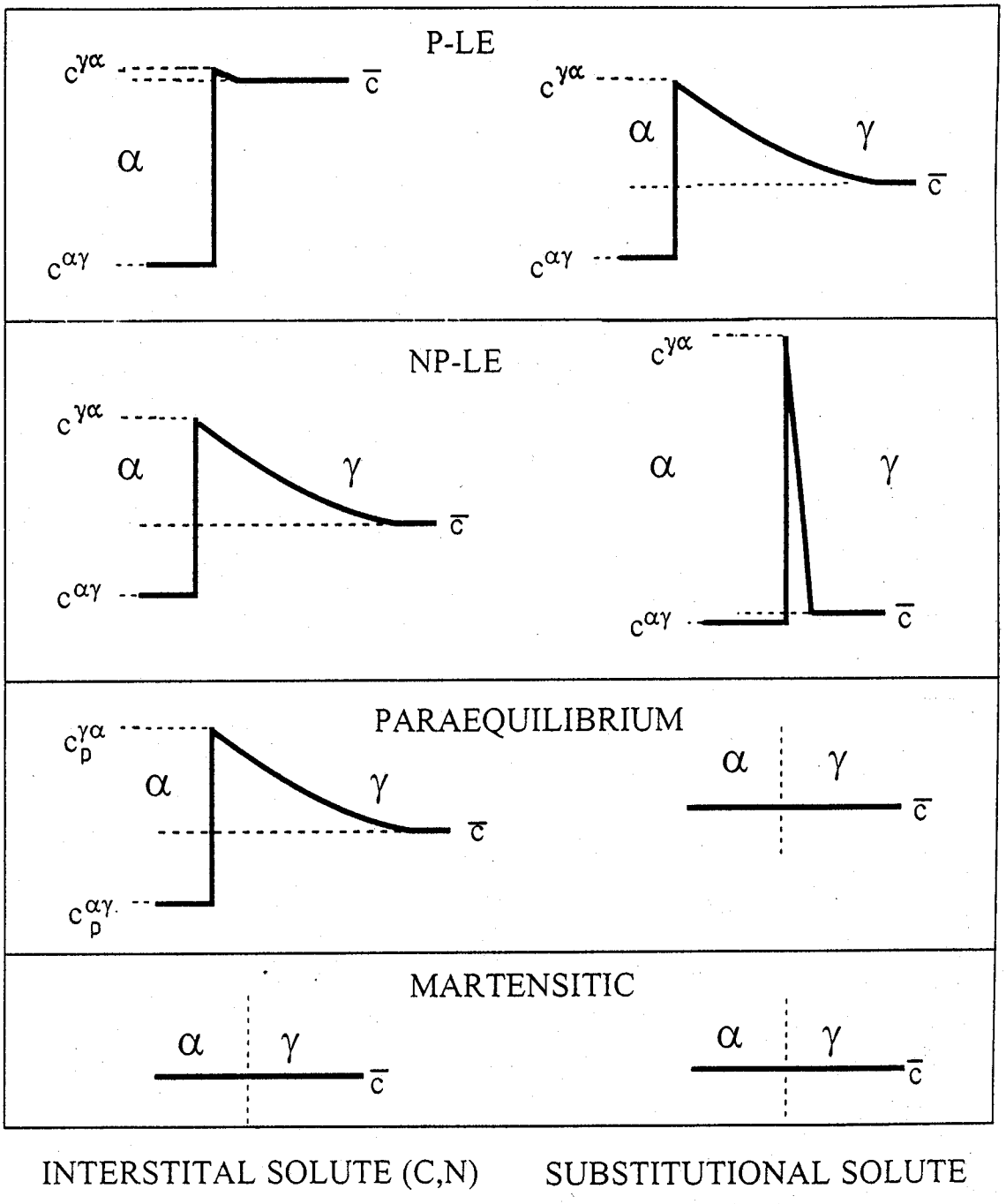

Figure 2.9: Schematic illustration of the composition variation in the vicinity of the transformation interface for a variety of growth mechanisms (Bhadeshia, 1992). Note that $c^{\alpha\gamma}$ and $c^{\gamma\alpha}$ are equilibrium concentrations in α and γ respectively, $c_p^{\alpha\gamma}$ and $c_p^{\gamma\alpha}$ are those for paraequilibrium and $\overline{c}$ is alloy composition.

This transformation requires a large driving force but no diffusion. The martensite transformation is then caused by diffusionless shear process so that there may not be a concentration change (Fig. 2.9) but there must be highly crystallographic in character. The orientation relationship between martensite and austenite normally may consist approximately of close–packed planes and the directions, such as Kurdjumov–Sachs or Nishiyama–Wasserman orientation relationships.

Kurdjumov-Sachs relationship: $\{111\}_\gamma \| \{011\}_{\alpha'}$ and $< 10\bar{1} >_\gamma \| < 11\bar{1} >_{\alpha'}$

Nishiyama-Wasserman relationship : $\{111\}_\gamma \| \{011\}_{\alpha'}$ and $< 11\bar{2} >_\gamma \| < 1\bar{1}0 >_{\alpha'}$

Moreover, because of diffusionless transformation, the rate can be extremely rapid. The transformation does not proceed until the undercooling below the critical temperature at which the difference of free energy between austenite and martensite reaches a critical value.

In summary, Fig. 2.9 shows the illustration for concentration profiles for interstitial and substitutional elements in each transformation between α and γ phases (Bhadeshia, 1992).

2.7 Overall transformation – Avrami theory –

When modelling precipitation, impingement must be accounted for. There are basically two types of impingement (Christian, 1975). Hard impingement is when particles growing from different sites touch. Soft impingement is when the particles interact via their diffusion fields. In this section, hard impingement will be introduced with the concept of extended volume (Avrami, 1940). Soft impingement will be described in a later section.

Consider that some precipitate particles (β) exist in matrix (α) without any impingement when the time is t as shown in Fig. 2.10 (a). In the next interval between t and $t + \Delta t$, some new nucleation, as represented by particles a and b in Fig. 2.10 (b), will occur. If the new nuclei form where there have already been particles, they should not be counted as a real volume increase. When new nucleation occurs where no particles have precipitated yet, the real volume increases. This reasoning applies also to any growth of pre–existing particles during the period Δt.

Extended volume includes not only the real volume but also any overlap of volume, *i.e.*, even previously transformed regions are able to contribute. Assuming random nucleation, possibility that a new transformation occurs in untransformed parent phase should be $(1 - V)$ where V

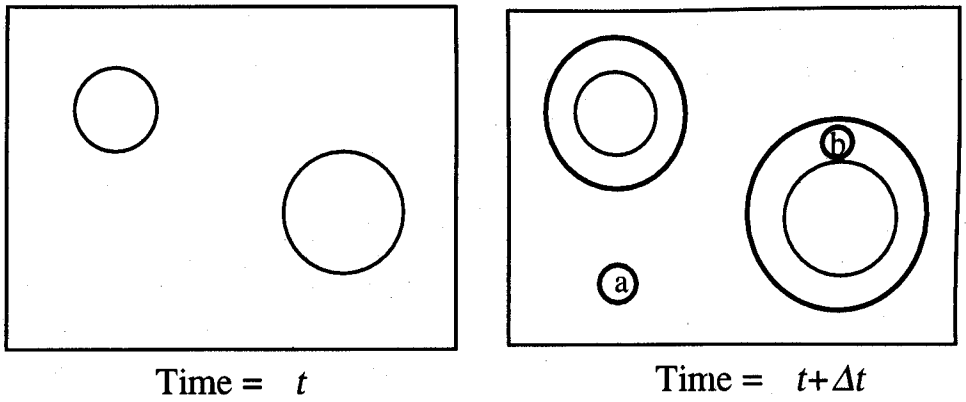

Figure 2.10: Schematic illustration of the change of particle volume with time, (a) time = t and (b) time = $t + \Delta t$. During Δt, particles a and b are assumed to nucleate. The volume of particle a is an increase in real volume. Volume of particles a and b should be counted as an increase in extended volume.

is real volume fraction and the total volume is assumed to be equal to one when the time is t. During the interval between t and $t + \Delta t$, the relationship between real volume fraction increase and extended volume fraction increase is therefore:

$$dV_\beta = (1 - V)dV_\beta^e \tag{2.38}$$

where dV_β and dV_β^e are changes of real volume fraction and extended volume fraction of β precipitation during the time increment dt respectively. When this equation is integrated, we obtain:

$$V_\beta = 1 - \exp(-V_\beta^e) \tag{2.39}$$

When precipitates occur homogeneously and are isotropic, the volume of a particle which nucleates after an incubation time, τ, is represented:

$$w_\tau = \begin{cases} \frac{4}{3}\pi v^3(t-\tau)^3 & t \geq \tau \\ 0 & t \leq \tau \end{cases} \tag{2.40}$$

where w_τ is volume from the nuclei which occur during the incubation time, τ, and v is the growth rate. The number of new nuclei occurring between $t = \tau$ and $t = \tau + d\tau$ is $Id\tau$, where I is the nucleation rate per unit volume. Assuming that the nucleation rate is constant, the change in the extended volume fraction during the interval $d\tau$ is given by :

$$dV_\beta^e = \frac{4}{3}\pi v^3 (t-\tau)^3 I d\tau \tag{2.41}$$

Integrating this equation, V_β^e can be obtained:

$$V_\beta^e = \frac{1}{3}\pi v^3 I t^4 \tag{2.42}$$

and then, the real volume fraction of precipitation can be calculated using equation 2.39.

$$V_\theta = 1 - \exp[-\frac{1}{3}\pi v^3 I(t)^4] \tag{2.43}$$

This is the Kolmogorov–Johnson– Mehl–Avrami equation for the assumed set of conditions.

The case described above is a special one with homogeneous nucleation. However, as most industrial materials are polycrystalline, nucleation may not occur homogeneously. The possibility of nucleation on grain boundaries may be higher than on other sites. Cahn (1956) considered three types of sites on grain boundaries: planes, edges and corners. In each case, the relationship between volume fraction and time was in the form; $V = 1 - \exp(-\kappa t^{m_a})$, generally called the Avrami equation. Table 2.1 shows the results for values of κ and m_a. Therefore, the Avrami equation has the general form as:

$$V = 1 - \exp(-\kappa t^{m_a}) \tag{2.44}$$

Where κ and m_a are constant but depend on the specific assumptions (Table 2.1).

Nucleation site	Time exponent: m_a	κ-value
Homogeneous nucleation	4	$\frac{\pi}{3} I v^3$
A plane on grain boundary	1	$2 S_{gb} L_{gb}$
An edge on grain boundary	2	$\pi L_{gb} v^2$
A corner on grain boundary	3	$\frac{4}{3}\pi N_c v^3$

Table 2.1: Values of m_a and κ in the general form equation 2.44 (Cahn, 1956), where I is nucleation rate, v is growth rate, S_{gb} is area of grain boundary per unit volume, L_{gb} is length of grain boundary edge per unit volume and N_c is density of grain boundary corners. All nucleation on the grain boundaries is assumed to occur before the growth.

2.8 Soft–impingement

The changes in the chemical composition of the matrix during precipitation are vital to the development of the precipitation process. Composition gradients develop in the matrix α and the gradients originating from different particles eventually interfere, changing the boundary conditions for the rate equations. Wert and Zener tried to deal with soft–impingement (1950), assuming that all nuclei were initially present, that the supersaturation was low enough to decrease particle growth and that the distance between particles is large. The boundary conditions about the time–dependent solute concentration $c(t)$ are given by:

$$c(\infty) = c^{\alpha\beta} \text{ and } c(0) = \overline{c} \tag{2.45}$$

where $c^{\alpha\beta}$ is equilibrium solute concentration in the matrix α at the interface between matrix α and precipitate β, $\overline{c}$ is the alloy composition of the solute. Then, the velocity of the interface v can be written in the similar formula to the equation 2.9.

$$v = \frac{D}{z_d} \frac{c(t) - c^{\alpha\beta}}{c^{\beta\alpha} - c^{\alpha\beta}} \tag{2.46}$$

Because all nuclei initially exist, the final radius of all particles r^f will be same. The volume fraction untransformed ζ can be written as:

$$\zeta = \left(\frac{r^I}{r^f}\right)^3 \tag{2.47}$$

where r^I is instantaneous radius. The following relationship is also obtained:

$$\frac{c(t) - c^{\alpha\beta}}{c^{\beta\alpha} - c^{\alpha\beta}} = 1 - \zeta \tag{2.48}$$

The diffusion distance z_d is approximately equal to r so that equation 2.49 is obtained:

$$\frac{d\zeta}{dt} = \frac{3D}{(r^f)^2} \frac{(\overline{c} - c^{\alpha\beta})}{(c^{\beta\alpha} - c^{\alpha\beta})} \zeta^{\frac{1}{3}} (1 - \zeta) \tag{2.49}$$

The solution of this equation is very complicated. Wert and Zener made a numerical integration about the change of ζ with time. Their result indicated that there is deviation towards the end of transformation, compared with that given by Avrami equation (Christian, 1975).

2.9 Simultaneous precipitation reactions in power plant steels

2.9.1 Introduction

The theory for overall transformation described above can deal only with one phase precipitating at any time. However, it is quite frequent for a number of solid–state transformations to occur concurrently, starting from the same parent phase. The transformations may occur at different rates, but the resulting competition for space or for the partitioning of driving force between the precipitating phases can be seminal to the development of many microstructures found in commercial steels. The overall transformation theory available for dealing with simultaneous transformations has been reviewed (Bhadeshia, 1999a). The theory discussed is generally applicable, but is illustrated with a specific case (Robson and Bhadeshia, 1997a: Jones and Bhadeshia, 1997: Kasuya *et al.*, 1999).

There are at least three circumstances in which a phase might transform into more than one product:

1. The equilibrium precipitate may be difficult to nucleate. Consequently, decomposition starts with the formation of one or more metastable phases which are kinetically favoured. These must eventually dissolve as equilibrium is approached. There are a typical example in secondary hardening steels. The formation of the metastable phase is accompanied by a reduction in free energy causing an exaggerated retardation of the stable phase.

2. All of the product phases may be at equilibrium; *e.g.* the transformation of austenite into a mixture of ferrite and graphite. However, the transformation products do not grow in a coupled manner and may be sufficiently separated in time to be treated as *sequential* rather than *simultaneous.*

3. The product phases may be coupled as in the formation of pearlite, with a common transformation front.

It is the first case which forms the subject of this review.

2.9.2 Basic concept

Suppose that phases β and θ are precipitating at the same time, a simple modification for two precipitates (β and θ) is that the equation 2.38 becomes a coupled set of two equations,

$$dV_\beta = \{1 - (V_\beta + V_\theta)\}dV_\beta^e \tag{2.50}$$

$$dV_\theta = \{1 - (V_\beta + V_\theta)\}dV_\theta^e \tag{2.51}$$

where V_β and V_θ are real volume fractions for each phase and V_β^e and V_θ^e are extended volume fractions for each phase, assuming that the total volume is one. The method can be used for any number of reactions happening together. The resulting set of equations must in general be solved numerically although a few analytical solutions are possible for special cases which we shall now illustrate.

2.9.3 Special cases

For the simultaneous formation of two phases β and θ whose extended volume fractions are related linearly (Robson and Bhadeshia, 1997a: Jones and Bhadeshia, 1997: Kasuya *et al.*, 1999):

$$V_\theta^e = B_1 V_\beta^e + C_2 \qquad \text{with} \qquad B_1 \geq 0 \qquad \text{and} \qquad C_2 \geq 0 \tag{2.52}$$

It can be shown (Kasuya *et al.*, 1999) that

$$V_\beta = \int \exp\left\{-(1+B_1)V_\beta^e + C_2\right\}\, dV_\beta^e \qquad \text{and} \qquad V_\theta = BV_\beta \tag{2.53}$$

If the isotropic growth rate of phase β is v_β and if all particles of phase β start growth at time $t = 0$ from a fixed number of sites N_V per unit volume then $V_\beta^e = N_V \frac{4\pi}{3} v_\beta^3 t^3$. On substitution of the extended volume fraction,

$$V_\beta = \frac{1}{1+B_1}\exp\{-C_2\}\left[1 - \exp\left\{-(1+B_1)N_V\frac{4\pi}{3}v_\beta^3 t^3\right\}\right] \qquad \text{with} \qquad v_\theta = B_1 v_\beta \tag{2.54}$$

The term $\exp\{-C_2\}$ is the fraction of parent phase available for transformation at $t = 0$; it arises because $1 - \exp\{-C_2\}$ of phase θ exists prior to commencement of the simultaneous reaction at $t = 0$. Thus, V_θ is the additional fraction of phase θ that forms during simultaneous reaction. When $C_2 = 0$, equations 2.54 reduce to the case considered by Robson and Bhadeshia (1997a). It is emphasised that $C_2 \geq 0$. A case for which $C_2 = 0$ and $B_1 = 8$ is illustrated in Fig. 2.11.

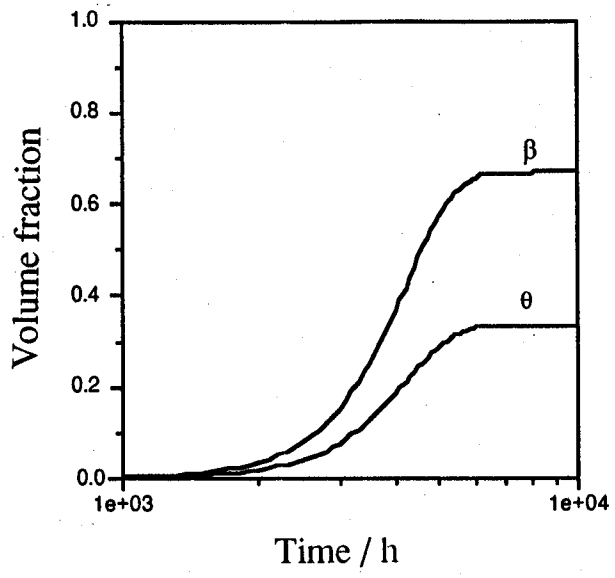

Fig. 2.11: Simultaneous transformation to phases α and β with $C_2 = 0$ and $B_1 = 8$.

For the case where the extended volume fractions are related parabolically (Kasuya *et al.*, 1999):

$$V_\beta = \exp\left\{-C_2\right\}\left[\sqrt{\frac{\pi}{4A_1}}\exp\left\{\frac{(1+B_1)^2}{4A_1}\right\}\left(\mathrm{erf}\left\{\frac{1+B_1}{\sqrt{4A_1}}+\sqrt{A_1}V_\beta^e\right\}-\mathrm{erf}\left\{\frac{1+B_1}{\sqrt{4A_1}}\right\}\right)\right]$$
$$V_\theta = \exp\left\{-C_2\right\}\left[1-\exp\left\{-A_1(V_\beta^e)^2+(1+B_1)V_\beta^e\right\}\right]-V_\beta \tag{2.55}$$

The volume fractions V_i for phase i again refer to the phases that form *simultaneously* and hence there is a scaling factor $\exp\{-C_2\}$ which is the fraction of parent phase available for coupled transformation to phases β and θ.

2.9.4 Complex simultaneous reactions in secondary hardening steels

Whereas the analytical cases are revealing, it is unlikely in practice for the phases to be related in the way described. This is illustrated for secondary hardening steels of the kind used commonly in the construction of power plant (Robson and Bhadeshia, 1997a). The phases interfere with each other not only by reducing the volume available for transformation, but also by removing solute from the matrix and thereby changing its composition. This change in matrix composition affects the growth and nucleation rates of the phases.

The calculations must allow for the simultaneous precipitation of M_2X, M_7C_3, $M_{23}C_6$, M_6C and Laves phase. M_3C is assumed to nucleate instantaneously with the paraequilibrium composition. Subsequent enrichment of M_3C as it approaches its equilibrium composition is accounted for. All the phases, except M_3C, are assumed to form with compositions close to equilibrium (Robson and Bhadeshia, 1997a). The driving forces and compositions of the precipitating phases are calculated using standard thermodynamic methods. Each metastable phase starts to dissolve when the solute concentration in the matrix which controls precipitation becomes below the calculated equilibrium concentration. Table 2.2 shows the conditions of nucleation and growth for each precipitate in secondary hardening steels (Robson and Bhadeshia, 1997a).

Precipitation	Nucleation and growth condition
M_3C	No nucleation but paraequilibrium growth of a number of particles followed by change in chemical composition
M_2X	Finite nucleation rate and diffusion–controlled linear growth of needles
$M_{23}C_6$	Finite nucleation rate and diffusion–controlled parabolic growth of spheroids
M_6C	Finite nucleation rate and diffusion–controlled parabolic growth of spheroids
Laves phase	Finite nucleation rate and diffusion–controlled parabolic growth of spheroids

Table 2.2: The calculation conditions of isothermal precipitation of secondary hardening steels in Robson and Bhadeshia model (1997a).

The interaction between the precipitating phases is accounted for by considering the change in the average solute level in the matrix as each phase forms. This treatment for soft–impingement is frequently called the "mean field approximation". It is necessary because the locations of precipitates are not predetermined in the calculations. Some details for each precipitation process are now introduced.

M_3C precipitation

M_3C is assumed to exist in the initial microstructure so that there is not a nucleation but has already been with paraequilibrium. The number of nucleation sites for cementite M_3C is found by following Takahashi and Bhadeshia (1991). The M_3C volume fraction can be calculated by

the assumption of almost zero solubility of carbon in ferrite. The volume fraction is then given by:

$$V_\theta = \frac{\overline{c}}{c^{\theta\alpha}} \quad \text{with} \quad c^{\theta\alpha} \simeq 0.25 \tag{2.56}$$

where V_θ is volume fraction of cementite. Venugopalan and Kirkaldy (1978) suggested that the average size of cementite before any Ostwald ripening is indicated empirically by:

$$\overline{r}^3 = (2.26 - 6.4 \times 10^{-3}T + 4.6 \times 10^{-6}T^2)V_\theta \times 10^{-3} \tag{2.57}$$

where $\overline{r}$ is the average size in μm and T is the tempering temperature in °C. Therefore, the number of M_3C particles per unit volume is given by

$$N_\theta = \frac{V_\theta}{\frac{4}{3}\pi\overline{r}^3} \tag{2.58}$$

The M_3C which is formed in paraequilibrium in power plant steel should change to equilibrium (Thomson, 1992). This requires the substitutional atom diffusion. Bhadeshia (1989) modelled the relationship between time t_c and a M_3C thickness d as:

$$t_c^{\frac{1}{2}} = \frac{d(\overline{c} - c_t)\pi^{\frac{1}{2}}}{4D^{\frac{1}{2}}(c^{\alpha\theta} - \overline{c})} \tag{2.59}$$

where c_t is the solute concentration in M_3C with the thickness of d, D is solute diffusion coefficient. The typical size of M_3C investigated experimentally by Robson for 10CrMoV (1996) and Thomson for $2\frac{1}{4}$Cr1Mo (1992) steels is 30 nm. Using this value of the thickness in equation 2.59, the relationship between time and concentration of substitutional solute atom in M_3C can be obtained. Metastable phases, including M_3C, should start to dissolve when the solute concentration in the matrix reaches the equilibrium level with the metastable phase.

Mean field approximation

Alloy carbide formation is likely to be controlled by the diffusion of substitutional solute atoms. The change of matrix composition during precipitation can affect the subsequent nucleation and growth process. As described in the section 2.8, some complex solutions have been suggested. For avoiding complexity, Robson and Bhadeshia suggested the mean field approximation for soft–impingement. Solute concentration changes are averaged at over the remaining matrix

phase as a method for dealing with soft–impingement (1997a). The dimensionless supersaturation is written

$$V^{Max} = \frac{(\overline{c} - c^{\alpha\beta})}{(c^{\beta\alpha} - c^{\alpha\beta})} \tag{2.60}$$

where V^{Max} is the maximum fraction for each phase. The effect of soft–impingement in the mean field approximation may be expressed in terms of an "extent of reaction" parameter, defined as:

$$\Phi = V'/V^{Max} \tag{2.61}$$

where V' is the fraction at any instance for each phase. Therefore, Φ changes from 0 to 1 during precipitation and can be defined for each phase. For simultaneous precipitation, Φ may be changed by occurrence of a new phase precipitating. If there are n phases forming simultaneously, then Φ_i for the ith phase is given by:

$$\Phi_i = \frac{\sum_{i=1}^{n} V_i'(c^{i\alpha} - c^{\alpha i})}{(\overline{c} - c^{\alpha i})} \tag{2.62}$$

where $c^{i\alpha}$ and $c^{\alpha i}$ are concentrations at the interface between ith phase and matrix α in the ith phase and in the matrix respectively, V_i' is the fraction at any instance for the ith phase.

Physically, Φ represents the fraction of excess solute remaining in the matrix with respect to the phase in question. Therefore, it is possible to make the approximation that the driving force ΔG_i for formation of each phase should be in proportion to $(1 - \Phi_i)$ as indicated in equation 2.63.

$$\Delta G_i = (1 - \Phi_i)\Delta G_{0i} \tag{2.63}$$

where ΔG_{0i} is the driving force at $t = 0$.

For M_3C, it must be necessary to calculate the value of Φ_{M_3C} differently. This is because M_3C nucleates with the paraequilibrium composition. Therefore, the value should include the composition change of diffusing solute atom.

$$\Phi_{M_3C} = \frac{(c - \overline{c}')}{(c^{M_3C\alpha} - \overline{c}')} \tag{2.64}$$

where $\overline{c}'$ is the mean concentration in the matrix at any time, which is

$$\overline{c}' = \frac{(\overline{c} - \sum_{i=1}^{n} V_i' c^{i\alpha})}{(1 - \sum_{n=1}^{n} V_i')} \tag{2.65}$$

Schematic composition profiles are shown in Fig. 2.12, (a) at a certain time, both β and γ are precipitating in matrix α and then (b) when solute concentration in matrix reaches the equilibrium with β, precipitation of β has been completed, and as γ precipitates further, removing solute, β will start to dissolve.

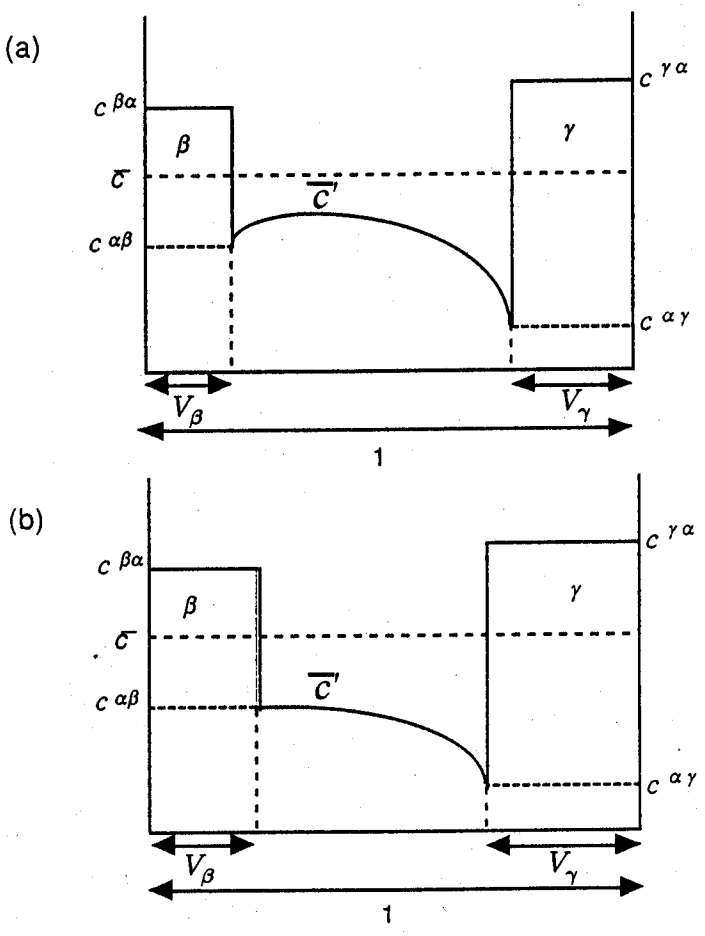

Figure 2.12: Distribution of solute when (a) both β and γ are precipitating, and (b) where the precipitation of β has been completed (Robson, 1996). Note that $\overline{c}'$ is solute concentration in the matrix α and that V_β and V_γ are phase volume fraction for β and γ respectively.

Dissolution of metastable phase

Fig. 2.13 shows schematic drawing of the concentration profile in case that there are β and γ phases in matrix α. In Fig. 2.13, it was illustrated that β phase was dissolving whilst γ phase was growing. When the solute concentration in the matrix, $\overline{c}'$, which may be decreased by the effect of soft–impingement falls below $c^{\alpha\beta}$, the metastable phase β will start to dissolve. Considering the mass balance between matrix α and precipitate β, equation 2.66 can be obtained.

$$\frac{dr}{dt}(c^{\beta\alpha} - c^{\alpha\beta}) = -D\frac{dc}{dx} \tag{2.66}$$

where D is the diffusion coefficient of the solute atom in matrix α. Using the Zener linearised gradient approximation (shown in Fig. 2.13 with a dotted line).

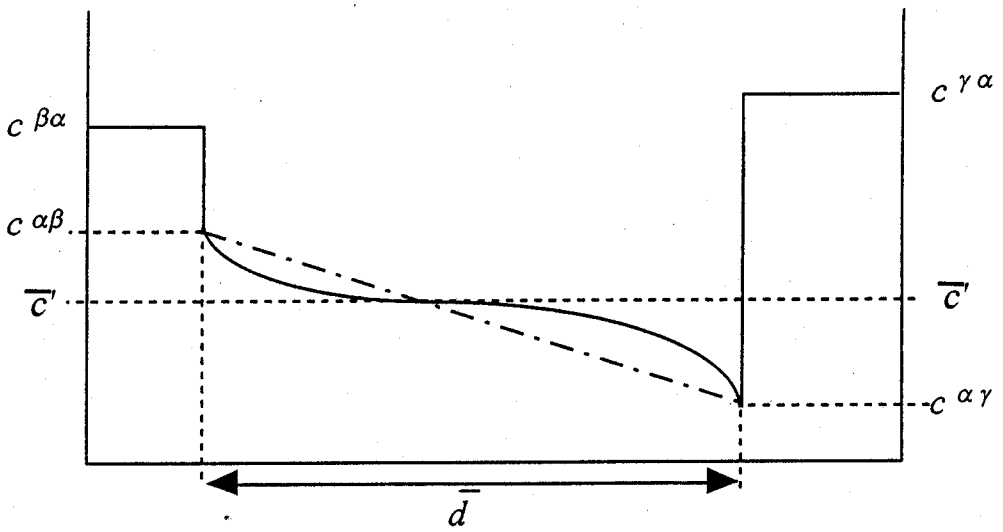

Figure 2.13: Schematic illustration of solute distribution when β is dissolving and γ is precipitating in matrix α (Robson, 1996). The dotted line represents the linearised concentration gradient approximation for dissolution. $\overline{c}'$ is the mean concentration in the matrix at any time.

The solute concentration gradient may be assumed as:

$$\frac{dc}{dx} = -\frac{(c^{\alpha\beta} - c^{\alpha\gamma})}{\overline{d}} \tag{2.67}$$

where $c^{\alpha\gamma}$ is the solute concentration in the matrix α which is in local equilibrium with γ phase and $\overline{d}$ is the mean diffusion distance between the β and γ precipitates, which is given by:

$$\overline{d} = (N_\beta + N_\gamma)^{-\frac{1}{3}} \tag{2.68}$$

where N_β and N_γ are a number of density for β and γ precipitates, which are assumed to be unchanged during dissolving. It is assumed that the whole process can be represented by a mean radius $\overline{r}$ for spherical particle and a mean length $\overline{l}$ for needle. With this assumption, the change of volume fraction for dissolving phase V_β with time can be described in equations 2.69a for spherical particles and 2.69b for needles.

$$\frac{dV_\beta}{dt} = 4\pi\overline{r}^2 \frac{D(c^{\alpha\beta} - c^{\alpha\gamma})}{\overline{d}(c^{\beta\alpha} - c^{\alpha\beta})} \tag{2.69a}$$

$$\frac{dV_\beta}{dt} = \frac{3\pi\overline{l}^3}{\phi^2} \frac{D(c^{\alpha\beta} - c^{\alpha\gamma})}{\overline{d}(c^{\beta\alpha} - c^{\alpha\beta})} \tag{2.69b}$$

where ϕ is the aspect ratio of needle phase.

In case of M_3C in paraequilibrium, the composition changes with time from paraequilibrium to equilibrium. When the value of Φ_{M_3C} in equation 2.64 is equal to one, dissolution starts, and then is dealt with in same way as for other metastable phases.

An example for power plant steels

A plot showing the predicted variation of volume fraction of each precipitate as a function of time at 600 °C is shown in Fig. 2.14. It is worth emphasising that there is no prior knowledge of the actual sequence of precipitation, since all phases are assumed to form at the same time, albeit with different precipitation kinetics. The fitting parameters common to all the steels are the interfacial energy terms for each phase and to some extent, the nucleation number densities (Robson and Bhadeshia, 1997a).

Consistent with experiments, the precipitation kinetics of $M_{23}C_6$ are predicted to be much slower in the $2\frac{1}{4}$Cr1Mo steel compared to the 10CrMoV and 3Cr1.5Mo steels. One contributing factor is that in the $2\frac{1}{4}$Cr1Mo steel a relatively large volume fraction of M_2X forms prior to $M_{23}C_6$. These deplete the matrix and therefore suppress $M_{23}C_6$ precipitation. The volume fraction of M_2X which forms in the 10CrMoV steel is relatively small, and there remains a considerable excess of solute in the matrix, allowing $M_{23}C_6$ to precipitate rapidly. Similarly, in

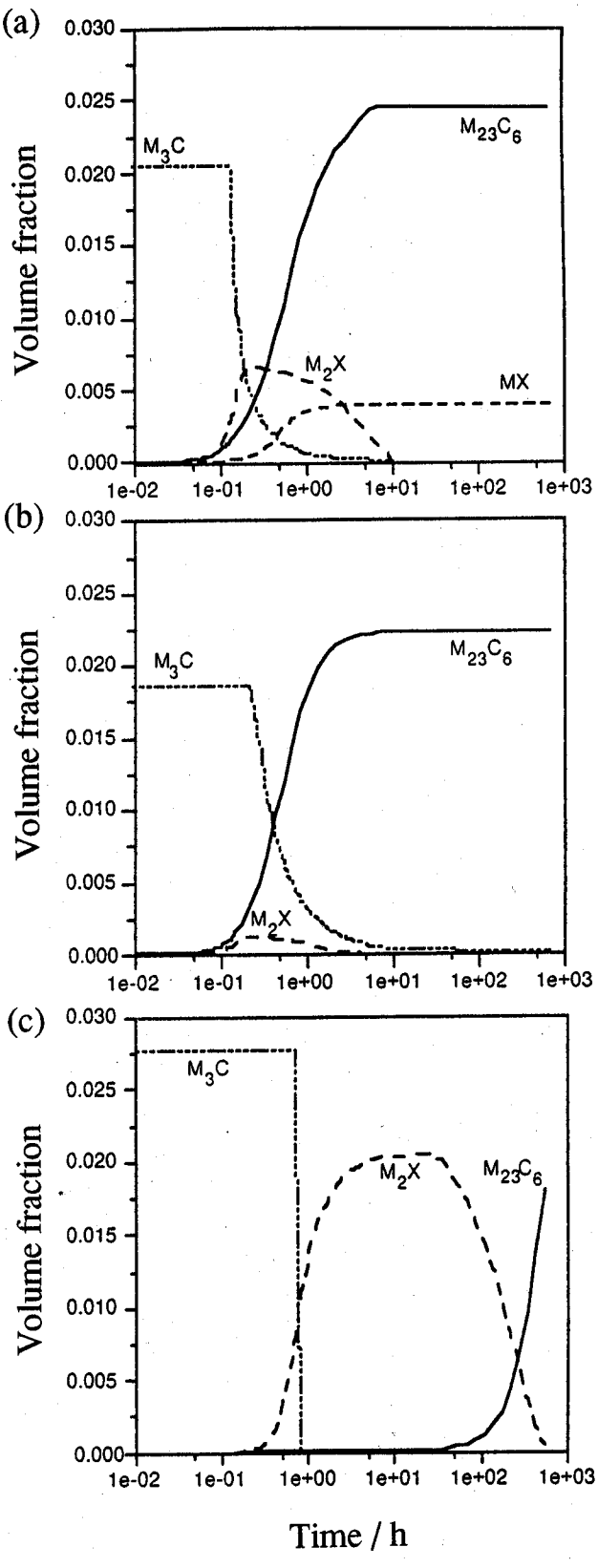

Fig. 2.14: The predicted evolution of precipitate volume fractions at 600 °C for three power plant materials (a) 10Cr–1.5Mo–0.2V–0.05Nb, (b) 3Cr–1.5Mo and (c) $2\frac{1}{4}$Cr–1Mo wt% steels (after Robson and Bhadeshia, 1997a).

the 3Cr1.5Mo steel the volume fraction of M_2X is insufficient to suppress $M_{23}C_6$ precipitation to the same extent as in the $2\frac{1}{4}$CrMo steel.

There have been some experimental investigations for $2\frac{1}{4}$Cr1Mo steel (Baker and Nutting, 1959: Nutting, 1999) so that the sequence of precipitation is known. The predicted time–temperature–precipitation diagram (TTP) for $2\frac{1}{4}$Cr1Mo steel by Robson and Bhadeshia model is shown in Fig. 2.15 (a), together with Baker and Nutting's experimental data (Robson, 1996). For 10CrMoV steel, high chromium heat–resisting steel with excellent creep resistance, similar data are shown in Fig. 2.15 (b) along with the predictions (Robson, 1996). There is good agreement between experiment and theory. Using the same model, Robson and Bhadeshia (1997a) predicted that the precipitation process for 3Cr1.5Mo steel would be quite different from that of $2\frac{1}{4}$Cr1Mo steel and more similar to that of 10CrMoV steel as shown in Fig. 2.14. However, there are no significant experimental data for this steel, so the result needs experimental verification.

2.10 Particle coarsening

Transformation is said to be complete when there is no significant change in the precipitate fraction over a period of time. However, coarsening may still occur. We note that it is traditional to separate transformation and coarsening but the two processes are in fact complied with capillarity. The classic theory of Ostwald ripening is due to Lifshitz and Slyozov (1958, 1961) and Wagner (1961) :

$$\overline{r}^3 - r_0^3 = \frac{8\sigma v^\beta D c^{\alpha\beta}}{9RT} t \tag{2.70}$$

where r_0 is the initial particle radius, σ is the interfacial energy, v^β is the molar volume of the phase β, D is the solute diffusion coefficient, $c^{\alpha\beta}$ is the equilibrium solute concentration in the matrix α at which $r \to \infty$, R is the gas constant, T is temperature in K, t is holding time at the isothermal heat treatment temperature. Note that this equation for particle coarsening is valid when the equilibrium volume fraction is small.

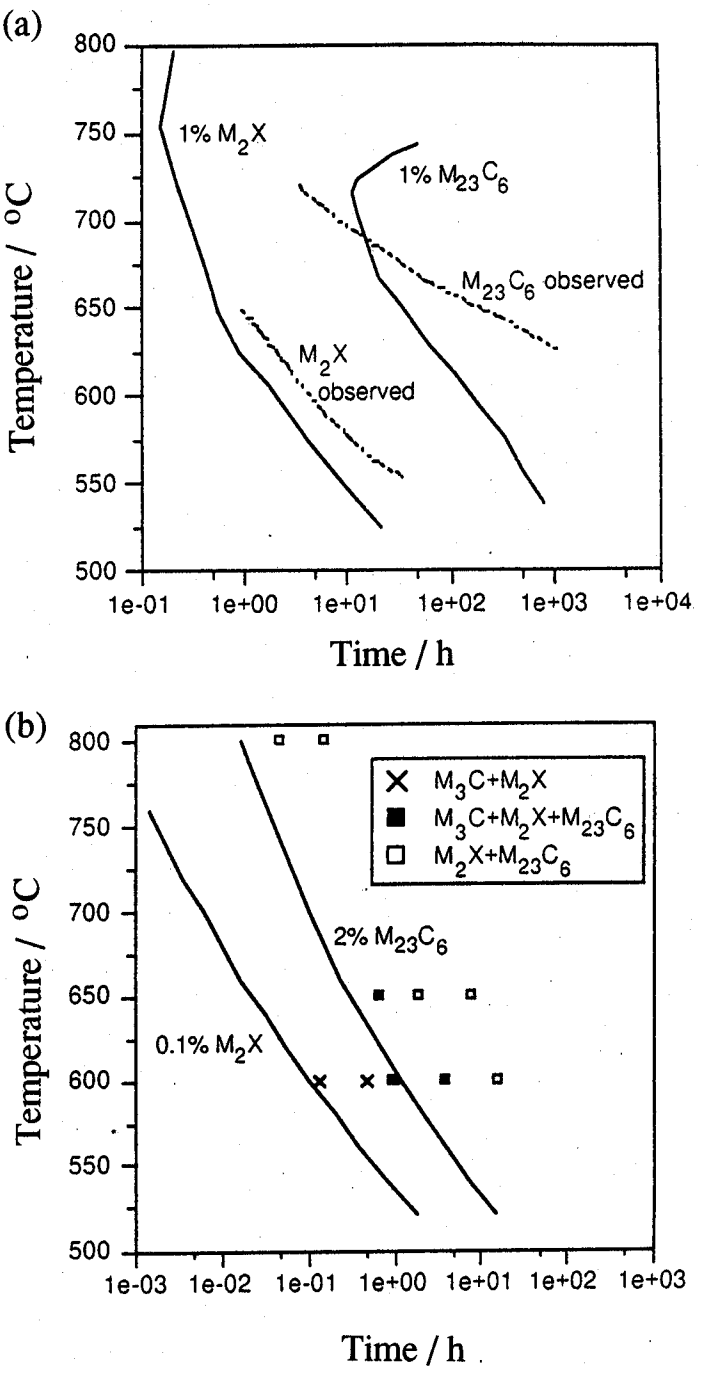

Figure 2.15: Predicted time–temperature–precipitation diagram for precipitates in (a) $2\frac{1}{4}$Cr1Mo steel and (b) 10CrMoV steel, together with experimental data of $2\frac{1}{4}$Cr1Mo steel by Baker and Nutting (1959) and 10CrMoV steel by Robson (1996).

2.11 Summary

Theory about the nucleation and growth of individual particles is fairly well–established. There has also been some progress in the theory for the overall transformation kinetics simultaneous transformations. In particular, the Johnson–Mehl–Avrami–Kolmogorov concept of extended volume can be adapted for the case where more than one reaction occurs at the same time. However, some of complex terms, for example capillarity and diffusion–controlled growth in a multicomponent system and the incorporation of coarsening as a natural phenomenon, have not yet been applied with sufficient rigour within the simultaneous precipitation framework. This is the primary aim of the work presented in this thesis.

CHAPTER THREE

Experimental procedures

3.1 Introduction

There are two main purposes to the experiments. Firstly, to verify the theory for simultaneous precipitation reactions in power plant steels. It is also intended to obtain particle size data for each precipitate to help establish whether size distributions can be reasonably modelled. Two of power plant steels were therefore selected for microstructual investigation. Fig. 3.1 is the general flow chart of the experimental procedures.

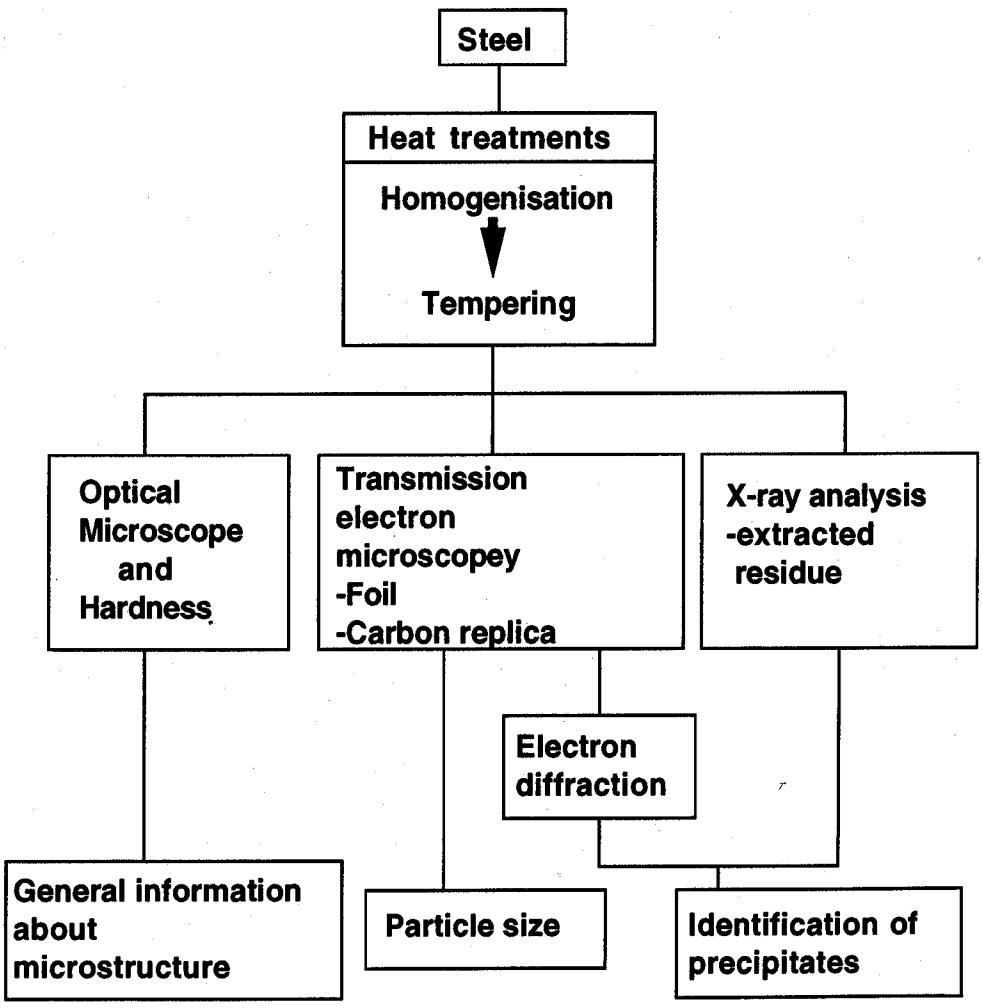

Figure 3.1: Experimental procedure.

Materials for this work were made on a laboratory scale. After homogenisation, the samples were tempered at a variety of temperatures and for time periods sufficiently long to produce the required microstructures. Optical and transmission electron microscopy were used to characterise the microstructures. The precipitates were identified using electron diffraction and X–ray analysis of extracted residues. The precipitate particle sizes were also measured from transmission electron micrographs.

3.2 Materials and processing conditions

Table 3.1 shows the chemical compositions of the alloys used. Fig. 3.2 shows the processing conditions for the steels.

Steel	C	Si	Mn	Cr	Mo	N
$2\frac{1}{4}$Cr1Mo	0.15	-	0.49	2.16	0.92	≤ 0.005
3Cr1.5Mo	0.10	-	0.98	2.98	1.50	≤ 0.005

Table 3.1: Concentration in wt% of the major alloying elements in $2\frac{1}{4}$Cr1Mo and 3Cr1.5Mo steels

These steels were vacuum–melted as 15 kg ingots, heated at 1250 °C for 30 minutes in an argon atmosphere, hot–rolled to 15 mm thickness plate and quenched from a finishing temperature of about 900 °C. From the plates, 3 mm and 8 mm diameter cylindrical specimens were machined for heat treatment. The specimens were sealed in silica tubes under a partial pressure of argon (about 150 mm Hg), before the homogenisation heat treatment. Using the thermodynamic software named MTDATA from the National Physical Laboratory (Hodson, 1989), the equilibrium phases for each steel were calculated as shown in Table 3.2. According to these results, both steels became fully austenite at temperatures above 1200 °C. Therefore, the homogenisation temperature was chosen to be 1250 °C where the samples were held for 3 days.

After the homogenisation treatment, the specimens were quenched into water with breaking silica tube. Then, specimens were sealed again and tempered at the expected service temperatures, 600 °C, 650 °C and 700 °C for a maximum of 1000 h. After tempering, all specimens were again quenched into water with breaking the tubes.

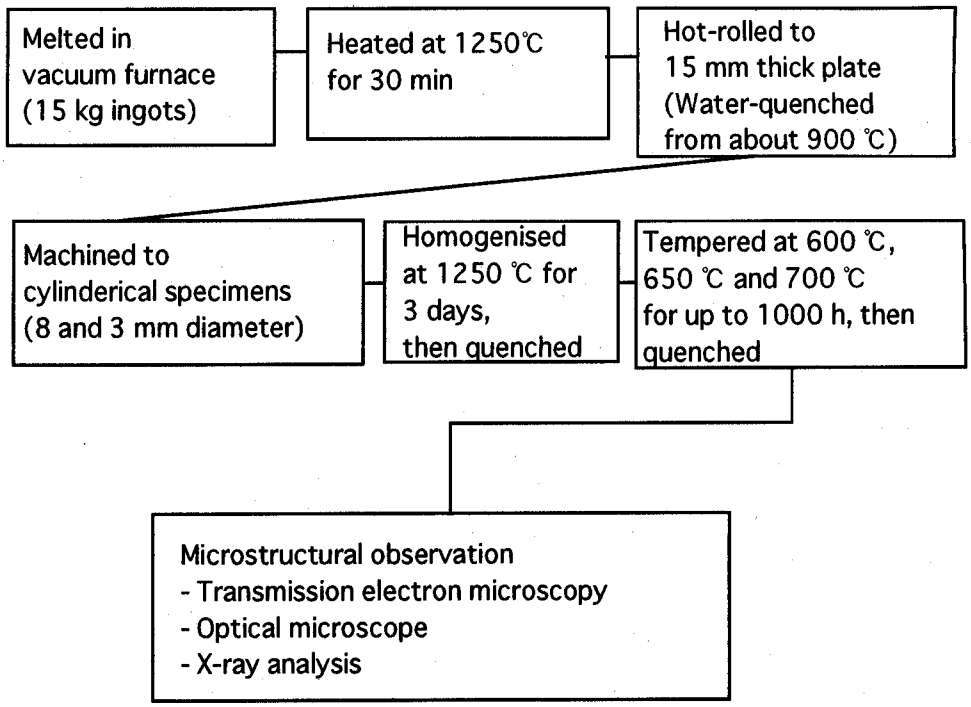

Figure 3.2: Processing conditions.

Steel	Equilibrium phases at each temperature		
	1200 °C	1250 °C	1300 °C
$2\frac{1}{4}$Cr1Mo	austenite	austenite	austenite
3Cr1.5Mo	austenite	austenite	austenite

Table 3.2: The equilibrium phases for each steel studied in this work, calculated using MTDATA and SGTE database. For the calculations, the steel composition in Table 3.1 are used and the phases allowed are liquid, austenite, ferrite, possible carbides and nitrides.

3.3 Optical microscopy

Specimens for optical microscopy were hot–mounted with acrylic moulding powder, and ground with silicon carbide paper down to 1200 grit and then polished with 6 and 1 μm diamond pastes. Specimens of both steels were etched with 2 vol.% nital (nitric acid in methanol). The optical microstructures were observed using an Olympus microscope.

3.4 Hardness measurements

Microhardness (Vickers) was measured with loads up to 1 kgf applied for 20 seconds. Five measurements were taken in each case.

3.5 Transmission electron microscopy (TEM)

TEM was performed using both a Philips 400T and a Jeol 2000FX transmission electron microscopes operated between 100 and 200 kV.

3.5.1 Sample preparation

Two types of specimens were examined using TEM; thin foils and carbon extraction replicas.

Thin foils were cut from bulk specimens as 3 mm diameter discs to about 500 μm thickness using a silicon carbide blade and cooling lubricant. Great care was taken not to bend the specimens. After cutting, the specimens were ground with silicon carbide paper to less than 60 μm thickness. Electropolishing was conducted using a twin jet electropolisher. The solutions for electropolishing are 5 vol.% perchloric acid, 20 vol.% glycerol and 75 vol.% industrial methanol for both steels. The electropolishing was performed with the solution at 0 °C, the electrical potential being set at 50 V for both steels.

Fig. 3.3 shows schematically the method for making a carbon extraction replica. The sample was mounted in the same way as for metallography and was etched in the same way. A carbon film was then applied on the etched surface using vacuum evaporation. The film was electrolytically etched in the solution of 5 vol.% hydrochloric acid in methanol at a constant potential of 1.5 V. The specimens were washed using methanol and then put into distilled water, where the carbon replicas could be collected on 3 mm diameter copper grids.

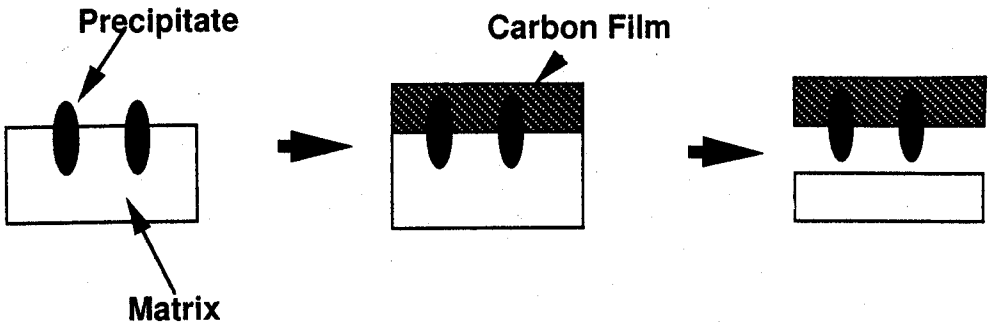

Figure 3.3: The method of making carbon extraction replicas.

Chemical etching with nital is satisfactory for the low alloyed steels as studied here. However, acids might dissolve some types of precipitates which were often found in high alloyed steels, in such case, electrolytic etching is preferable (Kurosawa, 1992).

3.5.2 Identification of precipitates using electron diffraction

Selected area electron diffraction using replica specimens is one of the most reliable methods to identify unknown precipitates. The intended precipitates are chosen using a selected area aperture and a corresponding diffraction pattern is obtained.

Some carbides in this work have very similar lattice parameters so that it is necessary to have an accurate camera length. Fig. 3.4 shows a schematic drawing of the geometry of diffraction.

R_{hkl} is the distance between the transmitted spot and the diffracted spot from hkl plane. θ_B is the Bragg angle corresponding to the hkl plane. L is the camera length. The relationship among them can be described as follows (Hirsch *et al.*, 1965).

$$R_{hkl}d_{hkl} = L\lambda \tag{3.1}$$

where d_{hkl} is the spacing of hkl planes and λ is wavelength, given by (Hirsch *et al.*, 1965):

$$\lambda = \frac{h}{2m_e eV_{ac}(1 + \frac{eV_{ac}}{2m_e C_l^2})} \tag{3.2}$$

where V_{ac} is the accelerating voltage, C_l is the speed of light in vacuum, h is the Planck constant, e is the charge on the electron and m_e is the electron mass.

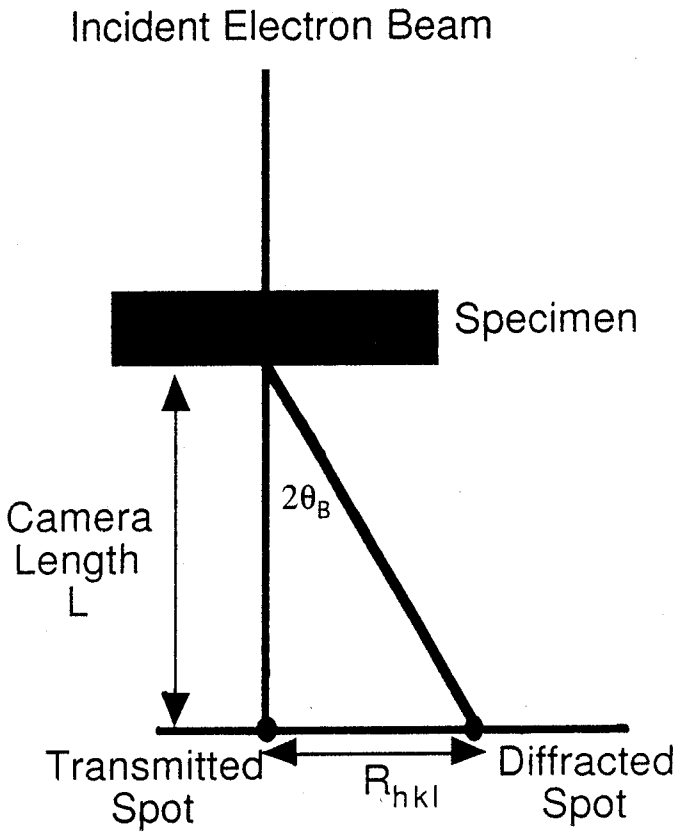

Figure 3.4: A schematic drawing of the geometry of diffraction in transmission electron microscopy. L, R_{hkl}, and θ_B are the camera length, distance between transmitted spot and diffracted spot in the diffraction pattern and the Bragg angle respectively.

The camera constant was calibrated using a gold film. Fig. 3.5 shows the diffraction pattern from a $< 001 >$ zone of gold when operating at 120 kV.

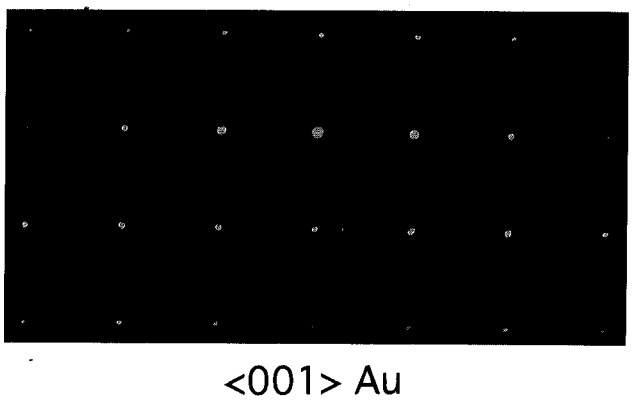

Figure 3.5: Diffraction pattern from a $< 001 >$ zone of gold when operating at 120 kV of accelerating voltage with 800 mm of camera length.

3.6 X–ray diffraction from electrolytical extraction residues

X–ray analysis of electrolytically extracted residues is a useful method to identify the types of precipitates. Precipitate particles were extracted electrochemically from samples whose surfaces has been cleaned by abrasion with a file. As shown in Fig. 3.6 (a), the specimens were dissolved at the anode at a constant electric potential relative to the platinum in the solution of 10 vol.% acetylaceton and 1 vol.% tetramethylammonium chloride (TMAC) in methanol. The constant electric potential was chosen to be between −100 mV and −200 mV against the standard of the saturated calomel electrode (SCE), where only the iron matrix dissolves as shown in Fig. 3.6 (b) (Kurosawa and Saeki, 1990). The residue was filtered using a sub–micron mesh (≤ 0.2 μm) to trap fine particles. To get as much amount of residue as possible in a short time, the filtration has been done by suction with vacuum pump. The particles were then studied using X–ray diffraction. X–ray analysis cannot only support the TEM observations which must be performed on small volume of sample, but also gives information about the quantity of each phase with a good accuracy.

3.7 Measurement of particle size

The microstructures were characterised mainly using carbon extraction replicas examined using TEM, particularly to identify the phase and to measure particle size. Cementite usually precipitates first in such power plant steels. The number densities of cementite were measured using the method of Ashby and Ebeling (1966). According to them, the relationship between the number density of the particles N_v and the number of the particles per unit area on the replica N_s is given by:

$$N_v = \frac{1}{\overline{x}}\{1 + (\frac{\delta}{\overline{x}})^2\}N_s \tag{3.3}$$

where $\overline{x}$ is a mean diameter of particles on replica, δ is the standard deviation of particle size. The sizes of cementite, which are necessary for the calculations of both the solute enrichment into cementite and the number density of the initial sites of cementite, were directly measured using TEM micrographs of the replicas and was determined by averaging at least 100 measurements in each case.

The lengths of M_2C (needle–shaped particles) were also directly measured with TEM micrograph of the replicas. The radii of M_7C_3 and $M_{23}C_6$ (sphere–like particle) were measured with

(a)

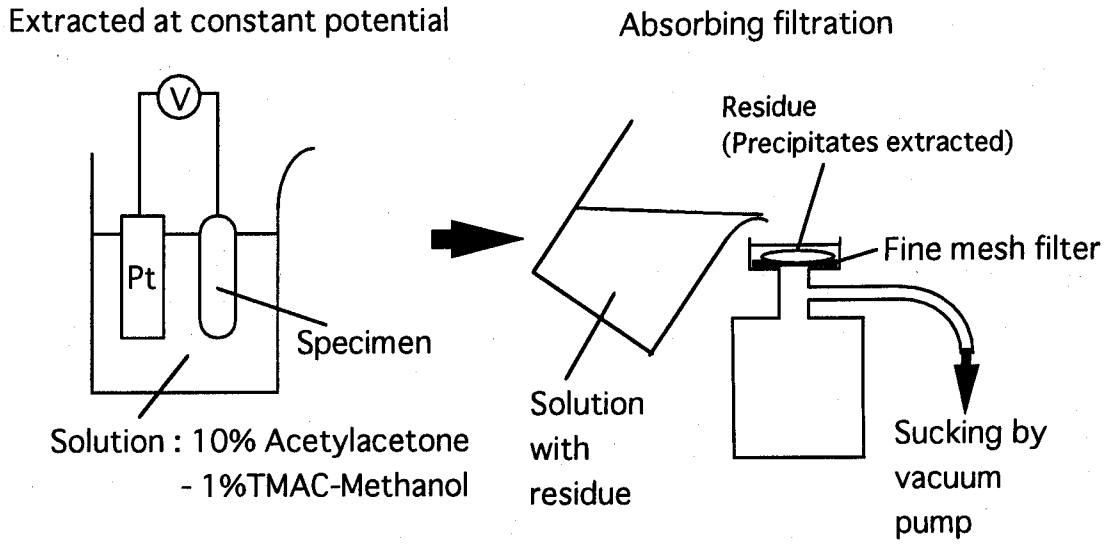

(b)

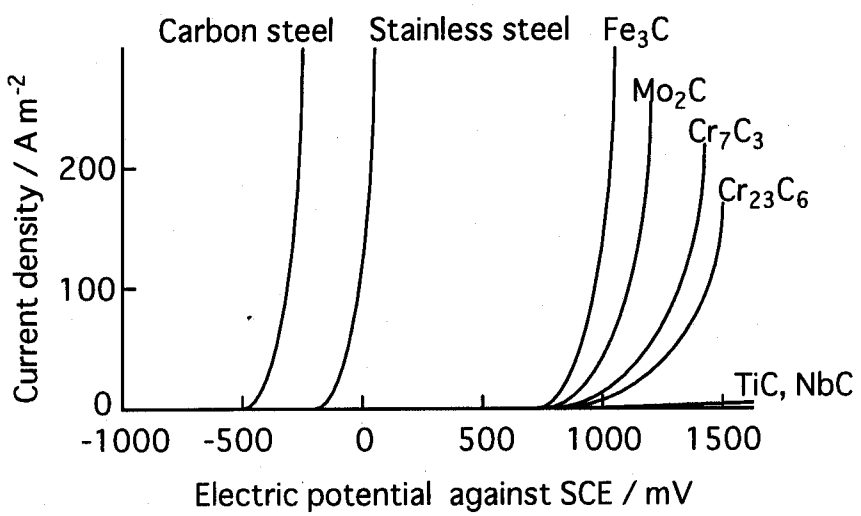

Figure 3.6: (a); A schematic drawing of the electrolytical extraction method. The specimens is made the anode at a voltage where only the iron matrix dissolves. Then, the solution containing extracted residue is filtrated through a fine mesh filter by suction with vacuum pump. (b); The relationship between the electric potential against SCE and current density of dissolution for matrix and each carbide (after Kurosawa and Saeki, 1990)

replica images and were determined assuming that the area of the particle is equal to that of the circle with the radius of r. The particle sizes were measured with at least 100 particles for needle–shaped carbide (M_2C) and 20 particles for sphere–like carbides (M_7C_3 and $M_{23}C_6$) in each case.

CHAPTER FOUR
Experimental verification

4.1 Introduction

As introduced in Chapter 2, a new theory has been proposed to deal with simultaneous transformation (Robson and Bhadeshia, 1997a, 1997b; Jones and Bhadeshia, 1997). It adapts the classical Avrami model (Kolmogorov, 1937; Johnson and Mehl, 1939; Avrami, 1939, 1940, 1941) to enable simultaneous precipitation reactions to be tackled. However, this new theory has only been tested against limited data and it contains a number of important approximations, some of which may not be generally valid.

In this chapter, firstly some of predictions made by Robson and Bhadeshia analysis are tested experimentally using 3Cr1.5Mo and $2\frac{1}{4}$Cr1Mo steels. Secondly, some of approximations in that analysis have been improved upon.

4.2 Previous experiments in literature

$2\frac{1}{4}$Cr1Mo steel

There has been a great deal of work on the precipitation sequences in $2\frac{1}{4}$Cr1Mo steel because of its popularity as an effective heat–resisting steel used in the construction of power plant (Kuo, 1953; Baker and Nutting, 1959; Beech and Warrigton, 1966; Leitnaker *et al.*, 1975; Klueh, 1978; Hippsley, 1981; Pilling and Ridley, 1982; Thomson and Bhadeshia, 1994a, 1994b). During tempering, alloy carbides eventually grow at the expense of iron carbides (Balluffi *et al.*, 1951). However, the processes prior to cementite precipitation are much faster than those afterwards. Nutting *et al.* (1959, 1999) investigated carbide sequences in $2\frac{1}{4}$Cr1Mo steel over a wide range of tempering temperatures and times as shown in Fig. 1.6.

3Cr1.5Mo steel

Data for the less popular 3Cr1.5Mo have not been investigated in similar detail but there is some information in the published literature (Smith and Nutting, 1957; Tunney *et al.*, 1978; Klueh and Nasreldin, 1987; Vitek and David, 1990). Table 4.1 shows the results of Klueh and Nasreldin (1987) which are not systematic enough to verify the calculated precipitation behaviour. Therefore, it is necessary to investigate the precipitation sequence experimentally

for 3Cr1.5Mo steel. Nevertheless, a rough precipitation sequence in 3Cr1.5Mo steel can be deduced from the published data as follows:

$$M_3C \rightarrow M_7C_3+M_2C \rightarrow M_7C_3+M_2C+M_{23}C_6 \rightarrow M_2C+M_{23}C_6+M_6C$$

Heat treatment	Detected precipitates
Normalised + 663 °C - 8 h tempered	$M_7C_3 + M_{23}C_6 + M_2C$
Normalised + 663 °C - 16 h tempered	$M_{23}C_6 + M_6C$
Normalised + 674 °C - 16 h tempered	$M_{23}C_6 + M_6C$
Normalised + 688 °C - 8 h tempered	$M_{23}C_6$
Normalised + 693 °C - 16 h tempered	$M_{23}C_6 + M_6C + U$
Normalised + 674 °C - 16 h tempered	$M_{23}C_6 + M_6C + U$
Quenched + 663 °C - 8 h tempered	M_7C_3
Quenched + 691 °C - 16 h tempered	$M_{23}C_6 + M_6C$
Quenched + 704 °C - 30 h tempered	$M_{23}C_6 + M_6C + U$

Table 4.1: The experimental results of 3Cr1.5Mo steel (Klueh and Nasreldin, 1987). Note that the treatment of "normalised" is air cooled from 955 °C and 565 °C for 2 h and that the treatment of "quenched" is water quenched from 955 °C and 565 °C for 2 h. "U" represents the presence of unidentified phases.

4.3 Experimental results

To get useful data for verification of the model and for particle sizes, which are necessary to create the new model described in Chapter 7, new experimental data about the sequence of carbide precipitation reactions in $2\frac{1}{4}$Cr1Mo and 3Cr1.5Mo power plant steels have been obtained using specimens tempered at 600 °C.

4.3.1 Optical microstructure and hardness

Fig. 4.1 shows the optical microstructures of (a) $2\frac{1}{4}$Cr1Mo and (b) 3Cr1.5Mo normalised at 1250 °C for 3 days before quenching into water. Both microstructures were found to be fully martensitic after quenching into water.

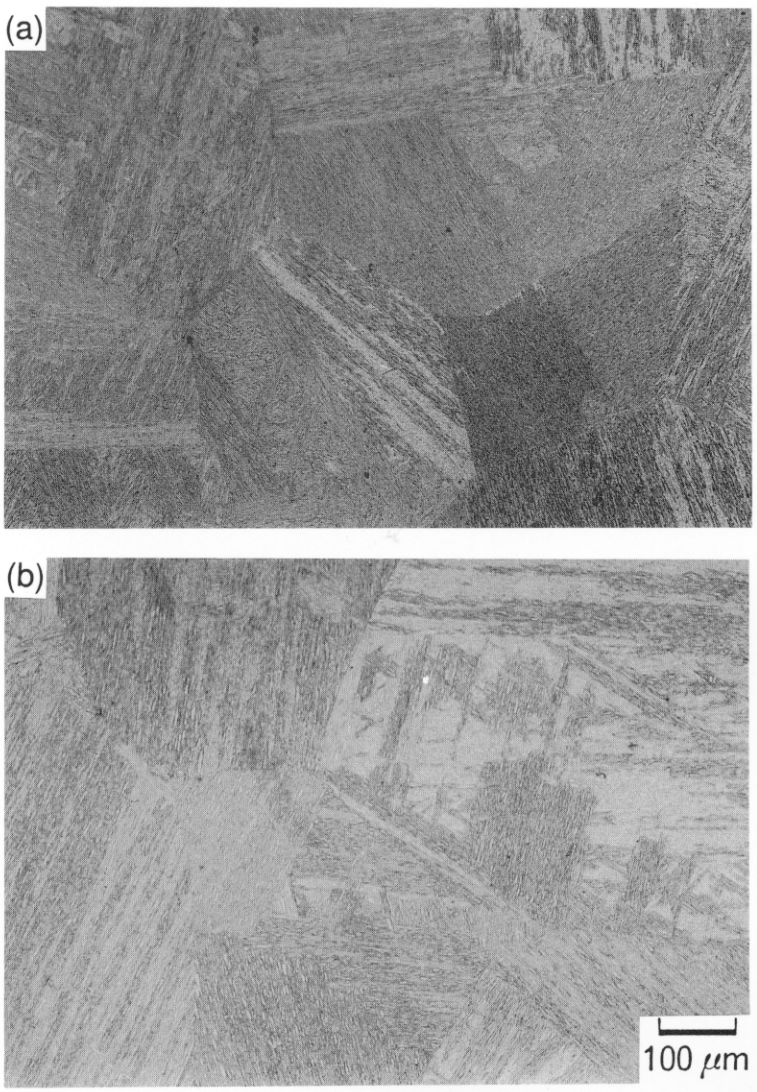

Figure 4.1: Martensite microstructures in (a) $2\frac{1}{4}$Cr1Mo and (b) 3Cr1.5Mo steels after quenching from 1250 °C into water.

Fig. 4.2 shows the change in Vickers hardness with tempering time at 600 °C. The hardness of both steels decreases similarly with increasing tempering time. Note that when compared against plain carbon steels, both alloys have a significant resistance to tempering because of the precipitation of alloy carbides, *i.e.* "a secondary hardening" phenomenon.

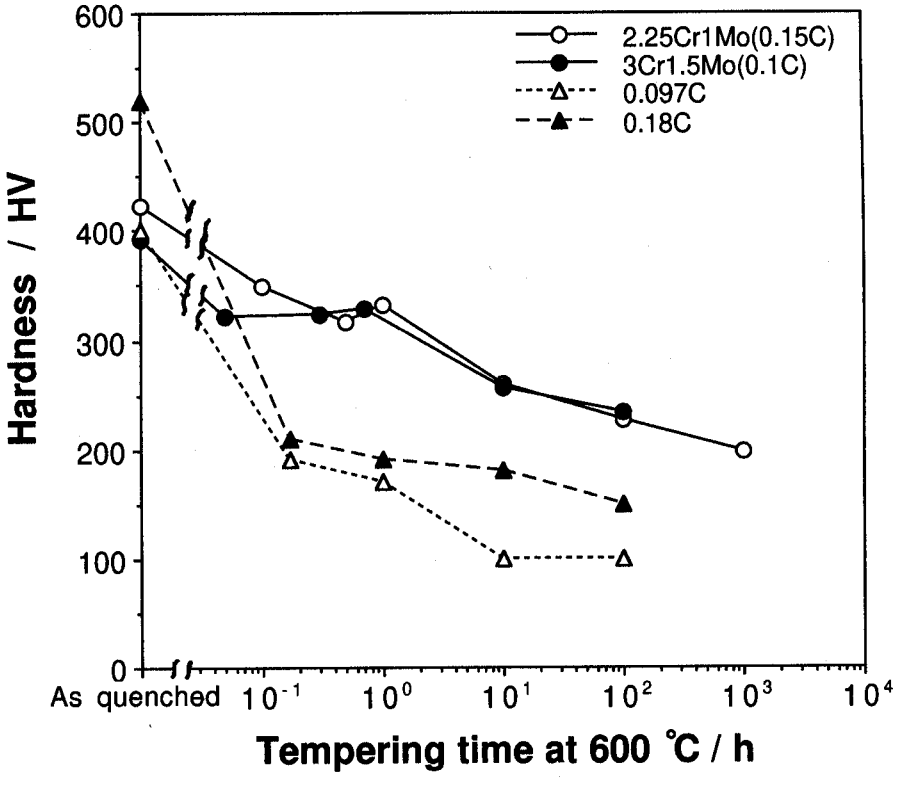

Figure 4.2: The change in Vickers hardness with tempering time at 600 °C for $2\frac{1}{4}$Cr1Mo and 3Cr1.5Mo steels together with data for plain carbon steels whose carbon contents are 0.097 wt% and 0.18 wt% (Speich, 1969).

4.3.2 X–ray analysis

Table 4.2 shows a summary of the X–ray analysis results of electrolytically extracted residues from $2\frac{1}{4}$Cr1Mo and 3Cr1.5Mo steels tempered at 600 °C.

Steels	Tempering condition	Precipitates detected			
		M_3C	M_2C	M_7C_3	$M_{23}C_6$
$2\frac{1}{4}$Cr1Mo	1250°C - 3 days normalised	W			
	600 °C - 0.1 h tempered	VS			
	600 °C - 0.5 h tempered	VS			
	600 °C - 1.0 h tempered	VS			
	600 °C - 10 h tempered	VS	VW		
	600 °C - 200 h tempered	VS	W	VW	
	600 °C - 1000 h tempered	VS	W	S	VW
3Cr1.5Mo	1250°C - 3 days normalised	W			
	600 °C - 0.05 h tempered	W			
	600 °C - 0.3 h tempered	VS		W	
	600 °C - 0.7 h tempered	VS	VW	S	
	600 °C - 10 h tempered	S	W	S	W
	600 °C - 100 h tempered	W	S	S	S

Table 4.2: X–ray analysis results for residues extracted from $2\frac{1}{4}$Cr1Mo and 3Cr1.5Mo steels tempered at 600 °C. The abbreviations, VS, S, W and VW mean very strong, strong, weak and very weak X–ray intensities, respectively

According to the X–ray data, there are differences in the carbide precipitation sequences for the $2\frac{1}{4}$Cr1Mo and 3Cr1.5Mo steels. In the $2\frac{1}{4}$Cr1Mo steel, M_2C can be detected earlier than M_7C_3, while in 3Cr1.5Mo steel M_2C follows the formation of M_7C_3. The X–ray intensity from M_2C in $2\frac{1}{4}$Cr1Mo steel remained rather weak even after 1000 h, while that in 3Cr1.5Mo steel was relatively strong after just 100 h of tempering heat treatment. As Robson (1997a) implied, the approach to equilibrium was faster in 3Cr1.5Mo steel than in $2\frac{1}{4}$Cr1Mo steel.

4.3.3 TEM observations

Table 4.3 shows a summary of results obtained using transmission electron microscopy (TEM) for the $2\frac{1}{4}$Cr1Mo and 3Cr1.5Mo steels.

Only M_3C could be detected in the $2\frac{1}{4}$Cr1Mo steel tempered at 10 h (Fig. 4.3) and most particles appeared to be in the form of irregular plates or needles. After 200 h of tempering, several arrays of needle–shaped precipitates within martensitic laths, a typical morphology of M_2C, were found (Fig. 4.4). When the tempering time increased to 1000 h, particles whose diffraction pattern contained streaks characteristic of M_7C_3 were clearly observed (Fig. 4.5).

For the 3Cr1.5Mo steel, Figs. 4.6 to 4.9 show transmission electron microstructures for the 0.05, 0.7, 10, 100 h tempered specimens respectively. At 0.05 h, most of the precipitates were M_3C particles as shown in Fig. 4.6. Between 0.05 h and 0.7 h, M_7C_3 started to precipitate with a shape which may be assumed to be approximately spherical. This persisted in the microstructure as shown in Fig. 4.7. Even when the tempering time was increased to 10 h or 100 h, a small amount of M_3C persisted in the microstructure as shown in Fig. 4.8. The M_3C particles were clearly getting smaller in size implying that they had started dissolving. Moreover, very small M_2C and $M_{23}C_6$ particles could also be observed. At 100 h, the fraction of M_2C and $M_{23}C_6$ increased as shown in Fig. 4.9. The change in M_2C fraction was particularly pronounced.

Steels	Tempering conditions	TEM observations
$2\frac{1}{4}$Cr1Mo	600 °C - 1 h tempered	Most precipitates were needle or plate–like M_3C
	600 °C - 10 h tempered	Most precipitates were needle or plate–like M_3C
	600 °C - 200 h tempered	M_3C + needle array of M_2C
	600 °C - 1000 h tempered	M_3C + M_2C + blocky M_7C_3
3Cr1.5Mo	600 °C - 0.05 h tempered	Needle or plate–like M_3C
	600 °C - 0.7 h tempered	M_3C + blocky M_7C_3
	600 °C - 10 h tempered	M_3C + M_7C_3 + needle M_2C + small particle $M_{23}C_6$
	600 °C - 100 h tempered	Smaller M_3C + M_7C_3 + M_2C + $M_{23}C_6$

Table 4.3: The results of TEM observations on $2\frac{1}{4}$Cr1Mo and 3Cr1.5Mo steels tempered at 600 °C for a variety of time periods

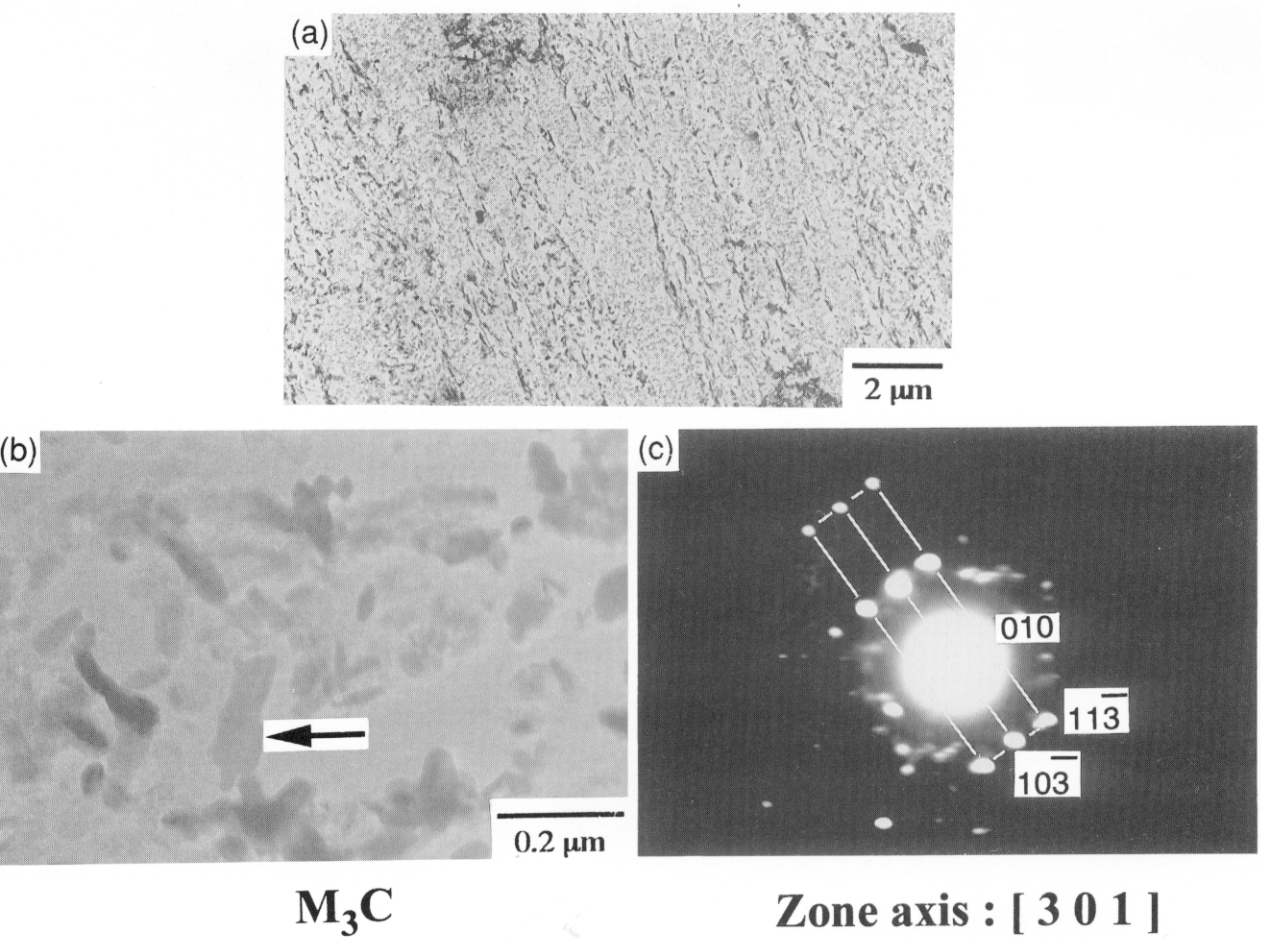

Figure 4.3: Transmission electron micrographs of $2\frac{1}{4}$Cr1Mo steel tempered at 600 °C for 10 h, (a) low magnification image, (b) high magnification image of M_3C and (c) electron diffraction pattern from M_3C. The arrow in (b) indicates the particle from which the electron diffraction pattern was obtained.

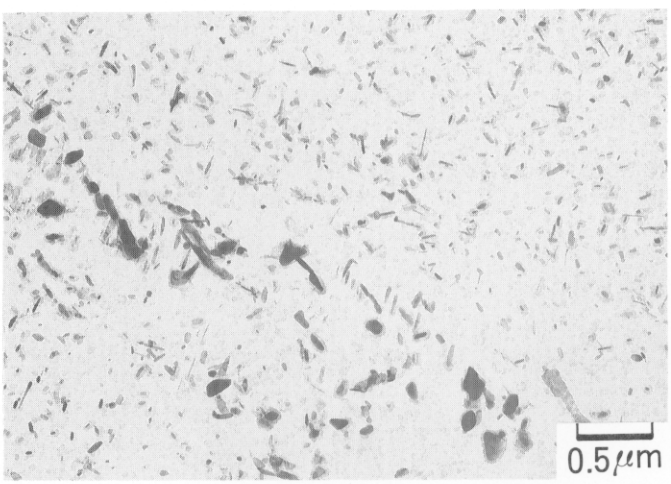

Figure 4.4: Transmission electron micrograph of $2\frac{1}{4}$Cr1Mo steel tempered at 600 °C for 200 h, showing numerous needles of M_2C.

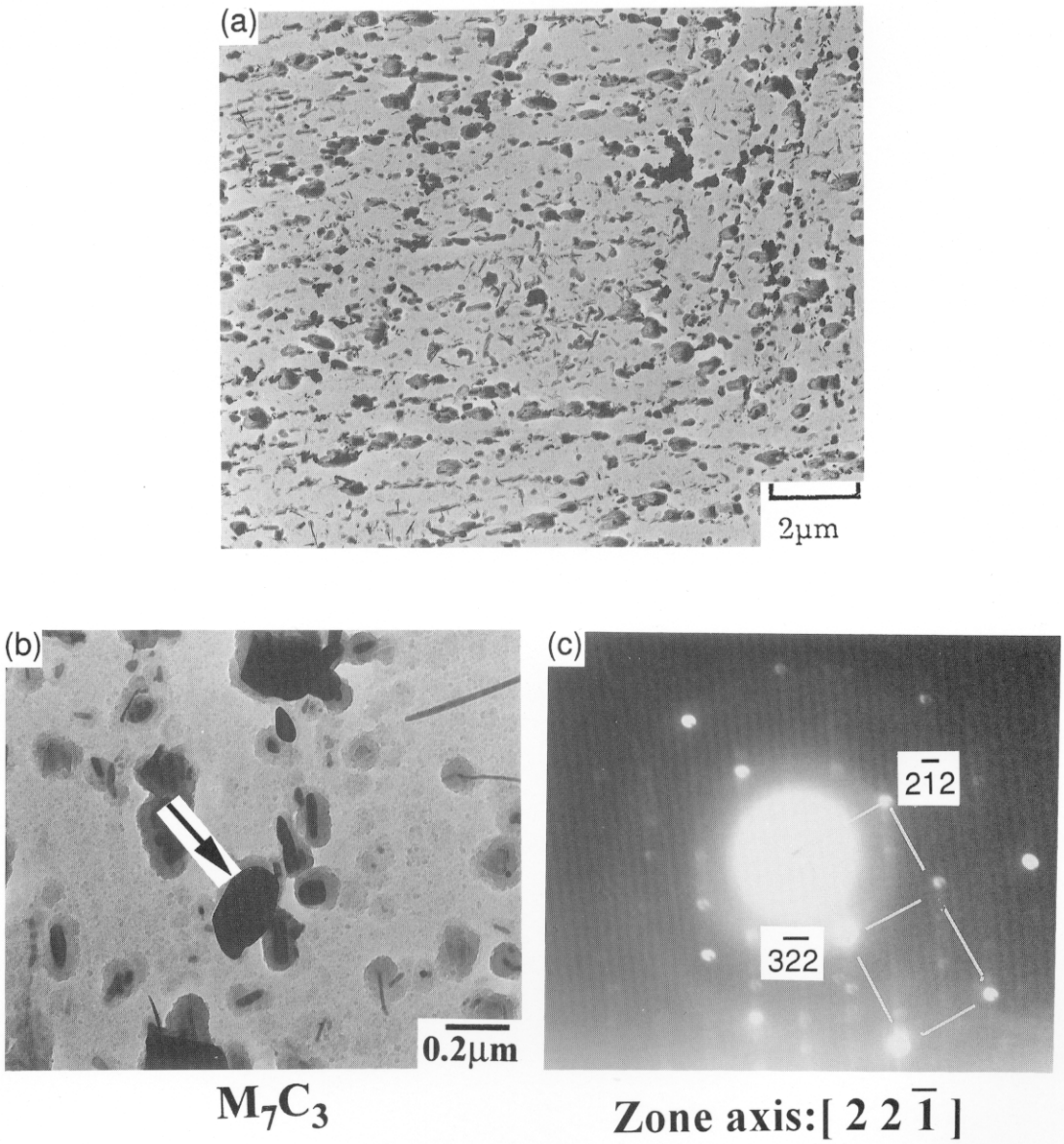

Figure 4.5: Transmission electron micrographs of $2\frac{1}{4}$Cr1Mo steel tempered at 600 °C for 1000 h, (a) low magnification image, (b) high magnification image of a particle of M_7C_3 and (c) electron diffraction pattern with streaks from M_7C_3. The arrow in (b) indicates the particle from which the electron diffraction pattern was obtained. In the diffraction pattern, there are streaks characteristic of M_7C_3 (Beech and Warrington, 1966).

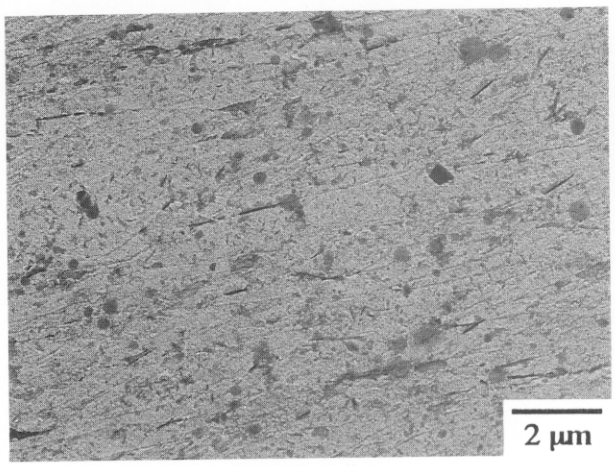

Figure 4.6: Transmission electron micrograph of 3Cr1.5Mo steel tempered at 600 °C for 0.05 h.

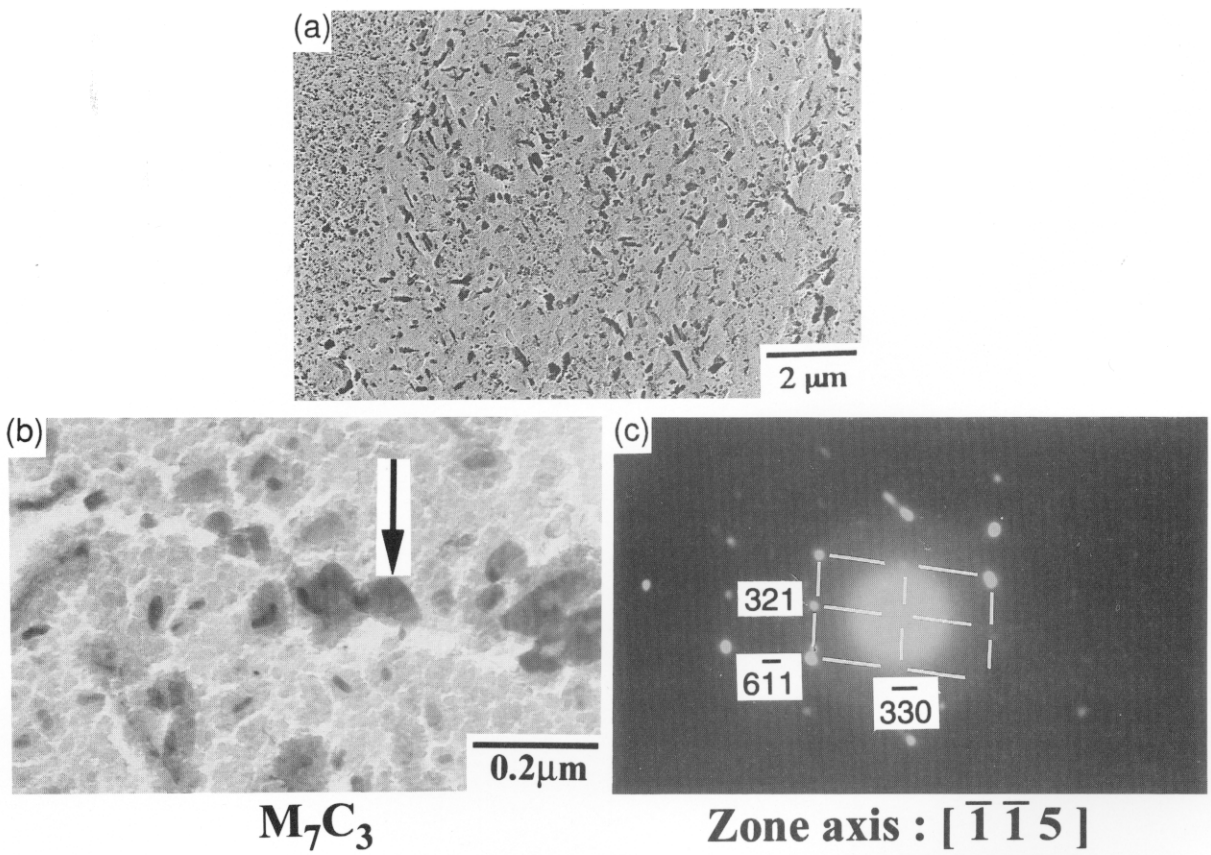

Figure 4.7: Transmission electron micrographs for 3Cr1.5Mo steel tempered at 600 °C for 0.7 h, (a) low magnification image, (b) high magnification image of M_7C_3 and (c) electron diffraction pattern from M_7C_3. The arrow in (b) indicates the particle from which the electron diffraction pattern was obtained. In the diffraction pattern, there are streaks characteristic of M_7C_3 (Beech and Warrington, 1966).

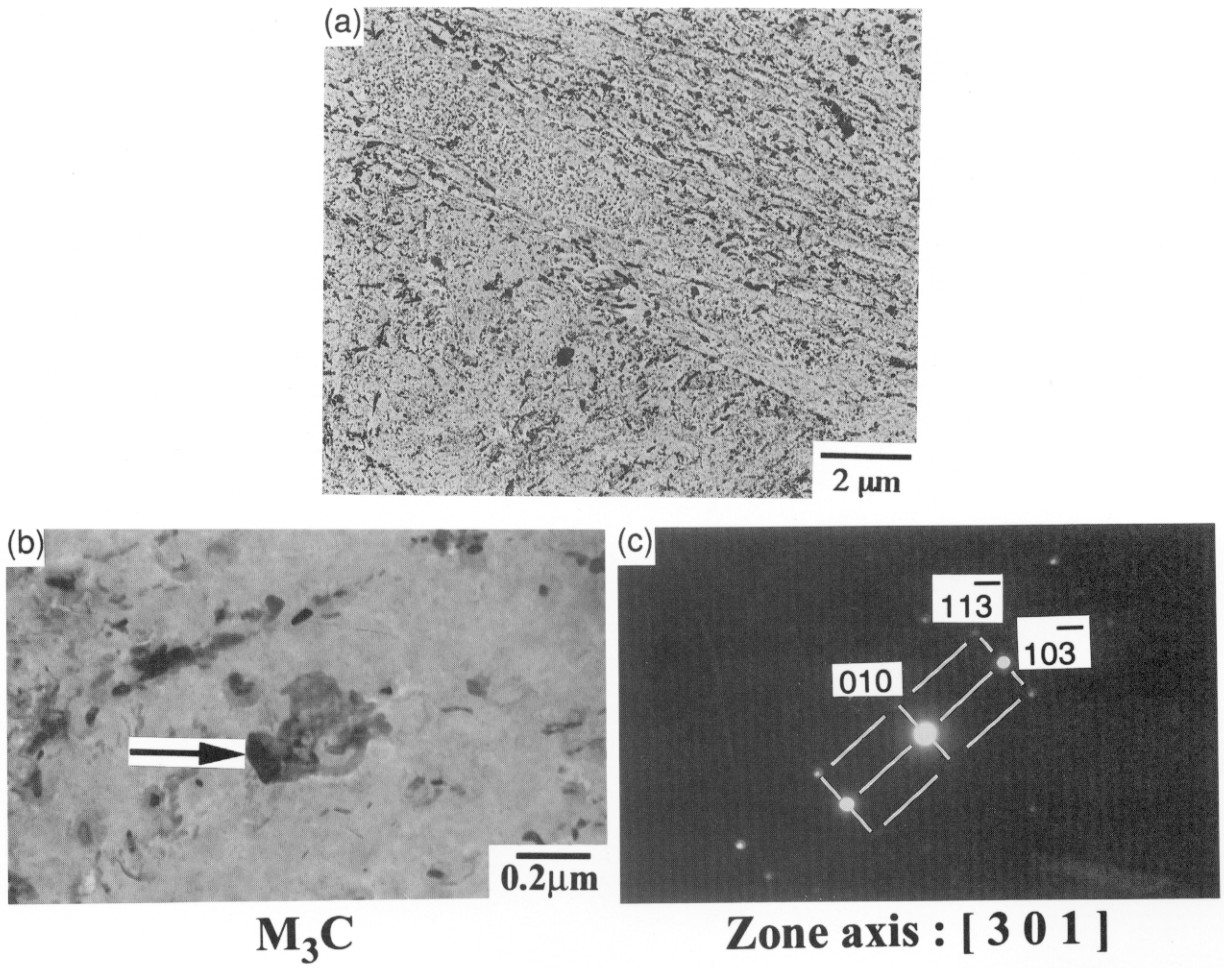

Figure 4.8: Transmission electron micrographs of 3Cr1.5Mo steel tempered at 600 °C for 10 h, (a) low magnification image, (b) high magnification image of M_3C and (c) electron diffraction pattern from M_3C. The arrow in (b) indicates the particle from which the electron diffraction pattern was obtained.

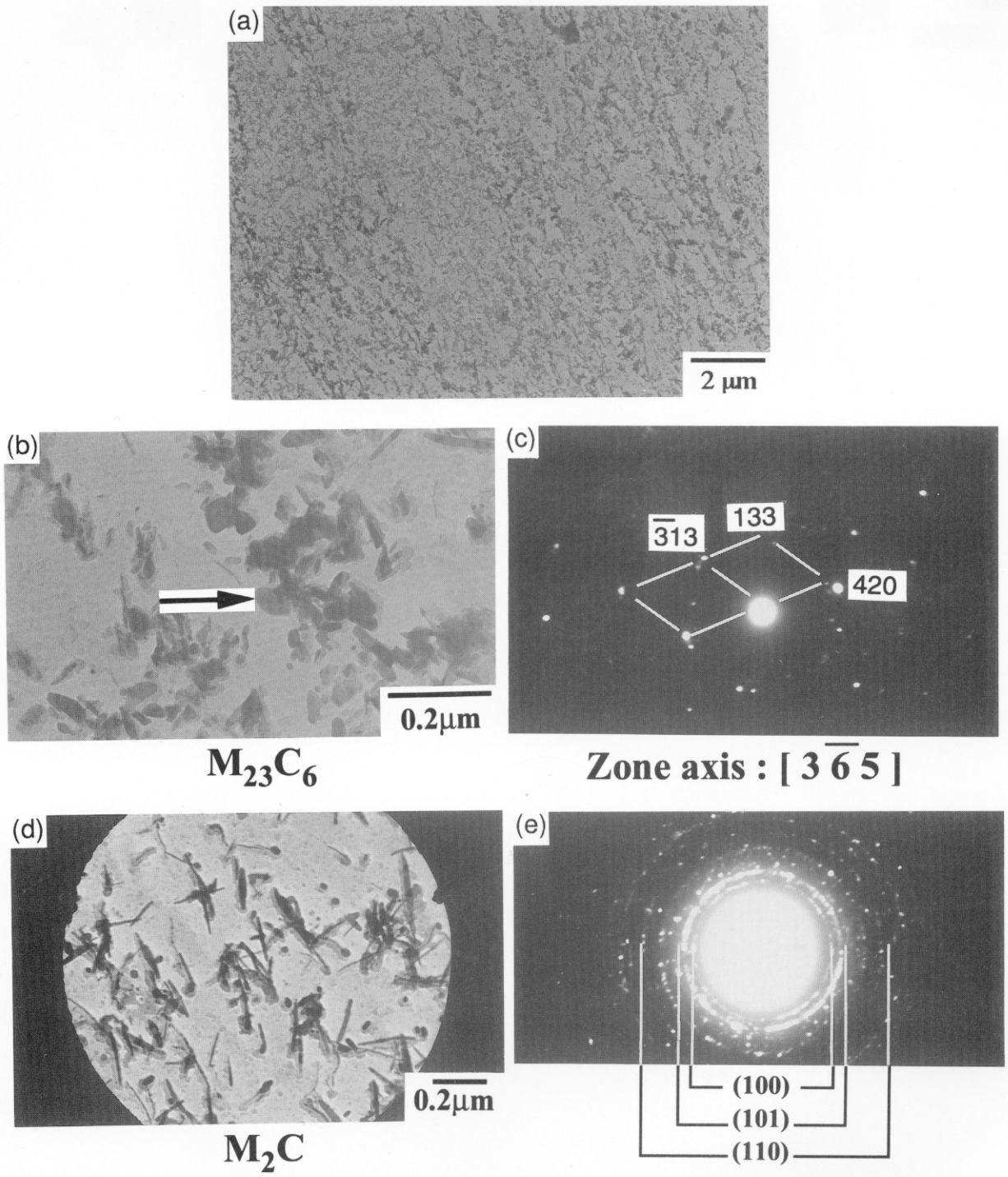

Figure 4.9: Transmission electron micrographs of 3Cr1.5Mo steel tempered at 600 °C for 100 h, (a) low magnification image, (b) high magnification image of $M_{23}C_6$ and (c) electron diffraction pattern from $M_{23}C_6$, (c) high magnification image of M_2C and (d) electron diffraction ring pattern from an array of M_2C particles. The arrow in (b) indicates the particle from which the electron diffraction pattern was obtained.

According to both the TEM observations and X–ray analysis of extracted residues, the precipitation sequences at 600 °C for both steels are as follows:

$2\frac{1}{4}$Cr1Mo; $M_3C \rightarrow M_3C+M_2C \rightarrow M_3C+M_2C+M_7C_3 \rightarrow M_3C+M_2C+M_7C_3+M_{23}C_6$

3Cr1.5Mo; $M_3C \rightarrow M_3C+M_7C_3 \rightarrow M_3C+M_7C_3+M_2C+M_{23}C_6 \rightarrow M_7C_3+M_2C+M_{23}C_6$

4.4 Verification

4.4.1 Comparison between theory and experiments

Fig. 4.10 shows calculations by Robson (1996) which are compared against published experimental data for (a) $2\frac{1}{4}$Cr1Mo steel by Baker and Nutting (1959) and (b) 3Cr1.5Mo steel by Klueh and Nasreldin (1987) and the present work respectively. The predictions are roughly consistent with the experimental results. However, as shown in Fig. 4.11, the approach to equilibrium in both 3Cr1.5Mo and $2\frac{1}{4}$Cr1Mo steels is much slower than predicted. This discrepancy is thought to be caused by some of the approximations and inconsistencies in the model, which are now discussed in detail. Table 4.4 and 4.5 shows adjustable parameters and the main assumptions for the calculations, respectively.

M_3C	Needle–shaped precipitate	Spherical precipitate
Number of nucleation sites: N_0	Number of nucleation sites: N_0	Number of nucleation sites: N_0
Thickness: d	Interfacial energy: σ	Interfacial energy: σ
	Diffusion–controlled species	Diffusion–controlled species
	Aspect ratio: ϕ	

Table 4.4: The adjustable variables in the Robson and Bhadeshia model.

Microstructural parameters	Diffusion–controlled growth
Constant number of pre–existing M_3C particles	Parabolic growth for spherical precipitates
(Constant initial number density of particles)	Lengthening with constant aspect ratio
Constant thickness of M_3C	for needle–shaped M_2C
Constant aspect ratio of needle–shaped M_2C	Controlled only by chromium in a binary system
Using mean particle size for each phase	No capillarity

Table 4.5: The main assumptions in the Robson and Bhadeshia model.

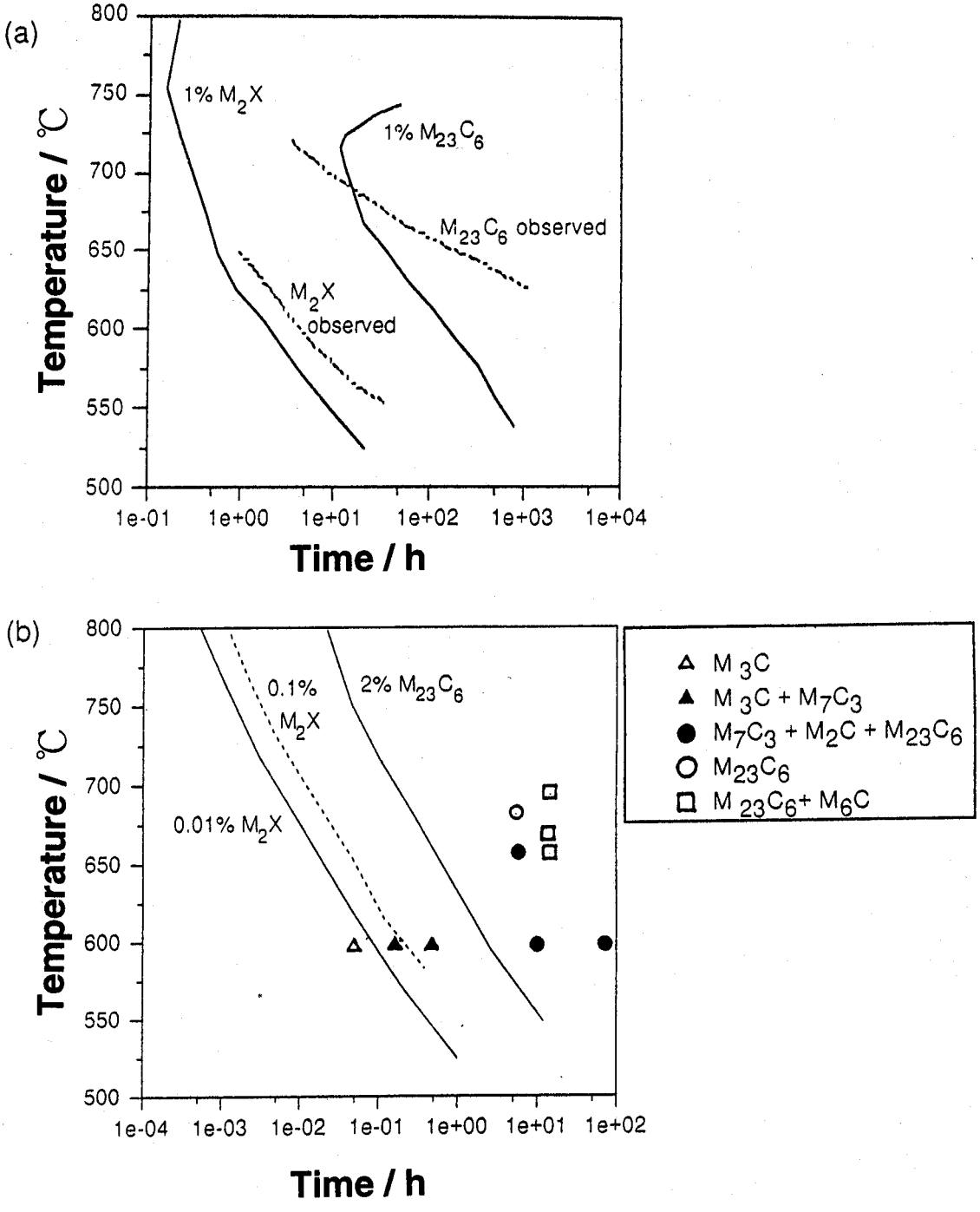

Figure 4.10: The precipitation prediction by the Robson and Bhadeshia model along with experimental data for (a) $2\frac{1}{4}$Cr1Mo steel by Baker and Nutting (1959) and for (b) 3Cr1.5Mo steel in which the data from 650 °C to 700 °C were obtained by Klueh and Nasreldin (1987) and the data at 600 °C were from the present work.

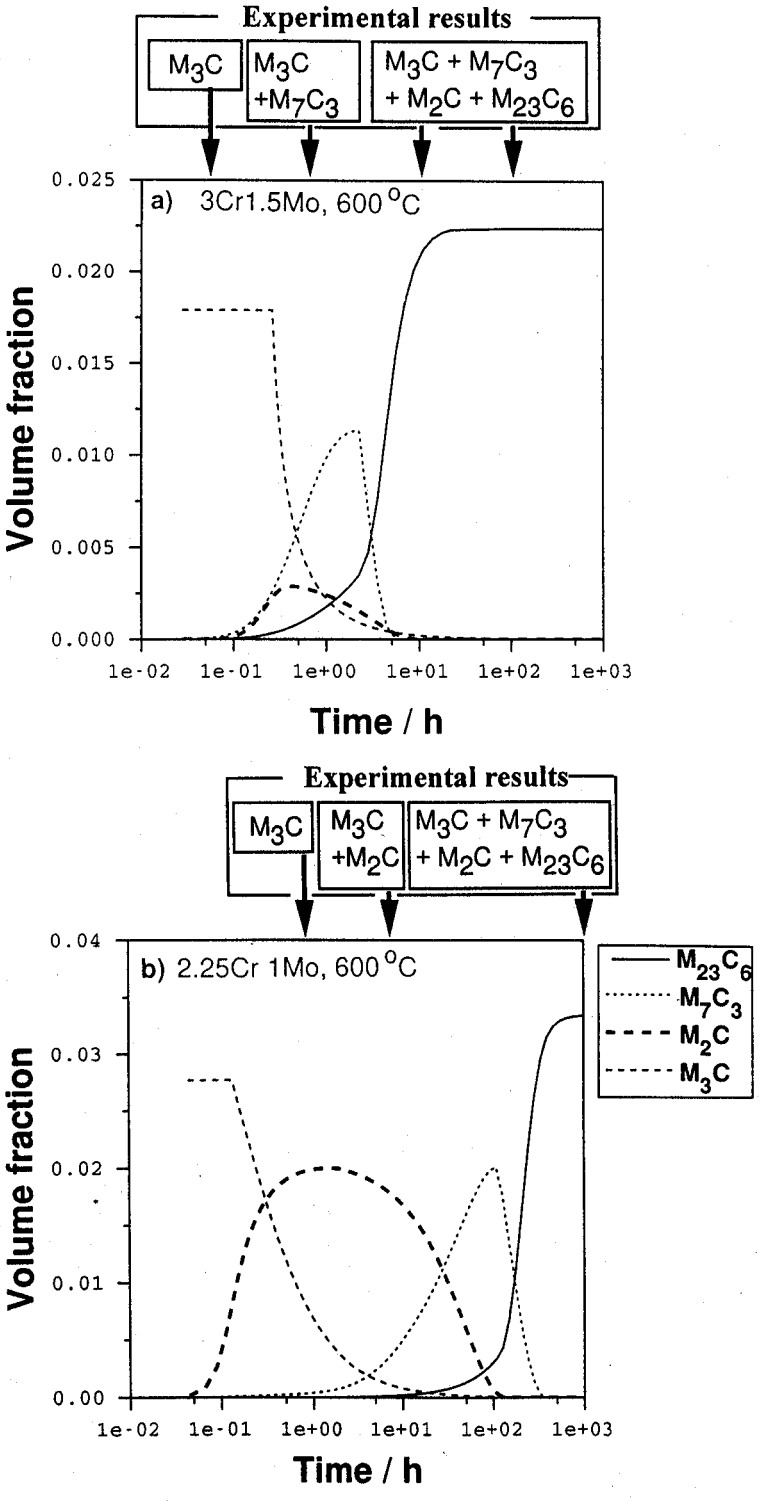

Figure 4.11: The prediction of the precipitation sequences by the Robson and Bhadeshia model along with experimental data for (a) 3Cr1.5Mo and (b) $2\frac{1}{4}$Cr1Mo steels tempered at 600 °C.

4.4.2 Difficulty 1: Cementite precipitation

M_3C particles have been assumed to be uniform in size for the calculations presented in Fig. 4.11, with the particle thickness set to 1 μm, a value which is inconsistent with the measured thickness. As shown in Fig. 4.12, the thickness of M_3C measured in the present work does not seem to change in the early stages of tempering and is almost the same for both steels. The thickness of particles on lath boundaries was about twice that of those within the laths.

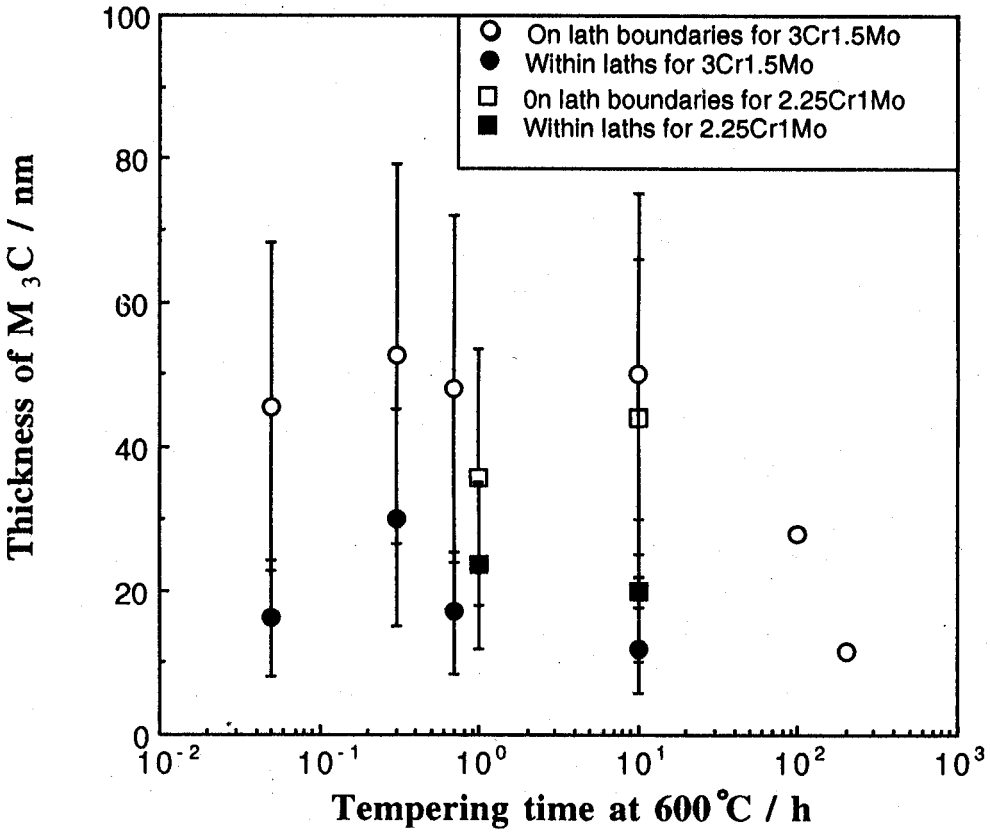

Figure 4.12: The thickness of M_3C on lath boundaries and within laths as a function of tempering time at 600 °C for $2\frac{1}{4}$Cr1Mo and 3Cr1.5Mo steels.

Considering that the total volume fraction must be a function of the carbon concentration and that the thickness is approximately constant for both steels before the dissolution of M_3C (θ), the initial number density of M_3C particles $N_{0\theta}$ must be a function of the carbon concentration.

If the effect of other alloying elements is neglected because both steels have approximately same size of M_3C, then it is expected that $N_{0\theta}$ increases with carbon concentration. Measuring $N_{0\theta}$ for both steels ($2\frac{1}{4}$Cr1Mo and 3Cr1.5Mo) in which carbon concentrations are 0.1 wt% and 0.15 wt% respectively, $N_{0\theta}$ (m^{-3}) was expressed empirically as a function of the carbon concentration w_c (wt%) as follows:

$$N_{0\theta} = 2.23 \times 10^{22} w_c - 1.0 \times 10^{21} \tag{4.1}$$

It is assumed that this empirical relationship may be applicable for steels with carbon concentration from 0.1 wt% to 0.15 wt%

4.4.3 Difficulty 2: The aspect ratio of M_2C

The aspect ratio (length/width) of M_2C needles was assumed to be constant at 15. The measurements indicated values between 10 and 20, so that the value of 15 may be taken to be reasonable.

4.4.4 Difficulty 3: Avrami theory

One difficulty in the application of Avrami theory is that the conversion of extended space into real space, necessary to account for impingement, prevents the calculations of anything but the volume fraction. Given that the total fraction of precipitates is small, this difficulty can be avoided by neglecting impingement altogether. It should then be possible to estimate size distributions.

4.4.5 Difficulty 4 : Diffusion-controlled growth in a multicomponent system

The original model treats the growth of all precipitates other than M_3C in terms of the diffusion of chromium alone, with the interface composition given by a tie–line passing through the mean alloy composition ($\overline{c}$). The analysis of diffusion–controlled growth therefore involves just one condition for mass conservation at the interface which is moving with a velocity v:

$$v(c_{Cr}^{\beta\alpha} - c_{Cr}^{\alpha\beta}) = D_{Cr}(\partial c_{Cr}/\partial z)_{z=z^*} \tag{4.2}$$

where $c_{Cr}^{\beta\alpha}$ and $c_{Cr}^{\alpha\beta}$ are the equilibrium concentrations of chromium in β (precipitate) and α (ferrite) phases respectively, D_{Cr} is the diffusion coefficient of chromium in the α phase and $(\partial c_{Cr}/\partial z)_{z=z^*}$ is the chromium concentration gradient in the α phase at the α / β interface.

As emphasised in the classic work of Kirkaldy (1958) and Coates (1973), this binary treatment is inadequate for ternary or higher order steels. This is because the diffusion coefficient of the interstitial solute can be many orders of magnitude greater than that of the substitutional solute. A second mass conservation equation for carbon must be simultaneously satisfied:

$$v(c_C^{\beta\alpha} - c_C^{\alpha\beta}) = D_C(\partial c_C/\partial z)_{z=z^*} \tag{4.3}$$

In such a case, the tie–line does not always pass though the alloy composition but has to be chosen properly for the simultaneous satisfaction of the mass conservation equations at any time.

Fig. 4.13 indicates the way in which the tie–lines shift in the steels starting with a microstructure containing paraequilibrium cementite in ferrite.

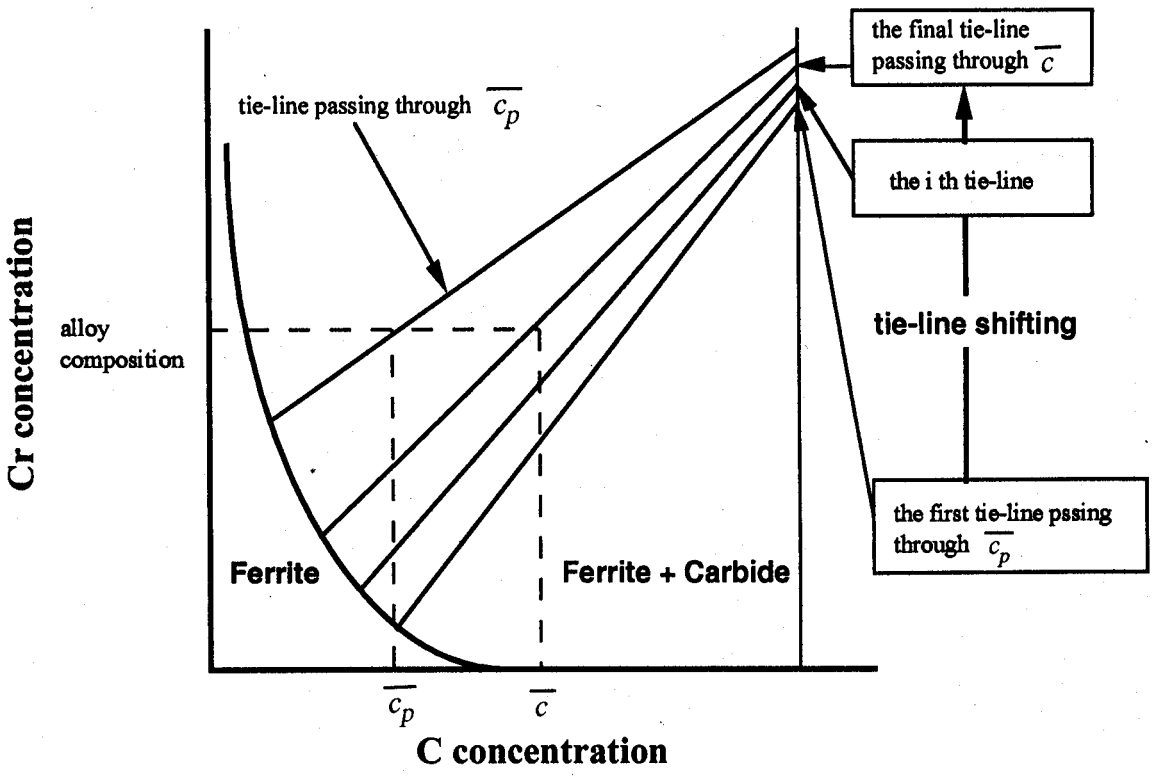

Figure 4.13: Schematic drawing for tie–line shifting in Fe–M–C system with the first precipitate as cementite by paraequilibrium. $\overline{c}_p$ is carbon concentration in the matrix which is in contact with paraequilibrium cementite.

To maintain local equilibrium at the moving interface, a tie–line must be chosen which reduces the driving force for carbon diffusion so that the slower moving chromium can keep pace with the carbon. Such a tie–line will not in general pass through the alloy composition. Indeed, the tie–line defining the interface compositions will not be constant but will shift towards $\overline{c}$ as precipitation progresses (Fig. 4.13) (Coates, 1973). Notice in Fig. 4.13 that the effective value $\overline{c}_p$ of $\overline{c}$ at the point where alloy carbide precipitation begins is the composition of the ferrite after the precipitation of cementite by a paraequilibrium mechanism.

4.5 New calculations for 3Cr1.5Mo steel

The measured microstructural parameters used in the new calculations are shown in Table 4.6. Table 4.7 shows the comparison of assumptions between Robson and Bhadeshia model and new calculations. The results for 3Cr1.5Mo steel are shown in Fig. 4.14 along with the experimental observations.

Microstructural parameters	The values in use
Number density of sites for M_3C	1.23×10^{21} m^{-3}
Thickness of M_3C on boundaries	50 nm
Thickness of M_3C within grains	20 nm
Aspect ratio of M_2C needles	15

Table 4.6: The measured values used in the new calculations for 3Cr1.5Mo steel.

Robson and Bhadeshia model	New calculations
Based on Avrami theory	Nucleation and growth but no treatment of impingement
Using mean particle size	Particle size distribution due to different nucleation times and growth rate
Diffusion–controlled growth in a binary system	Diffusion–controlled growth in Fe-Cr-C system

Table 4.7: The comparison of assumptions between the Robson and Bhadeshia model and new calculations.

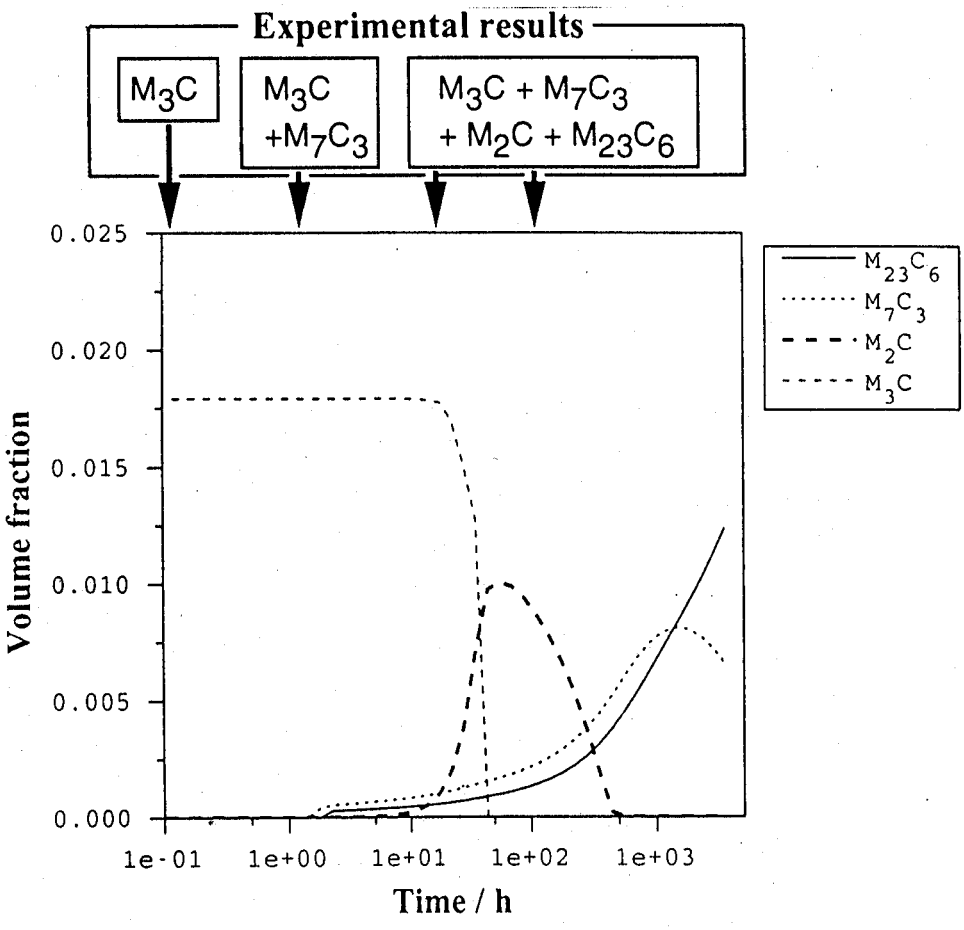

Figure 4.14: The new calculations for 3Cr1.5Mo steel tempered at 600 °C along with experimental observations.

As shown in Fig. 4.14, the new calculations are in better agreement with experimental data. However, the predictions of carbide precipitation are still faster than measured experimentally. Further work is needed to understand this remaining discrepancy.

4.6 Summary

New experimental data have been generated on $2\frac{1}{4}$Cr1Mo and 3Cr1.5Mo steels which were tempered from a martensitic state. These results indicated a need to modify a theory for the prediction of the kinetics of precipitation reactions by Robson and Bhadeshia. In particular, a multicomponent treatment of the diffusion–controlled growth of alloy carbides has been introduced a proper conservation of mass in the new calculations. The calculations for 3Cr1.5Mo have been carried out without the Avrami conversion of extended space into real space, a satisfactory approximation given the minute fraction of precipitates involved. The new prediction is in better agreement with experiments. However, the prediction for carbide precipitation in 3Cr1.5Mo steel is still faster than measured experimentally. This needs further investigation.

CHAPTER FIVE

Modelling precipitation of needle–shaped precipitates

5.1 Introduction

Creep–resistant steels rely on fine carbides including MX, M_2C, M_7C_3, M_6C and $M_{23}C_6$, where the "M" stands for a mixture of iron and substitutional solute atoms and "X" for interstitial solute atoms.

The heat treatment prior to service is carried out at a temperature which is in excess of about 500 °C in order to permit the substitutional atoms to diffuse in a reasonable time period, over the dimensions necessary for precipitate growth. Cementite and other transition iron–carbides can precipitate by a mechanism which requires only the carbon atoms to diffuse; such carbides can therefore precipitate at temperatures as low as 200 °C (Honeycombe and Bhadeshia, 1995). As a consequence, it is inevitable that iron carbide precipitation must precede that of the alloy carbides. It follows that the steel at first softens as the precipitation of iron carbides removes carbon from solid solution, but begins to harden again as a second reaction occurs in which alloy carbides start to precipitate at the expense of the less stable iron carbides. It is for this reason that such alloys are called "secondary hardening steels".

Secondary hardening steels are of great importance in the manufacture of power plant and in the petrochemical industry where creep must be avoided. As described in Chapter 2, attempts have recently been made to quantify the complicated sequence of precipitation reactions as a function of the alloy composition and heat treatment. Since the precipitation reactions involve a large set of reactions often occurring together, Robson and Bhadeshia (1997a) adapted the classical Avrami theory to deal with simultaneous transformations. Such work is of use in the design of new alloys. However, there are a number of fundamental problems which are outside of that framework of simultaneous transformations, associated with the growth of individual phases, which in the present work have been found to prevent accurate solutions:

Consumption of nucleation sites

In most of previous work, the nucleation rate has been calculated with the equation 2.3, $I = N_0(kT/h)\exp\{-(G^* + Q)/kT\}$. As suggested by Turnbull and Fisher (1948), when there is solute diffusion during nucleation, the equation is multiplied by the mole fraction of solute with Q being the activation energy for the diffusion of solute. When this equation is incorporated

into the Avrami overall transformation kinetics theory, an additional term $(1-V'/V^{eq})$ appears to allow for the fraction of the matrix which is eliminated from the transformation process as the reaction proceeds. The term accounts for the consumption of nucleation sites:

$$I' = \overline{c}\left(1 - \frac{V'}{V^{eq}}\right) N_0 \frac{kT}{h} \exp\left(-\frac{G^* + Q}{kT}\right) \tag{5.1}$$

where V' and V^{eq} are volume fraction at any instance and equilibrium volume fraction for a precipitate respectively.

Multicomponent diffusion

As described in Chapter 2, local equilibrium at the interface is a reasonable approximation for isothermal diffusion–controlled growth. It follows that for a binary alloy these compositions are given by a tie–line of the equilibrium phase diagram.

Solute is removed from the matrix as the precipitate grows but since the temperature is fixed during isothermal transformation, the interface compositions must remain fixed at $c^{\alpha\beta}$ and $c^{\beta\alpha}$ if local equilibrium is to be maintained. It follows that the rate at which solute is removed from the matrix (α) as the precipitate β grows must be equal to the flux of solute to the α/β interface:

$$v(c^{\beta\alpha} - c^{\alpha\beta}) = -D\frac{\partial c}{\partial z}\bigg|_{z=z^*} \tag{5.2}$$

where v is the interfacial velocity, z is the axis along the growth direction, z^* is the position of the interface and D is the solute diffusion coefficient in the matrix phase. The concentration gradient is evaluated at the position of the interface.

However, alloy carbide formation in practical steels involves the diffusion of both substitutional and interstitial solutes. Therefore, the binary Fe–M treatment as used in previous work (Robson and Bhadeshia, 1997a, 1997b) is inadequate for alloy carbide formation in practical steels, because the mass balance equation will not be satisfied for the interstitial solute. In general, it should be very complex to satisfy all mass conservation equations for each solute simultaneously. A ternary system, in which alloy carbide formation involved with both metallic solute and carbon, is the simplest approximation for alloy carbide formation in practical steels. There are two such equations for both carbon c and substitutional solute M which have to be

satisfied †:

$$v(c_M^{\beta\alpha} - c_M^{\alpha\beta}) = -D_M \left.\frac{\partial c_M}{\partial z}\right|_{z=z^*}$$
$$v(c_C^{\beta\alpha} - c_C^{\alpha\beta}) = -D_C \left.\frac{\partial c_C}{\partial z}\right|_{z=z^*} \qquad (5.3)$$

Because $D_M \ll D_C$, it would in general be impossible to satisfy these equations simultaneously for a tie–line passing through alloy composition $\bar{c}$. However, for a ternary alloy, there is an additional degree of freedom given by the phase rule so that there is a choice of tie–lines at any given temperature. The local equilibrium condition can be maintained by choosing a tie–line which either minimises the concentration gradient of carbon (thus allowing substitutional solute flux to keep pace) or maximises the gradient of the substitutional solute to compensate for its small diffusivity.

These concepts are well established in treatments of the growth of ferrite from austenite, but as a first approximation were not incorporated in the calculations of carbide precipitation kinetics (Hall *et al.*, 1972, Robson and Bhadeshia, 1997a, 1997b) where the diffusion–controlled growth was treated essentially as a binary Fe–M problem. It has been shown in Chapter 4 that the binary approximation leads to significant mass balance discrepancies.

Capillarity

The state of equilibrium between two phases changes with the curvature of the interface separating them. This well–established *capillarity effect* scales with the interfacial energy because additional work has to be done to create new interfacial area as a curved interface moves. The free energy of a carbide phase varies relatively sharply with deviations from the stoichiometric composition so it can be assumed that the carbide composition is not sensitive to the interface curvature. However, the equilibrium composition of the ferrite changes as follows (Christian, 1975, p. 181):

$$c_r^{\alpha\beta} = \left(1 + \frac{2\Gamma}{r}\right) c^{\alpha\beta} \qquad \text{with} \qquad \Gamma = \frac{\sigma v^\beta}{kT} \frac{1 - c^{\alpha\beta}}{c^{\beta\alpha} - c^{\alpha\beta}} \qquad (5.4)$$

where r is the radius of curvature at the tip, Γ is a capillarity coefficient which is directly proportional to the interfacial energy σ and $c^{\alpha\beta}$ is the solute concentration in matrix α which is in equilibrium with β when $r = \infty$. v^β is the molar volume of the β phase. The modified composition $c_r^{\alpha\beta}$ is therefore easy to estimate for a binary alloy. At some critical value of

† The equations presented here neglect cross–diffusion effects, *e.g.* the dependence of the flux of carbon on the gradient of M (Coates, 1973; Kirkaldy, 1958). This is considered to be a reasonable approximation in the present context due to the large differences in atomic mobilities.

$r = r_c$, $c_r^{\alpha\beta} = \overline{c}$ and growth ceases.

Equation 5.4 cannot simply be applied to a ternary alloy with two solutes, bearing in mind that the concentrations for carbon C and substitutional solute M in the matrix α at the interface, $c_C^{\alpha\beta}$ and $c_M^{\alpha\beta}$, are not independent but are connected by a tie–line of the phase diagram. A straightforward application to each solute in turn simply gives two different values of r (Robson, 1996), a situation of which is not physical since there is only one interface for both solutes. It does not appear from the literature that the problem of multicomponent capillarity within the constraint of local equilibrium has been solved.

Summary

Previous work (Hall *et al.*, 1972; Robson and Bhadeshia, 1997a, 1997b) on the calculations of the kinetics of precipitation reactions in secondary hardening steels has been based on carbide growth in binary Fe–M systems. This was justified by stating that since carbon diffuses rapidly, growth should be controlled by the slower diffusing M atom. We now know that this is not a reasonable approximation because it fails to ensure mass balance for all other species of atoms involved in the transformation. The binary approximation is also inappropriate because it leads to different tip radii for different solutes.

The aim of this chapter is to resolve these difficulties and to test the new methodology for needle–shaped precipitation using published data by Hall *et al.* (1972) for a ternary Fe–2Mo–0.1C wt% steel in which needle–shaped carbide M_2C precipitates after cementite in isothermal heat treatment.

The framework of the Avrami theory for simultaneous transformations as developed by Robson and Bhadeshia (1997a) is nevertheless necessary since cementite precipitation must precede that of M_2C even though Hall *et al.* insisted that cementite does not form.

5.2 Modelling carbide kinetics in Fe–Mo–C system

5.2.1 Cementite precipitation

For the most part, cementite precipitation and its subsequent enrichment and dissolution will be treated by the same way of Robson and Bhadeshia model (1997a), although some of microstructual parameters, thickness and the nucleation number density of cementite have been modified with the help of the new experimental data presented in Chapter 4.

Paraequilibrium formation of cementite

Cementite precipitation from supersaturated martensite occurs rapidly even at very low temperatures. This is because it forms by a mechanism which does not involve the diffusion of substitutional solutes or iron atoms, but just the interstitial carbon atom (Hultgren, 1947). The ratio of iron to substitutional solute atoms does not therefore change during this *paraequilibrium* (Hultgren, 1947; Rudberg, 1952; Aaronson *et al.*, 1966) transformation. In general, this ratio is far less than demanded by equilibrium.

In the context of secondary hardening steels, the time period for cementite precipitation is so small that it can be assumed that the starting microstructure already contains precipitates of cementite with paraequilibrium transformation.

Enrichment

The chemical composition of the cementite adjusts towards equilibrium from paraequilibrium during the heat treatment needed to induce molybdenum carbide precipitation. This process depletes the matrix of substitutional solute and hence must be taken into account in any model for molybdenum carbide precipitation. The theory for the enrichment of a cementite particle of thickness d has been described by Bhadeshia (1989):

$$t_c^{\frac{1}{2}} = \frac{d\pi^{\frac{1}{2}}(\overline{c} - c_t)}{4D^{\frac{1}{2}}(c^{\theta\alpha} - \overline{c})} \tag{5.5}$$

where c_t is the mean composition of the cementite (designated θ) at time t_c, D is the diffusion coefficient for the solute concerned and $c^{\theta\alpha}$ is the concentration in θ which is in equilibrium with the matrix α. Experiments shown in Chapter 4 indicated that the thickness of cementite is different when precipitated at the martensite lath boundaries ($\simeq$ 50 nm) when compared with that precipitated within the laths ($\simeq$ 20 nm). These are the values assumed in the present work and the particles at the boundaries have been modelled as a separate phase from those within the laths.

Site density

The volume fraction of cementite must depend on the carbon content, so it is reasonable to assume that the number density of cementite particle can also be expressed as a function of carbon content. The number density of cementite particles per unit volume $N_{0\theta}$ is found experimentally to be given by:

$$N_{0\theta} = 2.23 \times 10^{22} w_C - 10^{21} \qquad \mathrm{m}^{-3} \tag{5.6}$$

where w_C is the concentration of carbon in wt%. This empirical equation was established using 0.15 wt% C-2$\frac{1}{4}$Cr1Mo and 0.10 wt% C-3Cr1.5Mo steels as described in Chapter 4, so it might reasonably be expected to apply to tempered martensitic steels with carbon concentrations in the range from 0.10 to 0.15 wt%.

Dissolution

The cementite (θ) eventually must begin to dissolve as the precipitation of the thermodynamically more stable M_2C (β) gathers pace. The dissolution of cementite provides a source of solute for the growing M_2C. The dissolution for each particle begins when the mean concentration $\overline{c}$ becomes less than $c^{\alpha\theta}$, thereby driving the diffusion of solute from the cementite to the M_2C as schematically shown in Fig. 5.1. The dissolution velocity v_d is given by (Robson and Bhadeshia, 1996a):

$$v_d(c^{\theta\alpha} - c^{\alpha\theta}) = D\frac{c^{\alpha\theta} - c_r^{\alpha\beta}}{\overline{d}} \tag{5.7}$$

where $c^{\alpha\theta}$ and $c^{\theta\alpha}$ are the solute concentrations in the ferrite and cementite at the interface between ferrite and cementite. The mean distance between the cementite and M_2C particles $\overline{d}$ is given by:

$$\overline{d} = (N_\theta + N_\beta)^{-\frac{1}{3}} \tag{5.8}$$

where N_θ and N_β are the number densities of cementite and M_2C particles respectively.

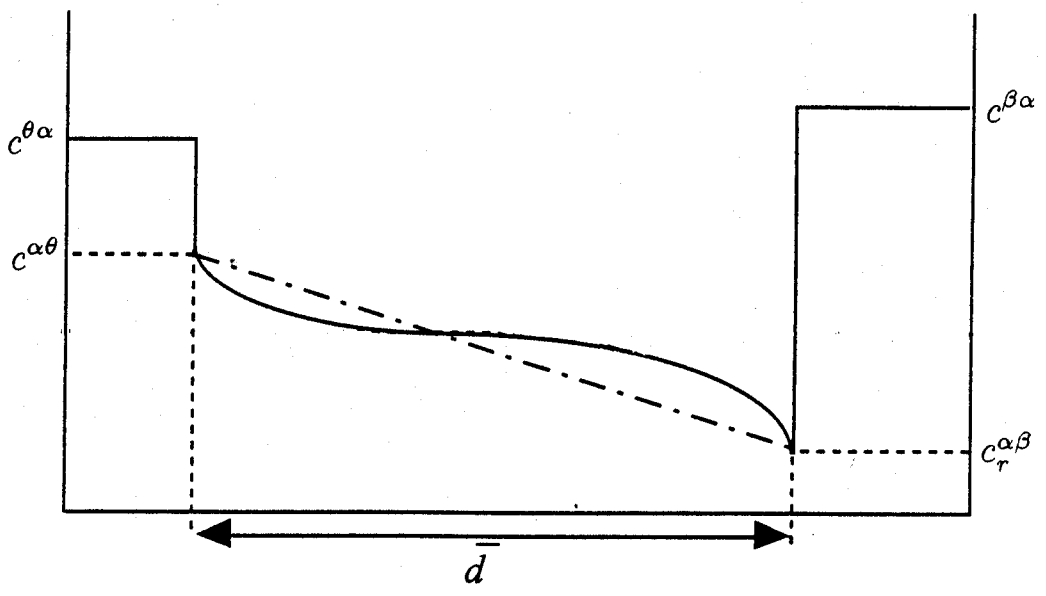

Fig. 5.1: A schematic illustration of solute distribution when cementite (θ) is dissolving and M_2C (β) is precipitating in the ferrite matrix(α) (Robson and Bhadeshia, 1997a).

5.2.2 M_2C precipitation

Nucleation

The nucleation is assumed to occur with a constant nucleation rate when soft–impingement does not occur. Classical nucleation theory (Turnbull and Fisher, 1948) is used to estimate the nucleation rate I' for M_2C together with the site consumption:

$$I' = \overline{c}\left(1 - \frac{V'}{V^{eq}}\right) N_{0\beta} \frac{kT}{h} \exp\left\{-\frac{G^* + Q^*}{kT}\right\}$$
$$G^* = \frac{16\pi\sigma^3}{3(\Delta G_v)^2} \tag{5.9}$$

where V' and V^{eq} are instantaneous and equilibrium fractions of M_2C respectively, $N_{0\beta}$ is the number density of nucleation sites for M_2C, h and k are the Planck and Boltzmann constants respectively, Q^* is the activation energy for the transfer of atoms across the nucleus/matrix interface, assumed to be the activation energy for volume diffusion (Turnbull and Fisher, 1948). T is the absolute temperature and ΔG_v is the chemical free energy change per unit volume. σ is the interfacial energy per unit area between the precipitate and the matrix.

Growth with tie–line shifting by soft–impingement

Fig. 5.2 shows a schematic isothermal section of the Fe–Mo–C phase diagram. The alloy has an average carbon concentration which is $\overline{c}_C$ but the carbon left in solution in the ferrite when cementite has precipitated, $c_C^{\alpha\theta}$ is the smaller concentration of carbon which is initially available for the precipitation of M_2C.

It was stated in Chapter 2 that there are two ways in which the mass conservation equations for Mo and C can be satisfied simultaneously. The first is to choose a tie–line which greatly increases the gradient of molybdenum to compensate for its low diffusivity. This would require the carbide to have virtually the same molybdenum concentration as the matrix with very little partitioning of Mo, but with a sharp concentration spike at the interface in order to maintain local equilibrium (NP–LE). This situation is only possible at very large driving forces (Coates, 1973; Kirkaldy, 1958). The case of secondary hardening steels refers, on the other hand, to precipitation at low supersaturations. In these circumstances, the only alternative is to choose a tie–line which reduces the gradient of carbon to such an extent that the flux of carbon is reduced to a level consistent with that of Mo. Following Coates (1973), this can be done by drawing a vertical construction line through the point **b** in Fig. 5.3, which represents the composition of the ferrite from which M_2C will precipitate. The intersection of the vertical line with the

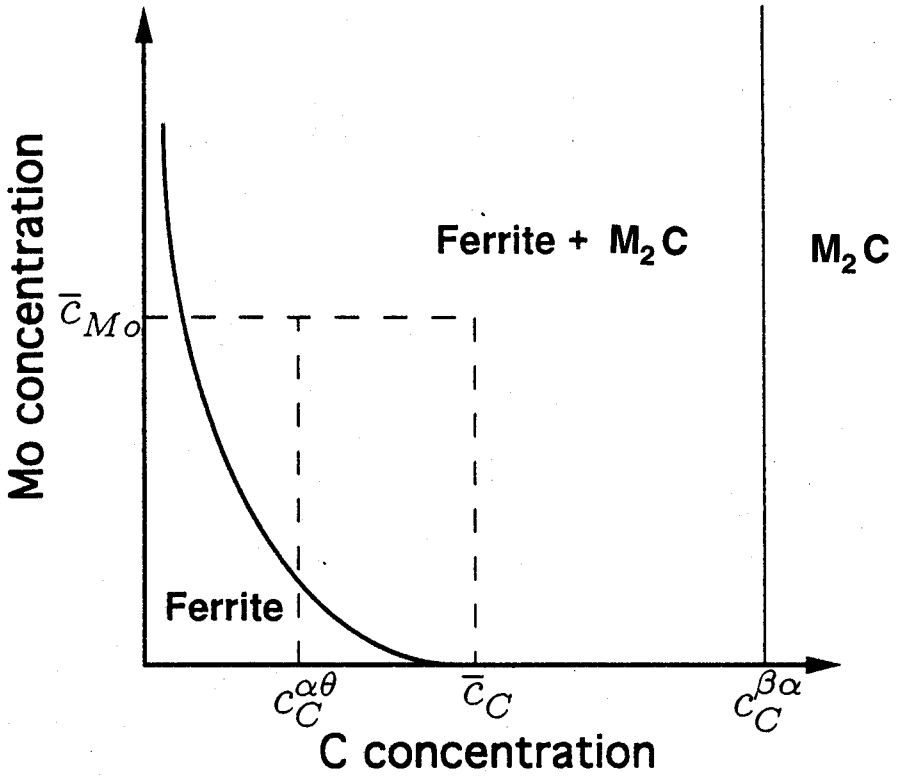

Fig. 5.2: A schematic isothermal section through the Fe–Mo–C phase diagram, showing the ferrite and M_2C phase fields.

$\alpha/(\alpha+\beta)$ phase field defines completely the tie–line which fixes the interface compositions in a manner which satisfies the two mass conservation conditions simultaneously because the large diffusion coefficient of carbon is compensated for by the very small concentration gradient of carbon (Coates, 1973; Ḳirkaldy, 1958). Note that this also maintains local equilibrium at the interface since the compositions at the interface (given by the points **c** and **d** for α and β respectively) are connected by a tie–line of the phase diagram.

The M_2C precipitation must deplete the solute concentration in the matrix (soft-impingement). The locus of the matrix composition at any instant is along the direction **b** → **e** (Fig. 5.3). Any change in the matrix composition also leads to a different choice of tie–line, the locus of $c^{\alpha\beta}$ being along **c** → **f**. This tie–line shifting (Coates, 1973) continues until the reaction stops when the tie–line intersects the average composition **a** and $c^{\alpha\beta} = \mathbf{f}$.

The changes in the chemical composition of the matrix during precipitation are vital to the development of the precipitation process. Composition gradients develop in the ferrite and the

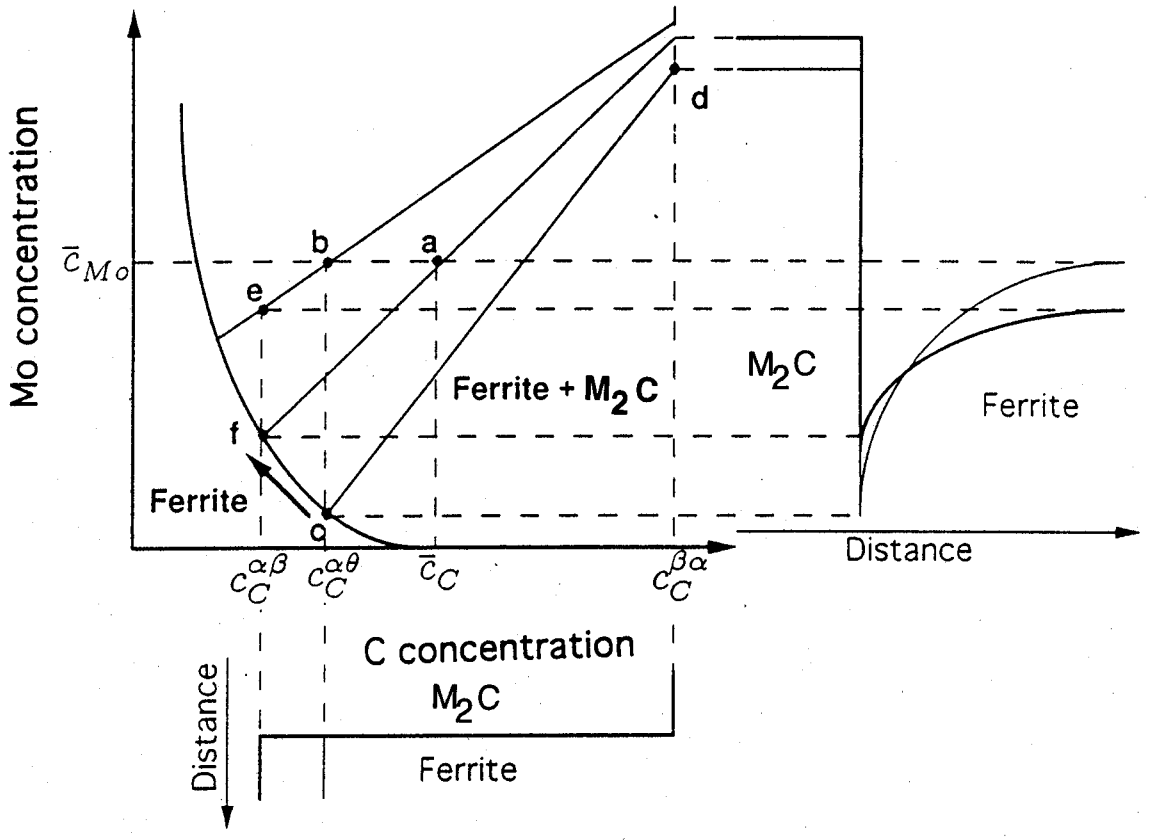

Fig. 5.3: A schematic isothermal section through the Fe–Mo–C phase diagram, showing the ferrite and M_2C phase fields. The alloy composition is plotted as point **a** whereas the composition of the ferrite after the precipitation of cementite is designated **b**.

gradients originating from different particles eventually interfere, changing the rate equations. This is taken into account using the so–called mean field approximation in which the changes are averaged out over the residual matrix (Robson and Bhadeshia, 1997a). The far field matrix composition seen by each precipitate is this averaged composition denoted $\overline{c}'$:

$$\overline{c}' = \overline{c} - \frac{V_\theta(c^{\theta\alpha} - \overline{c}) + V_\beta(c^{\beta\alpha} - \overline{c})}{1 - V_\theta - V_\beta} \tag{5.10}$$

where V_θ and V_β is the volume fraction of cementite and M_2C respectively.

The effect of soft-impingement in the mean field approximation may also be expressed in terms of an extent of reaction parameter with the dimensionless supersaturation.

$$\Phi_\beta = \frac{V'}{V^{Max}} \qquad \text{with} \qquad V^{Max} = \frac{\overline{c} - c^{\alpha\beta}}{c^{\beta\alpha} - c^{\alpha\beta}} \tag{5.11}$$

where V' is the instantaneous fraction and V^{Max} the maximum fraction of a given phase. The function Φ_β ranges from 0 to 1 and represents the fraction of excess solute remaining in the matrix relative to the equilibrium composition of the precipitate. It is assumed that the driving force for precipitation is related linearly to Φ:

$$\Delta G_\beta = (1 - \Phi_\beta)\Delta G_{0\beta} \tag{5.12}$$

where $\Delta G_{0\beta}$ is the driving force available before any precipitation of phase β.

Similar changes due to the enrichment of cementite can also be dealt with by defining:

$$\Phi_\theta = \frac{c - \overline{c}'}{c^{\theta\alpha} - \overline{c}'} \tag{5.13}$$

With these treatments, growth rate as indicated in Chapter 2 will be given by:

$$v = \frac{D\Omega_r}{z_d} \quad \text{with} \quad \Omega_r = \frac{\overline{c} - c_r^{\alpha\beta}}{c^{\beta\alpha} - c_r^{\alpha\beta}} \tag{5.14}$$

for

$$z_d = \frac{2(c^{\beta\alpha} - \overline{c})}{(c^{\beta\alpha} - c_r^{\alpha\beta})} r \tag{5.15}$$

where Ω_r is dimensionless supersaturation with capillarity effect. Therefore, another theory, capillarity, still be necessary to obtain velocity.

The method developed here to account for the capillarity effect in a ternary alloy involves the calculations of the α/α+M_2C (β) boundary on the isothermal section of the phase diagram, as a function of the radius of the curvature r at the interface. Equation 5.4 is used to calculate the concentration affected by capillarity effect $c_r^{\alpha\beta}$ for a fixed value of the interface radius of curvature. The growth velocity is then calculated using the method described in the previous section but with the curvature-modified phase boundary (Fig. 5.4).

A problem of the tip radius in a multicomponent system still remains. As Robson had calculated (1996), the values of the tip radius r for each solute were not unique but very different

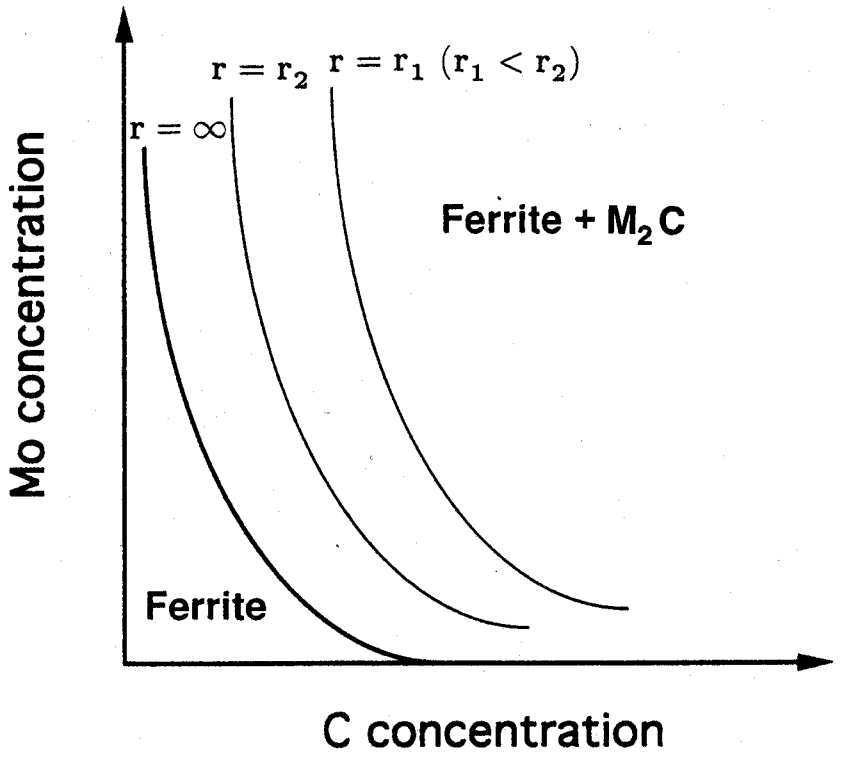

Fig. 5.4: A schematic illustration of the way the α/α+M_2C (β) phase boundary changes for a variety of values for radius of curvature r at the interface.

from each other. Table 5.1 shows the calculation results by Robson about the tip radius for a 10Cr wt% power plant steel with equation 5.16:

$$r = \frac{4c^{\alpha\beta}\Gamma}{(\overline{c} - c^{\alpha\beta})} \quad \text{with} \quad \Gamma = (\frac{\sigma v^{\beta}}{kT})(\frac{1 - c^{\alpha\beta}}{\overline{c} - c^{\beta\alpha}}) \tag{5.16}$$

	Cr	Fe	Mo	C	N
r / Å	913.2	230.1	1039.4	0.318	0.170

Table 5.1: The calculated tip radii of M_2X for each element in 10Cr wt% power plant steel by equation 5.16 (Robson, 1996).

Physically, the tip radius should be unique for a particle.

Trivedi's solution preserves the shape of the parabola at the particle tip with constant growth rate as shown in Fig. 5.5 (1970). The tip radius remains constant in the absence of soft–impingement. The problem here is how to decide the value of r and hence fix the velocity. Small tip radius makes fast velocity but this is opposite to capillarity effect since the driving force for growth became zero when $r \rightarrow r_c$. Therefore, the additional theory or assumption is needed. Zener proposed the velocity will go through maximum, although there is not a fundamental basis.

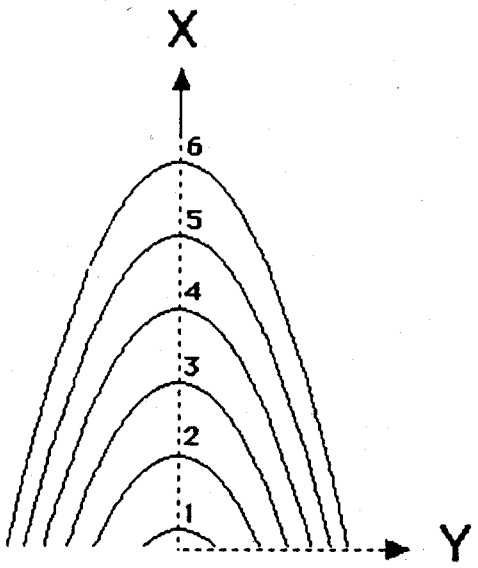

Fig. 5.5: A schematic illustration for the particle shape at the tip in which shape–preserving is assumed to be the same parabola along X. The sequence 1–6 along X illustrates the nature of the shape–preserving solution with constant growth rate (Trivedi, 1970).

In this way, the interface velocity can be plotted as a function of the radius r; such a function must go through a maximum because a large radius approximates to one–dimensional diffusion confined to regions normal to the interface, whereas the capillarity effect reduces the velocity as r approaches to the critical radius r_c at which growth stops. The maximum velocity can be obtained numerically and then be assumed to correspond to the actual growth velocity, an assumption known as the Zener hypothesis (1946).

This procedure solves all the problems described in the introduction of this chapter. It deals correctly with mass balance for both the diffusing species and the capillarity corrected concentrations for each solute give the same tip radius when inserted into equation 5.4.

5.3 Diffusion coefficient

The diffusion coefficient is given by:

$$D = D_0 \exp(-\frac{Q}{RT}) \tag{5.17}$$

where D_0 is the pre–exponent factor and Q is the activation energy for diffusion. Fridberg *et al.* reported diffusion coefficients for several solutes in ferrite and austenite. Table 5.2 shows diffusion coefficient of substitutional element Mo in ferrite, which are used here.

Element	D_0 / $m^2\ s^{-1}$	Q / J mol^{-1}
Mo	1.1×10^{-4}	240×10^3

Table 5.2: D_0 and Q values for molybdenum in ferrite (Fridberg *et al.*, 1969).

5.4 Thermodynamic calculations for M_2C in Fe–Mo–C ternary system

Phase diagrams are required for modelling nucleation and growth. The MTDATA program (Hodson, 1989) and SGTE database were used to estimate the Fe–Mo–C phase diagram for ferrite, cementite and M_2C. The method uses experimental data and works by combining the data from appropriate unary, binary and higher order sub–systems with thermodynamic theory to minimise the Gibbs free energy.

5.4.1 Driving force for nucleation

M_2C will form with cementite dissolution so that the reaction will be expressed as follows;

$$\alpha + M_3C \rightarrow \alpha' + M_2C \tag{5.18}$$

where α and α' represent the ferrite coexisting with M_3C and M_2C respectively. The free energy change for this reaction in Fe–2Mo–0.1C wt% steel which Hall *et al.* examined (1972)

was calculated using MTDATA. Fig. 5.6 shows the free energy change for the reaction in Fe–2Mo–0.1C wt% steel at high temperatures with M_3C in equilibrium and paraequilibrium states. The driving force decreases as temperature increases in both cases and that with M_3C as paraequilibrium was slightly larger than that with M_3C as equilibrium.

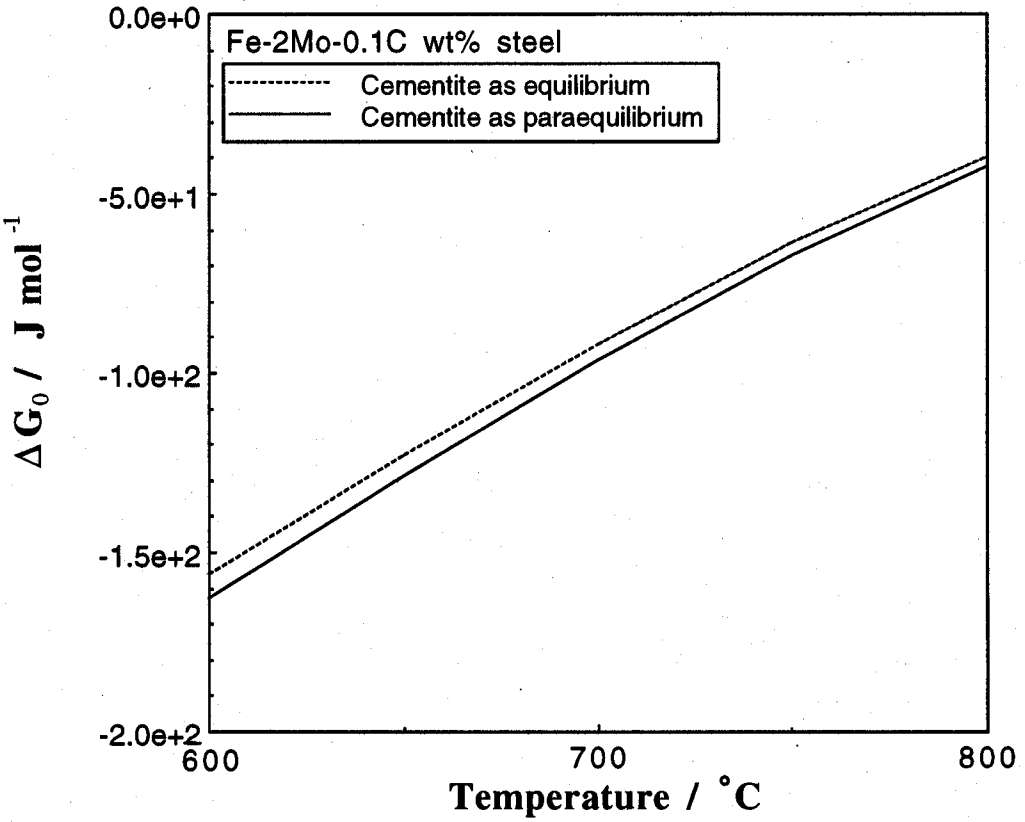

Fig. 5.6: The free energy change for the precipitation reaction of M_2C from cementite in ferrite with temperature for Fe–2Mo–0.1C wt% steel. The free energy changes of the reactions from both equilibrium cementite and paraequilibrium cementite were calculated using MTDATA.

The calculated values are not driving force for nucleation but overall free energy change for the reaction. Fig. 5.7 illustrates the free energy curves for the α and β phases.

The distance US represents the overall driving force for reaction ΔG_0 and PR presents the driving force for β nucleation ΔG_n. Although it really depends on the curvature of free energy

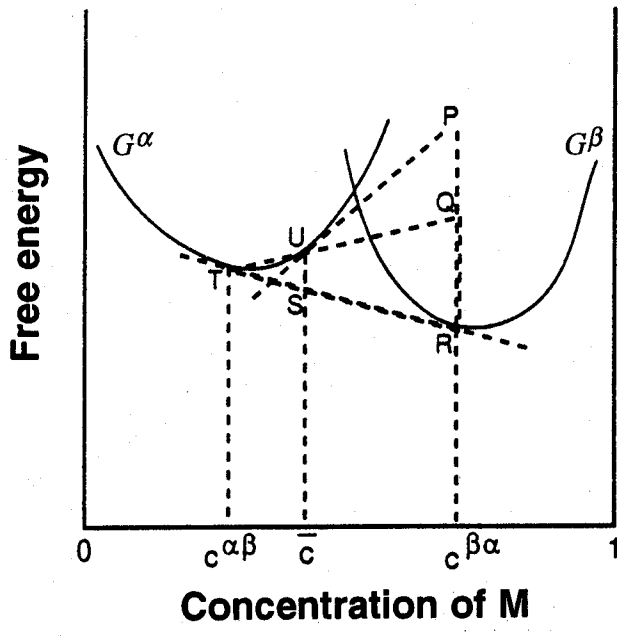

Fig. 5.7: Schematic free energy curves for nucleation of β phase from the matrix α, showing the way to obtain the driving force for nucleation.

for α phase, QR can be assumed to be approximately equal to PR. Then, QR is given by:

$$QR = \frac{c^{\beta\alpha} - c^{\alpha\beta}}{\bar{c} - c^{\alpha\beta}} \Delta G_0 = \frac{\Delta G_0}{V_\beta^{eq}} \tag{5.19}$$

Then, for a mole of nuclei,

$$\Delta G_n \simeq \frac{\Delta G_0}{V_\beta^{eq} v^\beta} \tag{5.20}$$

where V_β^{eq} is equilibrium volume fraction of β phase and v^β is the molar volume of β.

5.4.2 Equilibrium concentration and capillarity effect

The molybdenum concentration at the interface in the Fe–2Mo–0.1C wt% steel was calculated using MTDATA. Fig. 5.8 shows the changes of the equilibrium concentration of Mo in the matrix α at the interface $c_{Mo}^{\alpha\beta}$ with temperature.

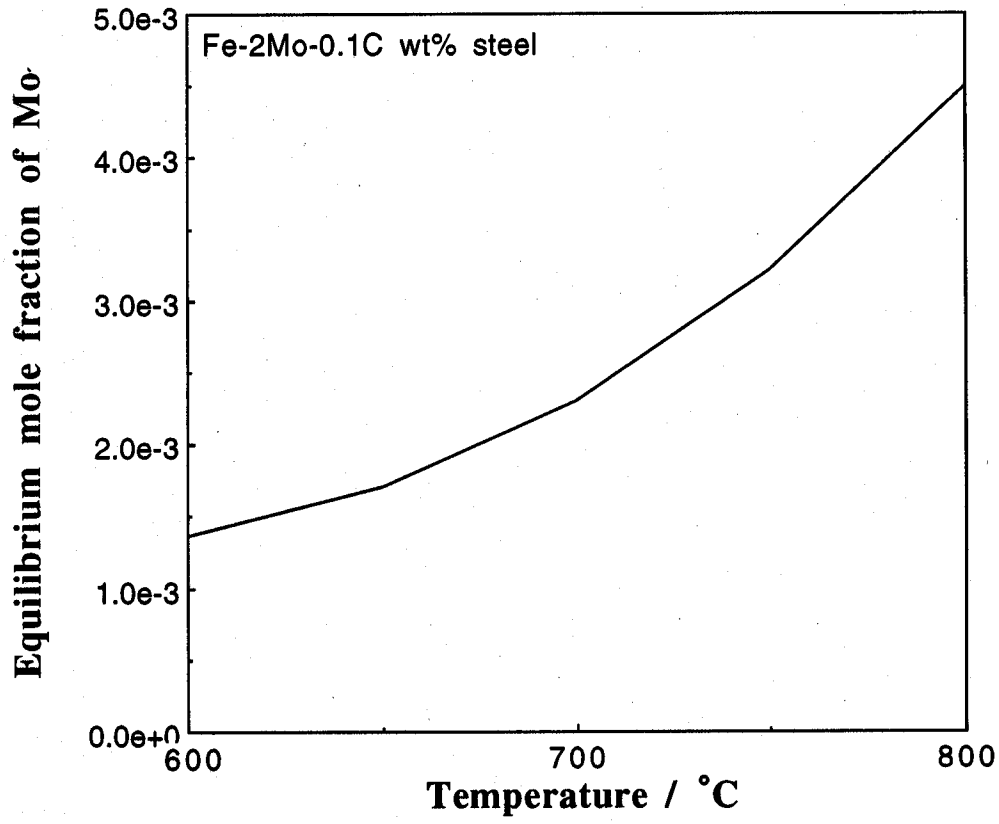

Fig. 5.8: Equilibrium molybdenum concentration in the ferrite matrix with M_2C calculated using MTDATA at high temperatures for Fe–2Mo–0.1C wt% steel.

The equilibrium concentration of Mo at the interface between matrix and precipitate increases as temperature increases. These are equilibrium concentrations determined by the tie–line passing through the alloy composition. In order to find how the tie–line shifting occurs in a multicomponent treatment, it is necessary to find the ferrite/M_2C phase boundary and how it is affected by capillarity. With MTDATA, the equilibrium phase boundary at which $r = \infty$ can be easily obtained. Using equation 5.4, it is possible to find how the phase boundary is modified by capillarity effect at each given tip radius. Fig. 5.9 shows the α/β phase boundary in the isothermal section at 700 °C for Fe–Mo–C system at each given tip radius. When $r = \infty$, the concentration becomes equal to that on the equilibrium phase boundary.

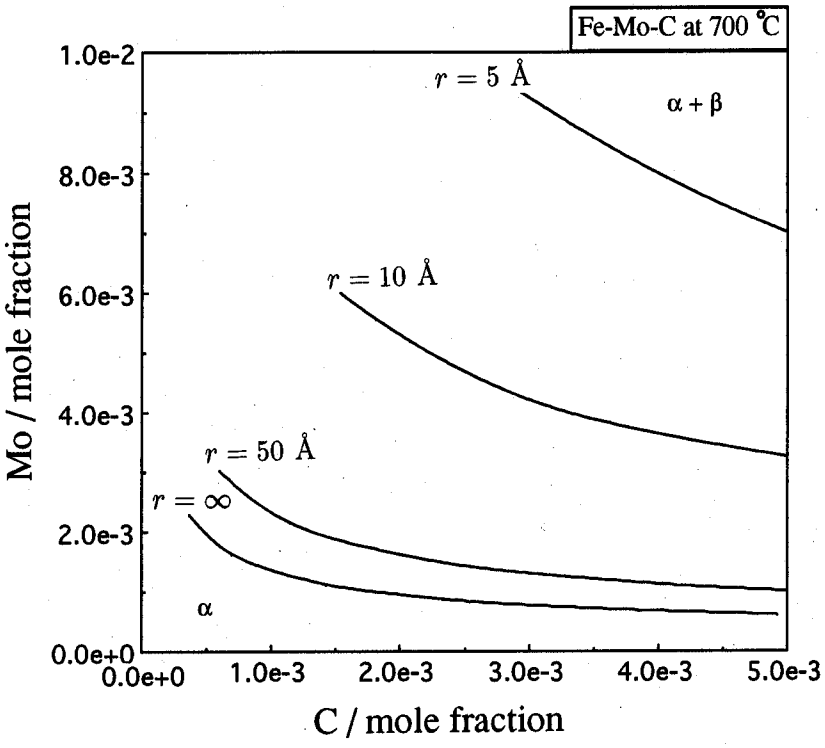

Fig. 5.9: The ferrite matrix (α) / M_2C (β) phase boundary at each given tip radius in the isothermal section at 700 °C for Fe–Mo–C system when the interfacial energy $\sigma = 0.20$ J m^{-2}.

5.5 Calculations for M_2C precipitation in Fe–Mo–C system

The lengthening rate of M_2C in tempered martensite has been measured by Hall *et al.* (1972) for a variety of temperatures in an alloy of composition Fe–2Mo–0.1C wt%. The rate is determined by measuring the length of the largest particle observed for a particular isothermal heat treatment time. Such data are then plotted as a function of time to estimate the lengthening rate. The original data were analysed assuming that it is only the diffusion of molybdenum which determines the lengthening rate of the M_2C needles; the growth rate was also assumed to be constant throughout the heat treatment.

Example calculations were carried out using the multicomponent model described earlier, beginning with a microstructure consisting of paraequilibrium cementite and ferrite in which M_2C eventually grows at the expense of the cementite. In this model, it is assumed that all reactions (cementite enrichment and M_2C precipitation) begin at the same time but occur in this case at different rates. Furthermore, the dissolution of cementite occurs naturally when the mean composition of the matrix falls below that consistent with its equilibrium with cementite, as

M_2C formation withdraws solute from the ferrite. Because of the multicomponent mass balance conditions inherent in the present form of the simultaneous transformations model, the dissolution of cementite occurs at a rate consistent with the precipitation of M_2C. Note that this is not the case with the earlier Robson and Bhadeshia model.

M_2C grows in the form of needles so the lengthening rate is a function of the tip radius. Fig. 5.10 shows the change of lengthening rate with time at a constant tip radius. In each case, the growth rate goes through a maximum which is assumed here to correspond to the actual growth rate at any instant of time. Notice also that the rate changes substantially with time because of soft–impingement and the associated tie–line shifting.

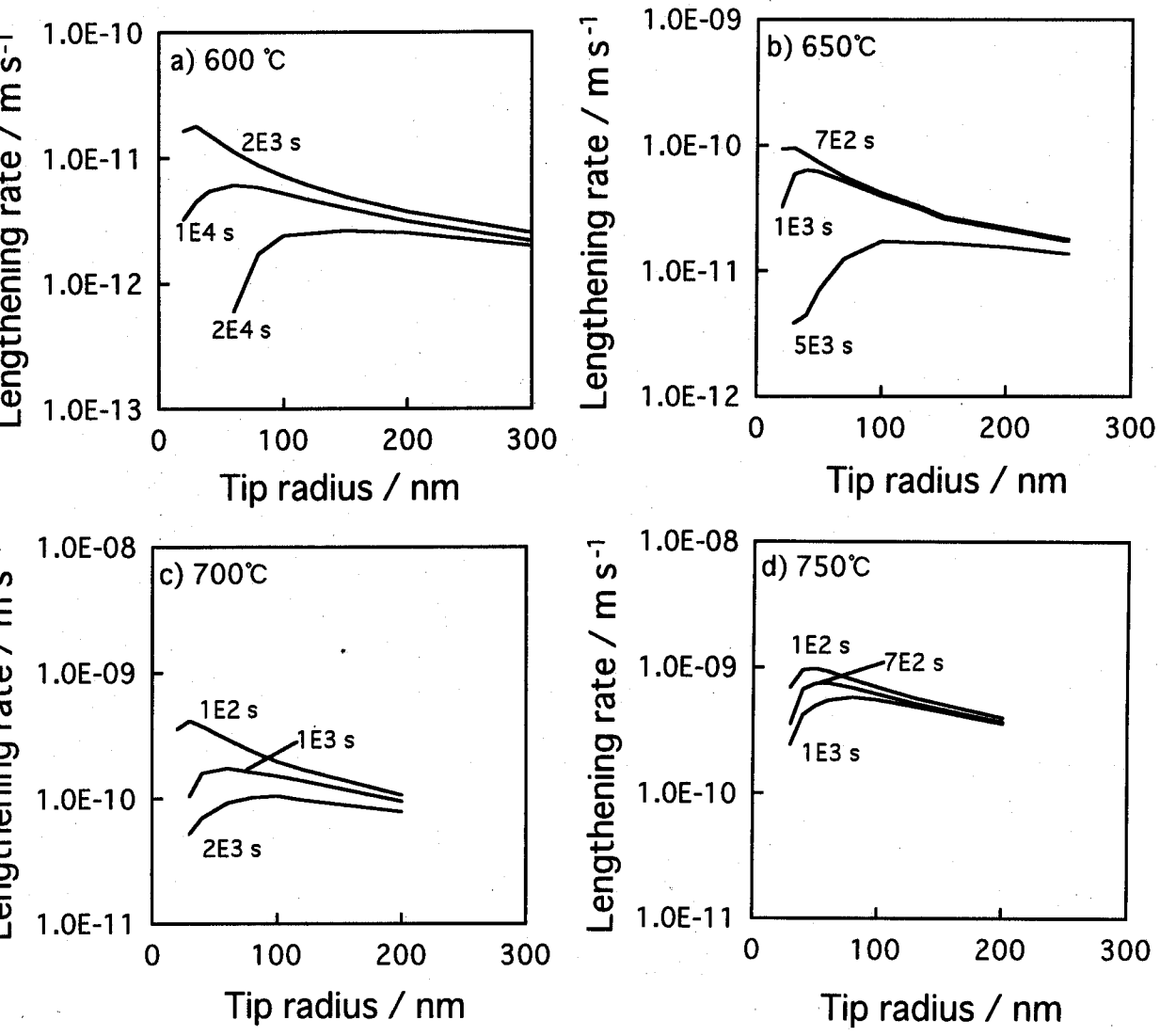

Fig. 5.10: The calculated growth rate of M_2C as a function of the needle tip radius, transformation time and temperature for a Fe–2Mo–0.1C wt% steel.

The radius r_m corresponding to the maximum velocity increases with time because the driving force for transformation decreases with the progress of precipitation (Fig. 5.11). For the same reason, at a fixed value of heat treatment time in the early stages, r_m also increases with the transformation temperature.

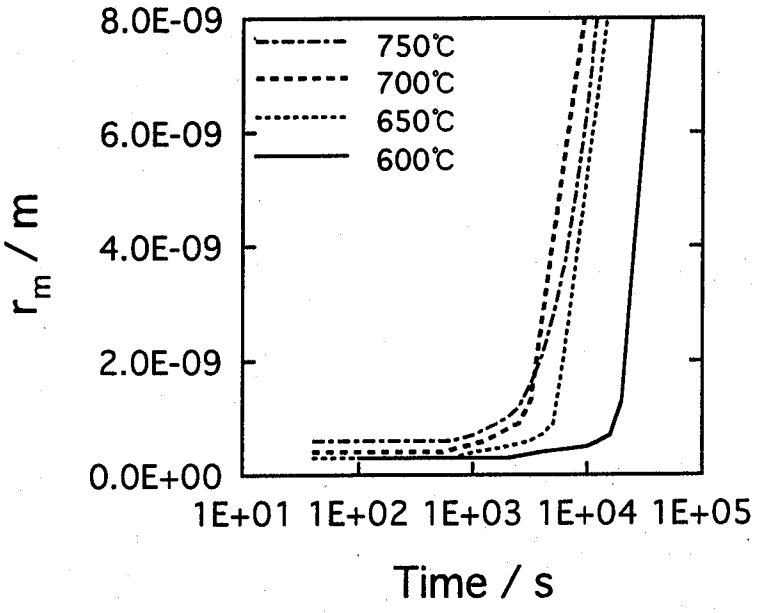

Fig. 5.11: The calculated needle tip radius r_m corresponding to the maximum growth rate, as a function of transformation time and temperature for a Fe–2Mo–0.1C wt% steel.

There are two unknown parameters, the site density of nucleation $N_{0\beta}$ and the interfacial energy σ between matrix and M_2C. This makes a complete comparison with Hall *et al.*'s data impossible. Nevertheless, the trends in the lengthening rate data can be predicted if both are taken to be adjustable parameters. Changing $N_{0\beta}$ can only affect the lengthening rate when soft–impingement between particles nucleated at different locations becomes important; it should not therefore affect the initial lengthening rate. The interfacial energy σ affects the growth rate though the concentration $c_r^{\alpha\beta}$. However, σ may not strongly affect it in the early stages of precipitation when $\overline{c} >> c_r^{\alpha\beta}$.

Table 5.3 shows the parameters used in the calculations. It is apparent from Fig. 5.12 that there is rather good detailed agreement between the experimental data and calculations. The curves for $N_{0\beta} = 1.45 \times 10^{21}\,\mathrm{m}^{-3}$ and $\sigma = 0.20\,\mathrm{J\,m}^{-2}$ emulate the data extremely well apart from the shift along the time axis (dashed curves). Note that the nucleation is assumed to start at $t = 0$ in this model.

The parameters	The values used in calculations
Interfacial energy	0.20 J m^{-2}
Site density	1.45 $\times 10^{21}$ m^{-3}

Table 5.3: The parameters used in the calculations for Fe–2Mo–0.1C wt% steel.

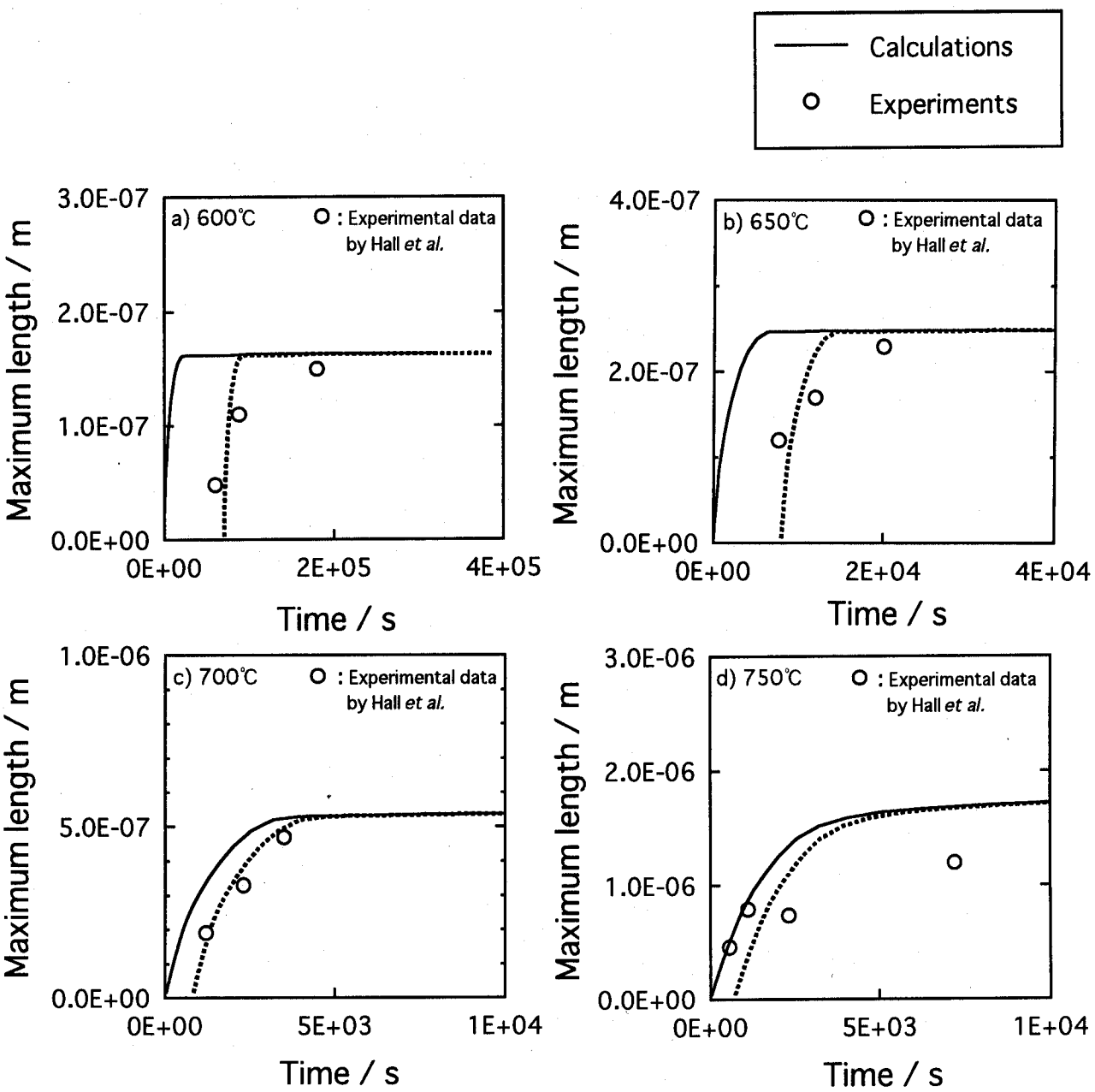

Fig. 5.12: A comparison between the calculated and measured particle dimensions as a function of time, temperature for the Fe–2Mo–0.1C wt% steel studied by Hall *et al.* (1972).

The growth rate is the slope of the curve and is shown in Fig. 5.13, as is the great reduction in rate due to soft-impingement as the volume fraction evolves (Fig. 5.14).

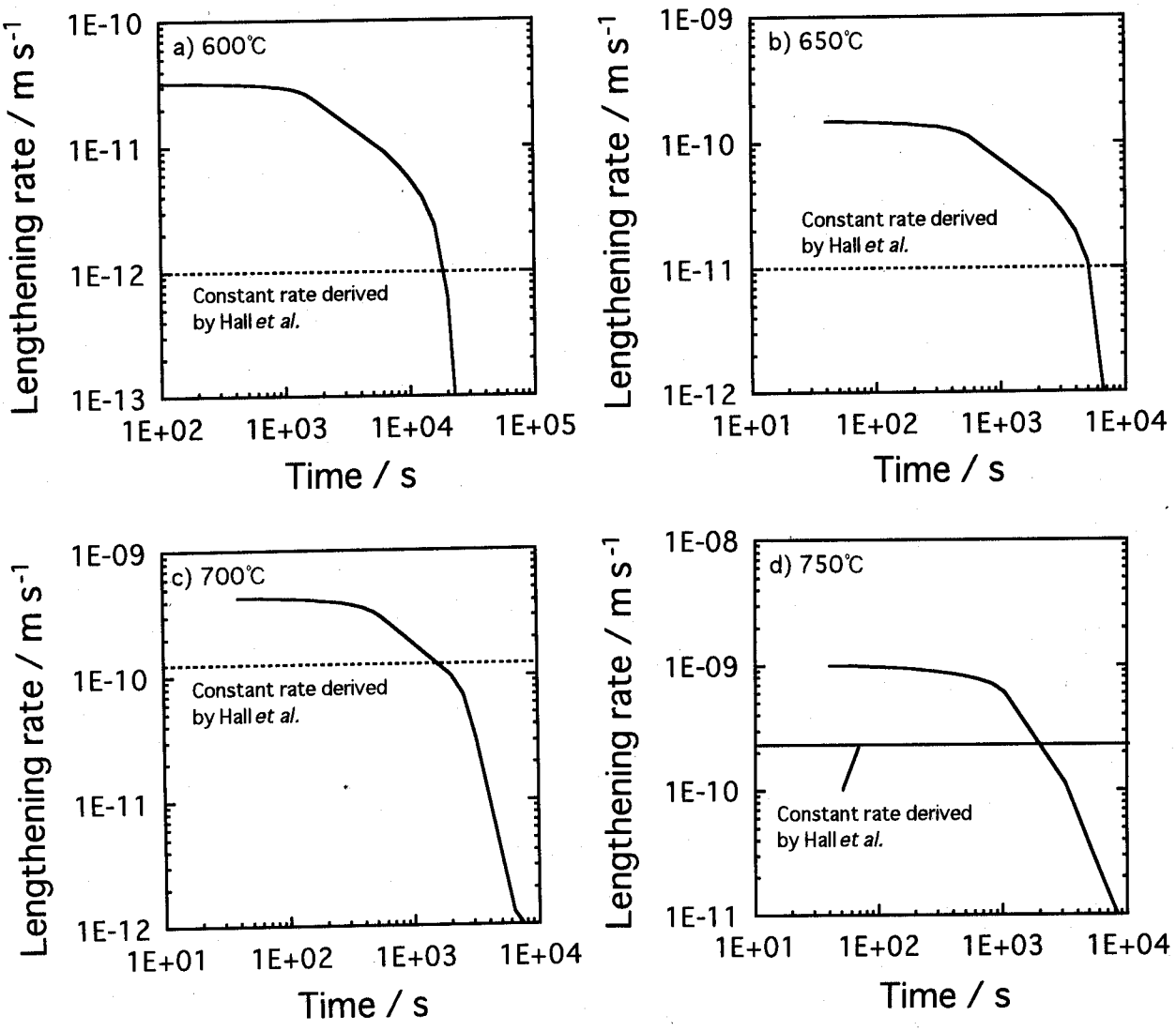

Fig. 5.13: The calculated lengthening rate of M_2C as a function of time and temperature for the optimum values of $N_{0\beta}$ and σ for the Fe–2Mo–0.1C wt% steel studied by Hall *et al.* (1972).

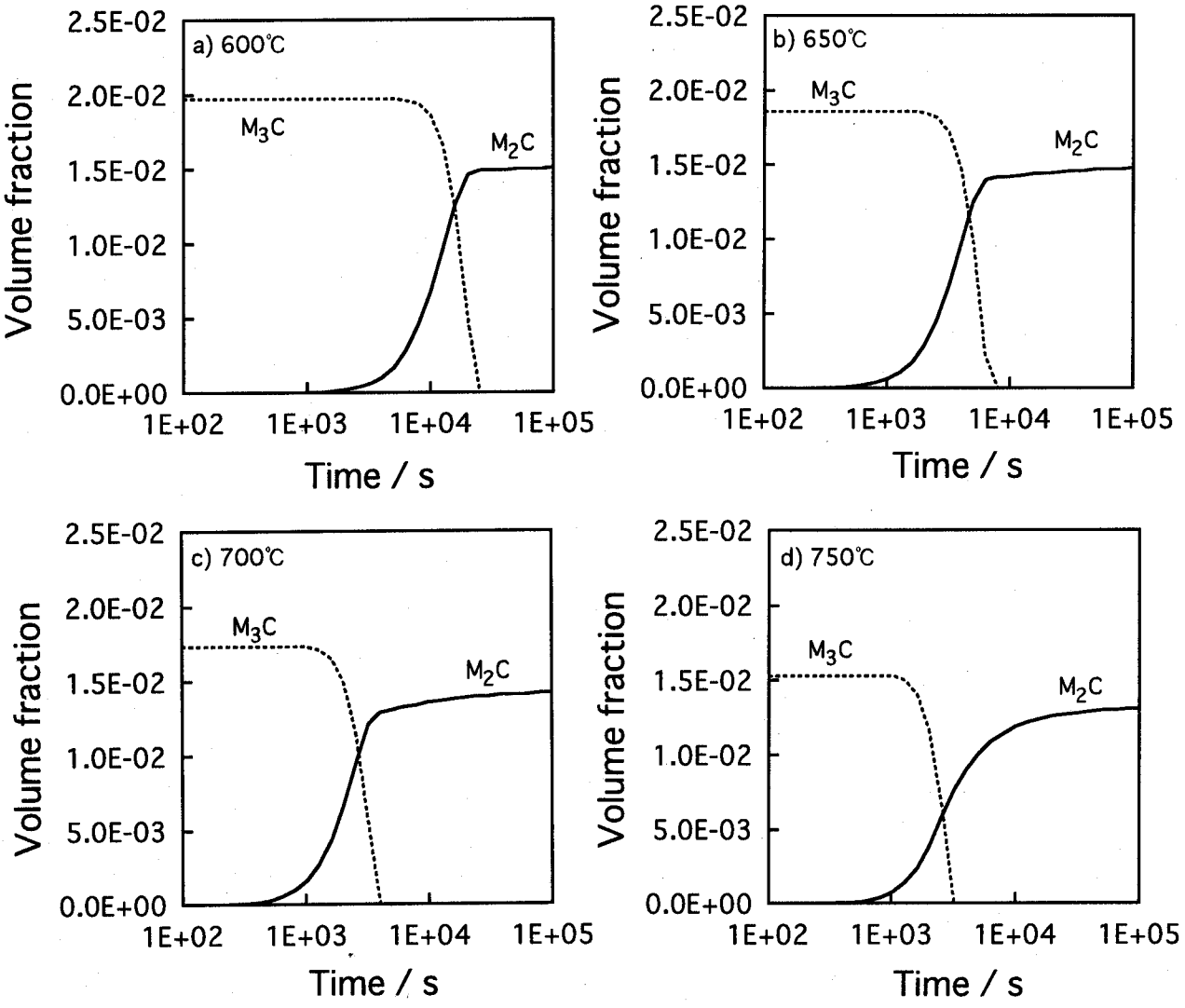

Fig. 5.14: The calculated fractions of cementite and M_2C as a function of time and temperature for the optimum values of $N_{0\beta}$ and σ for the Fe–2Mo–0.1C wt% steel.

This is in contrast to the original analysis where a best fit straight line is fitted to the whole set of isothermal data to derive a constant growth rate. Thus, the agreement between the constant growth rate derived by Hall *et al.* (1972) and the initial rate calculated (Fig. 5.13) is best at higher temperatures, since soft–impingement effects do not occur within the time scale of their experiments.

5.6 Summary

A methodology has been developed to deal with the growth of needle–shaped precipitate, molybdenum carbide, in a ternary alloy, taking proper account of mass balance during diffusion-controlled growth whilst at the same time dealing with multicomponent capillarity effects. The consumption of nucleation sites has also been considered. The method has been satisfactorily validated against published experimental data.

CHAPTER SIX

Modelling precipitation and coarsening of spherical precipitates

6.1 Introduction

Many steels contain substitutional solutes which have a strong affinity for carbon. Some of them, Nb, Ti and V, are strong carbide forming elements each of which in small concentrations has powerful effects during the thermomechanical processing of micro–alloyed steels. Very small carbide particles which interact with the recrystallisation and growth of austenite grains form, thereby preventing the coarsening of the grain structure, and leading to a corresponding increase in the strength and toughness.

Niobium carbide is one of the most important phases in the design of strong steels for structural applications. There has been a great deal of research on modelling niobium carbide precipitation during the hot deformation of steels (Akamatsu *et al.*, 1989; Dutta and Sellars, 1987; Saito *et al.*, 1988; Le Bon *et al.*, 1975). Its formation in ternary or higher order steels involves the diffusion of both substitutional and interstitial solutes as in the M_2C precipitation discussed in Chapter 5. Because these two kinds of solutes diffuse at vastly different rates, there are difficulties in adapting the theory for diffusion–controlled growth as applied to binary alloys. However, only one model has dealt consistently with the multicomponent nature of the precipitation process, or with the fact that the diffusion coefficients of niobium and carbon in austenite are vastly different (Akamatsu *et al.*,1989). However, even this model did not include a proper treatment of the nucleation site consumption.

The purpose of the work reported in this chapter was to develop a model for spherical particle precipitation in a multicomponent system, for which niobium carbide in austenite for isothermal heat treatment has been chosen as a typical case, taking into account the diffusion of both Nb and C, and the corresponding capillarity effects. This has been done within a framework of nucleation and growth theory which leads naturally to the coarsening problem as well. In this chapter, Fe–0.05Nb–0.1C wt% steel has been chosen as a typical high strength low alloy steel. The calculations for this steel have been compared with published data.

6.2 Modelling the kinetics of NbC in Fe–Nb–C system

NbC precipitation in austenite is eventually modelled as for M_2C precipitation described in

Chapter 5. However, unlike M_2C, the precipitation of NbC occurs directly from austenite and shape of NbC particles is approximated as spheres. The austenite is designated γ and NbC is designated ω in the discussion that follows.

6.2.1 Nucleation

Classical nucleation theory (Turnbull and Fisher, 1948), as described in Chapter 2, is used to estimate the nucleation rate per unit volume I' for NbC together with the site consumption:

$$I' = \bar{c}\left(1 - \frac{V'}{V^{eq}}\right) N_{0\omega} \frac{kT}{h} \exp\left\{-\frac{G^* + Q^*}{kT}\right\}$$
$$G^* = \frac{16\pi\sigma^3}{3(\Delta G_v)^2} \tag{6.1}$$

where V' and V^{eq} are instantaneous and equilibrium fractions of NbC respectively, $N_{0\omega}$ is the number density of nucleation sites for NbC.

6.2.2 Growth

The diffusion–controlled growth for NbC during isothermal heat treatment is assumed to occur with local equilibrium at the transformation front. The concentration profile which develops during the precipitation of a solute–rich phase from a matrix is illustrated in Fig. 6.1, where $c^{\gamma\omega}$ is the concentration of solute in austenite which is in equilibrium with niobium carbide and $c^{\omega\gamma}$ is the concentration of solute in ω which is in equilibrium with γ.

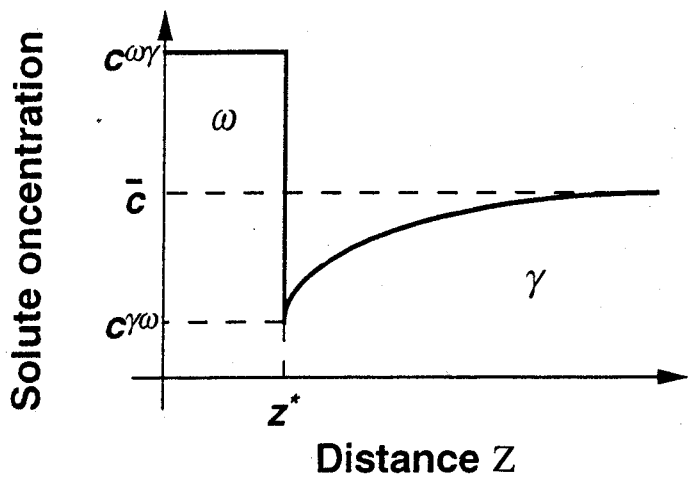

Fig. 6.1: An illustration of the solute concentration profile during diffusion-controlled precipitation of ω from γ.

These concentrations will change during precipitation in order to satisfy two mass conservation equations for carbon and niobium:

$$\begin{aligned} v(c_{Nb}^{\omega\gamma} - c_{Nb}^{\gamma\omega}) &= -D_{Nb}\left.\frac{\partial c_{Nb}}{\partial z}\right|_{z=z^*} \\ v(c_{C}^{\omega\gamma} - c_{C}^{\gamma\omega}) &= -D_{C}\left.\frac{\partial c_{C}}{\partial z}\right|_{z=z^*} \end{aligned} \tag{6.2}$$

where v is the velocity of interface, z is a co-ordinate normal to the interface, z^* is the position of the interface and D_{Nb} and D_C are diffusion coefficients for Nb and C in austenite respectively. Note that the concentration gradients are evaluated at the position of the interface, $z = z^*$.

It was already stated in Chapters 2 and 5 that there are two ways in which the mass conservation equations for both elements be satisfied simultaneously. The first is to choose a tie–line which greatly increases the gradient of niobium to compensate for its low diffusivity. This would require the carbide to have virtually the same niobium concentration as the matrix with very little partitioning of Nb, but with a sharp concentration spike at the interface in order to maintain local equilibrium (NP–LE). This situation is only possible at very large driving forces (Coates, 1973; Kirkaldy, 1958). However, this case refers to precipitation at low supersaturations. In these circumstances, the only alternative is to choose a tie–line which reduces the gradient of carbon to such an extent that the flux of carbon is reduced to a level consistent with that of Nb. Then, tie–line shifting due to soft–impingement will occur as for M_2C, but the details are different because NbC precipitates directly from austenite. Following Coates (1973), this can be done by drawing a vertical construction line through the point **a** in Fig. 6.2, which represents the composition of the austenite from which NbC will precipitate. The intersection of the vertical line with the $\gamma/(\gamma + \omega)$ phase field defines completely the tie–line which fixes the interface compositions in a manner which satisfies the two mass conservation conditions simultaneously because the large diffusion coefficient of carbon is compensated for by the very small concentration gradient of carbon (Coates, 1973; Kirkaldy, 1958). Note that this also maintains equilibrium locally at the interface since the compositions there (given by the points **b** and **c** for γ and ω respectively) are connected by a tie–line of the phase diagram. The precipitation of NbC must deplete the solute concentration in the matrix. The locus of the matrix composition at any instant is along the direction **a** $\rightarrow$ **d** (Fig. 6.2). Any change in the matrix composition also leads to a different choice of tie–line, the locus of $c^{\gamma\omega}$ being along **b** $\rightarrow$ **d** (Fig. 6.2). This tie–line shifting continues until the reaction stops when the tie–line intersects the average composition **a** and $c^{\gamma\omega} =$ **d**.

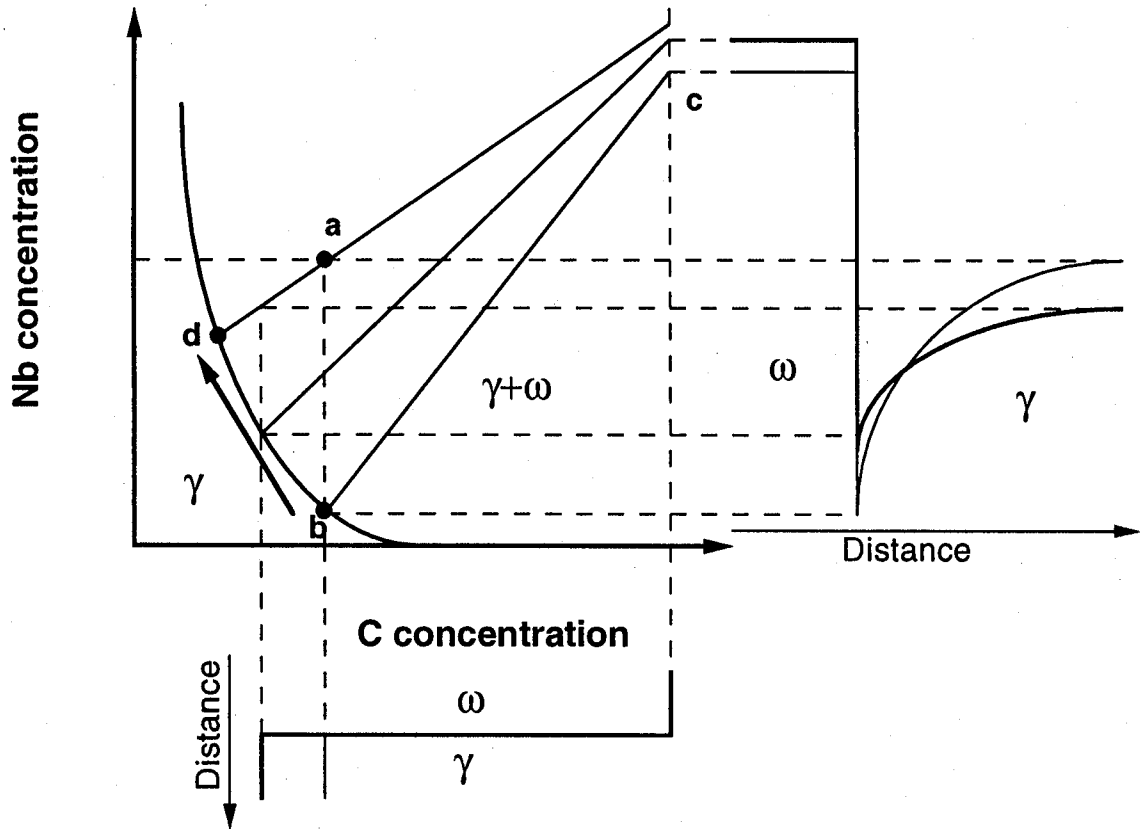

Fig. 6.2: An illustration of an isothermal section through the Fe–Nb–C phase diagram, showing the austenite (γ) and NbC (ω) phase fields. The alloy composition is plotted as point **a**.

The NbC precipitates are assumed to adopt spherical shapes. With diffusion–controlled growth, the growth of spherical particles should be parabolic with time as described in Chapter 2. For low supersaturations, the change of particle radius r with time is given approximately by (Christian, 1975):

$$r = \alpha_3 \sqrt{Dt} \quad \text{with} \quad \alpha_3 \simeq \sqrt{2 \frac{\overline{c} - c^{\gamma\omega}}{c^{\omega\gamma} - \overline{c}}} \tag{6.3}$$

where α_3 is called the three–dimensional parabolic rate constant.

The state of equilibrium between two phases changes with the curvature of the interface

separating them according to the well–established *capillarity effect*, which scales with the interfacial energy.

The free energy of a carbide phase varies relatively sharply with deviations from the stoichiometric composition so it can be assumed that the carbide composition is not sensitive to the interface curvature. However, the equilibrium composition of the matrix changes as follows (Christian, 1975, p. 181):

$$c_r^{\gamma\omega} = \left(1 + \frac{\sigma}{kT}\frac{2v^{\omega}}{r}\frac{1 - c^{\gamma\omega}}{c^{\omega\gamma} - c^{\gamma\omega}}\right)c^{\gamma\omega} \tag{6.4}$$

where $c_r^{\gamma\omega}$ is the solute concentration at the interface between NbC and the matrix γ, r is the radius of curvature at the particle tip but which, for spherical particles, may correspond to particle radius, v^{ω} is the molar volume of the ω phase. $c^{\gamma\omega}$ is now the solute concentration in the matrix γ which is in equilibrium with the precipitation ω when $r = \infty$. The modified composition $c_r^{\gamma\omega}$ is therefore easy to estimate for each solute. The method used here to account for the capillarity effect in a ternary alloy involves the calculations of the $\gamma/\gamma{+}\omega$ boundary on the isothermal section of the phase diagram, as a function of the particle radius r of the interface. Equation 6.4 is used to calculate $c_r^{\gamma\omega}$ with a value of the particle radius for each particle. The growth velocity can then be calculated using the curvature–modified phase boundary (Fig. 6.3).

Particles which are smaller than the size of a critical nucleus obviously cannot grow. Nucleation occurs by random fluctuations so that the growth part in the computational scheme must start beyond the nucleation stage. NbC precipitation leads to a depletion of solute in the matrix so that the mean concentration of solute at any instance $\overline{c}'$ must decrease as precipitation reactions progress. This is soft–impingement which is treated using the mean field approximation and then $\overline{c}'$ is given by:

$$\overline{c}' = \overline{c} - \frac{V_{\omega}(c^{\omega\gamma} - \overline{c})}{1 - V_{\omega}} \tag{6.5}$$

where V_{ω} is the volume fraction of the ω phase and $\overline{c}$ is alloy composition.

Particles nucleate at different times during the course of reaction, giving rise to a distribution of sizes. At any given stage of precipitation the small particles will grow at a smaller rate than a big particle because of the capillarity effect which reduces the supersaturation for small particles. The condition that particles nucleated can grow is given by :

$$(\overline{c}' - c_r^{\gamma\omega}) > 0 \tag{6.6}$$

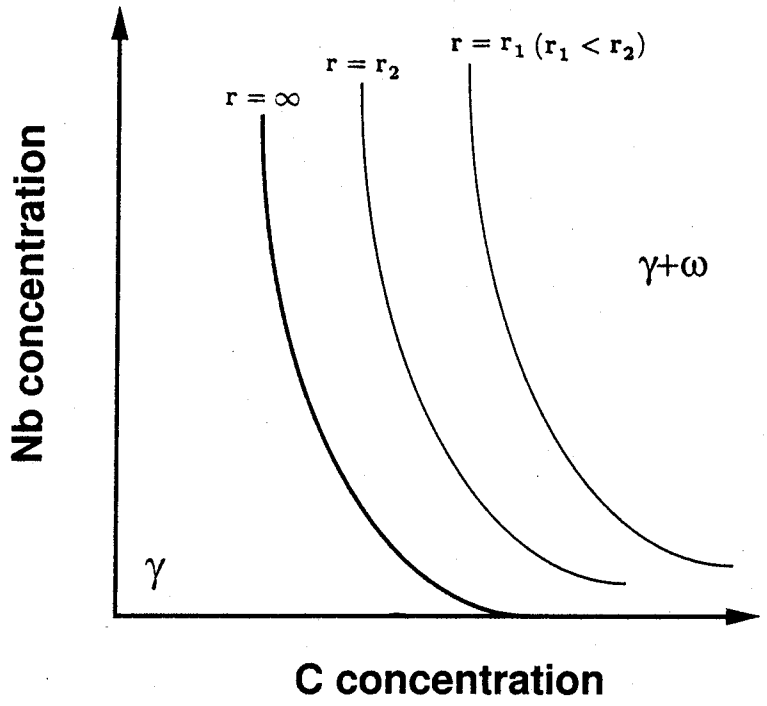

Fig. 6.3 : An illustration of the way the $\gamma/\gamma+\omega$ phase boundary changes for a variety of values of the radius of curvature r at the interface by Gibbs–Thomson effect for precipitation ω from γ.

The effect of soft–impingement in the mean field approximation may also be expressed approximately in terms of an extent of reaction parameter with the dimensionless supersaturation

$$\Phi_\omega = \frac{V'}{V^{Max}} \qquad \text{with} \qquad V^{Max} = \frac{\overline{c} - c^{\gamma\omega}}{c^{\omega\gamma} - c^{\gamma\omega}} \tag{6.7}$$

where V' is the instantaneous fraction and V^{Max} the maximum fraction of a given phase. The function Φ_ω ranges from 0 to 1 and represents the fraction of excess solute remaining in the matrix relative to the equilibrium composition of the precipitate. It is assumed that the driving force for precipitation is related linearly to Φ_ω:

$$\Delta G_\omega = (1 - \Phi_\omega)\Delta G_{0\omega} \tag{6.8}$$

where $\Delta G_{0\omega}$ is the driving force available before any precipitation of ω phase.

When the situation almost reaches equilibrium, big particles may have higher solute concentrations at the interface $c_r^{\gamma\omega}$ than the mean solute concentration in matrix $\overline{c}'$ while small particles may have lower solute concentrations than $\overline{c}'$. This in turn gives coarsening as a natural consequence of the precipitation theory.

6.3 Thermodynamic calculations for NbC in Fe–Nb–C system

The driving force for nucleation and the NbC/γ phase boundary in Fe–0.05Nb–0.1C wt% steel were calculated using MTDATA, which accesses internationally assessed thermodynamic data (Hodson, 1989).

6.3.1 Driving force for nucleation

Niobium carbide in austenite will form according to the following reaction:

$$\gamma \rightarrow \gamma' + NbC \tag{6.9}$$

where γ' represents the austenite coexisting with NbC. The free energy for the reaction ΔG_0 was calculated using MTDATA and Fig. 6.4 shows the calculations at elevated temperatures.

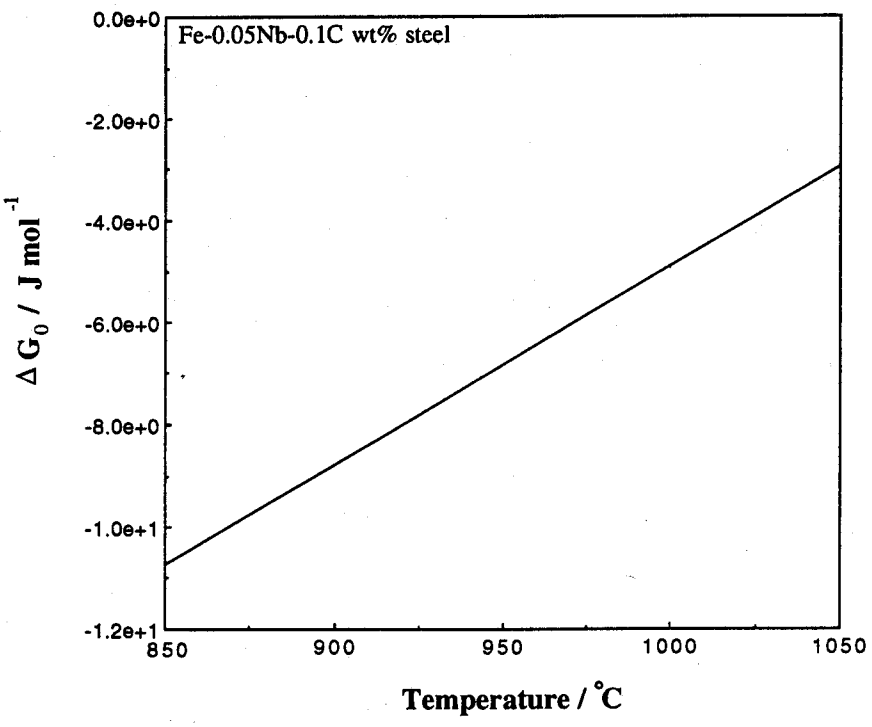

Fig. 6.4: The free energy change for the precipitation reaction of NbC in austenite with temperature for Fe–0.05Nb–0.1C wt% steel calculated using MTDATA.

The free energy change increases as temperature increases. With these results, the driving force for nucleation ΔG_n has been obtained as for M_2C (Chapter 5).

$$\Delta G_n = \frac{\Delta G_0}{V_\omega^{eq} v^\omega} \tag{6.10}$$

where V_ω^{eq} is equilibrium volume fraction of ω phase and v^ω is the molar volume of ω.

6.3.2 Equilibrium concentration and capillarity effect

The equilibrium concentrations for Fe–0.05Nb–0.1C wt% steel were calculated using MTDATA (Fig. 6.5). The concentration $c_{Nb}^{\gamma\omega}$ increases as temperature increases. Fig. 6.6 shows the γ/ω phase boundary in an isothermal section of the phase diagram for 900 °C with an illustration of the influence of capillarity.

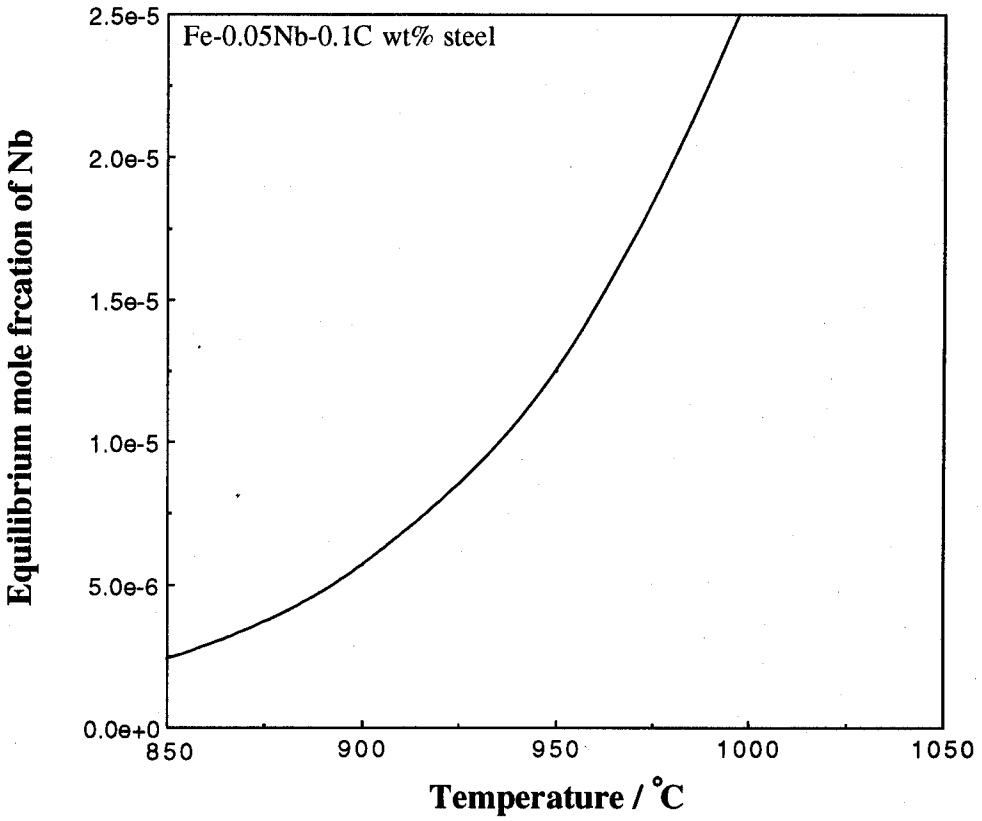

Fig. 6.5: Niobium concentration in austenite which is in equilibrium with NbC, calculated using MTDATA, as a function of temperature for Fe–0.05Nb–0.1C wt% steel.

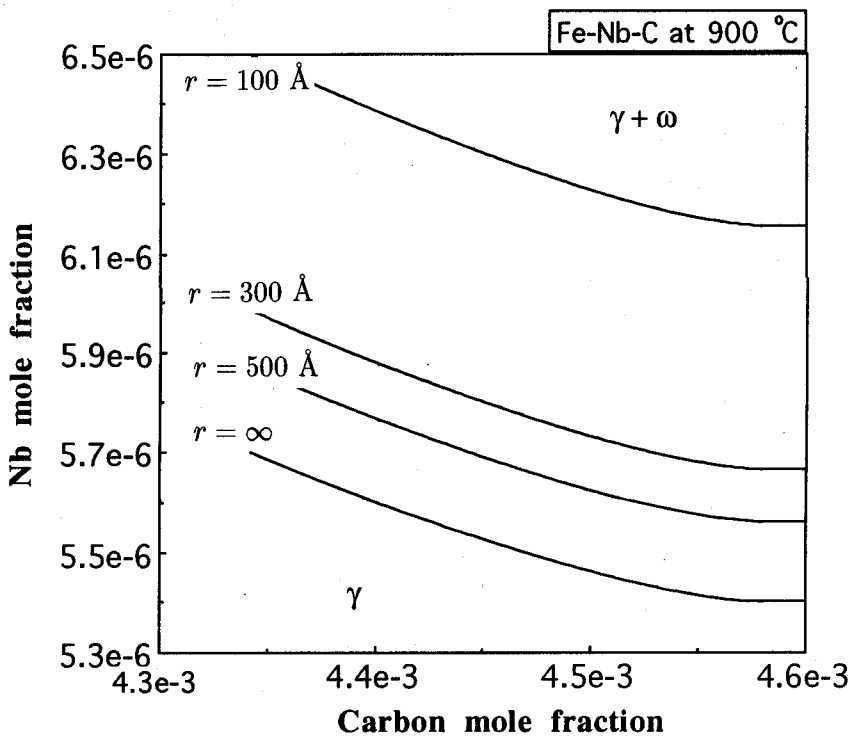

Fig. 6.6: The γ/ω phase boundaries in an isothermal section of the phase diagram for 900 °C with an illustration of the influence of capillarity when the interfacial energy is constant: $\sigma = 0.25$ J m^{-2}.

6.4 Calculations for NbC precipitation in a multicomponent framework

Calculations were carried out for a Fe–0.05Nb–0.1C wt% steel, a typical composition for a high strength low alloy steel, using the model described earlier.

Table 6.1 shows the values of the diffusion coefficient and activation energy for diffusion of Nb used for all calculations, which are from Metals Data Book issued by The Japan Institute of Metals (1993).

D_0 in diffusion coefficient of Nb	0.56 $\times 10^{-4}$ $m^2 s^{-1}$
Activation energy for diffusion of Nb	286 $\times 10^3$ J mol^{-1}

Table 6.1: D_0 in diffusion coefficient and activation energy for diffusion of Nb in austenite used in the calculations for Fe–0.05Nb–0.1C wt% steel (from Metals Data Book, (1993).

Effect of the initial site density and the interfacial energy

There are only two unknown parameters, the number density of nucleation sites for NbC N_{0_ω} and the precipitate/matrix interfacial energy per unit area σ. Fig. 6.7 shows the changes of volume fraction, the mean and maximum particle radius with N_{0_ω} and σ for 900 °C. As expected, smaller values of N_{0_ω} reduce the overall rate of reaction but lead to bigger particle radii. A smaller interfacial energy facilitates the reactions so that the equilibrium is achieved earlier.

Fig. 6.8 shows how the particle radius and volume fraction changes with time at 900 °C using reasonable values of $N_{0_\omega} = 10^{19}$ m^{-3} and σ= 0.25 J m^{-2}. The big particle, which nucleated in the early stages of precipitation, grows continuously even as the volume fraction approaches equilibrium. However, because of the capillarity effect, the small particle which nucleated late begins to dissolve even though the big one continues to grow.

Fig. 6.9 shows similar data for 850 °C and 950 °C.

Effect of Mn and Si

Mn and Si are common alloying elements in steels. Their thermodynamic effect on NbC precipitation can be investigated using the model presented here. Fig. 6.10 shows the effect of Mn and Si on the free energy change accompanying the formation of NbC from austenite and a concentration of in the matrix Nb $c_{Nb}^{\gamma\omega}$ which is in equilibrium with austenite at 900 °C.

Mn is predicted not to significantly affect either the free energy change or $c_{Nb}^{\gamma\omega}$. Although Si has an effect on both, the changes are not large. Fig. 6.11 shows the changes of volume fraction and particle sizes of NbC at 900 °C with N_{0_ω}=10^{19} m^{-3} and σ=0.25 J m^{-2} for Fe–0.05Nb–0.1C wt% and Fe–1Si–0.05Nb–0.1C wt% steels. There are only minor differences which might be neglected for all practical purposes.

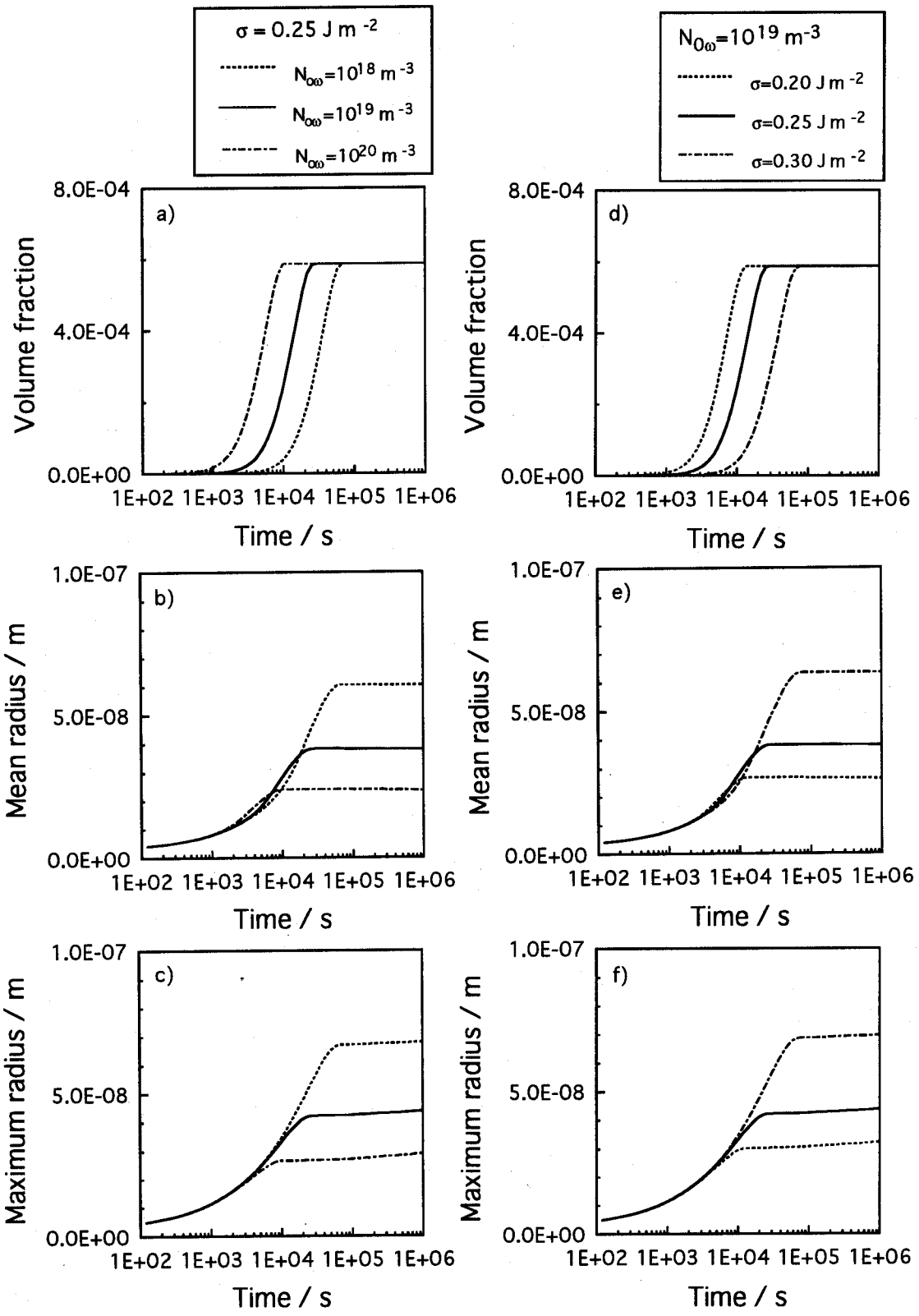

Fig. 6.7: Effect of the number density of nucleation sites $N_{0\omega}$: a)–c) and of the interfacial energy σ: d)–f) on the volume fraction and sizes of NbC precipitates in austenite. The equilibrium fraction of NbC at 900 °C is 0.00059.

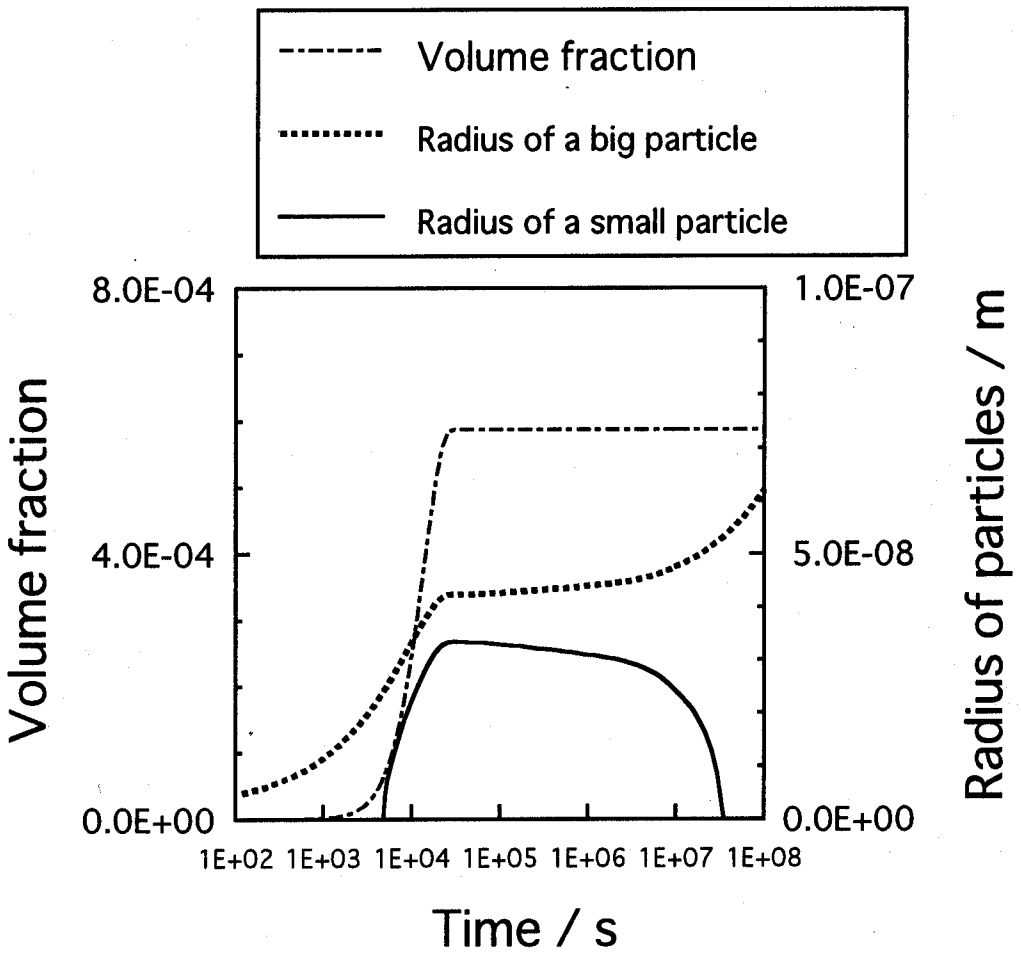

Fig. 6.8: Calculated data on the volume fraction and particle radius changes for NbC at 900 °C with $N_{0\omega}$=10 ^{19} m $^{-3}$ and σ=0.25 J m^{-2}.

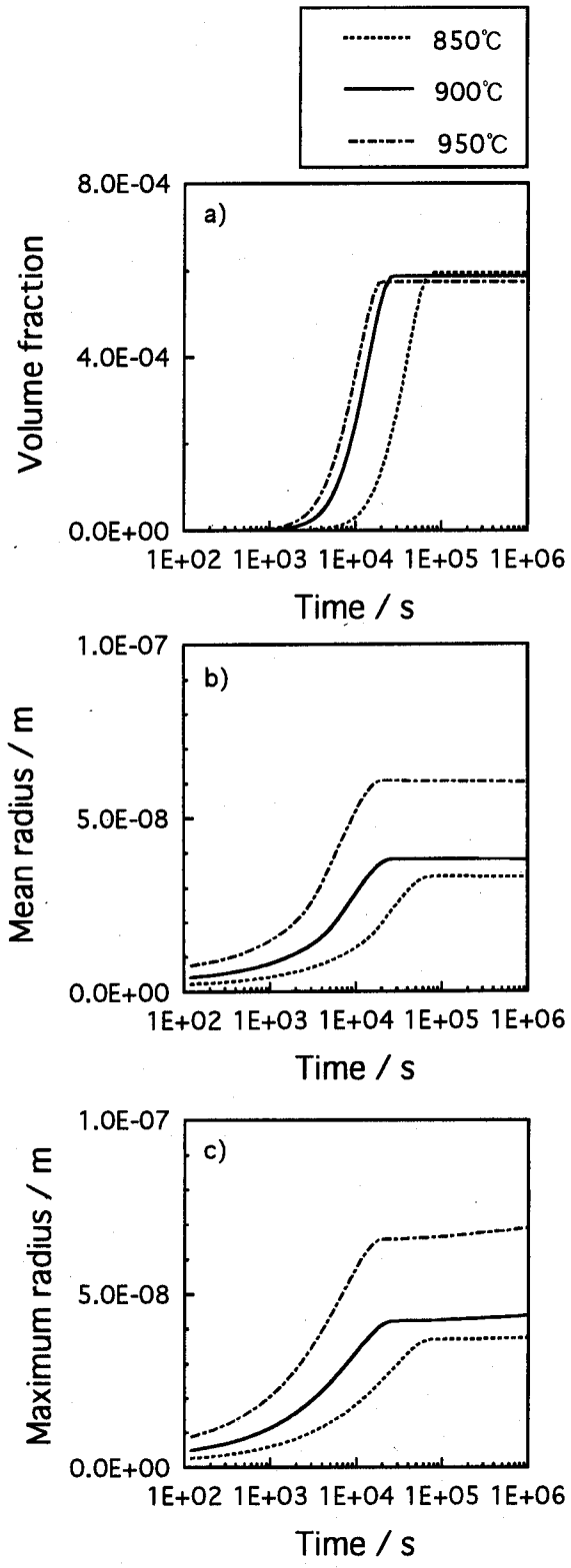

Fig. 6.9: The volume fraction and particle radii for NbC at 850 °C, 900 °C and 950 °C with $N_{0\omega}$=10 ^{19} m $^{-3}$ and σ=0.25 J m^{-2} as a function of time. The equilibrium fractions of NbC at 850 °C, 900 °C and 950 °C are 0.00059, 0.00059 and 0.00058 respectively.

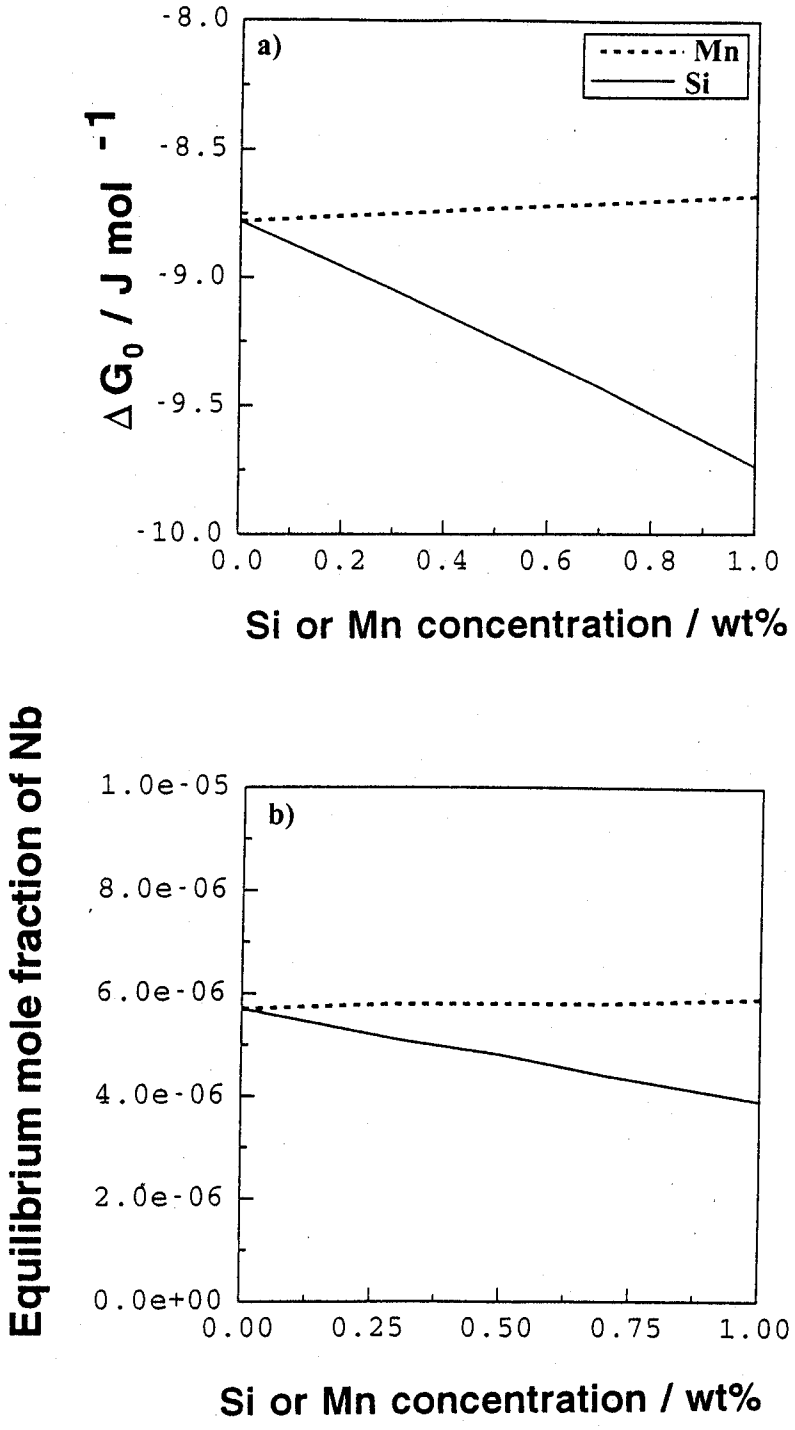

Fig. 6.10: Effect of Mn and Si (a) on the free energy change ΔG_0 for the precipitation of NbC from austenite and (b) on the equilibrium mole fraction of Nb in the matrix for Fe–0.05Nb–0.1C wt% steel at 900 °C.

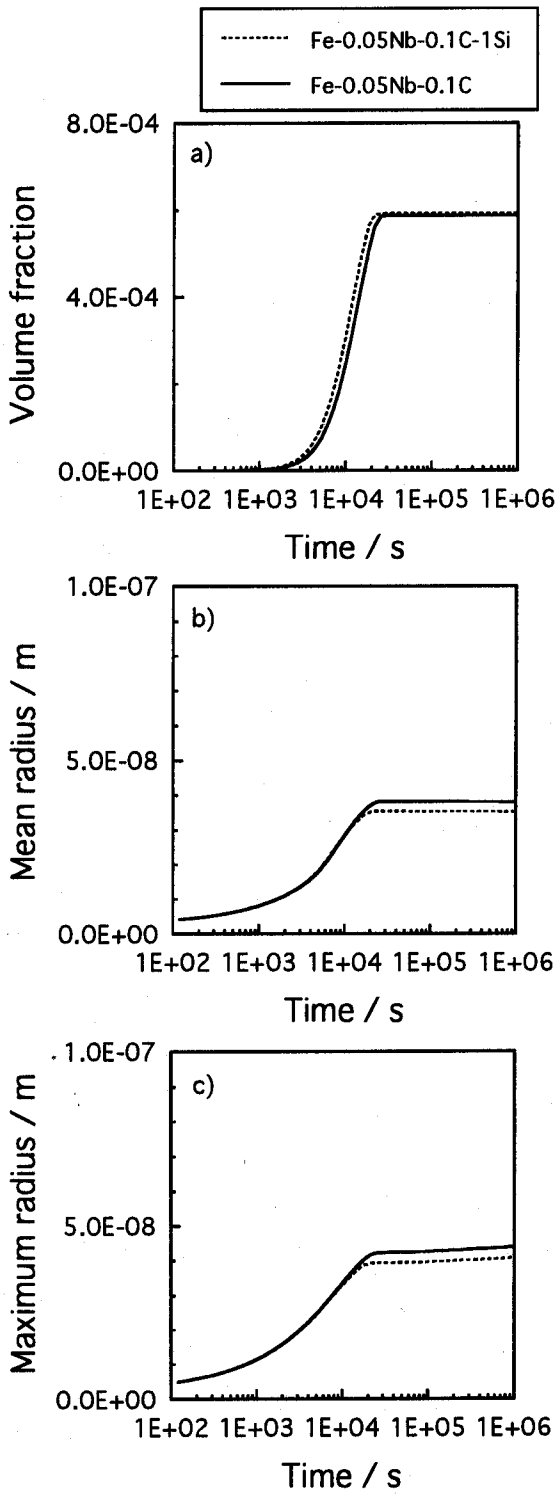

Fig. 6.11: The particle radii and volume fractions as a function of time at 900 °C in Fe–0.05Nb–0.1C wt% and Fe–1Si–0.05Nb–0.1C wt% steels.

From nucleation to coarsening

Fig. 6.12 shows the changes of the mean radius and number density of NbC at 900 °C in the austenite for Fe–0.05Nb–0.1C wt% steel. On approaching the equilibrium volume fraction, the mean radius changes very slowly indeed because coarsening is driven only by interfacial energy. This general behaviour has also been reported for a Cu-Ti alloy (Wagner and Kampmann, 1991). It was found that just before the number density started to decrease, the mean radius also decreased slightly. It is interesting and expected (Lifshitz and Slyozov, 1961) that as soon as coarsening properly sets in, the mean particle radius tends to change in proportion to $t^{\frac{1}{3}}$. This is described as Ostwald ripening.

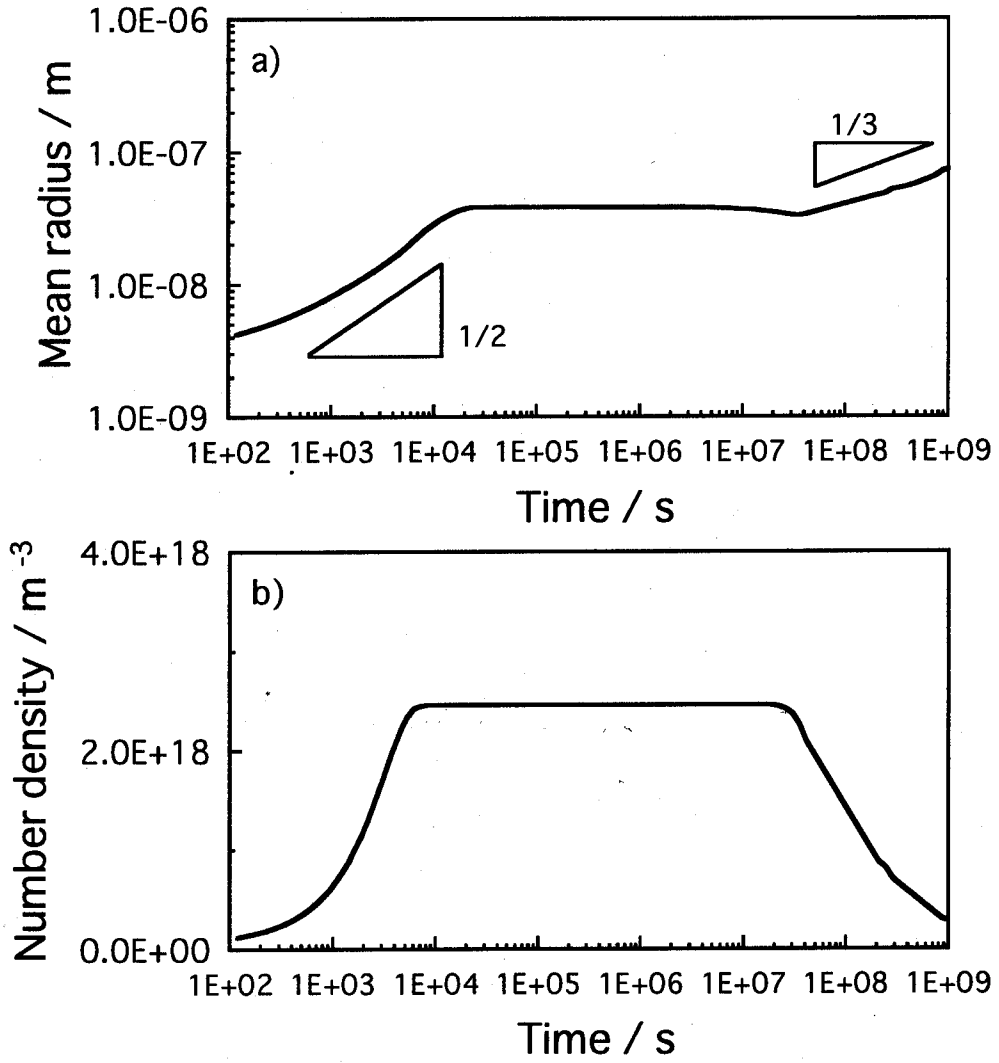

Fig. 6.12: The particle radius (a) and the number density (b) of NbC precipitates as a function of time at 900 °C in Fe–0.05Nb–0.1C wt% steel with $N_{0\omega}$=9×10 ^{19} m^{-3} and σ=0.26 J m^{-2}.

There is a small difficulty with the computation procedure associated with two calculations presented in Fig. 6.12 which cover all the stage of precipitation process, even though the time scales allowed in the coarsening stage are much longer than in the precipitation stage. The calculations require small time steps for numerical accuracy but this eventually leads to enormous computational times because of the relatively slow coarsening process. The consequent numerical error leads to a slight decrease in the mean radius prior to the onset of coarsening properly. It has been checked that this error increases as the time step is increased.

Comparison of NbC particle size between calculations and experiments

Although there are significant data about the precipitation of NbC during the hot deformation of austenite in micro–alloyed steels, similar data for isothermal heat treatment are difficult to find. Akamatsu *et al.* investigated NbC precipitation in Nb added micro–alloyed steels (1989). With their observations using transmission electron microscopy of samples isothermally heat treated at 900 °C in a Fe–0.045Nb–0.11C–0.26Si–1.1Mn wt% steel, they were able to estimate the NbC particle size as a function of time. These data are available for the early stages (less than holding time of 10^5 s) which eventually represent precipitation rather than coarsening. Calculations were done using an interfacial energy $\sigma = 0.26$ J m^{-2} and a fitted number density of nucleation sites $N_{0_\omega} = 9 \times 10^{19}$ m^{-3} as shown in Fig. 6.13. The particle size has error bars which correspond to two standard deviations. There is good agreement between theory and experiments.

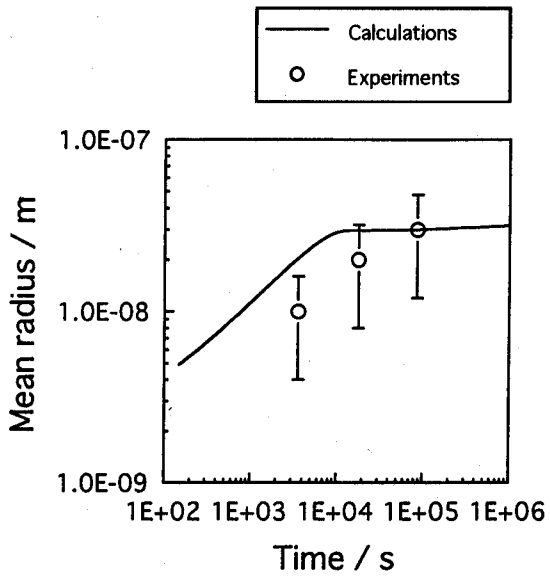

Fig. 6.13: A comparison between calculations and experimental data (Akamatsu *et al.*, 1989) for NbC particle growth with holding time at 900 °C in a Fe–0.045Nb–0.11C–0.26Si–1.1Mn wt% steel.

6.5 Summary

A methodology has been developed to deal with the growth of spherical precipitates, in this case, niobium carbide in a ternary alloy, properly taking into account mass balance during diffusion–controlled growth whilst at the same time dealing with capillarity effects and nucleation site consumption. The model has been able to simulate the whole of precipitation process including coarsening and the prediction was in good agreement with the published experimental data.

It is worth noting that the present work can be applied directly to strain–induced precipitation of NbC if the change in the number density of nucleation sites due to plastic strain is known explicitly, and assuming that the defect structure does not contribute to facilitating diffusion. Similarly, the effects of the dynamic recovery of deformation defects can in principle be incorporated via a time dependent nucleation site number density function, for example, of the kind used by Akamatsu *et al.* (1989).

CHAPTER SEVEN

Modelling simultaneous alloy carbide sequence

7.1 Introduction

It has been demonstrated that the models introduced in Chapters 5 and 6 can estimate changes in volume fractions and particle sizes of equilibrium alloy carbides in ternary steels whilst taking into account multicomponent diffusion and capillarity effects. Most practical steels contain many kinds of solutes and carbide phases, some of which are metastable, *i. e.*, not equilibrium phases.

The work presented here deals with multiple alloy carbide precipitation reactions in which the precipitates may be in the form of needles or spheres. The resulting calculations are tested against some critical new experimental data on 3Cr1.5Mo and $2\frac{1}{4}$Cr1Mo steels.

7.2 Modelling of multiple precipitation reactions

Some parts of the Robson and Bhadeshia model (1997a), *i. e.* cementite precipitation, classical nucleation and the mean field approximation, are still valid but the fitting parameters must clearly change because of the new physical principles in the modified theory. Other parts of the nucleation and growth theory for needle and sphere are dealt with as in Chapters 5 and 6 respectively. Table 7.1 summarised treatments for each carbide in 3Cr1.5Mo and $2\frac{1}{4}$Cr1Mo steels, which has been already investigated to be M_3C, M_2C, M_7C_3 and $M_{23}C_6$ in Chapter 4.

There is one part which has not yet been described. That is metastable alloy carbide dissolution. It will dissolve naturally when the mean solute concentration become below the equilibrium solute concentration of its carbide in the matrix, although Robson and Bhadeshia used the mean distance between particles. Fig. 7.1 shows schematic concentration profiles in which β is dissolving and γ is precipitating. Zener's linearised approximation was used for the gradient of solute concentration in the vicinity of the interface between precipitate and matrix.

7.3 Thermodynamic calculations for alloy carbides in power plant steels

Using MTDATA (Hodson, 1989), the driving forces for each alloy carbide and the relevant

Precipitates	Nucleation and growth condition
M_3C	Paraequilibrium cementite, the number density of cementite as a function of carbon concentration and enrichment of solute
M_2X	Finite nucleation rate and diffusion–controlled linear growth of needles with capillarity effect in a multicomponent system
M_7C_3 $M_{23}C_6$	Finite nucleation rate and diffusion–controlled parabolic growth of spheroids with capillarity effect in a multicomponent system

Table 7.1: The calculation conditions of isothermal precipitation of 3Cr1.5Mo and $2\frac{1}{4}$Cr1Mo steels.

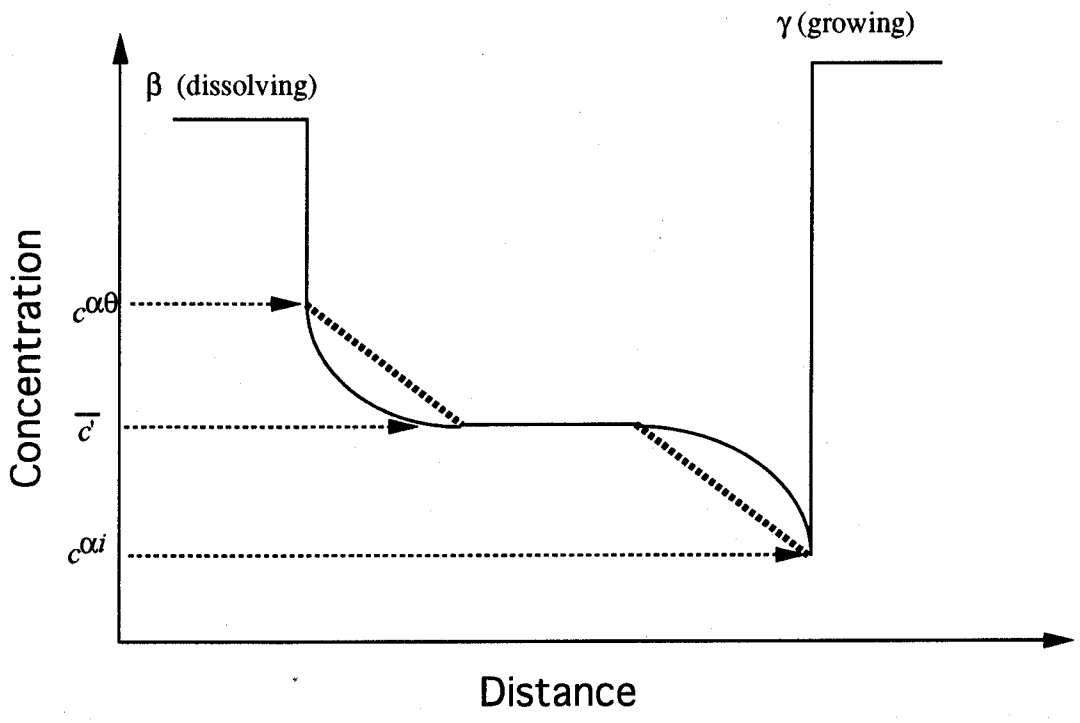

Fig. 7.1: A schematic illustration of solute concentration profile in which β is dissolving and γ is precipitating. The bold dotted lines are used here.

phase boundaries for 3Cr1.5Mo and $2\frac{1}{4}$Cr1.5Mo steels were calculated. The carbide reactions can be described as follows (Chapter 4), although in principle, all reactions start at $t = 0$ but occur at different rates:

3Cr1.5Mo: $M_3C \rightarrow M_3C+M_7C_3 \rightarrow M_3C+M_7C_3+M_2C+M_{23}C_6 \rightarrow M_7C_3+M_2C+M_{23}C_6$

$2\frac{1}{4}$Cr1Mo: $M_3C \rightarrow M_3C+M_2C \rightarrow M_3C+M_7C_3+M_2C \rightarrow M_3C+M_7C_3+M_2C+M_{23}C_6$

Since all reaction start at the beginning of tempering, the driving forces must at first be described to the initial microstructure with paraequilibrium cementite M_3C_{para}.

$$\alpha + M_3C_{para} \rightarrow \alpha' + M_2C \qquad (7.1a)$$

$$\alpha + M_3C_{para} \rightarrow \alpha'' + M_7C_3 \qquad (7.1b)$$

$$\alpha + M_3C_{para} \rightarrow \alpha''' + M_{23}C_6 \qquad (7.1c)$$

where α', α'' and α''' represent the ferrite coexisting with M_2C, M_7C_3 and $M_{23}C_6$ respectively. Fig. 7.2 shows the calculation results of ΔG_0 as a function of temperature for each reaction. The driving force per volume of precipitate can be obtained by dividing the free energy for each reaction by the equilibrium volume fraction of the precipitation as in Chapter 2.

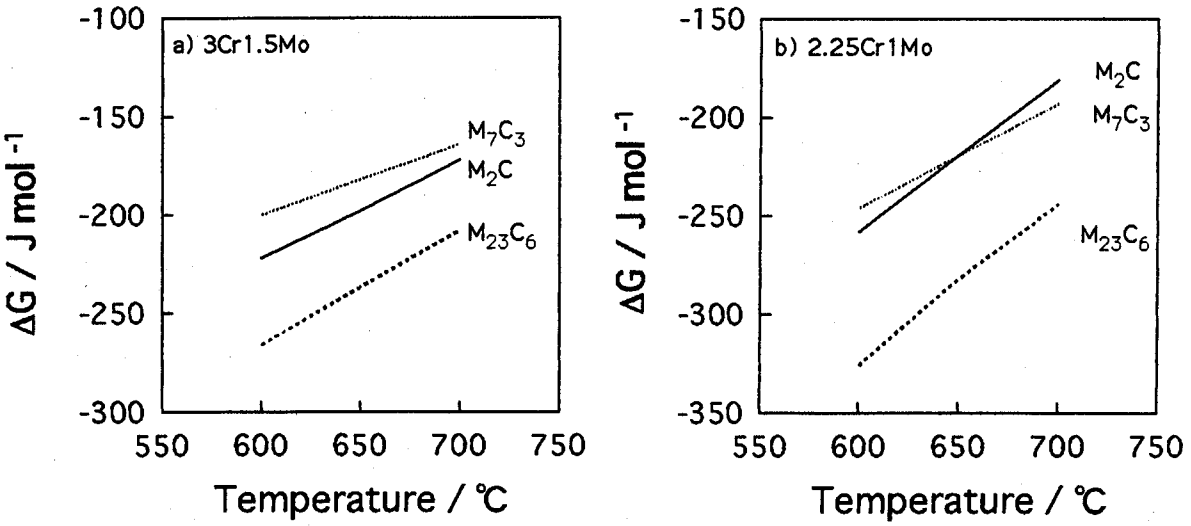

Fig. 7.2: The free energy changes at elevated temperatures for each carbide precipitation reaction in (a) 3Cr1.5Mo and (b) $2\frac{1}{4}$Cr1Mo steels calculated using MTDATA.

All of the alloy carbides contain certain amount of chromium so it is assumed that growth is controlled by its diffusion in a multicomponent system. Fig. 7.3 shows the changes of the Cr equilibrium concentration in matrix α with each carbide at the interface with temperature.

7.4 Particle size measurements

Using transmission electron microscopy (TEM) with carbon extraction replicas, the sizes of M_2C/needles, M_7C_3 and $M_{23}C_6$/spheres in $2\frac{1}{4}$Cr1Mo and 3Cr1.5Mo steels were measured directly. Because each alloy carbide precipitates at a different rate, the specific conditions of the samples used for the measurements are described in Table 7.2.

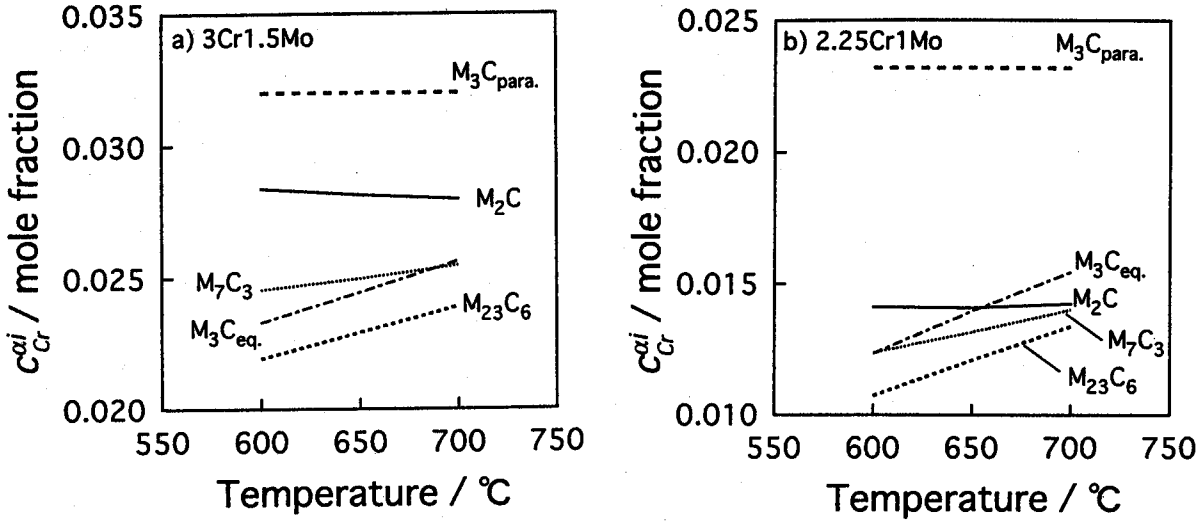

Fig. 7.3: The equilibrium concentration of Cr in α $c_{Cr}^{\alpha i}$ at elevated temperatures calculated using MTDATA for (a) 3Cr1.5Mo and (b) $2\frac{1}{4}$Cr1Mo steels. $M_3C_{para.}$ and $M_3C_{eq.}$ are cementite with paraequilibrium and equilibrium respectively.

Type of carbide	Steels	Measurement conditions
M_2C	3Cr1.5Mo	600 °C at 10, 50, 100, 200 h
		650 °C at 10 and 100 h
	$2\frac{1}{4}$Cr1Mo	600 °C at 10, 100 and 1000 h
		650 °C at 10 and 100 h
M_7C_3	3Cr1.5Mo	600 °C at 10, 100, 200 h
		650 °C at 10 and 100 h
	$2\frac{1}{4}$Cr1Mo	650 °C at 10 and 100 h
$M_{23}C_6$	3Cr1.5Mo	700 °C at 10 and 100 h

Table 7.2: Conditions describing the size measurements for each alloy carbide in 3Cr1.5Mo and $2\frac{1}{4}$Cr1Mo steels

7.5 Morphology of alloy carbides

Fig. 7.4 shows transmission electron micrographs of specimens tempered for 100 h or 200 h at a variety of temperatures for both steels. Apart from the specimens tempered at 700 °C, the micrographs predominantly show needle–shaped precipitates within the martensite laths. Small and blocky spherical precipitates can be found on the lath boundaries. Tempering at 700 °C, however, leads mainly to blocky precipitates with few needles.

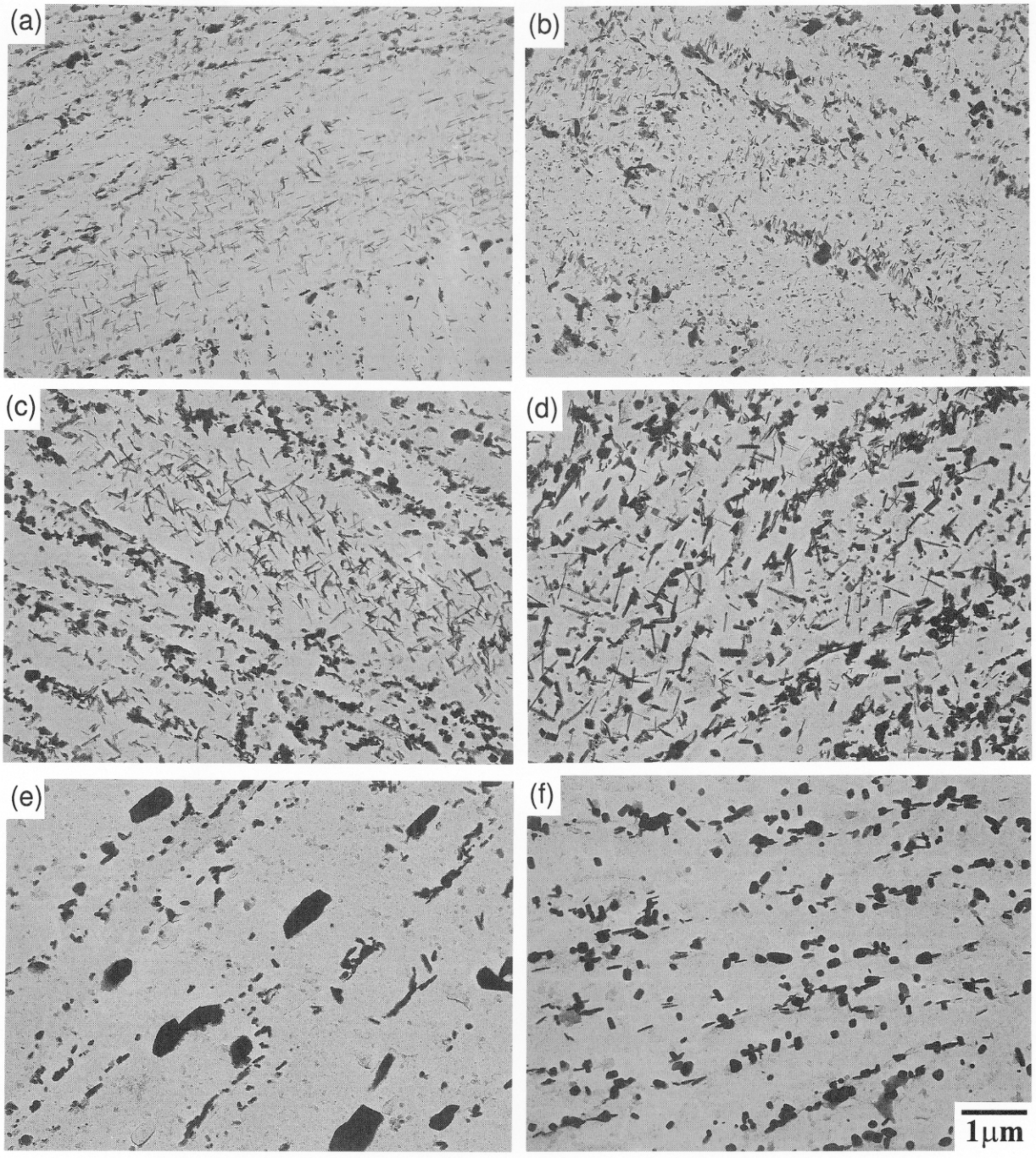

Figure 7.4: Transmission electron micrographs for (a) 3Cr1.5Mo and (b) $2\frac{1}{4}$Cr1Mo tempered at 600 °C for 200 h, (c) 3Cr1.5Mo and (d) $2\frac{1}{4}$Cr1Mo tempered at 650 °C for 100 h, (e) 3Cr1.5Mo and (f) $2\frac{1}{4}$Cr1Mo tempered at 700 °C for 100 h.

7.6 Particle size change

M_2C could easily be identified from its needle shape and using diffraction (Fig. 7.5). Fig. 7.6 shows how its size increases during tempering at 600 °C.

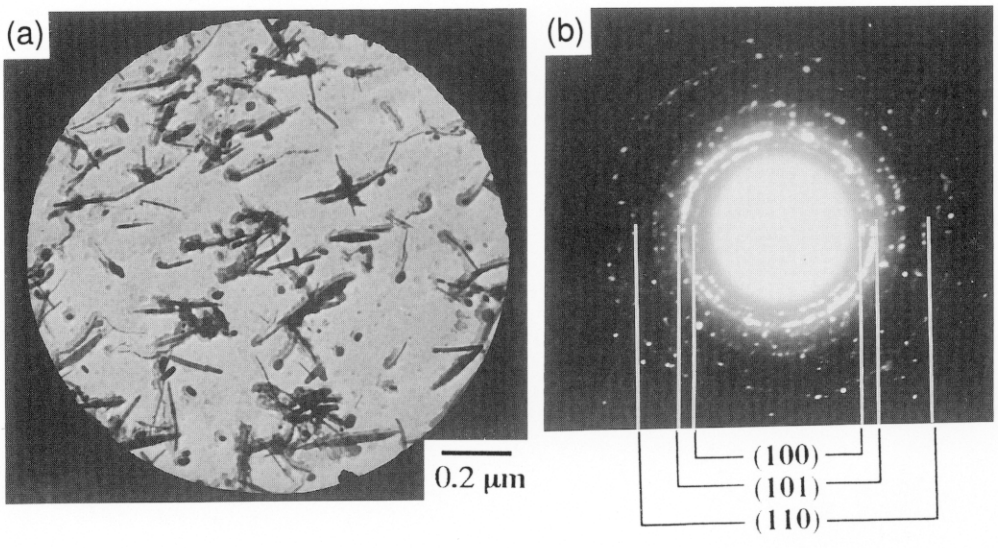

Figure 7.5: Extraction replica transmission electron micrographs of 3Cr1.5Mo steel tempered at 600 °C for 100 h, (a) Image of M_2C needles and (b) electron diffraction pattern from many M_2C particles.

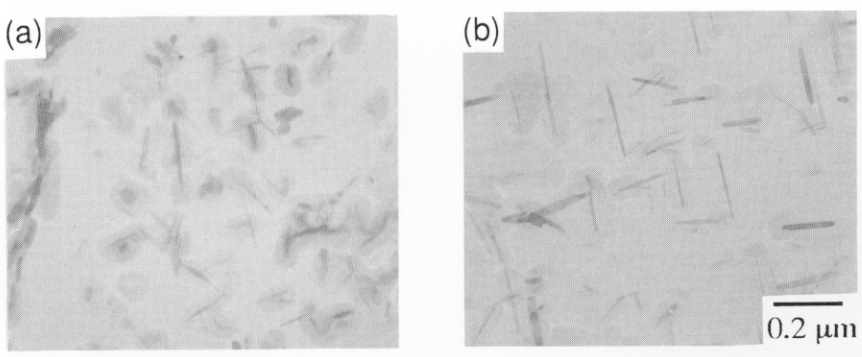

Figure 7.6: Extraction replica transmission electron micrographs of M_2C in 3Cr1.5Mo steel tempered at 600 °C for (a) 50 h and (b) 200 h.

M_7C_3 occurred as blocky almost spherical particles on the lath boundaries as shown in Fig. 7.7. The shape of M_7C_3 can be assumed as sphere. As already indicated by Beech *et al.* (1966), M_7C_3 particles often have a faulted structure so that streaks normal to the fault planes can be in its electron diffraction pattern. Fig. 7.8 shows how the M_7C_3 size evolves at 650 °C in $2\frac{1}{4}$Cr1Mo steel.

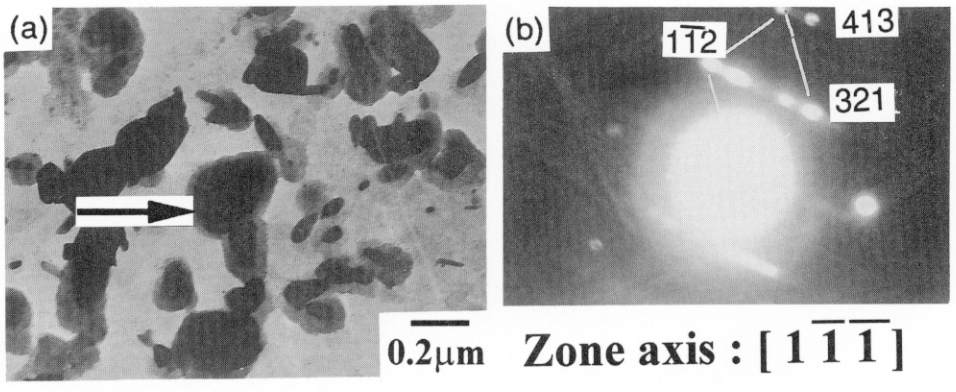

Figure 7.7: Extraction replica transmission electron micrographs of $2\frac{1}{4}$Cr1Mo steel tempered at 600 °C for 1000 h, (a) Image of M_7C_3 particles and (b) electron diffraction pattern from M_7C_3. The arrow in (a) indicates the particle from which the electron diffraction pattern was obtained. In the diffraction pattern, there were streaks characteristic of M_7C_3 (Beech *et al.*, 1966).

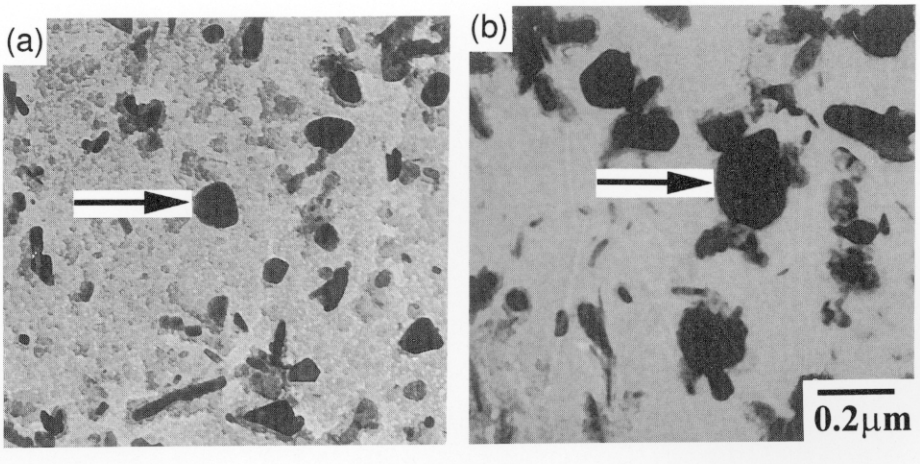

Figure 7.8: Extraction replica transmission electron micrographs of M_7C_3 in $2\frac{1}{4}$Cr1Mo steel tempered at 650 °C for (a) 10 h and (b) 100 h. Arrows indicate M_7C_3 particles.

$M_{23}C_6$ can also be found as a relatively sphere–like particle on the lath boundaries as shown in Fig. 7.9 with 3Cr1.5Mo steel tempered at 700 °C for 10 h. Fig. 7.10 shows $M_{23}C_6$ size change at 700 °C from 10 h to 100 h for 3Cr1.5Mo steel.

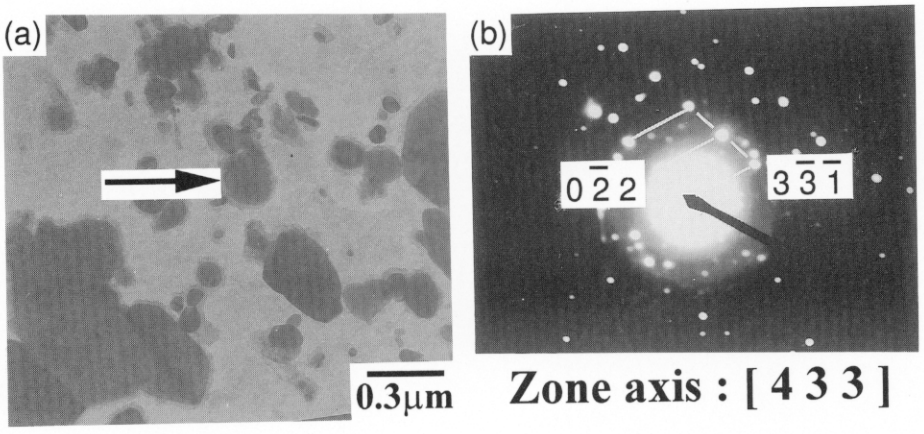

Figure 7.9: Extraction replica transmission electron micrographs of 3Cr1.5Mo steel tempered at 700 °C for 10 h, (a) Image of $M_{23}C_6$ particle and (b) electron diffraction pattern from $M_{23}C_6$. The arrow in (a) indicates the particle from which the electron diffraction pattern was obtained.

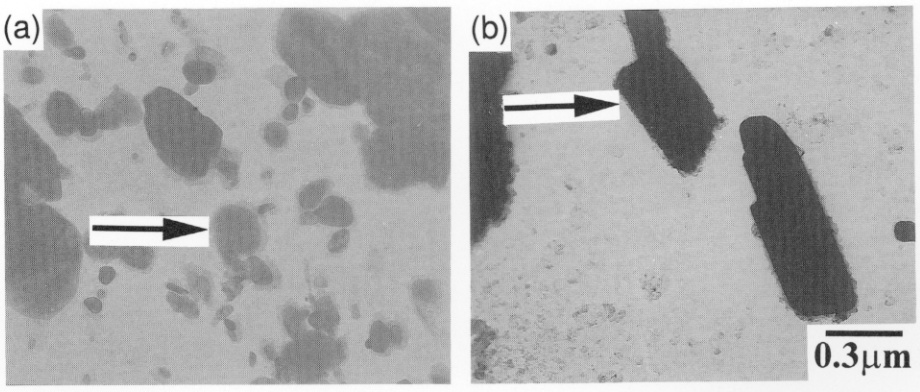

Figure 7.10: Extraction replica transmission electron micrographs of $M_{23}C_6$ in 3Cr1.5Mo steel tempered at 700 °C for (a) 10 h and (b) 100 h. Arrows indicate $M_{23}C_6$ particles.

7.7 Comparison between theory and experiments

7.7.1 Parameters

The measured microstructural parameters used in the new model are shown in Table 7.3 as well as fitting parameters. The diffusion coefficients listed by Fridberg *et al.* (1969) were used in the calculations. Table 7.4 shows a comparison of the assumptions in the original and the modified model.

The microstructural parameters	The values in use
Number density of sites for M_3C in 3Cr1.5Mo steel	1.23×10^{21} m^{-3}
Number density of sites for M_2C in 3Cr1.5Mo steel	6.15×10^{19} m^{-3}
Number density of sites for M_7C_3 in 3Cr1.5Mo steel	4.92×10^{19} m^{-3}
Number density of sites for $M_{23}C_6$ in 3Cr1.5Mo steel	9.84×10^{19} m^{-3}
Number density of sites for M_3C in $2\frac{1}{4}$Cr1Mo steel	2.35×10^{21} m^{-3}
Number density of sites for M_2C in $2\frac{1}{4}$Cr1Mo steel	1.41×10^{19} m^{-3}
Number density of sites for M_7C_3 in $2\frac{1}{4}$Cr1Mo steel	4.70×10^{19} m^{-3}
Number density of sites for $M_{23}C_6$ in $2\frac{1}{4}$Cr1Mo steel	4.70×10^{19} m^{-3}
Thickness of M_3C on lath boundaries for both steels	5.0×10^{-8} m
Thickness of M_3C within laths for both steels	2.0×10^{-8} m
Interfacial energy of M_2C	0.200 J m^{-2}
Interfacial energy of M_7C_3	0.256 J m^{-2}
Interfacial energy of $M_{23}C_6$	0.277 J m^{-2}
D_0 in diffusion coefficient for Cr	1.5×10^{-4} m^2 s^{-1}
Activation energy for both Cr and Mo diffusion	240×10^3 J mol^{-1}

Table 7.3: Parameter values used in the new model.

7.7.2 Volume fraction change

The calculations of volume fraction change for each carbide in both steels are shown in Fig. 7.11 along with the experimental observations. The new model correctly predicts the evolution of the carbide sequence.

Robson and Bhadeshia model	New model
- Based on Avrami theory	- Nucleation and growth but no treatment of impingement - Nucleation site consumption
- Using mean particle size	- Particle size distribution due to different nucleation times and growth rates
- Cr diffusion–controlled growth	- Diffusion–controlled growth in a multicomponent system
- No treatment of capillarity effect	- Capillarity effect in a multicomponent system

Table 7.4: Comparison of assumptions used in both models.

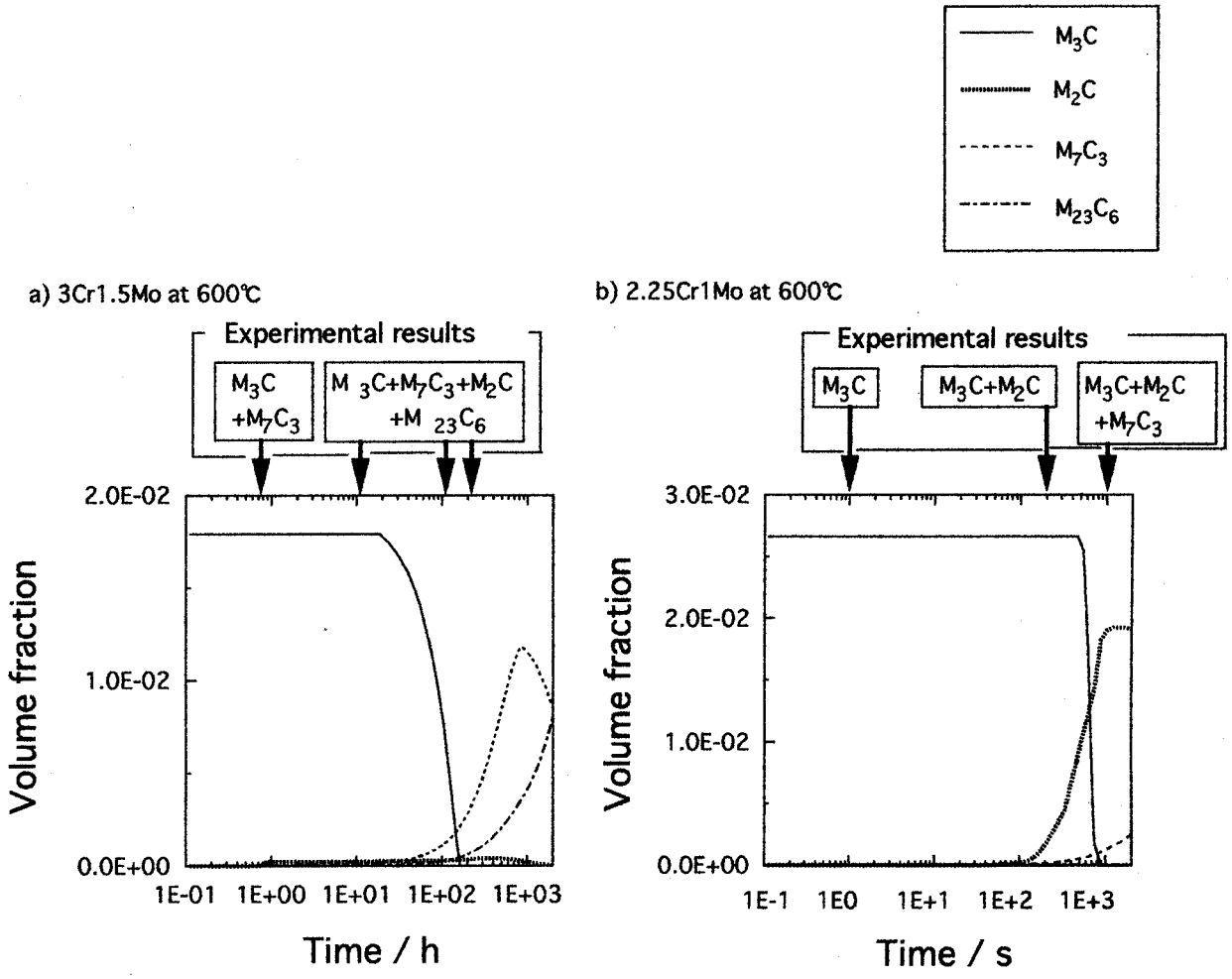

Figure 7.11: Calculations of multiple precipitation reactions for (a) 3Cr1.5Mo and (b) $2\frac{1}{4}$Cr1Mo steels at 600 °C using the new model for both steels.

7.7.3 Particle size change

Fig. 7.12 shows a comparison between experimental data (points) and theory (curves) of the maximum M_2C needle length. The calculations are reasonably consistent with experiments.

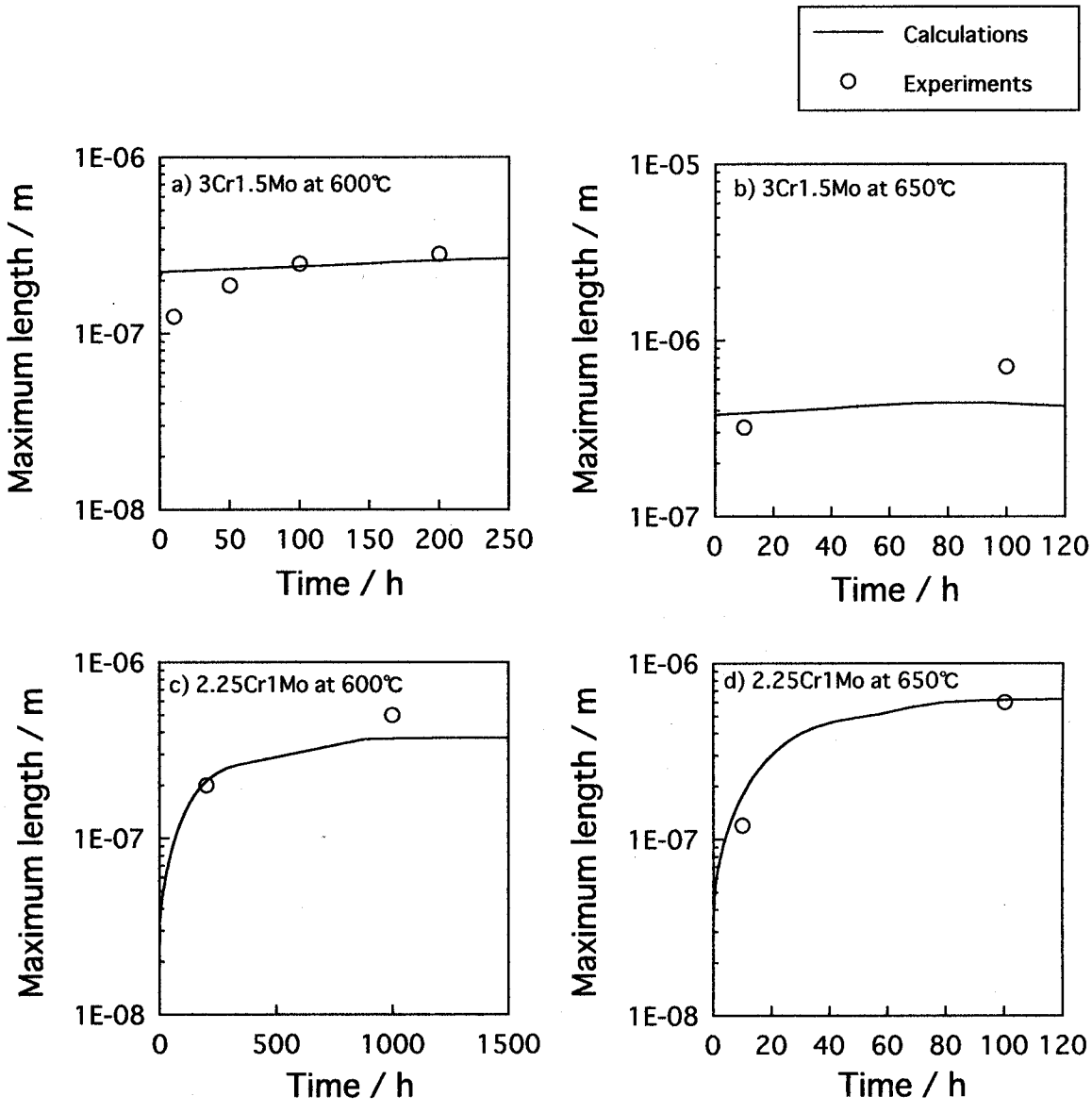

Figure 7.12: Comparison of the measured maximum needle length of M_2C versus calculations for 3Cr1.5Mo and $2\frac{1}{4}$Cr1Mo steels tempered at 600 °C and 650 °C.

Fig. 7.13 shows a comparison between experimental data (points) and theory (curves) of the mean M_7C_3 radius. The error bars on the experiments correspond to two standard deviations. Although there are detailed discrepancies, the results are reasonably consistent.

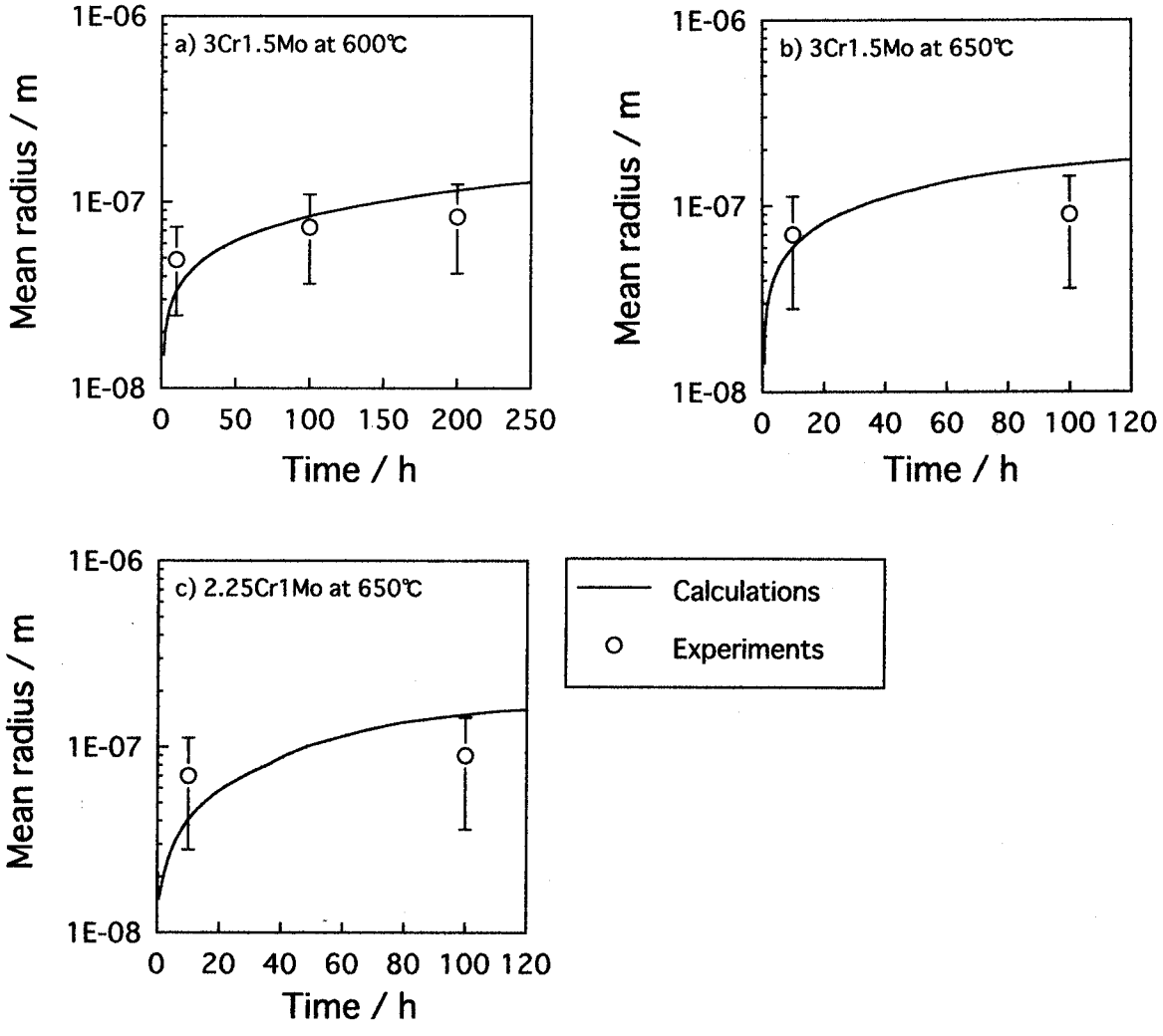

Figure 7.13: Comparison of the measured mean radius of M_7C_3 versus calculations for 3Cr1.5Mo and $2\frac{1}{4}$Cr1Mo steels tempered at 600 °C and 650 °C. The error bars correspond to two standard deviations.

Fig. 7.14 shows a comparison between experimental data (points) and theory (curves) of the mean $M_{23}C_6$ radius. The error bars on the experiments correspond to two standard deviations.

The results are reasonably consistent. $M_{23}C_6$ sometimes precipitates on grain boundaries and a collector–plate mechanism of diffusion may then dominate growth (Aaron and Aaronson, 1988). However, there are too many unknown parameters in the collector–plate model and hence this complexity has been neglected in the present work.

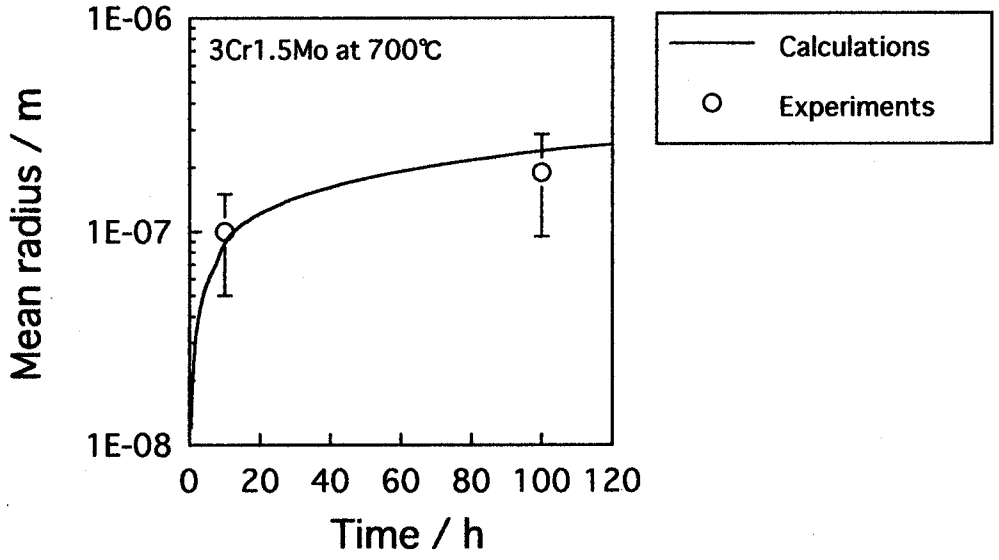

Figure 7.14: Comparison of the measured mean radius of $M_{23}C_6$ versus calculations for 3Cr1.5Mo and $2\frac{1}{4}$Cr1Mo steels tempered at 700 °C. The error bars correspond to two standard deviations.

7.8 Summary

A new model for multiple precipitation reactions has been established. It includes multicomponent treatments of both the diffusion–controlled growth and capillarity. The new calculations have been carried out without the Avrami conversion of extended space into real space, a satisfactory approximation given the minute fractions of precipitates involved. The new model shows good agreement with experimental data about not only volume fractions but also particle sizes for each alloy carbide in 3Cr1.5Mo and $2\frac{1}{4}$Cr1Mo steels.

CHAPTER EIGHT

Conclusions and suggestions for further work

A recent theory for simultaneous precipitation reactions has been tested experimentally with power plant steels in which many carbides and other compounds form together. Although this kind of modelling can be used in the design of new steels and in the estimation of creep, there are a number of fundamental problems which are outside of that framework of simultaneous transformations, associated with the growth of individual phases, which were demonstrated to prevent accurate solutions.

New methodologies have therefore been developed to deal with the growth of needle–shaped and spherical precipitates, taking proper account of mass balance during diffusion–controlled growth whilst at the same time dealing with multicomponent capillarity effects. The consumption of nucleation sites during the process of transformation was also considered. The methods have been satisfactorily validated against published experimental data. The models can estimate changes in volume fractions and particle sizes of equilibrium alloy carbides in ternary steels. Especially the model for spherical precipitates could simulate the whole of precipitation process including coarsening.

It is worth noting that the present work can be applied directly to strain–induced precipitation if the change in the number density of nucleation sites due to plastic strain is known explicitly, and assuming that the defect structure does not contribute to facilitating diffusion. Similarly, the effects of the dynamic recovery of deformation defects can in principle be incorporated via a time dependent nucleation site number density function, for example, of the kind used by Akamatsu *et al.* (1989).

Most practical steels contain many kinds of solutes and carbide phases, some of which are metastable, *i.e.*, not equilibrium phases. Therefore, new model for multiple precipitation reactions has been established as in Chapter 7, including multicomponent treatments of both the diffusion–controlled growth and capillarity. The new calculations have been carried out without the Avrami conversion of extended space into real space, a satisfactory approximation given the minute fractions of precipitates involved. The new model shows good agreement with experimental data about not only volume fractions but also particle sizes for each alloy carbide in 3Cr1.5Mo and $2\frac{1}{4}$Cr1Mo steels.

This new model can be applied to practical steels with MTDATA or possibly at least solubility

products. It is also possible to apply the theory for some well–known unresolved issues, for example, carbide formation during bainite transformation as Bhadeshia indicated (1999b). The work can be extended to predict strength and creep degradation, because the model permits the estimation not only of changes of volume fraction but also particle size distributions. Naturally, this would require the development of a relationship between the mechanism of deformation and the calculated microstructure.

The following problems could be investigated further to improve the precision of the predictions:

1) Specific characterisation of nucleation sites.

2) Measurement of interfacial energy using the Miyazaki method (1999).

3) Incorporation of cementite precipitation as a nucleation and growth process.

4) Better modelling of precipitation on grain boundaries.

APPENDIX ONE

Computer programs

This appendix presents the program listing which were used in Chapters 5, 6 and 7 and associated documentation following the MAP format (Bhadeshia, 1995).

1. Program for needle–shaped precipitate : M_2C

1.1 Provenance of Source Code

Nobuhiro FUJITA,
Phase Transformations Group,
Department of Materials Science and Metallurgy,
University of Cambridge,
Cambridge, U. K.

1.2 Purpose

To calculate the kinetics of carbides precipitating under diffusion–controlled growth and capillarity effect, with particular reference to the needle–shaped carbides in secondary hardening steels (Fe–Mo–C steel). In the calculations, the first carbide is assumed to be cementite.

1.3 Specification

This is a self–contained program.

1.4 Description

The program reads thermodynamic data (*e.g.* from MTDATA or Thermocalc) from a pre–established database. It then calculates the evolution of volume fractions and particle sizes with time for up to 4 carbides forming simultaneously.

1.5 References

Fujita, N and Bhadeshia, H. K. D. H.: *Materials Science and Technology* **15** (1999) 627-634.

1.6 Parameters

1.6.1 Input parameters

TK - double precision

Temperature in K.

DG - double precision array of size 4

Driving force for formation of carbides 1–4.

XB - double precision array of size 4

Mean composition of species 1–4 (mole fraction).

XC - double precision array of size 4 × 4

Equilibrium composition of species 1–4 in carbides 1–4 (mole fraction).

XA - double precision array of size 4 × 4

Composition of species 1–4 matrix in equilibrium with carbides 1–4 (mole fraction).

VMAX - double precision array of size 4

Maximum volume fraction of carbides 1–4.

SFEN - double precision array of size 4

Interfacial energy of carbides 1–4 (J m^{-2}).

NAD - double precision array of size 4

Nucleation site density factor for carbides 1–4.

CTYPE - double precision array of size 4

Morphology for carbides 1–4.

1 = Needle shaped

2 = Spherical

DS - double precision array of size 4

Species assumed to be controlling growth for phase 1–4.

CC - double precision

Mean carbon concentration (wt%).

GTHI - double precision

Thickness of cementite on boundaries (m).

THI - double precision

Thickness of cementite within grain (m).

DR - double precision array of size 4

The ratio of cementite density between on boundaries and with in grains.

1.6.2 Output parameters

T - double precision

Time in seconds.

VE - double precision array of size 4

Volume fraction of carbides 1–4.

SZEX - double precision array of size 4 × the number of time steps

The particle size for carbides 1–4.

1.7 Error Indicators

None.

1.8 Accuracy

No information supplied.

1.9 Further Comments

The program is set to read the input data from an ASCII text file "datain.d"and to write the results to file "dataout.d". An sample version of "datain.d"is provided.

1.10 Example

An example for cementite and M_2C precipitating in a ternary Fe–2Mo–0.1C wt% steel tempered at 600 °C.

1.10.1 Program data

Parameters	M_3C	M_2C
SFEN / J m^{-2}	0.0D0	0.20
NAD	1.0D0	1.0D0
CTYPE	0.0D0	1.0D0
DS	1.0D0	1.0D0
VMAX	1.97D-2	1.53D-2
VEQ	0.0D0	1.53D-2
DG / J mol−1	0.0D0	-1.6D2
VDIV	1.97D-2	1.53D-2
XB	1.14D-2	1.14D-2
XC	6.99D-2	5.97D-1
XA	1.02D-2	1.23D-4
CC / wt%	0.11D0	–
GTHI / m	5.0D-8	–
THI / m	2.0D-8	–
DR	0.9D0	–

Parameters	Values
DT: Time step / s	50
TK: Temperature / K	873

1.10.2 Program results

Time / s	VE for M_3C	VE for M_2C	Maximum SZEX for M_2C / m
0.10000D+03	0.19670D-01	0.47753D-08	0.32388D-08
0.20000D+03	0.19670D-01	0.52250D-07	0.64499D-08
0.40000D+03	0.19670D-01	0.65560D-06	0.12786D-07
0.60000D+03	0.19670D-01	0.29736D-05	0.19000D-07
0.80000D+03	0.19670D-01	0.87092D-05	0.25079D-07
0.10000D+04	0.19670D-01	0.19922D-04	0.31002D-07
0.14000D+04	0.19670D-01	0.67116D-04	0.42223D-07
0.16000D+04	0.19670D-01	0.10592D-03	0.47388D-07
0.20500D+04	0.19670D-01	0.22250D-03	0.57134D-07
0.26000D+04	0.19670D-01	0.36769D-03	0.64805D-07
0.32500D+04	0.19670D-01	0.59488D-03	0.73064D-07
0.40500D+04	0.19670D-01	0.98438D-03	0.82752D-07
0.51000D+04	0.19668D-01	0.16922D-02	0.94509D-07
0.64000D+04	0.19622D-01	0.28437D-02	0.10728D-06
0.80000D+04	0.19394D-01	0.45179D-02	0.12017D-06
0.10050D+05	0.18617D-01	0.68414D-02	0.13315D-06
0.12650D+05	0.16574D-01	0.96604D-02	0.14515D-06
0.15900D+05	0.12298D-01	0.12579D-01	0.15517D-06
0.20050D+05	0.49437D-02	0.14606D-01	0.16120D-06
0.25200D+05	0.00000D+00	0.14854D-01	0.16190D-06
0.31700D+05	0.00000D+00	0.14888D-01	0.16200D-06
0.39900D+05	0.00000D+00	0.14924D-01	0.16210D-06
0.50200D+05	0.00000D+00	0.14962D-01	0.16220D-06
0.63150D+05	0.00000D+00	0.15001D-01	0.16231D-06
0.79500D+05	0.00000D+00	0.15041D-01	0.16242D-06
0.10005D+06	0.00000D+00	0.15079D-01	0.16253D-06
0.12595D+06	0.00000D+00	0.15116D-01	0.16263D-06
0.15855D+06	0.00000D+00	0.15150D-01	0.16272D-06
0.19960D+06	0.00000D+00	0.15181D-01	0.16281D-06

1.10.3 Program text

```
C Program for needle–shaped precipitation M2C coexisting paraequilibrium
C cementite in a Fe–Mo–C ternary steel,
C Up to four phases and four controlling species.

      IMPLICIT REAL*8(A-H, K-Z),INTEGER(I, J)
      DOUBLE PRECISION SFEN(4),NAD(4),XB(4,4),XC(4,4),XA(4,4)
      DOUBLE PRECISION GMOD(4,4),DV(4),VMAX(4),VDIV(4)
      DOUBLE PRECISION VEQ(4),VES(4,200000),VE(4),TRT(200000)
      DOUBLE PRECISION DG(4),GRT(4),DVEXT(4),RMAX
      DOUBLE PRECISION GROLD(4),DX(4),XAINST(4,4),XAINSTR(4,200000)
      DOUBLE PRECISION RM(4),DGCHEM(4),CXBINST(4)
      DOUBLE PRECISION XBINST(4,4),C(4),GRCT(4,200000)
      DOUBLE PRECISION NP,XAINSTI(4,4),XAINSTG(4,4)
      DOUBLE PRECISION NR(4),SR(4,4),SRT(4),NMEX(4,200000)
      DOUBLE PRECISION DR,OGMOD(4,4),XCINST(4,4)
      DOUBLE PRECISION SZEX(4,200000),NPEX(4)
      DOUBLE PRECISION CC,CXA(4),CXB(4),CXC(4)
      INTEGER REG,DS(4),CTYPE(4),FLG(4),CNT,N,Y
      PI = 3.141592654
      BETA = 15.0D0
      IN1 = 1
      OU2 = 2
      OU3 = 3
      OPEN(UNIT = IN1,FILE="datain.d")
      OPEN(UNIT = OU2,FILE="dataout.d")

C IPHASE - Number of phases to calculate for
C ISPEC - Number of rate controlling diffusing species
C Read datain.d

      WRITE(*,*)'IS 1st PHASE CEMENTITE? YSE=0, NO=1'
```

```
      READ(IN1,*) Y
      DO 20 I=1,IPHASE
      WRITE(*,*)'PHASE ',I
      WRITE(*,*)'INTERFACIAL ENERGY OF NUCLEUS (J M-2)?'
      READ(IN1,*) SFEN(I)
      WRITE(*,*)'SITE DENSITY (RELATIVE TO 1st Phase) ?'
      READ(IN1,*) NAD(I)
      WRITE(*,*)'PHASE TYPE (1 - NEEDLE, 2 - SPHERICAL) ?'
      READ(IN1,*) CTYPE(I)
      WRITE(*,*)'SPECIES CONTROLLING DIFFUSION (1,2,3...) ?'
      READ(IN1,*) DS(I)
      WRITE(*,*)'MAXIMUM VOLUME FRACTION ?'
      READ(IN1,*) VMAX(I)
      WRITE(*,*)'EQUILIBRIUM VOLUME FRACTION ?'
      READ(IN1,*) VEQ(I)
      WRITE(*,*)'DRIVING FORCE FOR FORMING VOLUME V OF PPT (J) ?'
      READ(IN1,*) DG(I)
      WRITE(*,*)'VOLUME FRACTION V (FOR DRIVING FORCE) ?'
      READ(IN1,*) VDIV(I)
      DO 25 II=1,ISPEC
      WRITE(*,*)'SPECIES', II
      WRITE(*,*)'MEAN CONCENTRATION IN ALLOY ?'
      READ(IN1,*) XB(II,I)
      WRITE(*,*)'EQUILIBRIUM CONCENTRATION OF SPECIES IN PRECIPITATE ?'
      READ(IN1,*) XC(II,I)
      WRITE(*,*)'EQUILIBRIUM CONCENTRATION OF SPECIES IN MATRIX ?'
      READ(IN1,*) XA(II,I)
25          CONTINUE
20    CONTINUE
      WRITE(*,*)'TIME STEP ?'
      READ(IN1,*) DT
      WRITE(*,*)'ABSOLUTE TEMPERATURE ?'
      READ(IN1,*) TK
```

```
C This part if cementite is the first phase to form
C Necessary since it grows initially with paraequilibrium composition

      IF (Y.EQ.1) GOTO 10
      IF (Y .EQ. 0) THEN
      WRITE(*,*)'CARBON CONCENTRATION IN wt%'
          READ(IN1,*) CC
          WRITE(*,*)'RATIO OF PARTICLES AT BOUNDARY/INTRAGRANULAR?'
          READ(IN1,*) DR
          WRITE(*,*)'GRAIN BOUNDARY CEMENTITE THICKNESS / M ?'
          READ(IN1,*) GTHI
          WRITE(*,*)'INTRAGRANULAR CEMENTITE THICKNESS / M?'
          READ(IN1,*) THI

C Calculate initial number density of cementite particles
C Equation is from Nobu's experimental measurements

      NP = CC * 2.23D22 - 1.0D21
      NPL = DR * NP
      GBNP = (1-DR) * NP
      ENDIF
      VE(1) = VMAX(1)
      VL = VE(1) * DR * (THI)**(3.0D0) / (DR*(THI)**(3.0D0) +
       (1-DR)*(GTHI)**(3.0D0))
      VGB = VE(1) * (1-DR) * (GTHI)**(3.0D0) / (DR*(THI)**(3.0D0) +
       (1-DR)*(GTHI)**(3.0D0))
      XAINSTI(DS(I),1)=XA(DS(I),1)
      XAINSTG(DS(I),1)=XA(DS(I),1)
10      SRT(1) = 0.0D0
      ST = 0.0
      SR(DS(I),2) = 0.0
      ONXCI=XB(DS(I),1)
```

```
      GBXCI=XB(DS(I),1)
      FLG(1) = 0
      DO 11 I=1,IPHASE
      SR(DS(I),I) = 0.0D0
      CXB(I) = CXBINST (I)
      XAINST(DS(I),I)=XA(DS(I),I)
      XBINST((DSI),I)=XB(DS(I),I)
      XCINST(DS(I),I)=XC(DS(I),I)
11      CONTINUE

C Cementite complete
C Calculate diffusion coefficient D (m^2/s)

      CALL DIFCO(DMO,TK)

C Set initial state of soft-impingement

      DO 30 I=2,IPHASE
      GROLD(I) = 1.0D0
      OGMOD(DS(I),I)=2.0D0
      FLG(I) = 0
30      CONTINUE

C Step time

      CNT = 0
      TINST = 0.0D0
40      J = J + 1.0D0
      T = (20.0D0**(J/10.0D0)) + DT
      REG = 1
50      TINST = TINST + DT
      N = TINST / DT
      CNT = CNT + 1
```

```
C Calculations of soft-impingement
C SR(I) : solute I removed by reaction

      SR(DS(I),1) = VL*(ONXCI-XB(DS(I),1))+VGB*(GBXCI-XB(DS(I),1))
      SRT(DS(I)) = SR(DS(I),1) + (XCINST(DS(I),2)-XB(DS(I),2))*VE(2)
      VT=VL+VGB+VE(2)
      DX(1)=SRT(1) / (1-VT)
      GMOD(DS(I),1) = 1.0D0 - DX(1)/(XB(DS(I),1)-XA(DS(I),1))
      XBINST(DS(I),1) = XB(DS(I),1)-DX(1)
      DO 60 I = 2,IPHASE
      DX(I)=SRT(DS(I)) / (1-VT)
      XBINST(DS(I),I) = XB(DS(I),I)-DX(I)
      M=XBINST(DS(I0,I)-XAINST(DS(I),I)
      SAT=M/(XCINST(DS(I),I)-XAINST(DS(I),I))
      GMOD(DS(I),I)= 1- VE(I)/SAT
      IF (GMOD(DS(I),I) .LE. 0.0 .OR. M .LE. 0.0) THEN
      GMOD(DS(I),I) = 0.0D0
      ENDIF
      DGCHEM(I) = GMOD(DS(I),I)*DG(I)
60      CONTINUE
```

C Thermodynamic data for M_2C in the Fe-2Mo-0.1C wt% steel

```
C from MTDATA. This is for tie-line shifting.
C Here, DS(I)=1 : Mo

      IF (TK .EQ. 923) THEN
      CXBINST(2) = XBINST(1,2)*0.50544D+00-5.2690D-3
      IF (CXBINST(2) .LE. 0.000144D0) CXBINST(2)=0.000144D0
      F =(-3.8447D-2 * DLOG10 (CXBINST(2)))
      XCINST(1,2)= 0.50513 + F
      XAINST(1,2)=2.2427D-4 + 3.7986D-7 /
       CXBINST(2)-2.4115D-11*(1/CXBINST(2))**(2.0D0)
```

```
      ENDIF
      IF (TK .EQ. 973) THEN
      CXBINST(2) = -4.9781D-3+0.50878*XBINST(1,2)
      IF (CXBINST(2) .LE. 0.000364D+00) CXBINST(2)=0.000364D+00
      H =(-4.5255D-2 * DLOG10 (CXBINST(2)))
      XCINST(1,2)= 0.48398 + H
      XAINST(1,2)=3.3467D-4 + 1.4191D-6 / CXBINST(2)
       -4.7477D-10*(1/CXBINST(2))**(2.0D0)
       +7.9388D-14*(1/CXBINST(2))**(3.0D0)
      ENDIF
      IF (TK .EQ. 873) THEN
      CXBINST(2) = -5.4731D-3+0.50492*XBINST(1,2)
      IF (CXBINST(2) .LE. 0.000041D+00) CXBINST(2)=0.000041D+00
      XCINST(1,2)=0.65648 - 34.44 *
       CXBINST(2)+8503.0*(CXBINST(2))**(2.0D0)
       -8.1104D5*(CXBINST(2))**(3.0D0)
      XAINST(1,2)=1.1301D-4 + 1.2248D-7 / CXBINST(2)
       -4.7483D-12*(1/CXBINST(2))**(2.0D0)
       +7.5251D-17*(1/CXBINST(2))**(3.0D0)
      ENDIF
      IF (TK .EQ. 1023) THEN
      CXBINST(2) = -4.5589D-3+0.51604*XBINST(1,2)
      IF (CXBINST(2) .LE. 0.000753D+00) CXBINST(2)=0.000753D+00
      XCINST(1,2)=0.64088 - 25.336 * CXBINST(2)
       +4454.5*(CXBINST(2))**(2.0D0)-3.4644D5*(CXBINST(2))**(3.0D0)
      XAINST(1,2)=5.8507D-4 + 3.3409D-6 / CXBINST(2)
       -1.6445D-9*(1/CXBINST(2))**(2.0D0)
       +4.6268D-13*(1/CXBINST(2))**(3.0D0)
      ENDIF
63      DO 61 I = 2,IPHASE
      IF (XAINST(DS(I),I) .LE. 0.0 .OR. XCINST(DS(I),I) .LE. 0.0) THEN
      DGCHEM(I) = 0.0
      ENDIF
```

```
61      CONTINUE

C Enrichment or volume decrease of cementite

      IF (NPL .GT. 0.0) THEN
      RM(1) = (3.0D0 * VL)/((4.0D0 * NPL * PI))**(1.0D0/3.0D0)
      ELSE
      RM(1) = 0.0
      ENDIF
      IF (GBNP .GT. 0.0) THEN
      GBRM = (3.0D0 * VGB)/((4.0D0 * GBNP * PI))**(1.0D0/3.0D0)
      ELSE
      GBRM = 0.0
      ENDIF
      IF (ONXCI .LT. XC(DS(I),1)) THEN
      DXCI = ((4.0D0 * (DMO**(0.5)) * (XBINST(DS(I),1)
       -XAINSTI(DS(I),1))* (DT**(0.5)))/(THI * (PI**(0.5))))
      ENDIF
      IF (GBXCI .LT. XC(DS(I),1)) THEN
      GBDXCI = ((4.0D0 * (DMO**(0.5)) * (XBINST(DS(I),1)
       -XAINSTG(DS(I),1))* (DT**(0.5)))/(GTHI * (PI**(0.5))))
      ENDIF
      ONXCI = ONXCI + DXCI
      GBXCI = GBXCI + GBDXCI

C Cementite dissolves to provide solute to remaining precipitates
C Diffusion from cementite to precipitates controls the dissolution of cementite

      IF (XBINST(DS(I),1) .LT. XAINSTI(DS(I),1)) THEN
      VINCI = (DMO * (XAINSTI(DS(I),1)- XBINST(DS(I),1)))
       /(XCINST(DS(I),1) - XAINSTI(DS(I),1))*
       ((NPL + NPEX(2))**(1.0D0/3.0D0))
      ENDIF
```

```
      IF (XBINST(DS(I),1) .LT. XAINSTG(DS(I),1)) THEN
      VINCG = (DMO * (XAINSTG(DS(I),1) - XBINST(DS(I),1)))
       /(XCINST(DS(I),1) - XAINSTG(DS(I),1))*
       ((GBNP + NPEX(2))**(1.0D0/3.0D0))
      ENDIF
      RM(1) = RM(1) - VINCI
      GBRM = GBRM - VINCG
      IF (RM(1) .GT. 0.0D0) THEN
      DVFLUXI = (4.0D0 * PI / 3.0D0) * ((RM(1)**3.0D0)
       -(RM(1)-VINCI*DT)**3.0D0)
      ELSE
      RM(1) = 0.0D0
      NPL = 0.0D0
      VL = 0.0D0
      DVFULXI = 0.0D0
      ENDIF
      IF (GBRM .GT. 0.0D0) THEN
      DVFLUXG= (4.0D0 * PI / 3.0D0) * ((GBRM**3.0D0)
       -(GBRM-VINCI*DT)**3.0D0)
      ELSE
      GBRM = 0.0
      GBNP = 0.0
      VGB = 0.0D0
      ENDIF
      IF (DVFLUXI .LE. 0.0) DVFLUXI = 0.0
      IF (DVFLUXG .LE. 0.0) DVFLUXG = 0.0
      DV(1) = DV(1) + (NPL * DVFLUXI+
       GBNP * DVFLUXG)
      DVGB = DVGB + GBNP*DVFLUXG
      DVL = DVL + NPL*DVFLUXI
      NP = NPL + GBNP
      VE(1) = VL + VGB
70      CONTINUE
```

```
      DXCI =0.0D0
      GBDXCI =0.0D0
      VE(1) = VE(1) - DV(1)
      VGB = VGB - DVGB
      VL = VL - DVL
      IF (VE(1) .LT. 0.0D0) THEN
      VE(1) = 0.0D0
      DV(1) = 0.0D0
      ENDIF
      IF (VL.LT. 0.0D0) VL = 0.0D0
      IF (VGB.LT. 0.0D0) VGB = 0.0D0

C Precipitation or dissolution of other phases

      DO 80 I = 2,IPHASE
      IF (FLG(I) .EQ. 0) THEN
      IF (DGCHEM(I) .LT. 0.0D0) THEN
      CALL NURATE(NR(I),DGCHEM(I),SFEN(I),NAD(I),VDIV(I),TK,
      XBINST(DS(I),I),CC)
      ELSE
      NR(I) = 0.0D0
      ENDIF

C Only have growth if composition is different from bulk composition

      IF (XCINST(DS(I),I) .GT. XAINST(DS(I),I)) THEN
      IF (CTYPE(I) .EQ. 1) THEN


C Calculations for capillarity effect

      OGRT=0.0D0
      DO 62 IJI=2, 10000
```

```
      TRT(IJI) = IJI*1D-10
      MCAP=SFEN(I) * 3.0D0**(0.5D0)/2.0D0*3.002D-10**(2.0D0)
       *4.724D-10 / TK/1.380662D-23/2.0D0
       *(1-XAINST(DS(I),I))/(XCINST(DS(I),I)-XAINST(DS(I),I))
      XAINSTR(DS(I),I)=(1+2.0D0*MCAP/TRT(IJI))*XAINST(DS(I),I)
      IF (XAINSTR(DS(I),I) .LT. XBINST(DS(I),I)) THEN
      CALL GROWTH
       (GRT(I),CTYPE(I),XBINST(DS(I),I),XAINSTR(DS(I),I)
       ,XCINST(DS(I),I),XAINST(DS(I),I),DMO, TRT(IJI))
      IF (GRT(I) .GT. OGRT) THEN
      OGRT=GRT(I)
      ELSE
      GRT(I)=OGRT
      RMAX=TRT(IJI-1)
      GOTO 71
      ENDIF
      ENDIF
62      CONTINUE
      ENDIF
      ELSE
      GRT(I) = 0.0D0
      ENDIF
      ELSE
      NR(I)=0.0
      GRT(I)=0.0
      ENDIF
      IF(XAINST(DS(I),I) .LE. 0.0 .OR.
       XCINST(DS(I),I) .LE. 0.0) THEN
      GRT(I)=0.0
      ENDIF
71      CALL SIZE(RM(I),CTYPE(I),GRT(I),VE(I),NP,BETA)
      CALL CONST(C(I),CTYPE(I),GRT(I),BETA)
```

```
C For size distribution of particles nucleating/ growing

      IF (FLG(I) .EQ. 0) THEN
      NMEX(I,CNT)=NR(I) *(1-VE(I)/VMAX(I))* DT
      GRCT(I,CNT)=GRT(I)
      DO 88 IIJJ = 1,CNT
      IF (CNT .LE. 0) SZEX(I,IIJJ) = 0.0
      IF (IIJJ .LE. CNT) THEN
      IF (CTYPE(I) .EQ. 2) THEN
      SZEX(I,IIJJ)= SZEX(I,IIJJ) +
       GRT(I) * (DT)**0.5 * ((CNT-IIJJ+1)**0.5
       - (CNT-IIJJ)**0.5)
      ELSE
      SZEX(I,IIJJ)=SZEX(I,IIJJ) + (GRT(I) * DT)
      ENDIF
      ENDIF
88      CONTINUE
      VES(I,0) =0.0
      VES(I,CNT) = 0.0D0
      VE(I) = 0.0D0
      NPEX(I)=0.0
      DO 125 JJ=1,CNT
      IF (SZEX(I,JJ) .GT. 0.0D0) THEN
      IF (CTYPE(I) .EQ. 1) THEN
      VES(I,CNT) = VES(I,CNT) + NMEX(I,JJ) *
       PI *(SZEX(I,JJ))**3.0D0/ 4.0D0 / ((BETA)**2.0D0)
      ELSE
      VES(I,CNT) = VES(I,CNT) + NMEX(I,JJ) *
       4.0D0 * PI *(SZEX(I,JJ))**3.0D0 / 3.0D0
      ENDIF
      ELSE
      SZEX(I,JJ)=0.0
      NMEX(I,JJ)=0.0
```

```
      ENDIF
      NPEX(I) = NPEX(I) + NMEX(I,JJ)
125      CONTINUE
      IF (FLG(I) .EQ. 0) THEN
      DVEXT(I) = VES(I,CNT)-VES(I,CNT-1)
      SR(DS(I),I) = VES(I,CNT)*(XCINST(DS(I),I)-XB(DS(I),I))
      VE(I) = VES(I,CNT)
      ENDIF
      ENDIF

C Do not let VF fall below equilibrium value

      IF (VE(I) .LE. 0.0D0) VE(I) = 0.0D0
      IF (FLG(I) .EQ. 1) THEN
      FLG(I) = 2
      ENDIF
80     CONTINUE
      REG = 0
      ENDIF
      IF (TINST .GE. T) THEN
      WRITE(*,200) TINST,VE(1),VE(2),SZEX(2,1),GRT(2),RMAX
      WRITE(OU2,200) TINST,VE(1),VE(2),SZEX(2,1),GRT(2),RMAX
      GOTO 40
      ELSE
      GOTO 50
      ENDIF
200      FORMAT(1X,6D15.5)
999      STOP
      END
```

```
C*************************************************************
C CALLS SUBROUTINE FOR GROWTH DEPENDING ON PARTICLE TYPE

      SUBROUTINE GROWTH(GRT,CTYPE,XB,XAR,XC,XA,DMO,TRT)
      INTEGER CTYPE
      IMPLICIT REAL*8(A-H,K-Z),INTEGER(I,J)
      IF (CTYPE .EQ. 1) THEN
      CALL LINEARGROWTH (GRT,XB,XAR,XC,XA,DMO,TRT)
      ENDIF
      IF (CTYPE .EQ. 2) THEN
      CALL PARABOLGROWTH(GRT,XB,XA,XC,DMO)
      ENDIF
      RETURN
      END

C*************************************************************
C CALCULATES THE GROWTH RATE FOR LINEAR GROWTH (I.E. NEEDLES)

      SUBROUTINE LINEARGROWTH(GR,XB,XAR,XC,XA,DMO,TRT)
      IMPLICIT REAL*8(A-H,K-Z),INTEGER(I,J)
      GR =2.0D0*DMO/(2.0D0*TRT) *(XB-XAR)*(XC-XAR)/(XC-XB)/(XC-XB)
      RETURN
      END

C*************************************************************
C CALCULATES THE CONSTANT (ALPHA3) FOR PARABOLIC GROWTH

      SUBROUTINE PARABOLGROWTH(GC,XB,XA,XC,DMO)
      IMPLICIT REAL*8(A-H,K-Z),INTEGER(I,J)


C 'NATURAL' GROWTH PARAMETER (P. 488 CHRISTIAN)
```

```
      IF(XB .GE. XA) THEN
      ALPHA = (2.0D0**(0.5D0)) * ((XB - XA) ** (0.5D0))
       / ((XC - XB) ** (0.5D0))
      ELSE
      ALPHA = -(2.0D0**(0.5D0)) * ((XA - XB) ** (0.5D0))
       / ((XC - XB) ** (0.5D0))
      ENDIF
      GC = ALPHA * (DMO**(0.5D0))
      RETURN
      END

C*************************************************************
C CALCULATES AVERAGE PARTICLE SIZES

      SUBROUTINE SIZE(RM,CTYPE,GRT,VE,NP,BETA)
      IMPLICIT REAL*8(A-H,K-Z),INTEGER(I,J)
      INTEGER CTYPE
      PI = 3.141592654
      IF ((VE .EQ. 0.0D0) .OR. (NP .EQ. 0.0D0)) THEN
      RM = 0.0D0
      ELSE
      IF (CTYPE .EQ. 1) THEN
      RM = (4.0D0 * ((BETA**2.0D0) * VE)/(PI * NP)) ** (1.0D0/3.0D0)
      ENDIF
      IF (CTYPE .EQ. 2) THEN
      RM =((3.0D0 * VE)/(4.0D0 * NP * PI)) ** (1.0D0/3.0D0)
      ENDIF
      ENDIF
      RETURN
      END
```

```
C*************************************************************
C CALCULATES NUCLEATION RATE

      SUBROUTINE NURATE(NR1,DGCHEM,SFEN1,NAD1,VMAX,TK,XB,CC)
      IMPLICIT REAL*8(A-H,K-Z),INTEGER(I,J)
      K = 1.380662D-23
      NA = 6.022045D23
      H = 6.626176D-34
      SHAPE=1.0D0
      DGVOL = (DGCHEM/VMAX) * 1.44D5
      ACTIVE = (240.0D3)/NA
      PI = 3.141592654
      NUSITES = CC * 2.23D22 - 1D21
      N1 = NAD1 * NUSITES
      DGCRIT1 = (16.0D0*PI*((SFEN1*SHAPE)**3.0D0))/
     (3.0D0*(DGVOL**2.0D0))
      EPENT1 = -(DGCRIT1 + ACTIVE)/(K * TK)
      CONST1 = XB * (N1 * K * TK)/H
      NR1 = CONST1 * DEXP(EPENT1)
      RETURN
      END

C*************************************************************
C CALCULATES DIFFUSION COEFFICIENT OF MO IN FE

      SUBROUTINE DIFCO(DMO,TK)
      IMPLICIT REAL*8(A-H,K-Z),INTEGER(I,J)
      D0MO = 1.1D-04
      QMO = 240D03
      R = 8.314408694
      DMO = D0MO * DEXP(-QMO/(R*TK))
```

```
RETURN
END
```

1.11 Auxiliary Routines

The subroutines called by this program are :

GROWTH

LINEARGROWTH

PARABOLGROWTH

SIZE

NURATE

DIFCO

1.12 Keywords

simultaneous precipitation reactions, capillarity, secondary hardening steel

2. Program for spherical precipitate : NbC

2.1 Provenance of Source Code

Nobuhiro FUJITA,
Phase Transformations Group,
Department of Materials Science and Metallurgy,
University of Cambridge,
Cambridge, U. K.

2.2 Purpose

To calculate the kinetics of carbides precipitating under diffusion–controlled growth and capillarity effect, with particular reference to the spherical carbides in high strength low alloy steels (Fe–Nb–C steel).

2.3 Specification

This is a self–contained program.

2.4 Description

The program reads thermodynamic data (*e.g.* from MTDATA or Thermocalc) from a pre-established database. It then calculates the evolution of volume fractions and particle sizes with time for up to 4 carbides forming simultaneously.

2.5 References

Bhadeshia, H. K. D. H.: *Materials Algorithms Project* (1985) .

2.6 Parameters

2.6.1 Input parameters

TK - double precision

Temperature in K.

DG - double precision array of size 4

Driving force for formation of carbides 1–4.

XB - double precision array of size 4

Mean composition of species 1–4 (mole fraction).

XC - double precision array of size 4 × 4

Equilibrium composition of species 1–4 in carbides 1–4 (mole fraction).

XA - double precision array of size 4 × 4

Composition of species 1–4 matrix in equilibrium with carbides 1–4 (mole fraction).

VMAX - double precision array of size 4

Maximum volume fraction of carbides 1–4.

SFEN - double precision array of size 4

Interfacial energy of carbides 1–4 (J m^{-2}).

NAD - double precision array of size 4

Nucleation site density factor for carbides 1–4.

CTYPE - double precision array of size 4

Morphology for carbides 1–4.

1 = Needle shaped

2 = Spherical

DS - double precision array of size 4

Species assumed to be controlling growth for phase 1–4.

2.6.2 Output parameters

T - double precision

Time in seconds.

VE - double precision array of size 4

Volume fraction of carbides 1–4.

SZEX - double precision array of size 4 × the number of time steps

The particle size for carbides 1–4.

2.7 Error Indicators

None.

2.8 Accuracy

No information supplied.

2.9 Further Comments

The program is set to read the input data from an ASCII text file "datain.d"and to write the results to file "dataout.d". An sample version of "datain.d"is provided.

2.10 Example

An example for NbC precipitating in a ternary Fe-0.05Nb-0.1C wt% steel.

2.10.1 Program data

Parameters	NbC
SFEN / J m^{-2}	0.25D0
NAD / m^{-3}	1.0D19
CTYPE	2.0D0
DS	1.0D0
VMAX	5.9D-4
VEQ	5.9D-4
DG / J mol−1	-9.5D0
VDIV	5.9D-4
XB	3.0D-4
XC	5.0D-1
XA	5.7D-4

Parameters	Values
DT: Time step / s	50
TK: Temperature / K	1173

2.10.2 Program results

Time / s	VE	Maximum SZEX / m	Mean SZEX / m	Number density / m^{-3}
0.1200D+03	0.4013D-07	0.4921D-08	0.4202D-08	0.1187D+18
0.4200D+03	0.2950D-06	0.7777D-08	0.5833D-08	0.2965D+18
0.1020D+04	0.1867D-05	0.1153D-07	0.8166D-08	0.6486D+18
0.3020D+04	0.2229D-04	0.1931D-07	0.1350D-07	0.1688D+19
0.5020D+04	0.6899D-04	0.2459D-07	0.1809D-07	0.2293D+19
0.6120D+04	0.1036D-03	0.2695D-07	0.2066D-07	0.2419D+19
0.8320D+04	0.1829D-03	0.3088D-07	0.2546D-07	0.2459D+19
0.1152D+05	0.3031D-03	0.3517D-07	0.3049D-07	0.2459D+19
0.1852D+05	0.5091D-03	0.4058D-07	0.3645D-07	0.2459D+19
0.2172D+05	0.5612D-03	0.4173D-07	0.3768D-07	0.2459D+19
0.2552D+05	0.5854D-03	0.4225D-07	0.3822D-07	0.2459D+19
0.3012D+05	0.5881D-03	0.4232D-07	0.3828D-07	0.2459D+19
0.4852D+05	0.5881D-03	0.4242D-07	0.3826D-07	0.2459D+19
0.7852D+05	0.5881D-03	0.4256D-07	0.3824D-07	0.2459D+19
0.1081D+06	0.5881D-03	0.4268D-07	0.3823D-07	0.2459D+19
0.3331D+06	0.5881D-03	0.4329D-07	0.3812D-07	0.2459D+19
0.5401D+06	0.5881D-03	0.4352D-07	0.3808D-07	0.2459D+19
0.7451D+06	0.5881D-03	0.4373D-07	0.3804D-07	0.2459D+19
0.1030D+07	0.5881D-03	0.4400D-07	0.3798D-07	0.2459D+19
0.5135D+07	0.5881D-03	0.4575D-07	0.3748D-07	0.2459D+19
0.8320D+07	0.5881D-03	0.4701D-07	0.3695D-07	0.2459D+19
0.1349D+08	0.5881D-03	0.4855D-07	0.3608D-07	0.2459D+19
0.2185D+08	0.5881D-03	0.5055D-07	0.3449D-07	0.2448D+19
0.4158D+08	0.5881D-03	0.5439D-07	0.3347D-07	0.2085D+19
0.1283D+09	0.5882D-03	0.6407D-07	0.4467D-07	0.1099D+19
0.2868D+09	0.5882D-03	0.7289D-07	0.5196D-07	0.7064D+18
0.3957D+09	0.5882D-03	0.7783D-07	0.5418D-07	0.5904D+18
0.5460D+09	0.5882D-03	0.8384D-07	0.5891D-07	0.4734D+18
0.1434D+10	0.5883D-03	0.1059D-06	0.7101D-07	0.2373D+18
0.1684D+10	0.5883D-03	0.1102D-06	0.8616D-07	0.1780D+18

2.10.3 Program text

```
C Program for spherical shape precipitation NbC in a Fe–Nb–C steel
C Up to four phases and four controlling species

      IMPLICIT REAL*8(A-H,K-Z),INTEGER(I,J)
      DOUBLE PRECISION SFEN(4),NAD(4),XB(4,4),XA(4,4)
      DOUBLE PRECISION XC(4,4),VMAX(4),VDIV(4)
      DOUBLE PRECISION GMOD(4,4),SZMINMB(4),SZMAX(4)
      DOUBLE PRECISION DG(4),GRT(4),MSZEX(4)
      DOUBLE PRECISION VEQ(4),VES(4,2000000),VE(4)
      DOUBLE PRECISION GROLD(4),DX(4,4),DT
      DOUBLE PRECISION DGCHEM(4),CXBINST(4)
      DOUBLE PRECISION XBINST(4,4),RGRT(4,2000000)
      DOUBLE PRECISION NR(4),SR(4,4),SRT(4)
      DOUBLE PRECISION DR,OGMOD(4,4),XCINST(4,4)
      DOUBLE PRECISION SZEX(4,2000000),NPEX(4)
      DOUBLE PRECISION CXA(4),CXB(4),CXC(4),RSZEX(4,2000000)
      DOUBLE PRECISION NMEX(4,2000000),RCXA(4)
      DOUBLE PRECISION XAINST(4,4),RXAINST(4,4,2000000)
      INTEGER REG,DS(4),CTYPE(4),FLG(4),CNT,N,Y
      PI = 3.141592654
      IN1 = 1
      OU2 = 2
      OU3 = 3
      OPEN(UNIT = IN1,FILE="datain.d")
      OPEN(UNIT = OU2,FILE="dataout.d")

C IPHASE - Number of phases to calculate for
C ISPEC - Number of rate controlling diffusing species
C Read data

      DO 20 I=1,IPHASE
      WRITE(*,*)'PHASE ',I
```

```
      WRITE(*,*)'INTERFACIAL ENERGY OF NUCLEUS (J M-2)?'
      READ(IN1,*) SFEN(I)
      WRITE(*,*)'SITE DENSITY (M-3)?'
      READ(IN1,*) NAD(I)
      WRITE(*,*)'PHASE TYPE (1 - NEEDLE, 2 - SPHERICAL) ?'
      READ(IN1,*) CTYPE(I)
      WRITE(*,*)'SPECIES CONTROLLING DIFFUSION (1,2,3...) ?'
      READ(IN1,*) DS(I)
      WRITE(*,*)'MAXIMUM VOLUME FRACTION ?'
      READ(IN1,*) VMAX(I)
      WRITE(*,*)'EQUILIBRIUM VOLUME FRACTION ?'
      READ(IN1,*) VEQ(I)
      WRITE(*,*)'DRIVING FORCE FOR FORMING VOLUME V OF PPT (J) ?'
      READ(IN1,*) DG(I)
      WRITE(*,*)'VOLUME FRACTION V (FOR DRIVING FORCE) ?'
      READ(IN1,*) VDIV(I)
      DO 25 II=1,ISPEC
      WRITE(*,*)'SPECIES', II
      WRITE(*,*)'MEAN CONCENTRATION IN ALLOY ?'
      READ(IN1,*) XB(II,I)
      WRITE(*,*)'EQUILIBRIUM CONCENTRATION OF SPECIES IN PRECIPITATE ?'
      READ(IN1,*) XC(II,I)
      WRITE(*,*)'EQUIM CONCENTRATION OF SPECIES IN MATRIX ?'
      READ(IN1,*) XA(II,I)
25      CONTINUE
20      CONTINUE
      WRITE(*,*)'TIME STEP ?'
      READ(IN1,*) DT
      WRITE(*,*)'ABSOLUTE TEMPERATURE ?'
      READ(IN1,*) TK
10      SRT(DS(I)) = 0.0D0
      SR(DS(I),1) = 0.0D0
      ST = 0.0
```

```
      FLG(1) = 0
      CXBINST (1) = 0.00463
      XAINST(DS(I),1)=XA(DS(I),1)
      XBINST(DS(I),1)=XB(DS(I),1)
      XCINST(DS(I),1)=XC(DS(I),1)
11      CONTINUE

C Calculate diffusion coefficient D (m2/s)

      CALL DIFCO(DNB,TK)

C Set initial state of soft-impingement

      DO 30 I=2,IPHASE
      GROLD(I) = 1.0D0
      OGMOD(1,I)=2.0D0
      FLG(I) = 0
30      CONTINUE

C Step time ***********

      CNT = 0
      TINST = 0.0D0
40      J = J + 1.0D0
      T = (20.0D0**(J/10.0D0)) + DT
      REG = 1
50      TINST = TINST + DT
      N = TINST / DT
      CNT = CNT + 1
```

```
C Calculations of soft-impingement
C SR(I) : solute I removed by reaction

      SRT(DS(I)) = (XCINST(DS(I),1)-XB(DS(I),1))*VE(1)
      VT=VE(1)
      DX(DS(I),1)=SRT(DS(I)) / (1-VE(1))
      M=XBINST(DS(I),1)-XAINST(DS(I),1)
      SAT=M/(XCINST(DS(I),1)-XAINST(DS(I),1))
      GMOD(DS(I),1)= 1- VE(1)/SAT
      IF (GMOD(DS(I),I) .LE. 0.0 .OR. M .LE. 0.0)
       GMOD(DS(I),I) = 0.0D0
      DGCHEM(1) = GMOD(DS(I),1)*DG(1)
      XBINST(DS(I),1) = XB(DS(I),1)-DX(DS(I),1)
60      CONTINUE

C Thermodynamic data for NbC in the Fe-0.05Nb-0.1C wt% steel
C from MTDATA. Here, DS(I)=1 : Nb

      IF (TK .EQ. 1123) THEN
      CXBINST(1) = XBINST(DS(I),1)*1.0087D+00-4.3747D-3
      IF (CXBINST(1) .LE. 0.0043391D+00) CXBINST(1)=0.0043391D+00
      XAINST(DS(I),1)=4.2962D-6 -4.3366D-4 * CXBINST(1)
      XCINST(DS(I),1)=0.5
      ENDIF
      IF (TK .EQ. 1173) THEN
      CXBINST(1) = XBINST(DS(I),1)*.99133D+00+4.3367D-3
      IF (CXBINST(1) .LE. 0.004300D+0) CXBINST(1)=0.004300D+00
      XAINST(DS(I),1)=-1.0984D-3 + 0.74215 * CXBINST(1)
       -166.01*(CXBINST(1))**(2.0D0)+1.2357D4*(CXBINST(1))**(3.0D0)
      XCINST(DS(I),1)=0.5
      ENDIF
      IF (TK .EQ. 1223) THEN
      CXBINST(1) = XBINST(DS(I),1)*.99133D+00+4.3368D-3
```

```
      IF (CXBINST(1) .LE. 0.0043424D+0) CXBINST(1)=0.0043424D+00
      XAINST(DS(I),1)=2.2095D-5 - 2.2060D-3 * CXBINST(1)
      XCINST(DS(I),1)=0.5
      ENDIF
      IF (XAINST(DS(I),1) .LE. 0.0) DGCHEM(I) = 0.0
      IF (XCINST(DS(I),1) .LE. 0.0) DGCHEM(I) = 0.0

C Precipitation or dissolution of other phases

      IF (FLG(1) .EQ. 0) THEN
      IF (DGCHEM(1) .LT. 0.0D0) THEN
      CALL NURATE(NR(1),DGCHEM(1),SFEN(1),NAD(1),VDIV(1),
      XBINST(DS(I),1),TK)
      ELSE
      NR(1) = 0.0D0
      GRT(1)=0.0
      ENDIF

C Only have growth if composition is different from bulk composition

      IF (XCINST(DS(I),1) .GT. XAINST(DS(I),1) .AND.
       XCINST(DS(I),1) .GT. 0.0D0 .AND.
       XAINST(DS(I),1) .GT. 0.0D0 ) THEN
      DO 67 IIJJ=1,CNT
      IF (RSZEX(1,IIJJ) .EQ. 0.0D0) THEN
      CALL GROWTH
       (GRT(1),CTYPE(1),XBINST(DS(I),1),XAINST(DS(I),1)
       ,XCINST(DS(I),1),XAINST(DS(I),1),DNB)
      ELSE
      IF (RXAINST(1,DS(I),IIJJ) .LE. XCINST(DS(I),1) .AND.
       RCXA(1) .LE. CXC(1)) THEN
      CALL GROWTH
       (RGRT(1,IIJJ),CTYPE(1),XBINST(DS(I),1), RXAINST(DS(I),1,IIJJ)
```

```
     ,XCINST(DS(I),1),XAINST(DS(I),1),DNB)
      ENDIF
      ENDIF
67      CONTINUE
      ENDIF
      ELSE
      GRT(1) = 0.0D0
      ENDIF
      IF(XAINST(DS(I),1) .LE. 0.0 .OR.
       XCINST(DS(I),1) .LE. 0.0) THEN
      GRT(1)=0.0
      ENDIF

C For size distribution of particles nucleating/ growing

      IF (FLG(1) .EQ. 0) THEN
      NMEX(1,CNT)=NR(1) * (1-VE(I)/VMAX(I))*DT
      DO 88 IIJJ = 1,CNT
      IF (IIJJ .LE. CNT) THEN
      IF (RSZEX(1,IIJJ) .EQ. 0.0D0) THEN
      SZEX(1,IIJJ)= SZEX(1,IIJJ) +
       GRT(1) * (DT)**0.5 * ((CNT-IIJJ+1)**0.5
       - (CNT-IIJJ)**0.5)
      ELSE
      SZEX(1,IIJJ)= SZEX(1,IIJJ) +
       RGRT(1,IIJJ) * (DT)**0.5 * ((CNT-IIJJ+1)**0.5
       - (CNT-IIJJ)**0.5)
      ENDIF
      ENDIF
88      CONTINUE
      DO 89 IIJJ = 1,CNT
      IF (SZEX(1,IIJJ) .GE. 0.0) THEN
```

```
C Calculations of capillarity effect

      MCAP=SFEN(1) * 4.47D-10**(3D0)/4.0D0/TK/1.380662D-23
       *(1-XAINST(DS(I),1))/(XCINST(DS(I),1)-XAINST(DS(I),1))
      RXAINST(DS(I),1,IIJJ)=(1+2*MCAP/SZEX(1,IIJJ))*XAINST(DS(I),1)
      IF(NR(1) .GT. 0.0D0) THEN
      IF (RXAINST(1,1,IIJJ) .LE. XBINST(DS(I),1)) THEN
      RSZEX(1,IIJJ) = SZEX(1,IIJJ)
      ELSE
      RSZEX(1,IIJJ) = 0.0D0
      ENDIF
      ENDIF
      IF (NR(1) .EQ. 0D0) THEN
      RSZEX(1,IIJJ) = SZEX(1,IIJJ)
      ENDIF
      ENDIF
89      CONTINUE
      ENDIF
      VES(1,CNT) = 0.0D0
      VE(1) = 0.0D0
      DO 125 JJ=1,CNT
      IF (RSZEX(1,JJ) .LE. 0.0D0) THEN
      RSZEX(1,JJ)=0.0D0
      NMEX(1,JJ)=0.0D0
      ENDIF
      VES(1,CNT) = VES(1,CNT) + NMEX(1,JJ) *
       4.0D0 * PI * (RSZEX(1,JJ))**3.0D0 / 3.0D0
125     CONTINUE
      IF (FLG(1) .EQ. 0) THEN
      SR(DS(I),1) = VES(1,CNT)*(XCINST(1,I)-XB(DS(I),1))
      VE(1) = VES(1,CNT)
      ENDIF
      DO 110 JJII=1,CNT
```

```
      IF(RSZEX(1,JJII) .GT. 0.0D0) THEN
      IF (SZMAX(1) .LE. RSZEX(1,JJII)) SZMAX(1)=RSZEX(1,JJII)
      IF (SZMINMB(1) .GE. RSZEX(1,JJII))
       SZMINMB(1)=RSZEX(1,JJII)
      ENDIF
110       CONTINUE
      NPEX(1) = 0.0D0
      TSZ=0.0D0
      DO 115 JJII=1,CNT
      IF (NMEX(1,JJII) .LE. 0.0D0 .OR.
       RSZEX(1,JJII) .LE. 2.3D-10) THEN
      NMEX(1,JJII)=0.0D0
      RSZEX(1,JJII)=0.0D0
      ENDIF
      TSZ=TSZ+NMEX(1,JJII)*RSZEX(1,JJII)
      NPEX(1) = NPEX(1) + NMEX(1,JJII)
115       CONTINUE
      IF (NPEX(1) .GT. 0.0D0) MSZEX(1)=TSZ/NPEX(1)

C Do not let VF fall below equilibrium value

      IF (VE(1) .LE. 0.0D0) VE(1) = 0.0D0
      IF (FLG(1) .EQ. 1) THEN
      FLG(I) = 2
      ENDIF
80      CONTINUE
      REG = 0
      IF (FLG(1) .EQ. 1) THEN
      FLG(1) = 2
      ENDIF
      IF (TINST .GE. T) THEN
      WRITE(*,199) TINST,VE(1),
       RSZEX(DS(I),1),MSZEX(1),NPEX(1),
```

```
     SZMAX(1)
     WRITE(OU2,199) TINST,VE(1),
     RSZEX(DS(I),1),MSZEX(1),NPEX(1),
     SZMAX(1)
     GOTO 40
     ELSE
     GOTO 50
     ENDIF
199      FORMAT(12D13.4)
     STOP
999      STOP
     END

C*************************************************************
C CALLS SUBROUTINE FOR GROWTH DEPENDING ON PARTICLE TYPE

     SUBROUTINE GROWTH(GRT,CTYPE,XB,XA,XC,XAX,DNB)
     INTEGER CTYPE
     IMPLICIT REAL*8(A-H,K-Z),INTEGER(I,J)
     IF (CTYPE .EQ. 1) THEN
     CALL LINEARGROWTH (GRT,XB,XA,XC,XAX,DNB)
     ENDIF
     IF (CTYPE .EQ. 2) THEN
     CALL PARABOLGROWTH(GRT,XB,XA,XC,XAX,DNB)
     ENDIF
     RETURN
     END

C*************************************************************
C CALCULATES THE GROWTH RATE FOR LINEAR GROWTH (I.E. NEEDLES)

     SUBROUTINE LINEARGROWTH(GR,XB,XA,XC,XAX,DNB)
     IMPLICIT REAL*8(A-H,K-Z),INTEGER(I,J)
```

```
      GR =2.0D0*DNB/(2.0D0*TRT) *(XB-XAX)*(XC-XAX)/(XC-XB)/(XC-XB)
      RETURN
      END

C*************************************************************
C CALCULATES THE CONSTANT (ALPHA3) FOR PARABOLIC GROWTH

      SUBROUTINE PARABOLGROWTH(GC,XB,XA,XC,XAX,DNB)
      IMPLICIT REAL*8(A-H,K-Z),INTEGER(I,J)

      IF(XB .GE. XA) THEN
      ALPHA = (2.0D0**(0.5D0)) * ((XB - XA) ** (0.5D0))
       / ((XC - XB) ** (0.5D0))
      ELSE
      ALPHA = -(2.0D0**(0.5D0)) * ((XA - XB) ** (0.5D0))
       / ((XC - XB) ** (0.5D0))
      ENDIF
      GC = ALPHA * (DNB**(0.5D0))
      RETURN
      END

C*************************************************************
C CALCULATES NUCLEATION RATE

      SUBROUTINE NURATE(NR1,DGCHEM,SFEN1,NAD1,VMAX,XB,TK)
      IMPLICIT REAL*8(A-H,K-Z),INTEGER(I,J)
      K = 1.380662D-23
      NA = 6.022045D23
      H = 6.626176D-34
      SHAPE=1.0D0
      DGVOL = (DGCHEM/VMAX) * 1.437D5
      ACTIVE = (240.0D3)/NA
      PI = 3.141592654
```

```
      N1 = NAD1
      DGCRIT1 = (16.0D0*PI*((SFEN1*SHAPE)**3.0D0))/
       (3.0D0*(DGVOL**2.0D0))
      EPENT1 = -(DGCRIT1 + ACTIVE)/(K * TK)
      CONST1 = XB * (N1 * K * TK)/H
      NR1 = CONST1 * DEXP(EPENT1)
      RETURN
END
C*************************************************************
C CALCULATES DIFFUSION COEFFICIENT OF NB IN FE

      SUBROUTINE DIFCO(DNB,TK)
      IMPLICIT REAL*8(A-H,K-Z),INTEGER(I,J)
      D0NB = 5.6D-04
      QNB = 286D03
      R = 8.314408694
      DNB = D0NB * DEXP(-QNB/(R*TK))
      RETURN
      END
```

2.11 Auxiliary Routines

The subroutines called by this program are :

GROWTH

LINEARGROWTH

PARABOLGROWTH

NURATE

DIFCO

2.12 Keywords

simultaneous precipitation reactions, capillarity, high strength low alloy steel

3. Program for multiple precipitation reactions

3.1 Provenance of Source Code

Nobuhiro FUJITA,
Phase Transformations Group,
Department of Materials Science and Metallurgy,
University of Cambridge,
Cambridge, U. K.

3.2 Purpose

To calculate the kinetics of carbides precipitating under diffusion–controlled growth and capillarity effect, with particular reference to the carbides in power plant steels. In the calculations, the first carbide is assumed to be cementite.

3.3 Specification

This is a self–contained program.

3.4 Description

The program reads thermodynamic data (*e.g.* from MTDATA or Thermocalc) from a pre–established database. It then calculates the evolution of volume fractions and particle sizes with time for up to 5 carbides forming simultaneously.

3.5 References

Bhadeshia, H. K. D. H.: *Materials Algorithms Project* (1985) .

3.6 Parameters

3.6.1 Input parameters

TK - double precision

Temperature in K.

DG - double precision array of size 5

Driving force for formation of carbides 1–5.

XB - double precision array of size 5

Mean composition of species 1–5 (mole fraction).

XC - double precision array of size 5 × 3

Equilibrium composition of species 1–3 in carbides 1–5 (mole fraction).

XA - double precision array of size 5 × 3

Composition of species 1–3 matrix in equilibrium with carbides 1–5 (mole fraction).

VMAX - double precision array of size 5

Maximum volume fraction of carbides 1–5.

SFEN - double precision array of size 5

Interfacial energy of carbides 1–5 (J m^{-2}).

NAD - double precision array of size 5

Nucleation site density factor for carbides 1–5.

CTYPE - double precision array of size 5

Morphology for carbides 1–5.

1 = Needle shaped

2 = Spherical

DS - double precision array of size 5

Species assumed to be controlling growth for phase 1–5.

CC - double precision

Mean carbon concentration (wt%).

GTHI - double precision

Thickness of cementite on boundaries (m).

THI - double precision

Thickness of cementite within grain (m).

DR - double precision

The ratio of cementite density between on boundaries and with in grains.

3.6.2 Output parameters

T - double precision

Time in seconds.

VE - double precision array of size 5

Volume fraction of carbides 1–5.

SZEX - double precision array of size 5 × the number of time steps

The particle size for carbides 1–5.

3.7 Error Indicators

None.

3.8 Accuracy

No information supplied.

3.9 Further Comments

The program is set to read the input data from an ASCII text file "datain.d"and to write the results to file "dataout.d". An sample version of "datain.d"is provided.

3.10 Example

An example for multiple alloy carbide precipitation, cementite, M_2C, M_7C_3 and $M_{23}C_6$ in a 3Cr1.5Mo steel.

3.10.1 Program data

Parameters	M_3C	M_2C	M_7C_3	$M_{23}C_6$
SFEN / J m^{-2}	0.0D0	0.20	0.256	0.277
NAD	1.0D0	5.0D-2	4.0D-2	8.00D-2
CTYPE	0.0D0	1.0D0	2.0D0	2.0D0
DS	1.0D0	1.0D0	1.0D0	1.0D0
VMAX	1.79D-2	1.40D-2	1.55D-2	2.24D-2
VEQ	0.0D0	0.0D0	0.0D0	2.24D-2
DG / J mol−1	0.0D0	-2.48D2	-2.24D2	-2.91D2
VDIV	1.79D-2	1.40D-2	1.55D-2	2.24D-2
XB	3.20D-2	3.20D-2	3.20D-2	3.20D-2
XC	5.08D-1	2.60D-2	2.00D-2	2.84D-2
XA	3.0D-2	7.00D-4	8.00D-4	3.00D-4
CC / wt%	0.10D0	–	–	–
GTHI / m	5.0D-8	–	–	–
THI / m	2.0D-8	–	–	–
DR	0.9D0	–	–	–

Parameters	Values
DT: Time step / s	200
TK: Temperature / K	873

3.10.2 Program results

Time / h	Volume fraction				Particle sizes		
	M_3C	M_2C	M_7C_3	$M_{23}C_6$	M_2C (maximum)	M_7C_3 (mean)	$M_{23}C_6$ (mean)
1.00D0	1.79D-2	2.17D-4	0.00D00	0.00D00	2.24D-7	0.00D00	0.00D00
2.00D0	1.79D-2	2.18D-4	1.62D-5	0.00D00	2.24D-7	1.68D-8	0.00D00
3.06D0	1.79D-2	2.19D-4	2.64D-5	2.11D-6	2.25D-7	2.10D-8	1.64D-8
5.00D0	1.79D-2	2.21D-4	4.22D-5	5.14D-6	2.25D-7	2.56D-8	2.53D-8
6.89D0	1.79D-2	2.22D-4	5.68D-5	7.88D-6	2.26D-7	2.88D-8	3.02D-8
1.07D1	1.79D-2	2.24D-4	8.62D-5	1.35D-5	2.26D-7	3.39D-8	3.73D-8
2.05D1	1.77D-2	2.29D-4	1.67D-4	3.01D-5	2.28D-7	4.33D-8	5.01D-8
3.96D1	1.58D-2	2.38D-4	3.50D-4	6.92D-5	2.31D-7	5.63D-8	6.72D-8
6.14D1	1.32D-2	2.49D-4	5.93D-4	1.23D-4	2.34D-7	6.77D-8	8.19D-8
8.53D1	1.01D-2	2.61D-4	8.97D-4	1.90D-4	2.38D-7	7.81D-8	9.52D-8
1.19D2	5.42D-3	2.81D-4	1.38D-3	2.99D-4	2.44D-7	9.04D-8	1.11D-7
1.32D2	3.46D-3	2.90D-4	1.60D-3	3.48D-4	2.47D-7	9.51D-8	1.17D-7
1.48D2	1.36D-3	3.03D-4	1.85D-3	4.06D-4	2.50D-7	1.00D-7	1.23D-7
2.05D2	0.00D00	3.48D-4	2.91D-3	6.46D-4	2.62D-7	1.17D-7	1.44D-7
2.85D2	0.00D00	3.80D-4	4.48D-3	1.01D-3	2.69D-7	1.35D-7	1.67D-7
3.19D2	0.00D00	3.85D-4	5.14D-3	1.17D-3	2.70D-7	1.41D-7	1.76D-7
3.56D2	0.00D00	3.86D-4	5.86D-3	1.35D-3	2.71D-7	1.48D-7	1.84D-7
3.97D2	0.00D00	3.86D-4	6.64D-3	1.55D-3	2.71D-7	1.54D-7	1.93D-7
4.43D2	0.00D00	3.81D-4	7.47D-3	1.77D-3	2.70D-7	1.60D-7	2.02D-7
4.94D2	0.00D00	3.73D-4	8.34D-3	2.01D-3	2.68D-7	1.66D-7	2.11D-7
5.52D2	0.00D00	3.59D-4	9.22D-3	2.28D-3	2.64D-7	1.72D-7	2.20D-7
6.16D2	0.00D00	3.40D-4	1.01D-2	2.56D-3	2.60D-7	1.77D-7	2.29D-7
7.67D2	0.00D00	2.83D-4	1.15D-2	3.20D-3	2.45D-7	1.85D-7	2.46D-7
8.56D2	0.00D00	2.48D-4	1.18D-2	3.54D-3	2.34D-7	1.87D-7	2.55D-7
9.56D2	0.00D00	2.10D-4	1.16D-2	3.92D-3	2.22D-7	1.86D-7	2.63D-7
1.07D3	0.00D00	1.73D-4	1.13D-2	4.34D-3	2.08D-7	1.84D-7	2.73D-7
1.48D3	0.00D00	7.07D-5	1.01D-2	5.96D-3	1.54D-7	1.77D-7	3.03D-7
2.06D3	0.00D00	8.96D-6	8.27D-3	8.27D-3	7.74D-8	1.66D-7	3.38D-7

3.10.3 Program text

```
C Program for simultaneous transformations
C up to five phases and three controlling species,
C especially for power plant steels.
C This includes empirical data for 3Cr1.5Mo steel

      IMPLICIT REAL*8(A-H,K-Z),INTEGER(I,J)
      DOUBLE PRECISION SFEN(5),R,NGRT(300000),TSZ(5)
      DOUBLE PRECISION NAD(5),XB(3,5),XA(3,5)
      DOUBLE PRECISION XC(3,5),VMAX(5),VDIV(5),V(5)
      DOUBLE PRECISION GMOD(3,5),DV(5),TRT(300000)
      DOUBLE PRECISION DG(5),GRT(5),DVEXT(5),MSZEX(5)
      DOUBLE PRECISION VEQ(5),VES(5,300000),VE(5),SZMAX(5)
      DOUBLE PRECISION GROLD(5),DX(3,5),XAINSTR(2,5)
      DOUBLE PRECISION RM(5),DGCHEM(5),CXBINST(5),GRTC(5,300000)
      DOUBLE PRECISION XBINST(3,5),RGRT(5,300000),SZMINMB(5)
      DOUBLE PRECISION NP(5),XAINSTI(3,5),XAINSTG(3,5)
      DOUBLE PRECISION NR(5),SR(3,5),SRT(3),TR(300000)
      DOUBLE PRECISION DXCI(3),DR,OGMOD(3,5),XCINST(3,5)
      DOUBLE PRECISION SZEX(5,300000),NPEX(5),SZ(300000)
      DOUBLE PRECISION CC,CXA(5),CXB(5),CXC(5),RSZEX(3,300000)
      DOUBLE PRECISION NMEX(5,300000),RCXA(5)
      DOUBLE PRECISION XAINST(3,5),RXAINST(3,5,300000)
      INTEGER REG,DS(5),CTYPE(5)
      INTEGER FLG(5),CNT,N,Y
      PI = 3.141592654
      BETA = 15.0D0
      IN1 = 1
      OU2 = 2
      OU3 = 3
      OPEN(UNIT = IN1,FILE="datain.d")
      OPEN(UNIT = OU2,FILE="dataout.d")
```

```
C IPHASE - Number of phases to calculate for
C ISPEC - Number of rate controlling diffusing species

      IPHASE = 4
      ISPEC = 1

C Read data

      WRITE(*,*)'IS 1st PHASE CEMENTITE? YSE=0, NO=1'
      READ(IN1,*) Y
      DO 20 I=1,IPHASE
      WRITE(*,*)'PHASE ',I
      WRITE(*,*)'INTERFACIAL ENERGY OF NUCLEUS (J/M2)?'
      READ(IN1,*) SFEN(I)
      WRITE(*,*)'SITE DENSITY (RELATIVE TO 1st Phase) ?'
      READ(IN1,*) NAD(I)
      WRITE(*,*)'PHASE TYPE (1 - NEEDLE, 2 - SPHERICAL) ?'
      READ(IN1,*) CTYPE(I)
      WRITE(*,*)'SPECIES CONTROLLING DIFFUSION (1,2,3...) ?'
      READ(IN1,*) DS(I)
      WRITE(*,*)'MAXIMUM VOLUME FRACTION ?'
      READ(IN1,*) VMAX(I)
      WRITE(*,*)'EQUILIBRIUM VOLUME FRACTION ?'
      READ(IN1,*) VEQ(I)
      WRITE(*,*)'DRIVING FORCE FOR FORMING VOLUME V OF PPT (J) ?'
      READ(IN1,*) DG(I)
      WRITE(*,*)'VOLUME FRACTION V (FOR DRIVING FORCE) ?'
      READ(IN1,*) VDIV(I)
      DO 25 II=1,ISPEC
      WRITE(*,*)'SPECIES', II
      WRITE(*,*)'MEAN CONCENTRATION IN ALLOY ?'
      READ(IN1,*) XB(II,I)
      WRITE(*,*)'EQUILIBRIUM CONCENTRATION OF SPECIES IN PRECIPITATE ?'
```

```
      READ(IN1,*) XC(II,I)
      WRITE(*,*)'EQUIM CONCENTRATION OF SPECIES IN MATRIX ?'
      READ(IN1,*) XA(II,I)
25      CONTINUE
20      CONTINUE
      WRITE(*,*)'TIME STEP ?'
      READ(IN1,*) DT
      WRITE(*,*)'ABSOLUTE TEMPERATURE ?'
      READ(IN1,*) TK

C Cementite
C This part if cementite is the first phase to form
C Necessary since it grows initially with paraequilibrium composition

      IF (Y.EQ.1) GOTO 10
      IF (Y .EQ. 0) THEN
      WRITE(*,*)'CARBON CONCENTRATION IN wt%'
      READ(IN1,*) CC
      WRITE(*,*)'RATIO OF PARTICLES AT BOUNDARY/INTRAGRANULAR?'
      READ(IN1,*) DR
      WRITE(*,*)'GRAIN BOUNDARY CEMENTITE THICKNESS / M ?'
      READ(IN1,*) GTHI
      WRITE(*,*)'INTRAGRANULAR CEMENTITE THICKNESS / M?'
      READ(IN1,*) THI

C Calculate initial number density of cementite particles
C Equation is from Nobu's experimental measurements

      NP(1) = CC * 2.23D22 - 1.0D21
      NPL = DR * NP(1)
      GBNP = (1-DR) * NP(1)
      ENDIF
      V(1) = VMAX(1)
```

```
      VL = V(1) * DR * (THI)**(3.0D0) / (DR*(THI)**(3.0D0) +
     (1-DR)*(GTHI)**(3.0D0))
      VGB = V(1) * (1-DR) * (GTHI)**(3.0D0) / (DR*(THI)**(3.0D0) +
     (1-DR)*(GTHI)**(3.0D0))
      XAINSTI(DS(I),1)=XA(DS(I),1)
      XAINSTG(DS(I),1)=XA(DS(I),1)
10      SRT(1) = 0.0D0
      ST = 0.0
      SR(DS(I),2) = 0.0
      ONXCI=XB(DS(I),1)
      GBXCI=XB(DS(I),1)
      FLG(1) = 0
      DO 11 I=1,IPHASE
      SR(DS(I),I) = 0.0D0
      CXB(I) = 0.007
      CXBINST (I) = 0.007
      XAINST(DS(I),I)=XA(DS(I),I)
      XBINST(DS(I),I)=XB(DS(I),I)
      XCINST(DS(I),I)=XC(DS(I),I)
      IF (TK .EQ. 873) CXA(I) = 0.000045
      IF (TK .EQ. 923) CXA(I) = 0.000119
      IF (TK .EQ. 973) CXA(I) = 0.000276
11      CONTINUE

C Calculate diffusion coefficient D (m2/s)

      CALL DIFCO(DCR,TK)

C Set initial state of soft-impingement

      DO 30 I=2,IPHASE
      GROLD(I) = 1.0D0
      OGMOD(1,I)=2.0D0
```

```
      FLG(I) = 0
30      CONTINUE

C Step time ***********

      CNT = 0
      TINST = 0.0D0
40      J = J + 1.0D0
      T = (20.0D0**(J/10.0D0)) + DT
      REG = 1
50      TINST = TINST + DT
      N = TINST / DT
      CNT = CNT + 1

C Calculations of soft-impingement
C SR(1) : solute 1 removed by reaction

      SR(DS(I),1) = VL*(ONXCI-XB(DS(I),1))+VGB*(GBXCI-XB(DS(I),1))
      SRT(1) = SR(DS(I),1) + (XCINST(1,2)-XB(1,2))*VE(2)
       + (XCINST(1,3)-XB(1,3))*VE(3)
       + (XCINST(1,4)-XB(1,4))*VE(4)
      VT=V(1)+VE(2)+VE(3)+VE(4)
      DX(DS(I),1)=SRT(1) / (1-VT)
      DX(2,1)=SRT(2) / (1-VT)
      GMOD(DS(I),1) = 1.0D0 - DX(DS(I),1)/(XB(DS(I),1)-XA(DS(I),1))
      XBINST(DS(I),1) = XB(DS(I),1)-DX(DS(I),1)
      XBINST(2,1) = XB(2,1)-DX(2,1)
      DO 60 I = 2,IPHASE
      DX(DS(I),I)=SRT(DS(I0) / (1-VT)
      GMOD(DS(I),I) = (XBINST(DS(I),I)-XAINST(DS(I),I))/
       (XB(DS(I),I)-XA(DS(I),I))
      M=XBINST(DS(I),I)-XAINST(DS(I),I)
      SAT=M/(XCINST(DS(I),I)-XAINST(DS(I),I))
```

```
      GMOD(DS(I),I)= 1- VE(I)/SAT
      IF (GMOD(DS(I),I) .LE. 0.0 .OR. M .LE. 0.0) THEN
      GMOD(DS(I),I) = 0.0D0
      ENDIF
      DGCHEM(I) = GMOD(DS(I),I)*DG(I)
      XBINST(DS(I),I) = XB(DS(I),I)-DX(DS(I),I)
60      CONTINUE

C Thermodynamic data for alloy carbides in 3Cr1.5Mo steel
C from MTDATA. Here, DS(I)=1 : Cr, IPHASE=2 : M2C
C IPHASE=3 : M7C3, IPHASE=4 : M23C6

      IF (TK .EQ. 873) THEN
      CXBINST(2) = XBINST(1,2)*1.1580D+00-3.6626D-2
      IF (CXBINST(2) .LE. 3.73D-6) CXBINST(2)=3.73D-6
      XAINST(1,2)=-1.5193D-3 + 1.1054D-7 / CXBINST(2)
      XCINST(1,2)= 14899.3*(XAINST(1,2))**(3.0D0)
       -954.17*(XAINST(1,2))**(2.0D0)+25.41*(XAINST(1,2))+0.014
      CXBINST(3) = -1.7794D-2+0.56949*XBINST(1,3)
      IF (CXBINST(3) .LE. 7.24D-6) CXBINST(3)=7.24D-6
      XAINST(1,3)=-2.5997D-3 + 1.9499D-7 / CXBINST(3)
      XCINST(1,3)=-0.003 + 31.679*XAINST(1,3)
       -21.762*(XAINST(1,3))**(2.0D0)
       -1.652D4*(XAINST(1,3))**(3.0D0)
      CXBINST(4) = -1.2881D-2+0.41596*XBINST(1,4)
      IF (CXBINST(4) .LE. 2.474D-6) CXBINST(4)=2.474D-6
      XAINST(1,4)=-1.5632D-3 + 5.7336D-8 / CXBINST(4)
      XCINST(1,4)=7.2083D1*XAINST(1,4)
       -5.5023D3*(XAINST(1,4))**(2.0D0)
       +2.2971D5*(XAINST(1,4))**(3.0D0)
       -3.7824D6*(XAINST(1,4))**(4.0D0)+1.7461D-3
      ENDIF
      IF (TK .EQ. 923) THEN
```

```
CXBINST(2) = XBINST(1,2)*1.1061D+00-3.4046D-2
IF (CXBINST(2) .LE. 2D-5) CXBINST(2)=2D-5
XAINST(1,2)=-3.7875D-3+6.1648D-7 / CXBINST(2)
XCINST(1,2)=7.6893D-3+24.693*XAINST(1,2)
 -831.95*XAINST(1,2)**2.0D0
 +1.2237D4*XAINST(1,2)**3.0D0
CXBINST(3) = -1.8547D-2+0.60209*XBINST(1,3)
IF (CXBINST(3) .LE. 0.0000264D+00) CXBINST(3)=0.0000264D+00
XAINST(1,3)=-8.6748D-3+1.5806D-6/CXBINST(3)
 -4.0135D-11/CXBINST(3)**2.0D0
 +6.7807D-16/CXBINST(3)**3.0D0
 -2.9085D-21/CXBINST(3)**4.0D0
XCINST(1,3)=-4.6059D-3+32.727*XAINST(1,3)
 -351.45*(XAINST(1,3))**(2.0D0)
 -6418.8*(XAINST(1,3))**(3.0D0)
CXBINST(4) = -1.3991D-2+0.45971*XBINST(1,4)
IF (CXBINST(4) .LE. 6.0D-6) CXBINST(4)=6.0D-6
XAINST(1,4)=-3.1939D-3+3.3091D-7/CXBINST(4)
 -2.0207D-12/(CXBINST(4))**2D0
 +5.8514D-18/(CXBINST(4))**3D0
XCINST(1,4)=1.5642D-2 +37.287*XAINST(1,4)
 -840.07*(XAINST(1,4))**(2.0D0)
ENDIF
IF (TK .EQ. 973) THEN
CXBINST(2) = XBINST(1,2)*1.1059D+00-3.4240D-2
IF (CXBINST(2) .LE. 7.3D-5) CXBINST(2)=7.3D-5
XAINST(1,2)=-4.5648D-3+2.3666D-6/CXBINST(2)
XCINST(1,2)=1.0258D-2+19.756*XAINST(1,2)-302.36*XAINST(1,2)**2.0D0
CXBINST(3) = -1.9420D-2+0.64279*XBINST(1,3)
IF (CXBINST(3) .LE. 0.000080D+00) CXBINST(3)=0.000080D+00
XAINST(1,3)=-5.3968D-3+2.4358D-6/CXBINST(3)
XCINST(1,3)=-4.0675D-3 + 32.165*XAINST(1,3)-536.66*(XAINST(1,3))**(2.0D0)
CXBINST(4) = -1.5394D-2+0.51697*XBINST(1,4)
```

```
      IF (CXBINST(4) .LE. 0.000024) CXBINST(4)=0.000024
      XAINST(1,4)=-3.7064D-3 + 1.0013D-6 /
       CXBINST(4)-8.0637D-12 * (1/CXBINST(4))**(2.0D0)
      XCINST(1,4)=1.0076D-2 +30.253*XAINST(1,4)-600.72*(XAINST(1,4))**(2.0D0)
      ENDIF
      DO 61 I = 2,IPHASE
      IF (XAINST(DS(I),I) .LE. 0.0) THEN
      XAINST(DS(I),I) = 0.0
      DGCHEM(I) = 0.0
      ENDIF
      IF (XCINST(DS(I0,I) .LE. 0.0) THEN
      XCINST(DS(I0,I) = 0.0
      DGCHEM(I) = 0.0
      ENDIF
      IF (XCINST(DS(I),I) .LE. XBINST(DS(I),I)) THEN
      XAINST(DS(I),I) = 0.0
      XCINST(DS(I),I) = 0.0
      DGCHEM(I) = 0.0
      ENDIF
61      CONTINUE

C Enrichment or dissolution of cementite

      IF (NPL .GT. 0.0) THEN
      RM(1) = (3.0D0 * VL)/((4.0D0 * NPL * PI))**(1.0D0/3.0D0)
      ELSE
      RM(1) = 0.0
      ENDIF
      IF (GBNP .GT. 0.0) THEN
      GBRM = (3.0D0 * VGB)/((4.0D0 * GBNP * PI)) **(1.0D0/3.0D0)
      ELSE
      GBRM = 0.0
      ENDIF
```

```
      IF (ONXCI .LT. XC(DS(I),1)) THEN
      DXCI(1) = ((4.0D0 * (DCR**(0.5)) * (XBINST(DS(I),1)
     -XAINSTI(DS(I),1))* (DT**(0.5)))/(THI * (PI**(0.5))))
      ENDIF
      IF (GBXCI .LT. XC(DS(I),1) ) THEN
      GBDXCI = ((4.0D0 * (DCR**(0.5)) * (XBINST(DS(I),1)
     -XAINSTG(DS(I),1))* (DT**(0.5)))/(GTHI * (PI**(0.5))))
      ENDIF
      ONXCI = ONXCI + DXCI(1)
      GBXCI = GBXCI + GBDXCI

C Cementite dissolves to provide solute to remaining precipitates
C Diffusion from cementite to precipitates controls the dissolution of
C cementite

      DO 70 I = 2,IPHASE
      IF (XBINST(DS(I),I) .LT. XAINSTI(DS(I),1)) THEN
      VINCI = (DCR * (XAINSTI(DS(I),1)- XBINST(DS(I),I)))
     /(XCINST(DS(I),1) - XAINSTI(DS(I),1))*
     ((NPL + NPEX(I))**(1.0D0/3.0D0))
      ENDIF
      IF (XBINST(DS(I),I) .LT. XAINSTG(DS(I),1)) THEN
      VINCG = (DCR * (XAINSTG(DS(I),1)- XBINST(DS(I),I)))
     /(XCINST(DS(I),1) - XAINSTG(DS(I),1))*
     ((GBNP + NPEX(I))**(1.0D0/3.0D0))
      ENDIF
      RM(1) = RM(1) - VINCI * DT
      GBRM = GBRM - VINCG *DT
      IF (RM(1) .GT. 0.0D0) THEN
      DVFLUXI = (4.0D0 * PI / 3.0D0) * ((RM(1)**3.0D0)
     -(RM(1)-VINCI*DT)**3.0D0)
      ELSE
      RM(1) = 0.0D0
```

```
      NPL = 0.0D0
      VL = 0.0D0
      DVFULXI = 0.0D0
      ENDIF
      IF (GBRM .GT. 0.0D0) THEN
      DVFLUXG= (4.0D0 * PI / 3.0D0) * ((GBRM**3.0D0) -
     -(GBRM-VINCI*DT)**3.0D0)
      ELSE
      GBRM = 0.0
      GBNP = 0.0
      VGB = 0.0D0
      ENDIF
      IF (DVFLUXI .LE. 0.0) DVFLUXI = 0.0
      IF (DVFLUXG .LE. 0.0) DVFLUXG = 0.0
      DV(1) = DV(1) + (NPL * DVFLUXI+
     GBNP * DVFLUXG)
      DVGB = DVGB + GBNP*DVFLUXG
      DVL = DVL + NPL*DVFLUXI
      NP(1) = NPL + GBNP
      V(1) = VL + VGB
70      CONTINUE
      DXCI(1) =0.0D0
      GBDXCI =0.0D0
      V(1) = V(1) - DV(1)
      VGB = VGB - DVGB
      VL = VL - DVL
      IF (V(1) .LT. 0.0D0) THEN
      V(1) = 0.0D0
      DV(1) = 0.0D0
      ENDIF
      IF (VL.LT. 0.0D0) VL = 0.0D0
      IF (VGB.LT. 0.0D0) VGB = 0.0D0
```

```
C Precipitation or dissolution of other phases

      DO 80 I = 2,IPHASE
      IF (FLG(I) .EQ. 0) THEN
      IF (DGCHEM(I) .LT. 0.0D0) THEN
      CALL NURATE(NR(I),DGCHEM(I),SFEN(I),NAD(I),VDIV(I),TK,
      XBINST(DS(I),I),CC)
      ELSE
      NR(I) = 0.0D0
      GRT(i)=0.0
      ENDIF

C Only have growth if composition is different from bulk composition

      IF (XCINST(DS(I),I) .GT. XAINST(DS(I),I) .AND.
       XCINST(DS(I),I) .GT. 0.0D0 .AND.
       XAINST(DS(I),I) .GT. 0.0D0 ) THEN
      IF(CTYPE(I) .EQ. 1) THEN

C Calculations of capillarity

      MCAP=SFEN(I) * 3.0D0**(0.5D0)/2.0D0*3.002D-10**(2.0D0)
       *4.724D-10 / TK/1.380662D-23/2
       *(1-XAINST(DS(I),I))/(XCINST(DS(I),I)-XAINST(DS(I),I))
      OGRT=-1.0D0
      DO 62 IJI=2,10000
      TRT(IJI) = IJI*1D-10
      XAINSTR(DS(I),I)=(1+2.0D0*MCAP/TRT(IJI))*XAINST(DS(I),I)
      IF (XBINST(DS(I),I) .GT. XAINSTR(DS(I),I)) THEN
      CALL GROWTH
       (GRT(I),CTYPE(I),XBINST(DS(I),I),XAINSTR(DS(I),I)
       ,XCINST(DS(I),I),DCR,
       TRT(IJI))
```

```
      IF (GRT(I) .GE. OGRT) THEN
      OGRT=GRT(I)
      ELSE
      GRT(I)=OGRT
      NGRT(CNT)=GRT(I)
      TR(CNT)=TRT(IJI)
      R = TRT(IJI)
      SZ(CNT)=SZEX(I,1)
      GOTO 71
      ENDIF
      ELSE
      IF (NGRT(IJI) .GT. NGRT(IJI-1)) THEN
      R=TRT(IJI-1)
      CALL GROWTH
       (GRT(I),CTYPE(I),XBINST(DS(I),I),XAINSTR(DS(I),I)
       ,XCINST(DS(I),I),DCR, R)
      ENDIF
      ENDIF
62      CONTINUE
      ENDIF
      IF (CTYPE(I) .EQ. 2) THEN
      DO 67 IIJJ=1,CNT
      IF (RSZEX(I,IIJJ) .EQ. 0.0D0) THEN
      CALL GROWTH
       (GRT(I),CTYPE(I),XBINST(DS(I),I),XAINST(DS(I),I)
       ,XCINST(DS(I),I),DCR,TR(IJI))
      ELSE
      CALL GROWTH
       (RGRT(I,IIJJ),CTYPE(I),XBINST(DS(I),I),
       RXAINST(DS(I),I,IIJJ)
       ,XCINST(DS(I),I),DCR,TR(IJI))
      ENDIF
67      CONTINUE
```

```
      ENDIF
      ELSE
      GRT(I) = 0.0D0
      ENDIF
      IF(XAINST(DS(I),I) .LE. 0.0 .OR.
       XCINST(DS(I),I) .LE. 0.0) THEN
      GRT(I)=0.0
      ENDIF

C For size distribution of particles nucleating/ growing

71      IF (FLG(I) .EQ. 0) THEN
      NMEX(I,CNT)=NR(I) * (1-VE(I)/VMAX(I))* DT
      GRTC(I,CNT)=GRT(I)
      DO 88 IIJJ = 1,CNT
      IF (CNT .LE. 0) SZEX(I,IIJJ) = 0.0
      IF (IIJJ .LE. CNT) THEN
      IF (CTYPE(I) .EQ. 2) THEN
      IF (RSZEX(I,IIJJ) .EQ. 0.0D0) THEN
      SZEX(I,IIJJ)= SZEX(I,IIJJ) +
       GRT(I) * (DT)**0.5 * ((CNT-IIJJ+1)**0.5
       - (CNT-IIJJ)**0.5)
      ELSE
      SZEX(I,IIJJ)= SZEX(I,IIJJ) +
       RGRT(I,IIJJ) * (DT)**0.5 * ((CNT-IIJJ+1)**0.5
       - (CNT-IIJJ)**0.5)
      ENDIF
      ELSE
      SZEX(I,IIJJ)=SZEX(I,IIJJ) + (GRT(I) * DT)
      ENDIF
      ENDIF
88      CONTINUE
      IF (CTYPE(I) .EQ. 2) THEN
```

```
      DO 89 IIJJ = 1,CNT
      IF (SZEX(I,IIJJ) .NE. 0.0) THEN

C Capillarity for M7C3. Here, IPHASE=3 : M7C3

      IF (IPHASE .EQ. 3) THEN
      MCAP=SFEN(I) * 9.54D-29/TK/1.380662D-23/7
       *(1-XAINST(DS(I),I))/(XCINST(DS(I),I)-XAINST(DS(I),I))
      ENDIF

C Capillarity for M23C6. Here, IPHASE=4 : M23C6

      IF (IPHASE .EQ. 4) THEN
      MCAP=SFEN(I) * 10.638D-10**(3D0)/4.0D0/TK/1.380662D-23/23
       *(1-XAINST(DS(I),I))/(XCINST(DS(I),I)-XAINST(DS(I),I))
      ENDIF
      RXAINST(DS(I),I,IIJJ)=(1+2.0D0*MCAP/
       SZEX(I,IIJJ))*XAINST(DS(I),I)
      RCXA(I)=(1+2.0D0*CCAP/SZEX(I,IIJJ))*CXBINST(I)
      IF(NR(I) .GT. 0.0D0) THEN
      IF (RXAINST(DS(I),I,IIJJ) .LE. XBINST(DS(I),I)) THEN
      RSZEX(I,IIJJ) = SZEX(I,IIJJ)
      ELSE
      RSZEX(I,IIJJ) = 0.0D0
      ENDIF
      ENDIF
      IF (NR(I) .EQ. 0D0) THEN
      RSZEX(I,IIJJ) = SZEX(I,IIJJ)
      ENDIF
      ENDIF
89      CONTINUE
      ENDIF
      VES(I,0) =0.0
```

```
      VES(I,CNT) = 0.0D0
      VE(I) = 0.0D0
      DO 125 JJ=1,CNT
      IF (CTYPE(I) .EQ. 1) THEN
      VES(I,CNT) = VES(I,CNT) + NMEX(I,JJ) *
       PI *(SZEX(I,JJ))
       **3.0D0/ 4.0D0 / ((BETA)**2.0D0)
      ELSE
      VES(I,CNT) = VES(I,CNT) + NMEX(I,JJ) *
       4.0D0 * PI *(SZEX(I,JJ))**3.0D0 / 3.0D0
      ENDIF
125       CONTINUE
      ELSE
      NPEX(I) = 0.0D0
      ENDIF
      VE(I) = 0.0D0
      VES(I,CNT) = 0.0D0
      DO 126 JJ=1,CNT
      IF (CTYPE(I) .EQ. 1) THEN
      VES(I,CNT) = VES(I,CNT) + NMEX(I,JJ) *
       PI *(SZEX(I,JJ))**3.0D0/ 4.0D0 / ((BETA)**2.0D0)
      ELSE
      VES(I,CNT) = VES(I,CNT) + NMEX(I,JJ) * 4.0D0 * PI *
       (SZEX(I,JJ))**3.0D0 / 3.0D0
      ENDIF
126       CONTINUE
      VE(I) = VES(I,CNT)
      DVEXT(I) = VES(I,CNT)-VES(I,CNT-1)
      SR(DS(I),I) = VE(I)*(XCINST(DS(I),I)-XB(DS(I),I))
      SZMAX(I)=0.0D0
      SZMINMB(I)=0.0D0
      DO 110 JJII=1,CNT
      IF (CTYPE(I) .EQ. 2) THEN
```

```
      IF(RSZEX(I,JJII) .GT. 0.0D0) THEN
      IF (SZMAX(I) .LE. RSZEX(I,JJII)) SZMAX(I)=RSZEX(I,JJII)
      IF (SZMINMB(I) .GE. RSZEX(I,JJII))
       SZMINMB(I)=RSZEX(I,JJII)
      ENDIF
      ELSE
      IF(SZEX(I,JJII) .GT. 0.0D0) THEN
      IF (SZMAX(I) .LE. SZEX(I,JJII)) SZMAX(I)=SZEX(I,JJII)
      IF (SZMINMB(I) .GE. SZEX(I,JJII))
       SZMINMB(I)=SZEX(I,JJII)
      ENDIF
      ENDIF
110       CONTINUE
      NPEX(I) = 0.0D0
      TSZ(I)=0.0D0
      DO 115 JJII=1,CNT
      IF (CTYPE(I) .EQ. 2) THEN
      IF (NMEX(I,JJII) .LE. 0.0D0 .OR.
       RSZEX(I,JJII) .LE. 0.0D0) THEN
      NMEX(I,JJII)=0.0D0
      RSZEX(I,JJII)=0.0D0
      ENDIF
      TSZ(I)=TSZ(I)+NMEX(I,JJII)*RSZEX(I,JJII)
      NPEX(I) = NPEX(I) + NMEX(I,JJII)
      ELSE
      IF (NMEX(I,JJII) .LE. 0.0D0 .OR.
       SZEX(I,JJII) .LE. 0.0D0) THEN
      NMEX(I,JJII)=0.0D0
      SZEX(I,JJII)=0.0D0
      ENDIF
      TSZ(I)=TSZ(I)+NMEX(I,JJII)*SZEX(I,JJII)
      NPEX(I) = NPEX(I) + NMEX(I,JJII)
      ENDIF
```

```
115      CONTINUE
     IF (NPEX(I) .GT. 0.0D0) MSZEX(I)=TSZ(I)/NPEX(I)
90       CONTINUE
     ENDIF

C Do not let VF fall below equilibrium value

     IF (VE(I) .LE. 0.0D0) VE(I) = 0.0D0
     IF (FLG(I) .EQ. 1) THEN
     FLG(I) = 2
     ENDIF
80       CONTINUE
     REG = 0
     IF (FLG(1) .EQ. 1) THEN
     FLG(1) = 2
     ENDIF
     IF (TINST .GE. T) THEN
     WRITE(*,199) TINST/3600.0D0,
      V(1),VE(2),VE(3),VE(4),
      SZMAX(2),SZMAX(3),SZMAX(4),
      MSZEX(2),MSZEX(3),MSZEX(4)
     WRITE(OU2,201) TINST/3600.0D0,
      V(1),VE(2),VE(3),VE(4),
      SZMAX(2),SZMAX(3),SZMAX(4),
      MSZEX(2),MSZEX(3),MSZEX(4),
      XBINST(1,4)
     GOTO 40
     ELSE
     GOTO 50
     ENDIF
199      FORMAT(13D13.4)
201      FORMAT(13D13.4)
999      STOP
```

```
      END

C*************************************************************
C CALLS SUBROUTINE FOR GROWTH DEPENDING ON PARTICLE TYPE

      SUBROUTINE GROWTH(GRT,CTYPE,XB,XAR,XC,XA,DCR,TRT)
      INTEGER CTYPE
      IMPLICIT REAL*8(A-H,K-Z),INTEGER(I,J)
      IF (CTYPE .EQ. 1) THEN
      CALL LINEARGROWTH (GRT,XB,XAR,XC,XA,DCR,TRT)
      ENDIF
      IF (CTYPE .EQ. 2) THEN
      CALL PARABOLGROWTH(GRT,XB,XA,XC,DCR)
      ENDIF
      RETURN
      END

C*************************************************************
C CALCULATES THE GROWTH RATE FOR LINEAR GROWTH (I.E. NEEDLES)

      SUBROUTINE LINEARGROWTH(GR,XB,XA,XC,DCR,TR)
      IMPLICIT REAL*8(A-H,K-Z),INTEGER(I,J)
      GR =2.0D0*DMO/(2.0D0*TR) *(XB-XAR)*(XC-XAR)/(XC-XB)/(XC-XB)
      RETURN
      END

C*************************************************************
C CALCULATES THE CONSTANT (ALPHA3) FOR PARABOLIC GROWTH

      SUBROUTINE PARABOLGROWTH(GC,XB,XA,XC,DCR)
      IMPLICIT REAL*8(A-H,K-Z),INTEGER(I,J)
```

```
C 'NATURAL' GROWTH PARAMETER (P. 488 CHRISTIAN)

      IF(XB .GE. XA) THEN
      ALPHA = (2.0D0**(0.5D0)) * ((XB - XA) ** (0.5D0))
       / ((XC - XB) ** (0.5D0))
      ELSE
      ALPHA = -(2.0D0**(0.5D0)) * ((XA - XB) ** (0.5D0))
       / ((XC - XB) ** (0.5D0))
      ENDIF
      GC = ALPHA * (DCR**(0.5D0))
      RETURN
      END

C*********************************************************
C CALCULATES AVERAGE PARTICLE SIZES

      SUBROUTINE SIZE(RM,CTYPE,GRT,VE,NP,BETA)
      IMPLICIT REAL*8(A-H,K-Z),INTEGER(I,J)
      INTEGER CTYPE
      PI = 3.141592654
      IF ((VE .EQ. 0.0D0) .OR. (NP .EQ. 0.0D0)) THEN
      RM = 0.0D0
      ELSE
      IF (CTYPE .EQ. 1) THEN
      RM = (4.0D0 * ((BETA**2.0D0) * VE)/(PI * NP)) ** (1.0D0/3.0D0)
      ENDIF
      IF (CTYPE .EQ. 2) THEN
      RM =((3.0D0 * VE)/(4.0D0 * NP * PI)) ** (1.0D0/3.0D0)
      ENDIF
      ENDIF
      RETURN
      END
```

```
C*************************************************************
C CALCULATES NUCLEATION RATE

      SUBROUTINE NURATE(NR1,DGCHEM,SFEN1,NAD1,VMAX,TK,XB,CC)
      IMPLICIT REAL*8(A-H,K-Z),INTEGER(I,J)
      K = 1.380662D-23
      NA = 6.022045D23
      H = 6.626176D-34
      SHAPE=1.0D0
      DGVOL = (DGCHEM/VMAX) * 1.437D5
      ACTIVE = (240.0D3)/NA
      PI = 3.141592654
      NUSITES = CC * 2.23D22 - 1D21
      N1 = NAD1 * NUSITES
      DGCRIT1 = (16.0D0*PI*((SFEN1*SHAPE)**3.0D0))/
     (3.0D0*(DGVOL**2.0D0))
      EPENT1 = -(DGCRIT1 + ACTIVE)/(K * TK)
      CONST1 = XB * (N1 * K * TK)/H
      NR1 = CONST1 * DEXP(EPENT1)
      RETURN
      END

C*************************************************************
C CALCULATES DIFFUSION COEFFICIENT OF CR IN FE

      SUBROUTINE DIFCO(DCR,TK)
      IMPLICIT REAL*8(A-H,K-Z),INTEGER(I,J)
      D0CR = 1.5D-04
      QCR = 240D03
      R = 8.314408694
      DCR = D0CR * DEXP(-QCR/(R*TK))
      RETURN
      END
```

3.11 Auxiliary Routines

The subroutines called by this program are :

GROWTH

LINEARGROWTH

PARABOLGROWTH

SIZE

NURATE

DIFCO

3.12 Keywords

simultaneous precipitation reactions, capillarity, power plant steel

APPENDIX TWO

Precipitation in a power plant steel containing silicon

1 Introduction

Silicon is an essential alloying element with an important role in the deoxidation of steel. However, it may also affect the precipitation of carbides and especially that of cementite (Owen, 1954). It is said that this is because silicon has a very low solubility in cementite. This may lead a retardation of M_2C precipitation, consequently $M_{23}C_6$ formation may be rapid. In this appendix, an attempt has been made to simulate precipitation sequence in 3Cr1.5Mo with and without silicon using the new kinetic model and to verify with experimental data.

2. Experimental work

Experimental procedure

A block of the 3Cr1.5Mo steel described in Chapter 4 was re–melted to introduce additional silicon. The re–melted samples was swaged to 3 mm diameter rods. The samples were heat–treated at 1200 °C for 3 days as homogenisation, quenched into water and then tempered at 600 °C, as described in Chapter 3, for a variety of time periods. Table 1 compares the chemical compositions of the two steels. Electrolytically extraction residues and carbon extracted replicas were made as described in Chapter 3. X–ray diffraction and TEM observations were carried out to characterise the carbides.

steel	C	Si	Mn	Cr	Mo
3Cr1.5Mo	0.1	-	0.98	2.98	1.50
1.5Si-3Cr1.5Mo	0.1	1.5	0.92	2.99	1.46

Table 1: Concentrations in wt% of the major alloying elements in 3Cr1.5Mo and its silicon–enhanced variant.

Effect of Si on carbide precipitation

Table 2 shows the results obtained using X–ray analysis of electrolytically extracted residues. The precipitation trends are similar for the two steels, although the rate of precipitation is clearly retarded in the silicon–rich steel. Fig. 1 shows transmission electron microstructures for both steels after tempering at 600 °C for 0.7 h. As expected, there are fewer precipitates in the Si–rich steel at a stage where most of the particles are cementite. The complete set of observations confirm that silicon can be used to control the development of microstructure in secondary hardening steels.

Specimens	Tempering condition	Precipitates detected			
		M_3C	M_2C	M_7C_3	$M_{23}C_6$
3Cr1.5Mo	600 °C - 0.7 h tempered	VS	VW	S	
	600 °C - 10 h tempered	S	W	S	W
	600 °C - 100 h tempered	W	S	S	S
	600 °C - 200 h tempered	W	S	S	S
1.5Si3Cr1.5Mo	600 °C - 0.7 h tempered	W			
	600 °C - 10 h tempered	W	VW	W	
	600 °C - 100 h tempered	VS	W	S	VW
	600 °C - 200 h tempered	VS	S	S	W

Table 2: X–ray analysis results for 3Cr1.5Mo and 1.5Si–3Cr1.5Mo steels tempered at 600 °C. The abbreviations, VS, S, W and VW mean very strong, strong, weak and very weak X–ray intensities, respectively.

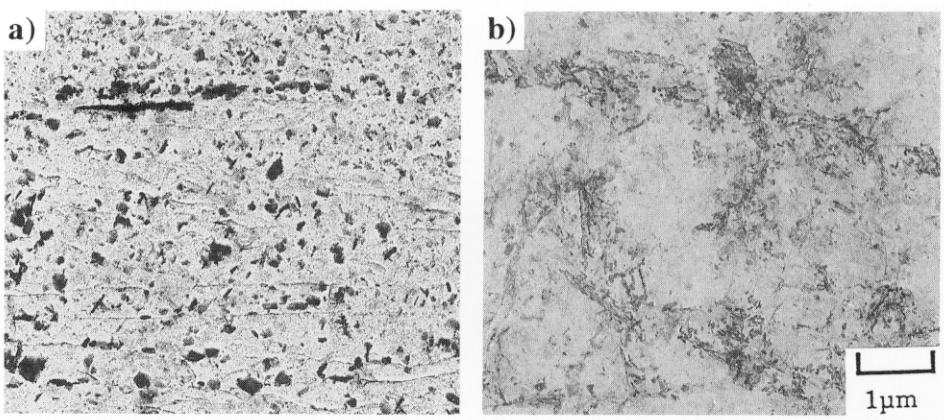

Figure 1: Transmission electron micrographs of (a) 3Cr1.5Mo and (b) 1.5Si–3Cr1.5Mo steels tempered at 600 °C for 0.7 h. The image are taken using extraction replica.

3. Thermodynamic calculations

The driving force for nucleation and the phase diagram for both steels were estimated using MTDATA. The driving forces for each alloy carbide nucleation were obtained assuming the following reactions:

$$\alpha + M_3C_{para} \rightarrow \alpha' + M_2C \quad (1a)$$

$$\alpha + M_3C_{para} \rightarrow \alpha'' + M_7C_3 \quad (1b)$$

$$\alpha + M_3C_{para} \rightarrow \alpha''' + M_{23}C_6 \quad (1c)$$

where α', α'' and α''' all represent the ferrite matrix coexisting with M_2C, M_7C_3 and $M_{23}C_6$ respectively. The reactions all began from a microstructure where the iron atom to substitutional solute atom ratio is uniform throughout (*i.e.* paraequilibrium). Table. 3 shows the calculation results of the free energy changes for the reactions. It is evident that an increase in the silicon concentration has led to a significant reduction in the free energy changes.

Steels	M_2C (1a)	M_7C_3 (1b)	$M_{23}C_6$ (1c)
3Cr1.5Mo	-222	-200	-266
1.5Si-3Cr1.5Mo	-178	-144	-216

Table 3: The free energy changes at 600 °C (J mol^{-1}) for each of the reactions described by equations 1.

4 Comparison between calculations and experiments

Using the same parameters shown in Table 7.2 and 7.3 in Chapter 7 for 3Cr1.5Mo steel, calculations for both steels has been done.

The calculations of volume fraction changes for each alloy carbide in both steels are shown in Fig. 2 along with the experimental results.

Si addition clearly seems to retard carbide sequence. This is because Si addition makes the driving force for each carbide nucleation small (Table 3). For this reason, especially M_7C_3 and $M_{23}C_6$ precipitation were significantly retarded. Although the calculations predict the correct

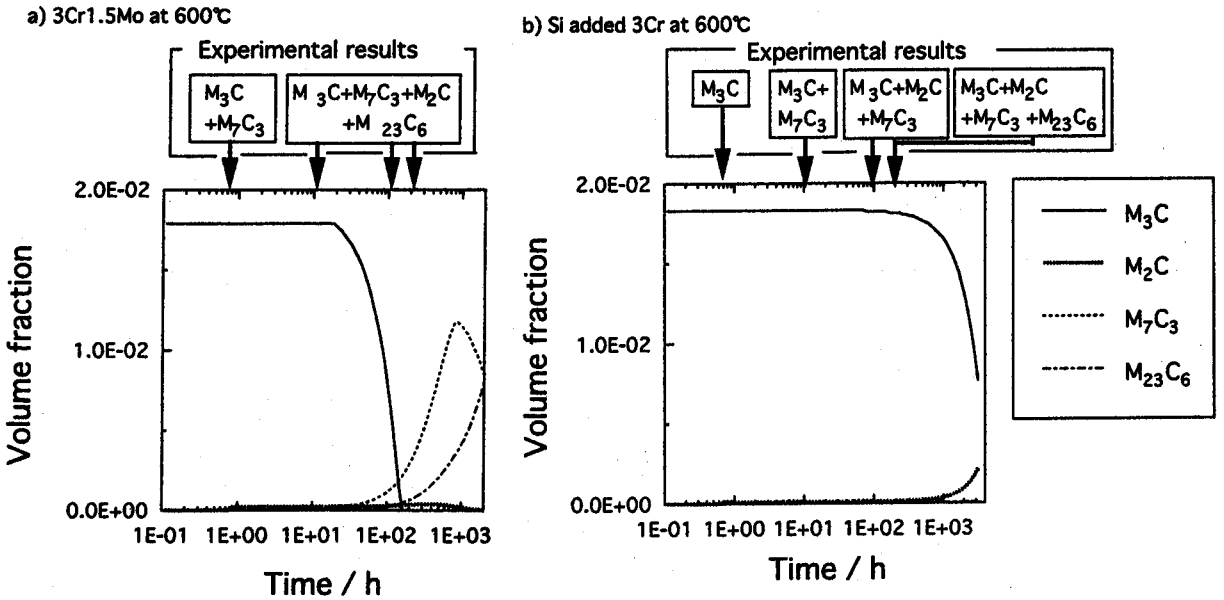

Figure 2: The calculations of multiple precipitation reactions at 600 °C by the new model for (a) a conventional 3Cr1.5Mo and (b) 1.5Si3Cr1.5Mo steels with experimental results.

trends, the detailed agreement with experimental data is not perfect for the silicon–modified steel. The reason for this is not clear. It is worth commenting in cementite precipitation in the early stage of tempering. Considering that the X–ray intensity of M_3C in Si added 3Cr1.5Mo steel changes from "weak" to "strong" between 0.7 h and 10 h, the calculations for Si added 3Cr1.5Mo steel are not in good agreement with experiments at the early tempering stage. In fact, even for a conventional 3Cr1.5Mo steel, the X–ray intensity of M_3C changed from "weak" to "very strong" for short tempering times between 0.05 h and 0.3 h at 600 °C (Table 4.1). This discrepancy may be caused by the assumption about cementite precipitation. As stated above, Si addition retarded cementite precipitation. According to Owen (1954), for the growth of ϵ carbide ($Fe_{2.4}C$) in Si added steels, it is necessary to remove Si from the vicinity of the carbide particle. However, the new model in this work does not include this kind of process for cementite formation but just solute enrichment. This may explain the luck of agreement

between calculations and experiments about cementite precipitation at the early tempering stages.

5. Summary

X–ray analysis results show that it is not completely justified, especially for Si–rich steel, to assume that the time required for cementite precipitation at 600 °C can be neglected. Nevertheless, in the absence of a model capable of treating this problem, calculations were conducted assuming a starting microstructure which is a paraequilibrium mixture of ferrite and cementite. The parameters used in the these calculations are as in Table 7.2 and 7.3. The results, which are presented in Fig. 2, show that whereas a general retardation of alloy carbide precipitation is predicted for the Si–rich steel, there are detailed discrepancies which could not be explained clearly.

APPENDIX THREE

Alloy carbide precipitation on grain boundaries

1 Introduction

As shown in Chapter 7, most of the $M_{23}C_6$ precipitated on boundaries between ferrite plates. The shape of particles appears anisotropic with growth being favoured parallel to the boundary plane.

An attempt is made here to see whether the collector–plate model, in which diffusion towards the precipitates is enhanced by the presence of the boundary, can be used to improve calculations.

2 Theory for grain boundary precipitation

Aaron and Aaronson's (1988) theory for the collector–plate considers two diffusion paths, one of which leads to thickening of the precipitate normal to the boundary plate and the other to lengthening along the grain boundaries. Fig. 1 shows how the solute is envisaged to arrive at the precipitate θ/matrix α interface. According to the theory, precipitate thickening is controlled by diffusion through the precipitation/matrix boundary diffusion and lengthening by volume diffusion. Considering mass conservation and Fick's law in each growth direction, thickness S and length R_l are given by:

$$S = 2\Phi t^{\frac{1}{2}} \text{ with } \Phi = \frac{2\delta D_b(c_r^{\alpha\theta} - c^{\alpha\theta})}{(1-\frac{\sqrt{2}}{2})g^2(c^{\theta\alpha} - c^{\alpha\theta})}, g = \left\{\frac{2D_v^{\frac{1}{2}}A(\overline{c} - c_r^{\alpha\theta})}{\pi^{\frac{3}{2}}r(c^{\theta\alpha} - c_r^{\alpha\theta})}\right\}^{\frac{1}{2}} \quad (1a)$$

$$R_l = gt^{\frac{1}{4}} \text{ with } g = \left\{\frac{2D_v^{\frac{1}{2}}A(\overline{c} - c_r^{\alpha\theta})}{\pi^{\frac{3}{2}}r(c^{\theta\alpha} - c_r^{\alpha\theta})}\right\}^{\frac{1}{2}} \quad (1b)$$

where δ is the thickness of the boundary, D_b and D_v are the boundary and volume diffusion coefficients respectively, r is the radius of curvature at the triple conjunction, A $(=d_v^2)$ is area of collector–plate.

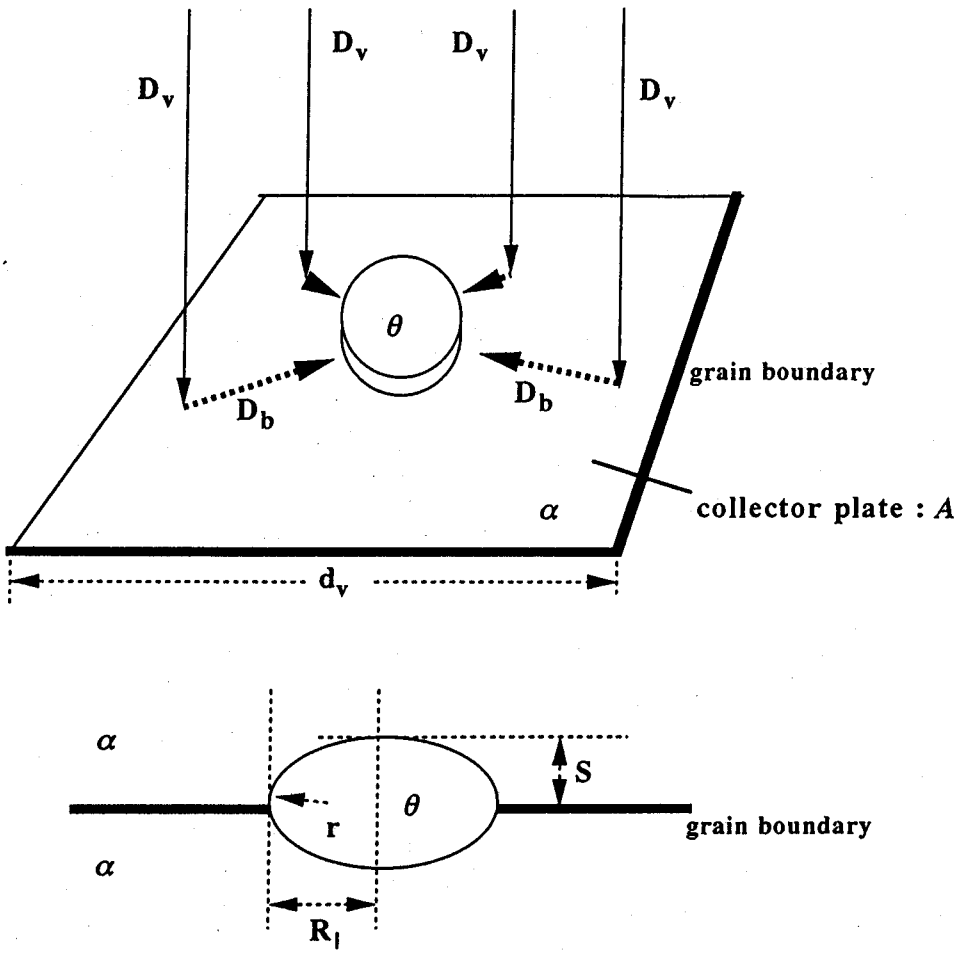

Figure 1: Schematic illustration of grain boundary precipitation θ with matrix α (Aaron and Aaronson, 1988).

3 Comparison between calculations and experiments

A calculation was done for the case where all $M_{23}C_6$ precipitates on grain boundaries for a sample of 3Cr1.5Mo steel tempered at 700 °C. Table 1 shows the parameters used for the calculations.

The interfacial energies of M_2C and M_7C_3 are as in Chapter 7. It is assumed that the boundary diffusion coefficients for Cr at α/α and α/θ boundaries are identical. The values of D_{b0} and δ are due to Fridberg *et al.* (1969), Huntz *et al.* (1967) and Fisher (1951).

Exploitation of the theory requires more microstructural parameters, A and r, both of which

The parameters	The values in use
Number density of sites for M_2C	1.23×10^{21} m^{-3}
Number density of sites for M_7C_3	4.92×10^{19} m^{-3}
Number density of sites for $M_{23}C_6$	2.46×10^{16} m^{-3}
Interfacial energy of M_2C	0.200 J m^{-2}
Interfacial energy of M_7C_3	0.256 J m^{-2}
Interfacial energy of $M_{23}C_6$ on grain boundaries	0.20 J m^{-2}
δD_0 in grain boundary diffusion coefficient for Cr	8.0×10^{-14} m^{3}s^{-1}
Grain boundary width : δ	5.0×10^{-10}m
Activation energy for grain boundary diffusion of Cr	195 $\times 10^3$ J mol^{-1}
Area of collector plate : A	5.0×10^{-13} m^2
Tip radius at triple conjunction : r	5.0×10^{-8} m

Table 1: Details of the parameters used in the calculations.

are difficult to justify and are treated here as fitting parameters.

Transmission electron microscopy was used to measure the thickness S and the length R_l of $M_{23}C_6$ on grain boundaries, averaging the data over 20 particles.

Fig. 2 shows that although a reasonable fit can be obtained between experiments and theory, the utility of following these procedures is, in the present context, doubtful given the increase in the number of fitting parameters.

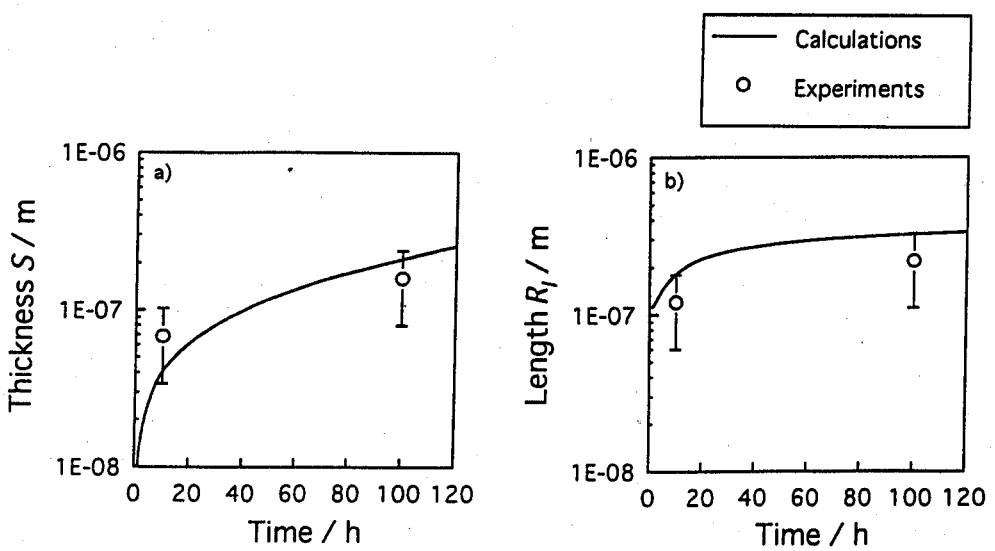

Figure 2: Calculated and measured values of (a) the thickness S and (b) the length R_l of $M_{23}C_6$ on grain boundaries following tempering at 700 °C.

APPENDIX FOUR
Solubility products

1. Introduction

Thermodynamic data form an essential foundation for kinetic theory. Unfortunately, they are not always available so an attempt is made here to get useful information on the precipitation of Fe_3Nb_3C type carbide precipitation in ferritic stainless steel using solubility products.

2. Material

Table 1 shows the chemical composition of Nb alloyed ferritic stainless steel, which is used in the manufacture of exhaust manifolds for cars. This is because of the requirement to reduce emission using high exhaust gas temperatures of over 900 °C. Niobium in solid solution is very effective to improve the high temperature strength (Fujita *et al.*, 1996). It is important to know how much of the niobium precipitates and the fraction which remains in solid solution.

steel	C	Si	Mn	Cr	Nb	N
19Cr–0.8Nb	0.014	0.3	0.2	19.6	0.78	0.016

Table 1: Concentration in wt% of the major alloying elements in the Nb alloyed ferritic stainless steel studied here.

Table 2 shows the results of chemical and X–ray analysis of extracted residues from the samples aged at 950 °C and 1000 °C for 19Cr–0.8Nb wt% steel. In the early stage of aging, Nb(C,N), Laves phase : $(Fe,Cr)_2Nb$ and Fe_3Nb_3C were clearly detected. When the aging time was greater, the intensity of Laves phase became weaker and Fe_3Nb_3C was found to be a prominent phase. According to a chemical analysis of extracted residues, most of the nitrogen precipitated, probably as NbN. The ratio of atomic fractions of Fe to Nb approached unity as the aging time increased. This implies that Laves phase, which contains more iron than required by stoichiometry in Fe_3Nb_3C, dissolves to give way to Fe_3Nb_3C. This in turn indicates that the equilibrium phases in 19Cr–0.8Nb steel should be NbN and Fe_3Nb_3C.

Aging condition	Concentration in precipitates / wt%				Detected precipitation		
	Nb	N	Fe	Cr	Nb(C,N)	Laves	Fe_3Nb_3C
1000 °C - normalised	0.204	0.014	0.214	0.042	S	W	VS
950 °C - 1.0 h aged	0.407	0.015	0.326	0.051	VS	VS	VS
950 °C - 50 h aged	0.432	0.013	0.247	0.044	VW	VW	VS
950 °C - 100 h aged	0.443	0.014	0.234	0.041	VW	-	VS
1000 °C - 20 h aged	0.362	0.015	0.171	0.037	W	-	VS

Table 2: X–ray and chemical analyses of extraction residues from 19Cr–0.8Nb wt% steel. VW means very weak, W means weak, S means strong and VS means very strong X–ray intensities respectively.

3. Parameters for calculations

Nucleation

The driving force for nucleation can be obtained with the free energy change for precipitation reactions as described in Chapter 2.

$$\Delta G_n = \frac{\Delta G}{v^\beta V_\beta} \tag{1}$$

where ΔG_n and ΔG are the driving force for nucleation and overall free energy change of the precipitation reaction respectively. Fe_3Nb_3C will precipitate from Nb supersaturated ferrite as follows:

$$3[Nb] + 3[Fe] + [C] \rightleftharpoons Fe_3Nb_3C \tag{2}$$

where $[Nb]$, $[Fe]$ and $[C]$ are the concentrations in solution in ferrite. The activity of pure solid Fe_3Nb_3C can be taken to be unity and assuming that the activities of the other elements are equivalent to the concentrations, the free energy change of precipitation ΔG is given by:

$$\Delta G = \Delta G_0 + RT\ln\frac{1}{[Nb]^3[Fe]^3[C]} \tag{3}$$

Since at equilibrium, $\Delta G = 0$.

$$\Delta G_0 = RT\ln[Nb]^3[Fe]^3[C] \tag{4a}$$

so that,

$$\ln[Nb]^3[C] = \frac{A_2}{T} + B_2 \text{ with } A_2 = \frac{\Delta G_0}{R},\ B_2 = -\ln[Fe]^3 \qquad (4b)$$

This is known as the solubility product which of course can be used to estimate ΔG, if values of A_2 and B_2 are available. As shown in Table 2, the amounts of Nb in solid solution finally are 0.35 wt% and 0.44 wt% at 950 °C and 1000 °C respectively. These are assumed to represent the equilibrium concentrations. Assuming that all the nitrogen is precipitated as NbN and that [Fe] is constant, it is possible to calculate the equilibrium volume fraction and concentrations in the ferrite at the interface for Nb and C. Tables 3 and 4 shows the calculated equilibrium volume fraction and concentrations respectively.

Temperature	Equilibrium volume fraction of Fe_3Nb_3C
950 °C	4.26×10^{-3}
1000 °C	3.05×10^{-3}

Table 3: Calculated equilibrium volume fractions of Fe_3Nb_3C at 950 °C and 1000 °C for 19Cr–0.8Nb steel.

Temperature	$x_{Nb}^{\alpha\beta}$	$x_{Nb}^{\beta\alpha}$	$x_C^{\alpha\beta}$	$x_{Nb}^{\beta\alpha}$
950 °C	2.08×10^{-3}	4.29×10^{-1}	3.68×10^{-5}	1.43×10^{-1}
1000 °C	2.61×10^{-3}	4.29×10^{-1}	2.10×10^{-4}	1.43×10^{-1}

Table 4: Calculated equilibrium mole fractions at the interface Fe_3Nb_3C β / ferrite α for Nb and C. $x^{\alpha\beta}$ and $x^{\beta\alpha}$ represent equilibrium mole fractions in matrix and in precipitate respectively.

By plotting the relationship between "ln[Nb]^3[C]" and "$\frac{1}{T}$", the constants A_2 and B_2 in the equation 4b can be obtained. Table 5 shows the calculated values of A_2 and B_2.

Constant	Values
A_2/K^{-1}	–75432
B_2	32.94

Table 5: Calculated values of A_2 and B_2.

Growth

For growth, as described in Chapters 5 and 6, it is necessary in a multicomponent steel to deal with tie–line shifting due to soft–impingement. The tie–line shifting will basically happen along the phase boundary between the precipitate and matrix. Because the solubility product corresponds to the phase boundary, this information can be obtained using equation 4b.

4. Calculations of kinetics for Fe_3Nb_3C in ferritic stainless steel

Kinetic calculations were carried out using parameters shown in Table 6. The diffusion coefficient of Nb in ferrite is due to Fridberg *et al.* (1969).

The microstructural parameters	The values in use
Number density of sites	1.0×10^{16} m^{-3}
Interfacial energy	0.27 J m^{-2}
D_0 in Diffusion coefficient for Nb	1.3×10^{-4} m^2 s^{-1}
Activation energy for diffusion of Nb	240×10^3 J mol^{-1}

Table 6: The parameters used in the kinetic calculations of Fe_3Nb_3C precipitation in 19Cr–0.8Nb steel.

Fig. 1 shows the changes of volume fraction, mean particle size and number density with aging time at 1000 °C. Unfortunately, there were not appropriate data for verification. Therefore, it is necessary to adjust some of parameters, the number density of sites and interfacial energy, with experimental data. However, the calculations represent the whole of precipitation process from nucleation to coarsening (as in Chapter 6). Note that the calculations are so sensitive to solubility product data that it is vital to use a precise data of solubility product.

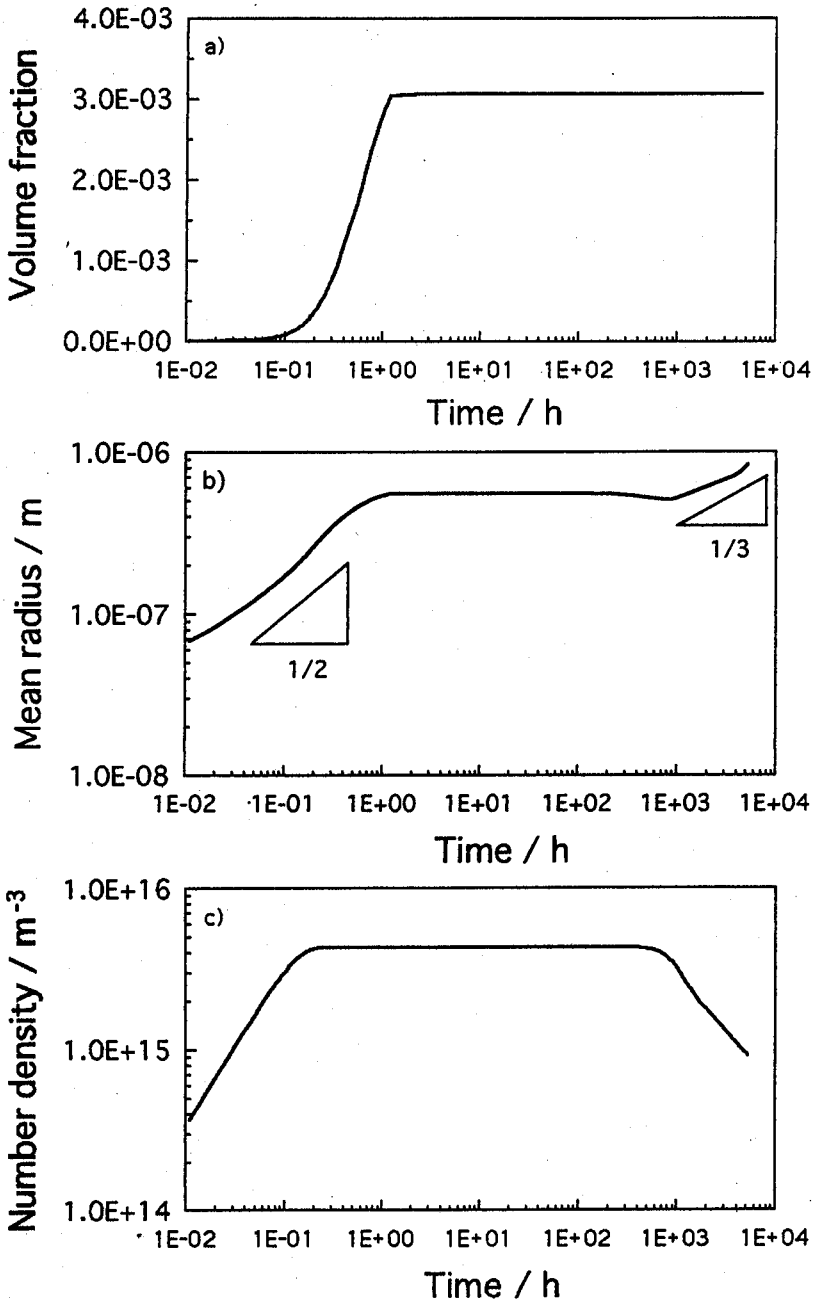

Figure 1: Changes of (a) volume fraction, (b) mean particle size and (c) number density of Fe_3Nb_3C with aging time at 1000 °C for 19Cr–0.8Nb wt% steel.

5. Summary

New experimental data giving the solubility product have been generated for Fe_3Nb_3C in a ferritic stainless steel. Although there is no verification of the resulting kinetic calculations, the precipitation kinetics seem reasonable.

REFERENCES

Aaron, H. B. and Aaronson, H. I.: *Acta Metallurgica* **18** (1988) 699–711.

Aaronson, H. I. and Domain, H. A.: *Transactions of the Metallurgical Society of AIME* **236** (1966) 781–796.

Akamatsu, Matsumura, Y., S., Senuma, T. Yada, H. and Ishikawa, S.: *Tetsu to Hagane* **75** (1989) 933–940.

Akamatsu, S., Senuma, T. and Hasebe, M.: *Iron and Steel Institute of Japan International* **32** (1992) 275–282.

Andersson, J–O., Höglund, L. and , J.: *Fundamentals and Applications of Ternary Diffusion,* ed. Purdy, G. R., Pergamon Press, New York (1990) 153–163.

Andrews, K. W., Dyson, D. J. and Keown, S. R.: *Interpretation of Electron Diffraction Patterns,* Hilger and Watts, London (1967) .

Ashby, M. F. and Ebeling, R.: *Transactions of the Metallurgical Society of AIME* **236** (1966) 1396–404.

Avrami, M.: *Journal of Chemical Physics* **7** (1939) 1103–1112.

Avrami, M.: *Journal of Chemical Physics* **8** (1940) 212–224.

Avrami, M.: *Journal of Chemical Physics* **9** (1941) 177–184.

Baker, R. G. and Nutting, J.: *Journal of the Iron and Steel Institute* **192** (1959) 257–268.

Balluffi, R. G. , Cohen, M. and Averbach, B. L.: *Transactions of the American Society of Metals* **43** (1951) 497–526.

Barrett, C. R. and Sherby, O. D.: *Transactions of the American Institute of Mining and Metallurgical Engineers* **233** (1965) 1116–1119.

Beech, J. and Warrington, D. H.: *Journal of Iron and Steel Institute* **204** (1966) 460–468.

Bhadeshia, H. K. D. H.: *Progress in Materials Science* **29** (1985) 321–386.

Bhadeshia, H. K. D. H.: *Materials Science and Technology* **5** (1989) 131–137.

Bhadeshia, H. K. D. H.: *Bainite in steels,* The institute of Materials (1992) .

Bhadeshia, H. K. D. H.: *Materials Algorithms Project* (1985) .

Bhadeshia, H. K. D. H.: *Solid–Solid Phase Transformations '99,* ed. Koiwa, M., Otsuka, K. and Miyazaki, T., Japan Institute of Metals (1999a) 1445–1452.

Bhadeshia, H. K. D. H.: *Materials Science and Engineering* **A273–275** (1999b) 58–66.

Björbo, A.: *Microstructural changes in a 12Cr steel during creep", Report of Royal Institute of Technology,* Sweden (1994) 11.

Bon, A. Le., Vernis, J. R. and Rossard, C.: *Metal Science* **9** (1975) 36–40.

Cahn, J. W.: *Acta Metallurgica* **4** (1956) 449–459.

Christian, J. W.: *Theory of Transformations in Metals and Alloys, Part 1 2nd Edition,* Pergamon Press, Oxford (1975) .

Coates, D. E.: *Metallurgical Transactions* **4** (1977) 2313–2325.

Dutta, B. and Sellars, M.: *Materials Science and Technology* **3** (1987) 197–206.

Esaka, K., Koyama, K., Matsumura, Y. and Tashiro, M.: *Proceedings of International Conference on HSLA Steels '85,* The Chinese Society of Metals (1985) 959–968.

Fisher, J. C.: *Journal of Applied Physics* **22** (1951) 74–77.

Fridberg, J., Törndahl, L-E. and Hillert, M.: *Jernkontorets Annaler* **153** (1969) 263–276.

Fujita, N., Ohmura, K., Kikuchi, M., Suzuki, T., Funaki, S. and Hiroshige, I.: *Scripta Materialia* **35** (1996) 705–710.

Gustafson, Å., Höglund, L. and , J.: *Advanced Heat Resistant Steel for Power Generation,* ed. Viswanathan, R. and Nutting, J., The Institute of Materials (1998) 270–276.

Hall, M. G., Kinsman, K. R. and Aaronson, H. I.: *Metallurgical Transactions A* **3A** (1972) 1320–1322.

Hillert, M.: *Jernkontorets Annaler* **141** (1957) 757–789.

Hippsley, C. A.: *Metal Science* **15** (1981) 137–147.

Hirsch, P. B., Howie, A., Nicholson, R. B., Pashley, D. W., and Whelan, M.J.: *Electron Microscopy of Thin Crystals, Butterworths, London* (1969) .

Hodson, S. M.: *MTDATA-Metallurgical and Thermochemical Databank,* National Physical Laboratory, Teddington, U. K. (1989) .

Honeycombe, R. W. K. and Bhadeshia, H. K. D. H.: *Steels, Microstructure and Properties 2nd ed.,* Edward Arnold (1995) .

Hultgren, A.: *Transactions of the American Society of Metals* **39** (1947) 915–968.

Huntz, A.–M., Aucotutier, M. and Lacombe, P.: *Compt. Rend., Sér. C* **265** (1967) 554–557.

Jack, D. H. and Jack, K. H.: *Materials Science and Engineering* **11** (1973) 1–27.

Johnson, W. A. and Mehl, R. F.: *Transactions of the American Institute of Mining and Metallurgical Engineers* **135** (1939) 416–458.

Jones, S. J. and Bhadeshia, H. K. D. H.: *Acta Metallurgica* **45** (1997) 2911–2920.

Kasuya, T., Ichikawa, K., Fujii, M. and Bhadeshia, H. K. D. H.: *Materials Science and Technology* **15** (1999) 471–473.

Kirkaldy, J. S.: *Canadian Journal of Physics* **36** (1958) 907–916.

Klueh, R. L.: *Materials Science and Engineering* **35** (1978) 239–253.

Klueh, R. L. and Nasreldin, A. M.: *Metallurgical Transactions A* **18A** (1987) 1279–1290.

Kougami, K. and Isaka, H.: *Tetsu to Hagane* **76** (1990) 1043–1052.

Kuo, K.: *Journal of the Iron and Steel Institute* **173** (1953) 363–375.

Kurosawa, F: *Current Advanced in Materials and Processes, Report of ISIJ Meeting* **5** (1992) 434–437.

Kurosawa, F and Saeki, M.: *Tetsu to Hagane* **76** (1990) 483–494.

Kurzydlowski, K. J. and Zielinski, W.: *Metal Science* **18** (1984) 223–224.

Leitnaker, J. M., Klueh, R. L. and Laing, W. R.: *Metallurgical Transactions A* **6A** (1975) 1949–1955.

Lifshitz, I. M. and Slyozov, V. V.: *Soviet Physics JETP* **35** (1959) 331–339.

Lifshitz, I. M. and Slyozov, V. V.: *Journal of Physics and Chemistry of Solids* **19** (1961) 35–50.

Liu, W. J., and Jonas, J. J.: *Metallurgical Transactions* **19A** (1988) 1403–1415.

Masuyama, F.: *Advanced Heat Resistant Steel for Power Generation,* ed. Viswanathan, R. and Nutting, J., The Institute of Materials (1998) 33–48.

McLean, D.: *Mechanical Properties of Metals,* John Wiley Sons, Inc. USA (1962) .

Metals Data Book, issued by The Japan Institute of Metals (1993) .

Meyer, L., Heisterkamp, F. and Musechenborn, W.: *Microalloying '75,* Union Carbide Corporation, New York (1976) 153–167.

Miyahara, K., Hwang, J. H., Shimoide, Y., Iwamoto, T. and Hosoi, Y.: *Journal of Japan Institute of Metals* **59** (1995) 512–518.

Miyazaki, T.: *Solid–Solid Phase Transformations '99,* ed. by Koiwa, M., Otsuka, K. and Miyazaki, T., Japan Institute of Metals (1999) 15–22.

Nutting, J.: *Advanced Heat Resistant Steel for Power Generation,* ed. by Viswanathan, R. and Nutting, J., The Institute of Materials (1998) 12–30.

Okamoto, R. and Suehiro, H.: *Tetsu to Hagane* **84** (1998) 650–657.

Owen, S. W.: *Transactions of the American Society for Metals* **46** (1954) 813–828.

Pilling, J. and Ridley, N.: *Metallurgical Transactions A* **13A** (1982) 557–563.

Pitch, W. and Schrader, A.: *Archiv fuer das Eisenhuttenwesen* **29** (1958) 715–721.

Purdy, G. R.: *Materiel Science Journal* **5** (1971) 81–84.

Robson, J. D.: *Ph.D. Thesis,* University of Cambridge, U. K. (1996) .

Robson, J. D. and Bhadeshia, H. K. D. H.: *Materials Science and Technology* **13** (1997a) 631–639.

Robson, J. D. and Bhadeshia, H. K. D. H.: *Materials Science and Technology* **13** (1997b) 640–644.

Rudberg, E.: *Jernkontorets Annaler* **136** (1952) 91–112.

Saito, Y., Shiga, C. and Enami, T.: *Proceedings of International Conference on Physical Metallurgy of Thermomechanical Processing of Steel and Other Metals,* ed. Tamura, I., Japan **2** (1988) 753–760.

Sellars, M.: *Materials Science Forum* **284-286** (1998) 73–82

Senior, B. A.: *Materials Science and Engineering* **119A** (1989) L5-L8.

Shaw, S. W. K. and Quarrell, A. G.: *Journal Iron and Steel Institute* **185** (1957) 10–22.

Smith, E. and Nutting, J.: *British Journal of Applied Physics* **7** (1957) 214–217.

Speich, G. R.: *Transactions of the American Institute of Mining and Metallurgical Engineers* **245** (1969) 2553–2564.

Takahashi, M. and Bhadeshia, H. K. D. H.: *Materials Science Technology* **6** (1990) 592–603.

Tamura, I., Ouchi, C., Tanaka, T. and Sekine, H.: *Thermomechanical Processing of High strength Low Alloy Steels,* Butterworths (1988) .

Tanaka, T.: *International Metals Review* **26** (1981) 185–212.

Thomson, R. T. and Bhadeshia, H. K. D. H.: *Materials Science and Technology* **10** (1994a) 193–203.

Thomson, R. T. and Bhadeshia, H. K. D. H.: *Materials Science and Technology* **10** (1994b) 205–208.

Thomson, R. T.: *Ph.D. Thesis,* University of Cambridge, U. K. (1992) .

Trivedi, R.: *Acta Metallurgica* **18** (1970) 287–296.

Tunney, R. J., Lorimer, G. W. and Ridley, N.: *Metal Science* **12** (1978) 271–276.

Turnbull, D. and Fisher, J. C.: *Journal of Chemical Physics* **17** (1949) 71–73.

Venugopalan, D. and Kirkaldy, J. S.: *Hardenability Concepts with Applications to Steel, AIME Conference,* New York (1978) 249–218.

Vitek, J. M. and David, S. A.: *Metallurgical Transactions A* **21A** (1990) 2021–2036.

Vyrostkova, A., Kroupa, A, Janovec, J. and Svoboda, M.: *Acta Metallurgica* **46** (1998) 31–38.

Wagner, C: *Zeitshrift Elektochemie* **65** (1961) 581–591.

Wert, C. and Zener, C.: *Journal of Applied Physics* **21** (1950) 5–8.

Woodhead, J. and Quarrell, A. G.: *Journal of Iron and Steel Institute* **203** (1965) 605–620.

Yakel, H. L.: *International Metals Reviews* **30** (1985) 17–40.

Yamanaka, M., Otoguro, Y., Miura, F. and Zaizen, T.: *Seitetu Kenkyu,* Nippon Steel Corporation, Japan **331** (1967) 33–39.

Zener, C.: *Transactions of the American Institute of Mining and Metallurgical Engineers* **167** (1946) 550–595.

Zener, C quoted by Smith, C. S.: *Transactions of the American Institute of Mining and Metallurgical Engineers* **175** (1948) 15–51.